STUDY OF CONE PENETRATION IN SILICA SANDS USING DIGITAL IMAGE CORRELATION (DIC) ANALYSIS AND X-RAY COMPUTED TOMOGRAPHY (XCT)

by

Eshan Ganju

A Dissertation

Submitted to the Faculty of Purdue University

In Partial Fulfillment of the Requirements for the degree of

Doctor of Philosophy

Lyles School of Civil Engineering

West Lafayette, Indiana

August 2021

THE PURDUE UNIVERSITY GRADUATE SCHOOL

STATEMENT OF COMMITTEE APPROVAL

Dr. Monica Prezzi, Co-chair

Lyles School of Civil Engineering

Dr. Rodrigo Salgado, Co-chair

Lyles School of Civil Engineering

Dr. Weinong Chen

School of Aeronautics and Astronautics

Dr. Steven T. Wereley

School of Mechanical Engineering

Approved by:

Dr. Dulcy Abraham

To Sarita Ganju, Ashwagosha Ganju, and Maithilee Motlag.

ACKNOWLEDGMENTS

I would like to express my gratitude to my advisors, Professor Monica Prezzi and Professor Rodrigo Salgado, for their generosity, patience, and guidance during my Ph.D. I have learned a lot from them, and I am indebted to them for their support and encouragement. I would also like to acknowledge my committee members, Professor W. Chen, and Professor S. Wereley. It was my pleasure to have them on my Ph.D. committee and I am grateful for the advice and suggestions.

I would like to thank my friends and colleagues: Fei, Ayda, Ruben, Vibhav, Jeehee, Mustafa, Firas, Siddarth, Vasundhara, Rubin, Rameez, Abhishek, Muskaan, and Himneet for their support and encouragement. A special thanks to William and Ann Schmidt, for their kindness, and for the wonderfully engaging conversations we have had over the many years. I would also like to thank Kevin Brower, and Harry Tidrick, for helping with the experiments in Bowen Laboratory and for being patient with all my questions and requests.

A special thanks to my parents, Ashwagosha Ganju and Sarita Ganju, and my younger sister, Sugosha Ganju, for their love and support over the many years, and for instilling in me the curiosity, patience, and persistence that I am so grateful for. And finally, I would like to thank my dearest wife, Maithilee Motlag. We met at the start of our Ph.Ds., here at Purdue, and it has been seven wonderful years since then. Thank you for being my constant companion, my sounding board, and my bedrock.

TABLE OF CONTENTS

LIST OF TABLES

LIST OF FIGURES

LIST OF SYMBOLS

σ:	Total vertical stress
σ_{yield}:	Yield stress
e:	Void ratio (volume of voids/volume of solids)
e_{min}:	Minimum void ratio
e_{max}:	Maximum void ratio
D_{50}:	Particle size for which 50% of the soil is smaller by mass
C_{U}:	Coefficient of uniformity
C_{C}:	Coefficient of curvature
G_{s}:	Specific gravity
S:	Sphericity
R:	Roundness
ϕ_{c}:	Critical state friction angle
K_0:	Coefficient of earth pressure at rest
D_{R}:	Relative density
C:	Slope of the e vs log σ curve
$\sigma_{\mathrm{f,avg}}$:	Average particle fracture stress
B_{r}:	Relative breakage parameter
N:	Fabric tensor
F:	Deviatoric fabric tensor
F_{q}:	Anisotropy scalar
q_{c}:	Cone resistance
f_{s}:	Sleeve resistance
u:	Pore pressure

ABSTRACT

Cone penetration in sands is a complex process: it contains several challenges that geomechanicians face, such as large displacements, large strains, strain localization, and microscale phenomena such as particle crushing and sand fabric evolution. In order to gain a deeper understanding of the penetration process and the mechanisms controlling penetration resistance, capturing these displacement and strain fields and microscale phenomena is necessary. Furthermore, as more sophisticated theoretical models become available for the simulation of the cone penetration problem, the experimental validation of those methods becomes vital.

This dissertation presents a multiscale study of the cone penetration process in silica sands. The penetration problem is investigated using a combinational approach consisting of calibration chamber experiments, digital image correlation (DIC) analysis, and X-ray computed Tomography (XCT) scans. Three silica sands with different particle characteristics are used in the experimental program. These three sands have similar particle size distributions; however, they differ in particle morphologies and particle strengths. These differences allow a study of the effect of microscale sand properties on the macroscale response of the sands to the cone penetration process. The three silica sands used in this research are fully characterized using laboratory experiments to obtain particle size distributions, particle morphologies, particle crushing strengths, minimum and maximum packing densities, and critical-state friction angles. Subsequently, both dense and medium-dense samples of the three sands are compressed in a uniaxial loading device placed inside an X-ray microscope (XRM) and scanned at multiple stress levels during uniaxial compression. Results from uniaxial compression experiments indicate that: (1) the compressibility of the sands is closely tied to particle morphology and strength, and (2) the anisotropy in the

orientations of interparticle contact normals generally increases with axial stress; however, this increase is limited by the occurrence of particle crushing in the sample.

Subsequently, cone penetration experiments are performed under different confinement levels on dense samples of the three sands in a special half-cylindrical calibration chamber equipped with DIC capabilities. For each penetration experiment, incremental displacement fields around the cone penetrometer are obtained using DIC analysis, and these incremental displacement fields are further analyzed to compute the incremental strain fields. A novel methodology is developed to obtain the shear-band patterns that develop around the penetrometer automatically. Furthermore, differences in the shear-band patterns in deep and shallow penetration environments are also investigated. Results show that strain fields tend to localize intensely near the penetrometer tip, and the shear bands tend to develop along the inclined face and near the shoulder of the penetrometer. Significant differences in the shear band patterns in deep and shallow penetration environments are also observed.

After each cone penetration experiment, a specially developed agar-impregnation technique is used to collect *minimally disturbed* sand samples from around the penetrometer tip. These agar-impregnated sand samples are scanned in the XRM to obtain 3D tomography data, which are further analyzed to quantify particle crushing around the penetrometer tip. The results show that: (1) for a given sample density, the amount of crushing around the cone penetrometer depends on the confinement and the sand particle characteristics, (2) the level of crushing is not uniform around the penetrometer tip, with more severe crushing observed near the shoulder of the penetrometer, and (3) the regions with more severe particle crushing around the penetrometer approximately overlap with regions of high shear strain and volumetric contraction. A framework is also proposed to obtain the ratio of penetration resistance in more crushable sands to penetration resistance in less crushable sands. Furthermore, a novel resin-impregnation technique is also developed to collect *undisturbed* sand samples from around the penetrometer tip. The resin-impregnated sand sample collected after one of the penetration experiments is scanned in the XRM to obtain the 3D tomography data, which is then analyzed to obtain the distribution of interparticle contact normal orientations at multiple locations around the penetrometer tip. These analyses indicate that the interparticle contact normals tend to orient themselves with the incremental principal strains around the penetrometer: below the penetrometer tip, the interparticle contact normals orient vertically upwards, while closer to the shoulder of the penetrometer, the interparticle contact normals become more radially inclined.

Data presented in this dissertation on penetration resistance, incremental displacement fields, incremental strain fields, particle crushing, and interparticle contact normal orientations around the cone penetrometer are aimed to be useful to researchers working on the multiscale modeling of penetration processes in granular materials and aid in the further development of our understanding of penetration processes in sands.

1 INTRODUCTION

In the cone penetration test (CPT), a conical tipped penetrometer is pushed into the ground at a steady rate of penetration till the desired depth of penetration or refusal (hard rock layer) is reached (Lunne et al. 1997; Salgado 1993). During the CPT, the cone resistance q_c, the sleeve resistance f_s, and the pore pressure u are measured. These measurements are used in practice to obtain soil stratigraphy (Begemann 1965; Douglas and Olsen 1981; Ganju et al. 2017; Jefferies and Davis 1991; Olsen and Mitchell 1995; Ramsey 2002; Robertson 1990, 2009; Sanglerat et al. 1974; Schneider et al. 2012; Tumay 1985; Zhang and Tumay 1999), assess site variability (Bombasaro and Kasper 2016; Cao et al. 2010; Fenton 1999; Firouzianbandpey et al. 2015; Ganju et al. 2019; Salgado et al. 2015, 2019; Stuedlein et al. 2012; Uziellia et al. 2005; Xiao et al. 2018; Yang et al. 2021), evaluate liquefaction potential (Carraro et al. 2003; Chen et al. 2015; Robertson 2010; Robertson and Campanella 1985; Robertson and Wride 1998; Salgado et al. 1997a), and design foundation elements (Fugro Engineers B. V. 2004; Han et al. 2019; Jardine et al. 2005; Karlsrud et al. 2005; Lehane et al. 2005b).

The apparent simplicity of the CPT however hides considerable complexity: the cone penetration problem contains all challenges that geomechanicians face: large displacements, large rotations, large strains, strain localization, soil-interface shearing, particle crushing and soil fabric evolution (Arshad 2014; Salgado 2014). To gain insights into the mechanisms that control the penetration resistance in the CPT, the penetration process in soils has been studied using a wide range of experimental techniques ranging from conventional calibration chamber experiments (Huang 1991; Lunne et al. 1997; Salgado 1993; Salgado et al. 1998) , to, more recently, calibration chamber experiments with digital image correlation (DIC) analysis (Arshad et al. 2014; White and Bolton 2004), penetration experiments in photo-elastic soil analogues (Allersma 1982; Guzman et al. 2020; Iskander 2010; Omidvar et al. 2012, 2015), and X-ray Computed Tomography scans of penetration processes (Doreau-Malioche 2018; Doreau-Malioche et al. 2019; Paniagua et al. 2013, 2014, 2018).

With the potent tools of Digital image correlation (DIC) analysis and X-ray Computed Tomography (XCT) scans, new avenues of research on the penetration process have opened up. These tools have enabled the possibility of quantifying, with greater accuracy, not only the large displacement, and strain fields that develop around the cone penetrometer but also the strain localizations, particle crushing, and soil fabric around the penetrometer tip. The objective of the research presented in this dissertation is the study of the penetration process in silica sands using the tools of DIC and XCT, in particular, to assess the effect of microscopic sand properties (particle strength and particle morphology) on the behavior of sands undergoing penetration processes. Three silica sands with different particle characteristics are used in the experimental program. The three sands have similar particle size distributions; however, they differ in particle strength and morphology. These differences allow a study of the effect of microscale sand properties on the macroscale response of the sand to the cone penetration process.

This dissertation is divided into four main chapters. Chapter 2 presents a thorough characterization of the three silica sands used in this research along with the results and analyses of uniaxial compression experiments performed on the three sands. Cylindrical samples of the three sands are compressed in a loading device placed inside an X-ray microscope (XRM) and scanned at multiple stress levels during uniaxial compression. The 3D tomography data of the samples obtained from the XRM at different stress levels are analyzed to obtain the distributions of particle size, particle morphology, and interparticle contact normals within the sample.

Chapter 3 reports the results of penetration experiments performed in a special half-cylindrical calibration chamber equipped with digital image correlation (DIC) capabilities. To study the penetration process in a deep and a shallow environment, both a cone penetrometer (diameter d = 38 mm) and a model footing (width B = 90 mm) are used in the penetration experiments. Incremental displacement and strain fields in the soil domain are obtained by DIC analysis. Furthermore, the zero-extension line concept is used to study shear strain localization in the soil domain, and a novel method is proposed to automatically obtain the orientation of shear band patterns from the incremental strain fields.

Chapter 4 provides data on the crushing of sands around the penetrometer tip for cone penetration experiments carried out in dense samples of the three silica sands. The penetration experiments are performed under three different confinements in the same DIC calibration chamber as that presented in Chapter 3. After the penetration experiments, a specially developed agar-impregnation technique is used to collect sand samples near the penetrometer tip. These agar-impregnated sand samples are scanned using a high-resolution X-ray microscope (XRM) to obtain 3D tomography data of the sand around the penetrometer. Analysis of the 3D tomography data of the samples collected around the penetrometer provides us with the distribution of the particle sizes in the soil domain, allowing us to quantify the level and distribution of particle crushing around the penetrometer tip. The data on the crushing around the penetrometer tip is supplemented with data on the incremental strain fields in the soil domain. Furthermore, a framework is proposed to obtain the ratio of q_c in more crushable sands to q_c in less crushable sands.

Chapter 5 presents data on the evolution of sand fabric around the cone penetrometer. A cone penetration experiment is performed in a dense air-pluviated sample of the Ottawa 20-30 sand prepared in the half-cylindrical calibration chamber. At the end of the penetration experiment, a specially developed resin-impregnation technique is used to collect undisturbed sand samples around the cone penetrometer. The resin-impregnated sand sample is scanned in an X-Ray Microscope (XRM) to obtain 3D XCT data of the sand around the cone tip. Since the sample is undisturbed, the XCT data is analyzed to obtain the distribution of interparticle contact orientations–fabric–at multiple locations around the cone penetrometer. Information about the sand fabric is supplemented with the incremental displacement and strain field in the soil domain obtained from the DIC analysis of the images collected during the penetration experiment.

Additionally, a summary of the incremental displacement and strain fields around the cone penetrometer is presented in Appendix A for the cone penetration experiments performed for this dissertation. These incremental displacement and strain fields correspond to penetration experiments carried out on dense samples of the three tests sands under different confinement levels. The DIC analysis procedure followed to obtain these incremental displacement and strain fields is described in Chapter 3. The data presented in Appendix A is meant to supplement the displacement and strain fields presented in Chapters 3-5.

2 EFFECT OF PARTICLE CHARACTERISTICS ON THE EVOLUTION OF PARTICLE SIZE, PARTICLE MORPHOLOGY, AND FABRIC OF SANDS LOADED UNDER UNIAXIAL COMPRESSION

This chapter has been submitted as a paper to a peer-reviewed journal.

2.1 Introduction

Initial effective stress levels in geomechanics range from a few kilopascals near the ground surface to several megapascals in deep geological environments (Haimson and Doe 1983; Liao et al. 2003; Rebaï et al. 1992; Zoback et al. 1980; Zoback and Healy 1992), around cone penetrometers (Allersma 1982, 1987; Allersma and Broere 2002; Woo 2015) or near the tip of pile foundations driven in sand or gravel (Briaud et al. 1989; Ganju et al. 2020a; Han et al. 2019; Lehane et al. 2005a; Wang and Zhao 2014; Yang et al. 2016). The large stresses and strains experienced by soils under these conditions can cause particle crushing, leading to changes in the stress-strain response of the material. To increase the reliability of geostructures in the built environment, it is important to understand how soils respond to compressive stresses large enough to cause crushing of its constituent particles. Numerical and experimental studies have been performed over the last few decades to gain insights into the response of soils to high compressive stresses under various stress paths (Alikarami et al. 2014; Barr et al. 2019; Graham et al. 2004; Karatza et al. 2018; Lee and Farhoomand 1967; Mesri and Vardhanabhuti 2009a; Peng et al. 2020; Wu et al. 2021; Xiao et al. 2020; Yu 2019; Zhao et al. 2016; Zheng and Tannant 2016).

Under uniaxial compression, the stress-strain response of sand, which is usually represented in a plot of void ratio (e) vs. logarithm of axial stress (σ), may be approximated by a bi-linear relationship with the point of maximum curvature on the curve conventionally identified as the "yield point" of the soil and the stress at the yield point as the yield stress σ_{yield} (Hagerty et al. 1993; McDowell 2002; McDowell et al. 1996; Nakata et al. 2001a; b). The section of the e vs log σ curve before the yield point is referred to as the re-compression curve (RCC), and the section after the yield point is referred to as the virgin compression curve or the limiting compression curve (LCC) (Mitchell and Soga 2005; Pestana and Whittle 1995; Salgado 2008). The magnitude of the slope of the RCC is always smaller than that of the LCC.

Terzaghi and Peck (1948) were among the first to present data on the uniaxial compression of sands with experiments performed on loose and dense sand samples compressed to stresses high enough to cause particle crushing. They indicated that the change in compressibility (yielding) of the sand samples was associated with the crushing of the sand particles, and that the addition of angular (more crushable) particles, such as those of crushed mica, caused this yielding to occur at lower stresses. This suggested that the change in compressibility of the sands under uniaxial compression was to some extent tied to the crushing of its particles.

Other experimental studies on the uniaxial compression of sands followed that of Terzaghi and Peck (1948). Roberts and de Souza (1958) also found that sand samples with angular particles were more compressible than those with well-rounded particles. They also showed that the stress level at which the sand particles started to crush was affected by the void ratio (e) of the sample–more crushing was observed for loose samples than dense samples–and that σ_{yield} of loose samples were also lower than those of dense samples.

Hendron (1963) carried out compression experiments on sands with different gradations and reported that well-graded sands tended to have a higher σ_{yield} than poorly-graded sands when starting from the same initial relative density D_R. He also observed that the coefficient of lateral earth pressure at rest K_0 increased with an increase in vertical effective stress for stress levels exceeding 7 MPa. Hagerty et al. (1993) performed uniaxial compression experiments on sands to very high stress levels (maximum of 689 MPa) and found that, at extremely high stresses (~600 MPa), the compressibility of sands was very similar to that of natural sandstones.

McDowell and Bolton (1998) tied the compressibility of sand samples to the tensile strength of the constituent sand particles. They found that (1) the tensile strength of the sand particles followed the Weibull distribution (Weibull 1951) and (2) the σ_{yield} for a sand compressed under uniaxial compression was proportional to the average tensile strength of the particles. Nakata et al. (2001a) reported that the curvature of the e vs log σ curve near σ_{yield} decreases with an increase in the coefficient of uniformity C_{U} of the soil and that the particles undergo more gradual crushing (e.g., chipping and grinding of asperities) instead of sudden fracture (grain splitting) as the C_{U} of the soil increases. Cavarretta et al. (2010) indicated that particle morphology has a much more significant impact on the macroscopic response of sand than the surface roughness of the particles, suggesting that the high contact stresses that appear during loading may break the asperities at the points of contact, making the particle shape the dominant property controlling macroscopic behavior at large stresses; this observation was also supported to some extent by the experimental findings of Nardelli and Coop (2019).

Recently, X-ray computed tomography (XCT) has been used to investigate the behavior of soils under different loading paths and at different scales (Alshibli and Reed 2010; Andò et al. 2013, 2020; Desrues et al. 2010; Viggiani et al. 2015). With XCT, the behavior of sands under uniaxial compression has been studied non-destructively, allowing the capture of the evolution of particle crushing (Cil et al. 2017a; Cil and Alshibli 2014; Karatza et al. 2017; Okubadejo et al. 2017; Parab et al. 2014; Zhao et al. 2015, 2019), particle morphology (Karatza et al. 2019; Seo et al. 2020), and interparticle contact orientations (Alam et al. 2018; Fonseca et al. 2016) during compression. Significant insights from these studies will be discussed in more detail later in the paper.

The goal of this paper is to study how initial particle characteristics (particle morphology and particle strength) affect the evolution of crushing, morphology, and the distribution of interparticle contact orientation–which can be used to define the fabric of the sand–in sand samples loaded under uniaxial compression. We focus mainly on the response of silica sands to uniaxial compressive stresses ranging from 0 MPa to 30 MPa. We performed uniaxial compression experiments on dense and medium-dense cylindrical samples of three poorly graded silica sands that have similar particle-size distributions but different particle strength and morphology characteristics. The compression experiments were performed inside an X-ray Microscope (XRM), which allowed us to collect 3D topographies of the sand samples at multiple stress levels during loading. From the compression experiments, we obtained the stress-strain response of the sand samples to the applied load. Analyzing the 3D tomography data, we obtained the discrete digital representations of the particles in the samples. From the analyses of these digital representations, we obtained the distributions of particle size, the particle morphology, and the interparticle contact orientations as the sand sample was loaded in compression.

2.2 Materials and methods

2.2.1 Test sands

We performed uniaxial compression experiments on three predominantly siliceous sands: #2 Q-Rok (2QR), Ohio Gold Frac (OGF) and Ottawa 20-30 (OTC). Figure 2.1 shows the particle-size distributions for the three test sands obtained from sieve analysis (ASTM D6913-17 2017), and the images of sand particles taken using a microscope (Model No. SM-4TZ-144A, AmScope, Irvine, California) and an 8-megapixel eye-piece camera (Model No. MU-800, AmScope, Irvine, California). Table 2.1 presents the values of average particle size (D_{50}), coefficient of uniformity (C_U), coefficient of curvature (C_C), and the USCS classification (ASTM D2487-17 2006) for the three test sands. The three sands have similar particle-size distributions; however, they differ in particle morphology and particle strength.

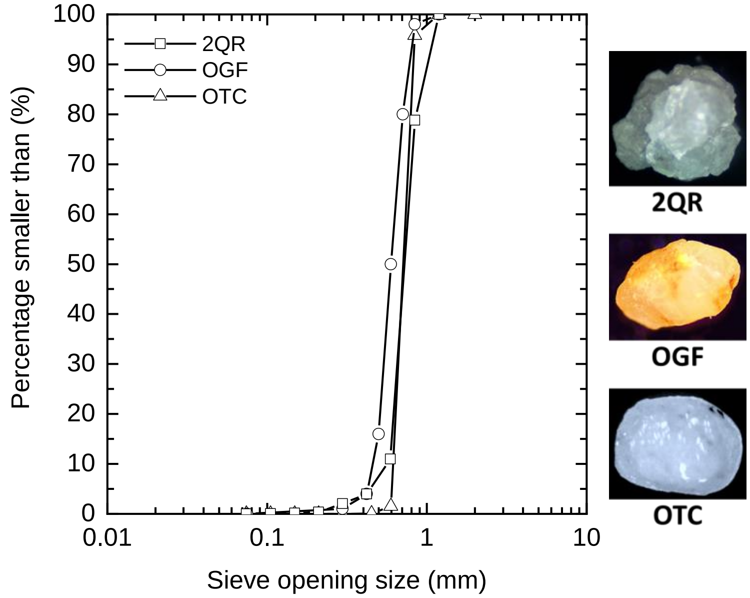

Figure 2.1 Particle-size distribution for the three test sands from sieve analysis following ASTM-D6913 (2017).

Table 2.1 Properties of #2 Q-Rok (2QR), Ohio Gold Frac (OGF), and Ottawa 20-30 (OTC) sand obtained from laboratory experiments.

Sand	D_{50}	C_U	C_C	USCS	S_{avg}	R_{avg}	e_{min}	e_{max}	ϕ_c
2QR	0.73	1.4	1	SP	0.74	0.24	0.67	0.99	33.0
OGF	0.62	1.4	1	SP	0.73	0.37	0.61	0.89	32.5
OTC	0.72	1.4	1	SP	0.79	0.74	0.50	0.75	29.3

NOTE: D_{50} is the particle size greater than the size of particles making up 50% of the soil by weight. It was obtained from sieve analysis following ASTM D6913 (ASTM D6913-17 2017). C_U and C_C are the coefficients of uniformity and curvature, determined from the particle size distribution curves obtained from sieve analysis. USCS is the Unified Soil Classification System (ASTM D2487-17 2006), and "SP" in the USCS represents a poorly-graded sand. The void ratios e_{min} and e_{max} are the minimum and maximum void ratios, respectively, determined following ASTM D4254 (ASTM D4254-16 2016). To check whether particle crushing had taken place during the e_{min} experiments, we carried out sieve analysis of the sand samples before and after the e_{min} experiments and found no change in the particle size distribution curves for all three sands. S_{avg} and R_{avg} are the average sphericity (aspect ratio) and Wadell's roundness (Wadell 1932) of the test sands. The friction angle ϕ_c is the critical-state friction angle of the sands obtained from drained triaxial compression experiments.

Two parameters–roundness (R) and sphericity (S)–were used to quantify the particle morphologies of the test sands. R is defined as the ratio of the average radius of curvature of the corners of the particle to the radius of the largest circle that can be inscribed inside the particle boundaries (Wadell 1932). S is defined as the ratio of the width to the length of the particle obtained by fitting an ellipse to the 2D image of the particle (Zheng and Hryciw 2015); this definition for S fits well the widely used particle morphology charts proposed by Krumbein and Sloss (1951). Initial R and S were obtained from analysis of over 90 2D images of each sand and Table 2.1 presents the values of average sphericity (S_{avg}) and average roundness (R_{avg}) for the test sands. The three sands have similar S_{avg} in the range of 0.73-0.79; however, in terms of R_{avg}, the three sands are very different. The 2QR sand (#2 Q-Rok) has the lowest R_{avg} value (R_{avg}= 0.24). The OTC sand (Ottawa 20-30) has the highest R_{avg} value (R_{avg} = 0.74), and the OGF sand (Ohio Gold Frac) has an intermediate R_{avg} value (R_{avg} = 0.37).

As with the R_{avg}, the three sands have very different values of particle strengths. To measure the strength of the particles, we carried out single-particle uniaxial compression experiments on individual particles of the OGF and 2QR sands at the Argonne National Laboratory (ANL) in

Chicago, Illinois. These experiments were performed by quasi-statically compressing a sand particle between two smooth loading platens until the particle completely fractured. Fifty particles of each sand were loaded in this manner to obtain a distribution of the nominal fracture stress (σ_f), which was computed as:

$$\sigma_f = \frac{F}{d_0^2} \tag{2.1}$$

where F is the load level at which the sand completely fractured, and d_0 is the nominal particle diameter taken as the approximate distance between loading platens at the start of compression. The data for the OTC sand was obtained from Cil and Alshibli (2012). The probability of survival $P_s(\sigma)$ of a sand grain under an applied stress σ is generally captured by the Weibull distribution (Weibull 1951) as:

$$P_s(\sigma) = e^{-\left(\frac{\sigma}{\sigma^*}\right)^m} \tag{2.2}$$

where σ^* and m are fitting parameters: σ^* captures the stress level at which 37% of the loaded particles survive crushing, and m, called the Weibull modulus, captures the spread of the fracture stresses. A large m indicates that particles of the sand fracture over a narrow range of normalized stress (σ/σ^*) , while a small m indicates that the particles fracture over a wide range of σ/σ^*. Table 2.2 presents a summary of the average fracture stress $\sigma_{f,avg}$ and the fitting parameters, σ^* and m, of the Weibull distribution for the test sands obtained from the analysis of the distributions of σ_f. From the data, we can see that 2QR has the weakest particles with a $\sigma_{f,avg}$ of 22 MPa and σ^* of 23 MPa. OGF has stronger particles than 2QR, with a $\sigma_{f,avg}$ of 75 MPa and σ^* of 84 MPa. The OTC sand particles are the strongest, with a $\sigma_{f,avg}$ of 128 MPa and σ^* of 144 MPa. The values of m range from 1.15 (for 2QR) to 2.82 (for OTC), indicating that the weaker 2QR sand particles have a greater variability in fracture stresses than the stronger OTC sand particles. The values of m

reported here in general agree with values reported by Nakata et al. (2001b), who also observed that sands with lower σ^* tend to have lower values of m.

Table 2.2 Values of average fracture stress ($\sigma_{f,avg}$) and Weibull fitting parameters (σ* and m) from single particle compression experiments carried out on the #2 Q-Rok (2QR), Ohio Gold Frac (OGF), and Ottawa 20-30 (OTC) sand.

Sand	$\sigma_{f,avg}$ (MPa)	Weibull fitting parameters	
		σ^* (MPa)	m
2QR	21.76	22.97	1.15
OGF	75.17	84.13	1.59
OTC	127.57	143.61	2.82

The comparatively lower $\sigma_{f,avg}$ and σ^* of 2QR can be explained by (1) the low R_{avg} of 2QR particles (see Table 2.1), and (2) the presence of internal defects (cracks) in the 2QR particles (see Figure 2.2). The low R_{avg} is due to local surface asperities, which become stress concentration points when the particles are loaded (Altuhafi et al. 2016; Hagerty et al. 1993). The presence of internal defects makes the particles more susceptible to crushing (Zhao et al. 2015). 2QR has the lowest R_{avg} of the three sands; therefore, it is more prone to high stress concentration points during loading. Furthermore, an average 2QR particle (shown in in Figure 2.2(a)) has more internal defects than an average OGF particle (shown in Figure 2.2(b)), and thus the 2QR particles are more easily crushed at lower stresses. The particles of the OTC sand have the highest R_{avg} of the three sands and, at the same time, few or no internal defects (Druckrey 2016; Druckrey and Alshibli 2016); therefore, the values of $\sigma_{f,avg}$ and σ^* for the OTC sand are comparatively higher than those for the OGF and 2QR sands.

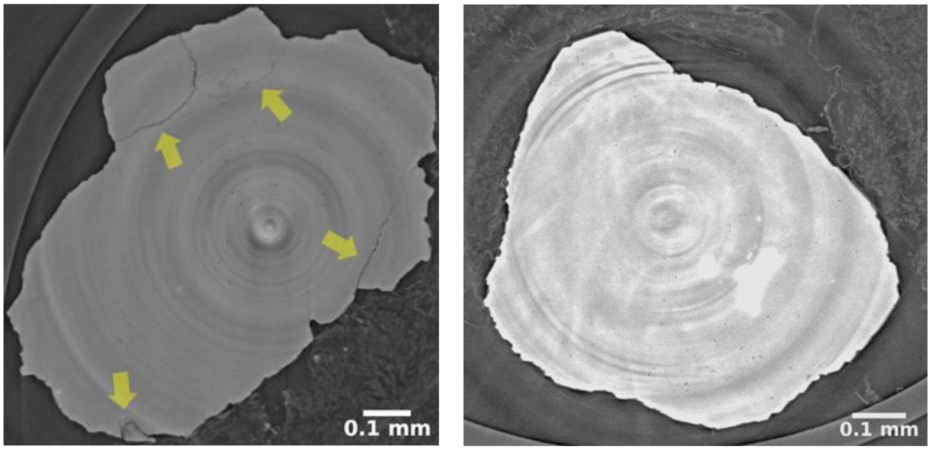

Figure 2.2 High resolution XCT scans of uncrushed particles of: (a) the 2QR sand, with annotations showing internal defects; and (b) the OGF sand with little-to-no internal defects.

As a result of these differences at the microscale, the three sands show differences in behavior at the macroscale. Table 2.1 presents the values of critical state friction angles (ϕ_c) for the three test sands obtained from consolidated-drained triaxial compression experiments. The triaxial compression experiments were performed under a confining stress of 100kPa on samples prepared at a relative density (D_R) of 50%. 2QR, with the lowest R_{avg}, has the highest critical-state friction angle ϕ_c of 33^o; OGF, with an intermediate R_{avg}, has a slightly smaller ϕ_c of 32.5^o; and OTC, with the highest R_{avg}, has the smallest ϕ_c of 29.3^o. The larger ϕ_c for sands with smaller R_{avg} can be explained by the greater interlocking of surface asperities of the particles during shearing (Alshibli and Cil 2018). The greater interlocking of particles also explains the comparatively larger e_{min} and e_{max} observed for the more angular sands.

2.2.2 Uniaxial compression experiments

To further investigate the differences in the macroscopic behavior of the three sands, we carried out uniaxial compression experiments on the sands using two cylindrical molds with different dimensions. Figure 2.3 shows the schematics and labeled images of the two molds. The small mold has an internal diameter of 8 mm (11-13 D_{50}) and is made of aluminum (aluminum was chosen to facilitate X-ray imaging). The large mold has an internal diameter of 51 mm (70-80 D_{50}) and is made of carbon steel. The cylindrical sand samples were prepared in the molds by air-pluviation followed by light tapping of the external walls of the mold to achieve the desired D_R.

Figure 2.3 presents a summary of the experiments performed using the large and small compression molds. The maximum compressive stress in these experiments was 90 MPa. Sand samples in the large mold were compressed slowly at a strain rate of 1%/min using an Instron loading device (Model No. 120BTE502040, Instron, Norwood, Massachusetts). Sand samples in the small mold were also compressed at a strain rate of 1 %/min using a Deben loading device (Model No. CT5000RT, Deben, UK) placed inside a Zeiss X-ray Microscope (Model No. VERSA-510 3D X-ray Microscope (XRM), Zeiss, Pleasanton, California).

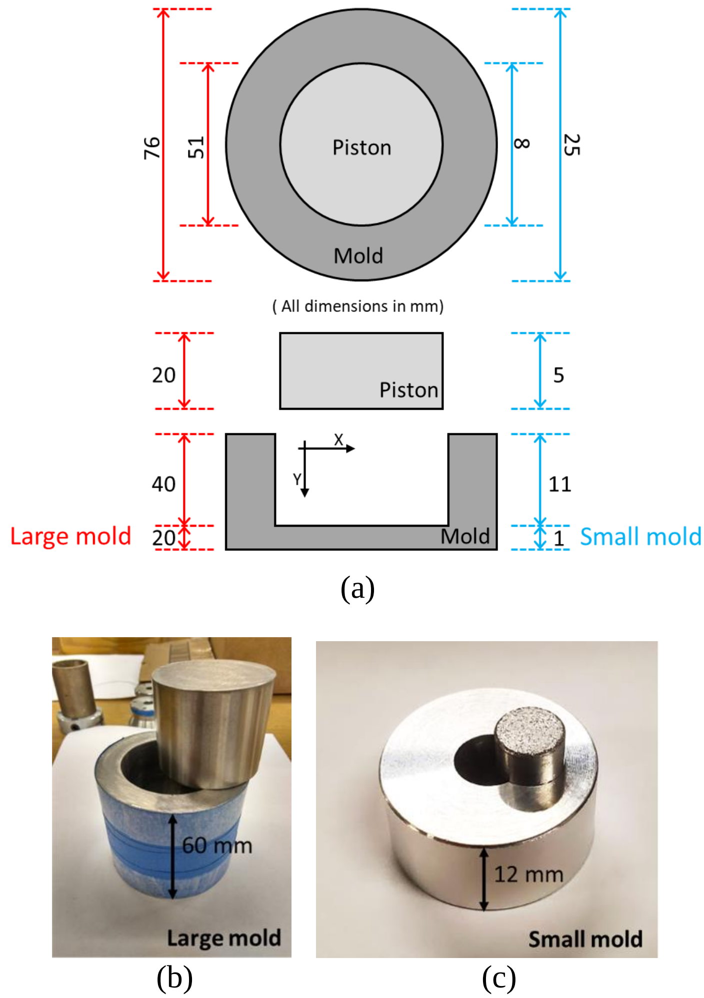

Figure 2.3 Uniaxial compression molds:(a) schematics showing the dimensions of the large and small compression molds used in the uniaxial compression experiments (not drawn to scale; the dimensions provided on the left and right sides of the figure are for the large and small molds, respectively), (b) image of the large mold, and (c) image of the small mold.

2.2.3 3D X-ray Computed Tomography (XCT) scans

The dense 2QR, OGF and OTC sand samples and the medium-dense OTC sand sample compressed in the small mold were scanned using the X-ray Microscope (XRM) at multiple stress levels during compression. Figure 2.4(a) shows a labeled image of the XRM, the sand sample, and the loading device.

Table 2.3 Summary of uniaxial compression experiments carried out in the large and small molds.

Experiment ID	Mold	Sand	Initial void ratio	Initial relative density (%)	State
S-2QR-D	Small	2QR	0.73	81	Dense
S-OGF-D		OGF	0.63	91	Dense
S-OTC-D		OTC	0.54	84	Dense
S-OTC-MD		OTC	0.61	56	Medium-dense
L-2QR-D	Large	2QR	0.74	79	Dense
L-OGF-D		OGF	0.63	91	Dense
L-OTC-D		OTC	0.51	92	Dense
L-OTC-MD		OTC	0.62	52	Medium-dense

The Deben loading device used to compress the sand has a special vitreous glassy carbon wall that allows the X-rays to pass through practically unaffected. As the X-ray photons pass through the sample, the sand particles (and the mold) absorb X-ray photons proportionally to their X-ray attenuation coefficient (Als-Nielsen and McMorrow 2011). The X-ray photons that pass through the sample unabsorbed are captured by the detector, which produces a radiograph of the sample. The Zeiss XRM captures multiple radiographs of the sample by rotating the sample 360° in increments of ~0.11°. A total of 3,201 radiographs were collected for each sample at each stress level of interest. The 3,201 radiographs were used to produce 3D tomography data of the scanned sample following a suitable reconstruction technique (Zeiss 2016). Figure 2.4(b) shows a vertical slice of the 3D tomography data for the dense OTC sand at the 0 MPa stress level obtained in this manner.

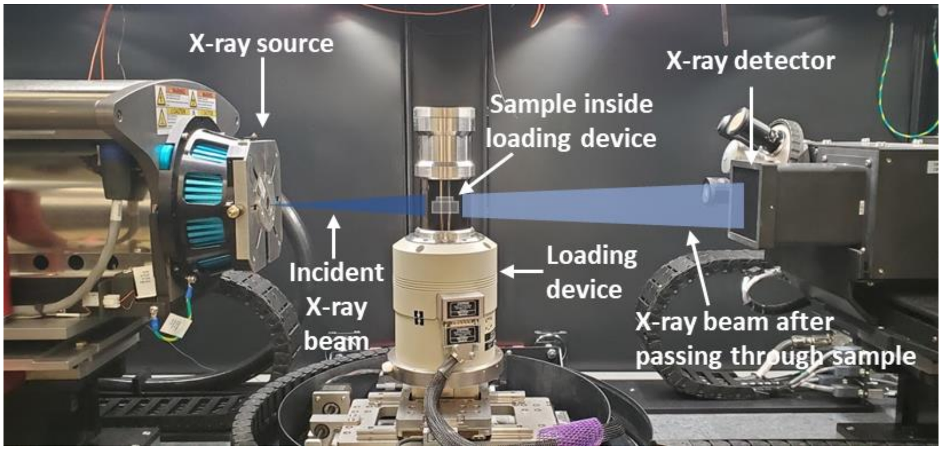

(a)

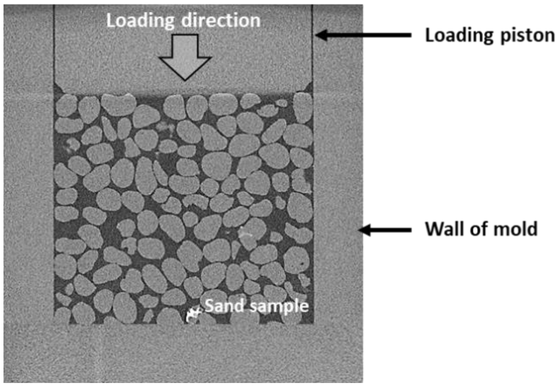

(b)

Figure 2.4 X-ray Computed Tomography (XCT) scans of cylindrical sand samples to obtain 3D tomography data: (a) small mold scanned inside uniaxial compression device placed inside an XCT scanner, (b) cross-section of 3D tomography data showing the loading piston, the sand particles (dense OTC) and the compression mold.

The 3D tomography data from XCT scans are stored in the form of a sequence of 2D images. Each 2D image represents a finite slice of the scanned sample, therefore, each pixel in a 2D image represents a finite 3D cubic volume in the sample (pixels in the tomography data are referred to as *voxels* or volume elements). All the scans were carried out at a resolution of 11.93×10^{-3} mm/voxel, which implies that the edge of the cubic voxel has a physical length of $11.93\ 10^{-3}$ mm. The corresponding volume of each voxel for all the current scans is 1.697×10^{-6} mm^3. This resolution corresponds to 50-60 voxels across the D_{50} of the test sand and is considered high enough to capture particle size and interparticle contact with high precision and accuracy (Wiebicke et al. 2017).

Each voxel in the tomography data is assigned an integer value which quantifies the relative X-ray attenuation coefficient of the corresponding volume in the scanned sample. We use 16-bit images to store the tomography data, and thus each voxel can have an integer value ranging from 0, representing a void, to 65,535 ($=2^{16} - 1$), representing a material with high X-ray attenuation coefficient. These integer values are generally referred to as the grey level intensity (GLI) values of the voxels. The sand particles have a relatively higher GLI value than the voids surrounding them. This allows us to distinguish the particles from the voids, as seen in Figure 2.4(b). The 3D tomography for all four samples was obtained and stored in this manner.

To ensure uniformity and scan quality, the same scanning procedure was followed for all the samples. After the sand sample was formed in the small aluminum mold, it was placed inside the loading device positioned between the X-ray source and the detector. The sample was loaded to the desired stress level using the loading device, and the stress was maintained for 5-15 minutes to allow the sample height to stabilize. This was done to minimize any movement within the sample during the XCT scan. The loading piston was then locked in place to fix the sample height, and the sample was scanned using the XRM to obtain the 3D tomography data. A drop in stress was observed over the duration of the scan, but this drop in stress was less than 1 MPa at the 30 MPa stress level for all three sands. After the scanning was complete, the sample was loaded to the next stress level and scanned again following the same procedure. This process was repeated until the sample had been scanned at all the desired stress levels. Table 2.4 presents a summary of the XCT scans. The stress levels at which the scans were carried out were selected to highlight important features in the response of the sand to loading under uniaxial compression.

Table 2.4 Summary of X-ray computed tomography (XCT) scans carried out on cylindrical samples of dense 2QR, OGF, and OTC samples, and the medium-dense OTC sample in the X-ray Microscope (XRM).

CT scan ID	Sand	Initial void ratio	Initial density	Void ratio during scan	Vertical stress during scan (MPa)
CT-2QR-D-0	2QR	0.73	81	0.734	0
CT-2QR-D-1				0.726	1
CT-2QR-D-2				0.722	2
CT-2QR-D-10				0.698	10
CT-2QR-D-30				0.591	30
CT-2QR-D-90				0.345	90
CT-OGF-D-0	OGF	0.63	91	0.634	0
CT-OGF-D-2				0.624	2
CT-OGF-D-10				0.613	10
CT-OGF-D-30				0.562	30
CT-OGF-D-90				0.361	90
CT-OTC-D-0	OTC	0.54	84	0.541	0
CT-OTC-D-10				0.517	10
CT-OTC-D-30				0.499	30
CT-OTC-D-90				0.359	90
CT-OTC-MD-0	OTC	0.61	56	0.609	0
CT-OTC-MD-1				0.600	1
CT-OTC-MD-10				0.585	10
CT-OTC-MD-30				0.560	30

2.3 Results and discussions

2.3.1 Results from compression experiment in large and small molds

Figure 2.5 presents the vertical strain (ε) versus log σ plots for the sands loaded in the large and small molds. From these plots, we can see that the sand samples loaded in the small mold have a slightly stiffer response to compression loading than the samples loaded in the large molds. The yield stress σ_{yield} is slightly greater for the samples loaded in the small mold, and this difference may be attributed to the differences in initial sample conditions and sample size effects (Shi et al. 2016; Suescun-Florez et al. 2020). In general, however, the shapes of the curves are similar for the two molds and the curves match reasonably well, particularly at large stresses.

Figure 2.6 shows the variation of the void ratio e and of the slope C of the e vs log σ curve (represented in the y-axis in the right side of the figure) with the applied vertical stress σ for the dense 2QR, OGF, and OTC sand samples and for the medium-dense OTC sand sample loaded in the large mold. For all three sands, C increases from an initial low value (<0.01) to a value in the 0.4 – 0.5 range, which generally agrees with the values of the slope of the limiting compression curve (LCC) of sands reported in literature (Pestana and Whittle 1995).

As can be seen in Figure 2.6, C reaches a small peak after the yield point is crossed. According to Nakata et al. (2001a), in the case of uniformly graded sands, significant particle splitting occurs between σ_{yield} and the stress $\sigma_{\text{C-max}}$ at which C reaches its peak value. In Table 2.5 we present the values of σ_{yield} and $\sigma_{\text{C-max}}$ for the uniaxial compression experiments performed in this research. While significant particle crushing is reported to take place between σ_{yield} and $\sigma_{\text{C-max}}$, this does not imply that no particle crushing takes place at stress levels lower than σ_{yield}. As indicated by Karatza et al. (2019), some amount of particle breakage does takes place prior to the reaching the conventional σ_{yield}. Furthermore, for dense sand samples, as minimal void space is available for particle movement, the increase in compressibility in the vicinity of σ_{yield} is generally attributed to particle rearrangement caused by particle crushing; however, for lower density samples (such as the medium-dense OTC sample), due to the availability of void space, the increase in compressibility is attributed to particle rearrangement caused by both slippage at interparticle contacts and some minimal particle crushing (surface grinding and chipping) (Mesri and Vardhanabhuti 2009b).

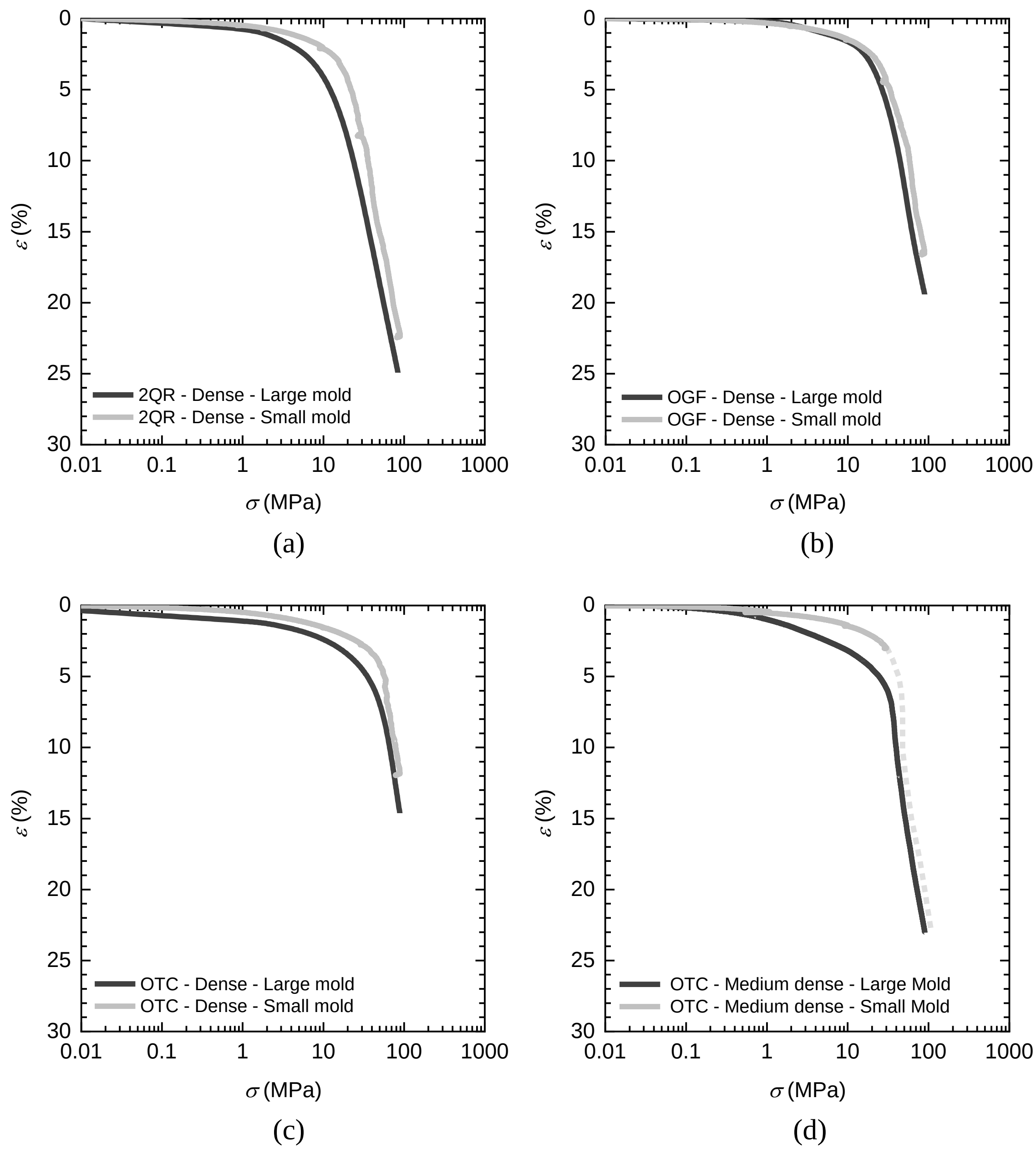

Figure 2.5 Vertical strain (ε) versus log of vertical stress (σ) curves from uniaxial compression experiments carried out in the large and small molds for (a) dense 2QR sand samples, (b) dense OGF sand samples, (c) dense OTC sand samples, and (d) medium-dense OTC sand samples.

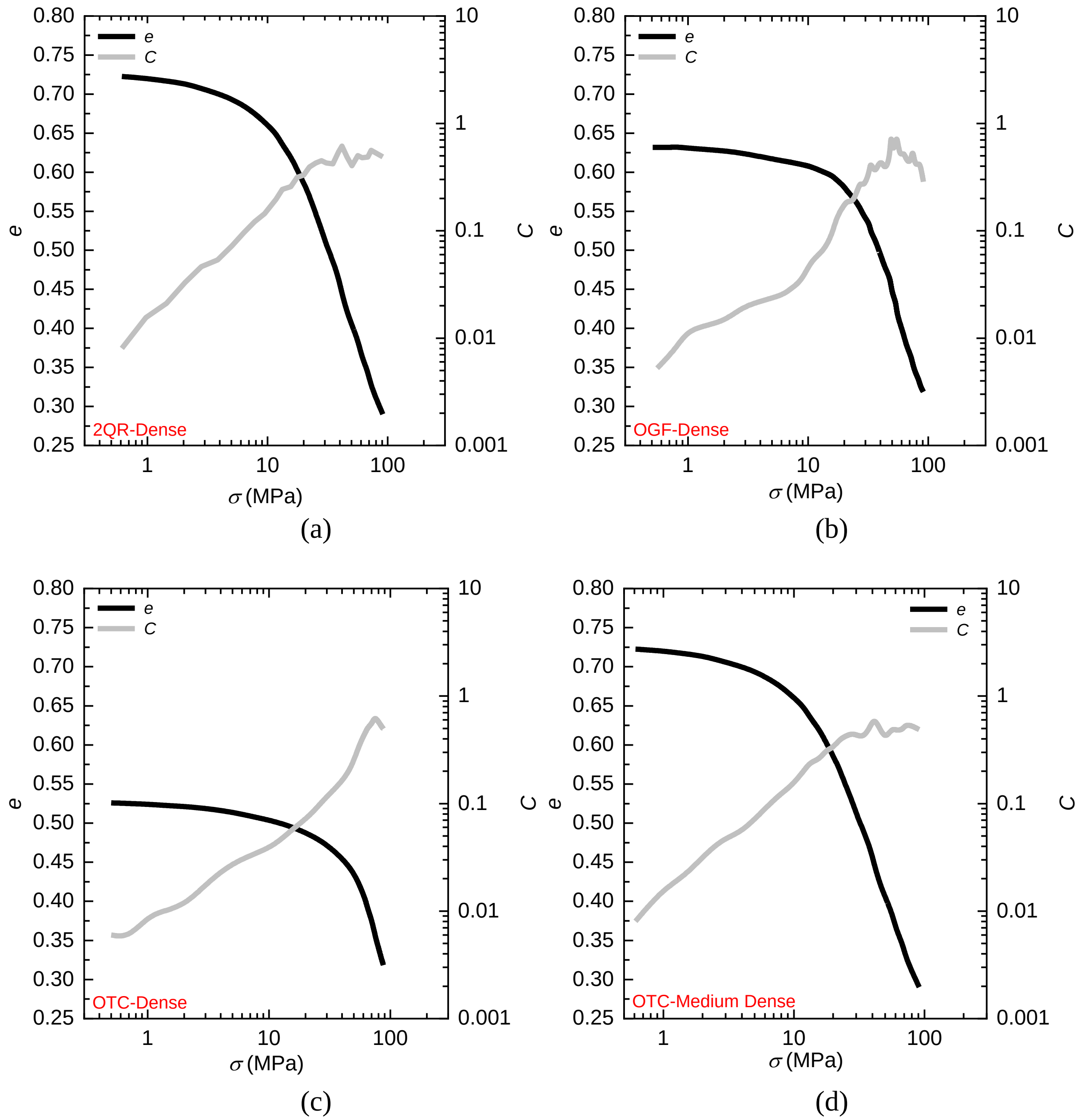

Figure 2.6 Variation of void ratio (e) and slope (C) of e vs log σ curve with applied vertical stress (σ) for (a) the dense 2QR sand sample, (b) the dense OGF sand sample, (c) the dense OTC sand sample, and (d) the medium-dense OTC sand sample.

Table 2.5 Stress values at yield (σ_{yield}) and at maximum slope (C) of the e vs log σ curve ($\sigma_{C\text{-}max}$) for uniaxial compression experiments carried out in the large compression mold, and the ratio of the yield stress (σ_{yield}) to the average particle fracture stress ($\sigma_{f,avg}$).

Sample	σ_{yield} (MPa)	$\sigma_{C\text{-}max}$ (MPa)	$\sigma_{yield}/\sigma_{f,avg}$
2QR-D	6.96	45.67	0.32
OGF-D	25.08	55.94	0.33
OTC-D	43.60	80.33	0.34
OTC-MD	23.35	45.32	0.18

Table 2.5 also presents the ratio of the σ_{yield} to $\sigma_{f,avg}$ for the four sand samples loaded under uniaxial compression. This ratio appears to be in a narrow range of 0.32-0.34 for the dense 2QR, OGF and OTC samples. For a poorly-graded silica sand sample, it is known that σ_{yield} is a function of the initial D_R and the particle strength; therefore, σ_{yield} normalized by $\sigma_{f,avg}$ can be expected to be a function of D_R alone. Given that all the dense sand samples had comparable initial D_R, the range of $\sigma_{yield}/\sigma_{f,avg}$ observed from the experimental data was narrow, as expected. For samples with lower initial D_R, this ratio was expected to be lower, as is observed for the medium-dense OTC sample, for which $\sigma_{yield}/\sigma_{f,avg}$ has a value of 0.18.

2.3.2 Analysis of 3D tomography data from XRM

Figure 2.7 shows vertical slices through the center of the 3D tomography data for the three dense and one medium-dense sand samples scanned at different stress levels. From the slices, we can see that, at low stress levels (< 10 MPa), no particle crushing is observable; however, at the maximum applied stress of 90 MPa, the majority of the particles for all the three sands crush into smaller pieces of varying sizes. The stress levels corresponding to the XCT scans in which we first observe crushing differ for the three sands.

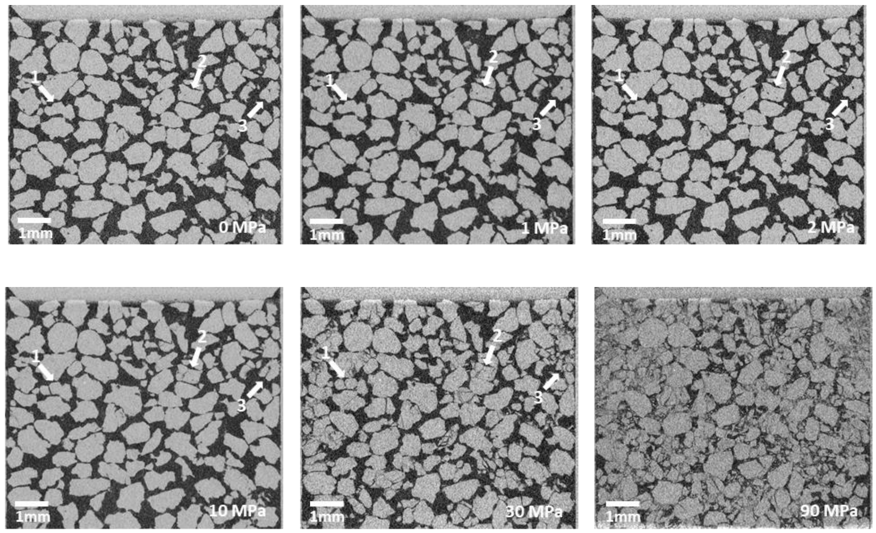

(a)

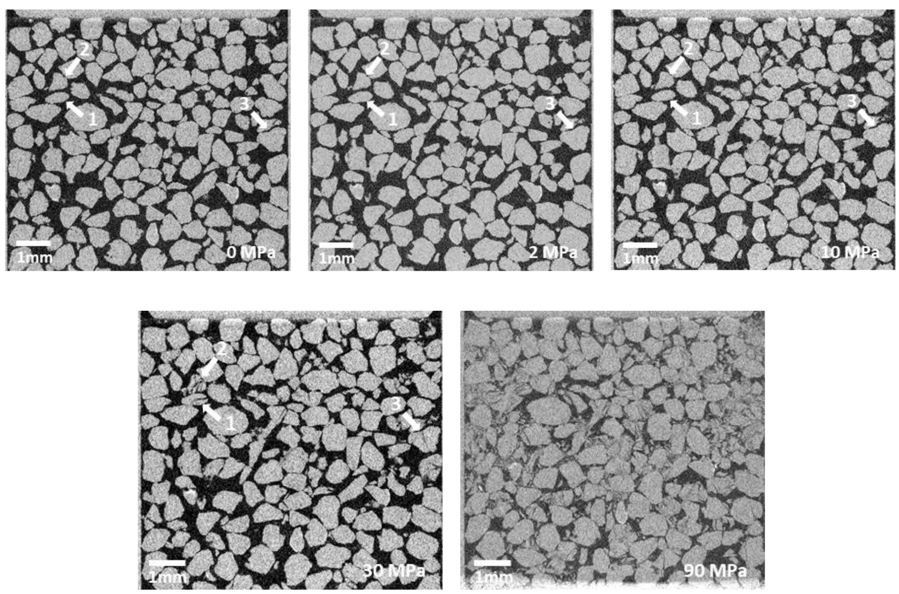

(b)

Figure 2.7 Vertical slices through the 3D tomography data of (a) dense 2QR sample (initial D_R= 81%) at stress levels of 0 MPa, 1MPa, 2 MPa, 10 MPa, 30 MPa, and 90 MPa, (b) dense OGF sample (initial D_R= 91%) at stress levels of 0 MPa, 2 MPa, 10 MPa, 30 MPa, and 90 MPa, (c) dense OTC sample (initial D_R= 84%) at stress levels of 0 MPa, 10 MPa, 30 MPa, and 90 MPa, and (d) medium-dense OTC sample (initial D_R= 56%) at stress levels of 0 MPa, 1MPa, 10 MPa, and 30 MPa, with numbered arrows identifying particle that undergo damage at different stress levels for each sample.

Figure 2.7 continued

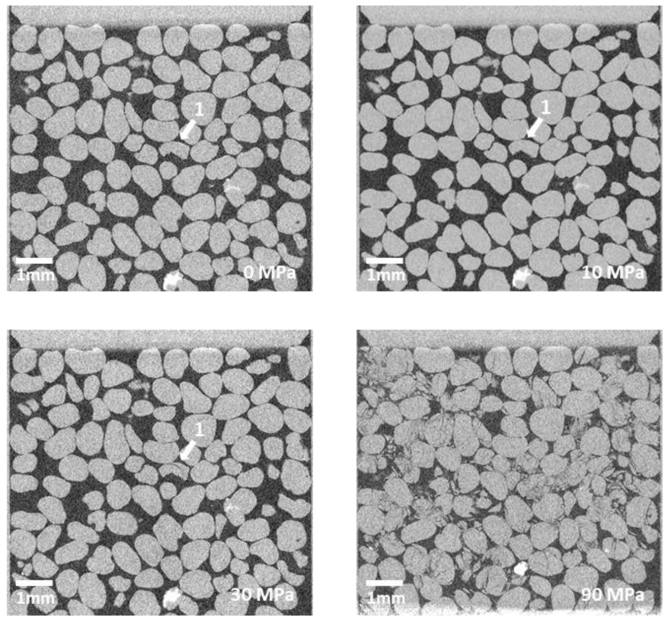

(c)

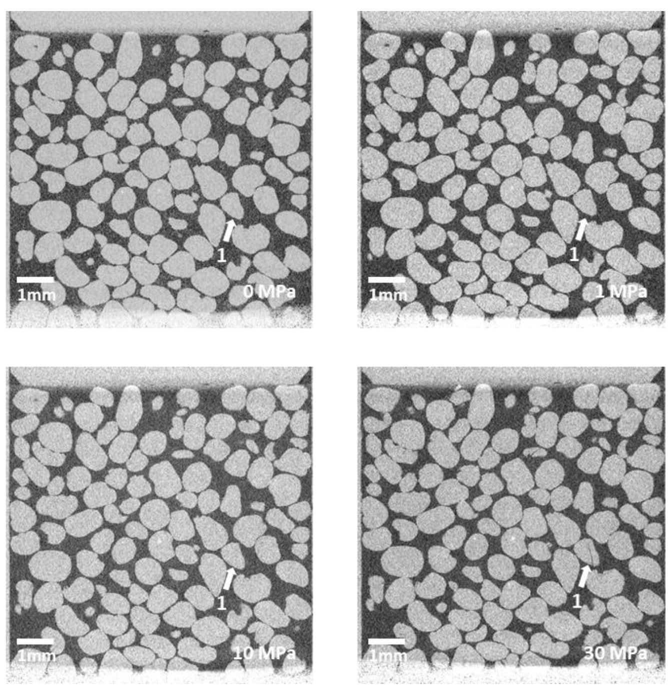

(d)

For the dense 2QR sand sample, we can clearly see in Figure 2.7(a), that particles marked with numbered arrows show no signs of crushing in the XCT scans at 1 and 2 MPa but start developing fractures or splits in the scan carried out at 10 MPa. At 30 MPa, many more particles undergo crushing and, at 90 MPa, most particles are completely pulverized, even if some larger particles remain intact, surrounded by smaller particles. Similar observation can be made for the scans performed on the dense OGF sample. For the OGF sand, the numbered arrows in Figure 2.7(b) show examples of particles that undergo crushing during loading. Visually, the level of crushing seems less than that of the 2QR sample at the same stress level. This may be attributed to the higher $\sigma_{f,avg}$ of the OGF sand particles. Similar to 2QR at 90MPa, most of the particles of the OGF sample are completely pulverized, with only a few large particles surviving crushing. Because the XCT scan data are only available at discrete stress levels, we cannot precisely quantify the stresses at which particle crushing initiates.

For the dense OTC samples, very limited particle crushing can be observed for stresses up to 30 MPa (see in Figure 2.7(c)). Similarly to what Karatza et al. (2019) observed, the XCT scans reveal small amount of particle damage at the 30 MPa stress level (for example, see the numbered arrow shown in the Figure 2.7(c)). However, these instances are few, and even though they are captured in the segmentation process, they do not affect the particle size distribution (these results will be shown in the next section).

For the medium-dense OTC sample, shown in Figure 2.7(d), we see very little particle crushing in the scan at 30 MPa. As for the dense OTC sample, inspection of the XCT data for the medium-dense OTC sample reveals some particle damage [for example, see the numbered arrow shown in the Figure 2.7(d)]. However, this minimal amount of crushing does not affect the particle size distribution (these results will be shown in the next section).

The 3D tomography data collected from the XCT scans can be processed to obtain digital representations of the particles, which can then be analyzed to obtain a quantitative measure of the degree of particle crushing in the samples with loading. To obtain digital representations of the particles from the 3D tomography data, five steps are generally followed: (1) binarization of the 3D tomography data to identify voxels belonging to solid particles (solid voxels) and voxels belonging to void space (void voxels), (2) calculation of the Euclidean distances from the centers of solid voxels to the centers of the nearest void voxel for the entire binarized tomography data, (3) location of local maxima of the Euclidean distances in the tomography data, (4) watershed segmentation, and (5) correction of over-segmentation. Figure 2.8 shows a graphical outline of these steps, which are explained next.

In the first step, the voxels corresponding to the solid particles in the 3D tomography data are differentiated from the voxels corresponding to the voids by a process called binarization. Voxels in the 3D tomography data that correspond to solid particles have a higher grey level intensity (GLI) value (are brighter) than the voxels corresponding to voids (see Figure 2.8(a)). To binarize the 3D tomography data, a GLI threshold is chosen, and the voxels that have a GLI value equal to or greater than the chosen threshold are assigned a value of 1 (solid voxels), while the voxels that have a GLI value lower than the threshold are assigned a value of 0 (void voxels) (see Figure 2.8(b)). For the present study, we followed a method that computes a physically meaningful threshold value by matching the *e* computed from the tomography data to the *e* obtained from physical measurements (Andò 2013). From the precise physical measurements before the compression test, we know the initial *e* of the sample, and from the initial *e* and the stress-strain response of the sample to uniaxial loading, we can calculate the *e* of the sample at each stress level. To obtain a physically meaningful threshold, we first make an initial guess of the GLI threshold using the widely used binarization method by Otsu (1979). We then binarize the 3D tomography data, using the initial guess, and calculate the *e* from the binarized data by dividing the cumulative volume of the void voxels by the cumulative volume of the solid voxels. If the calculated *e* differs from the value obtained from physical measurements, we iteratively update the GLI threshold until we get a match.

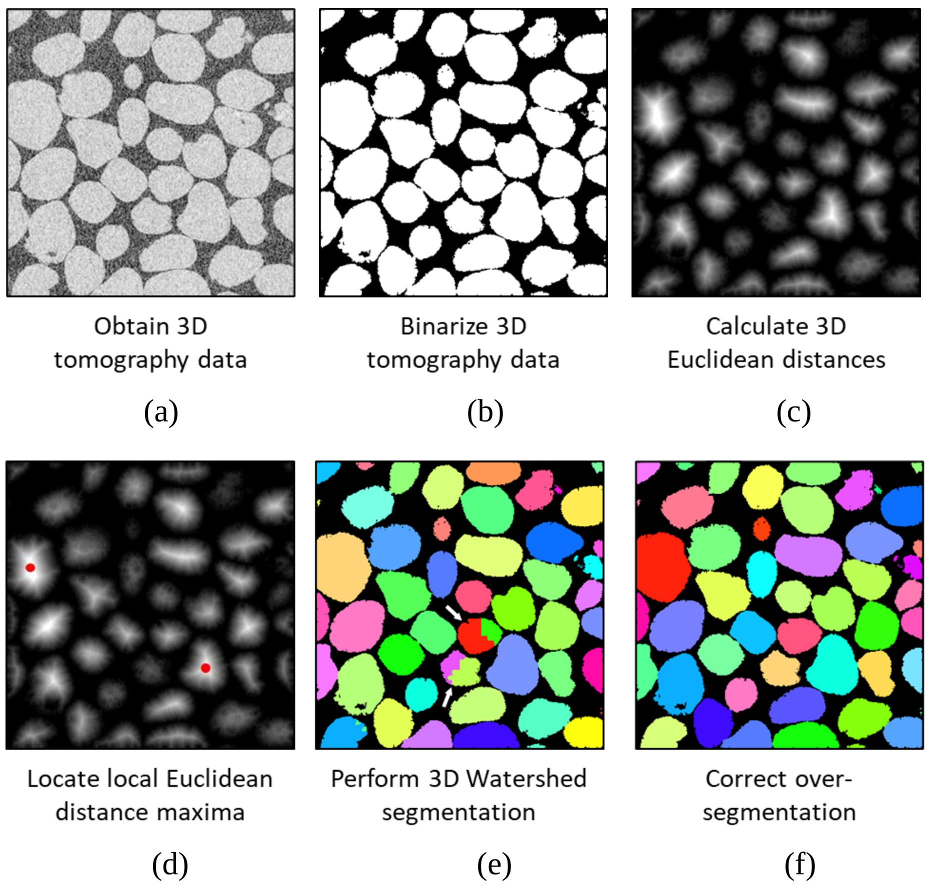

Figure 2.8 Outline of the steps followed to obtain digital representations of physical particles from the 3D tomography data: (a) acquire 3D tomography data, (b) binarize the 3D tomography data, (c) compute 3D Euclidean distances, (d) locate local Euclidean distance maxima, (e) perform 3D watershed segmentation (white arrows showing over-segmentation), (f) correct over-segmentation.

After the 3D tomography data is binarized, the next step is to obtain the Euclidean distances for voxels in the binarized data. For each solid voxel in the binarized tomography data, the distance from it to the nearest void voxel is calculated (this distance is called the Euclidean distance) and assigned to the solid voxel. Figure 2.8(c) shows the 3D Euclidean distances computed from the binarized tomography data. The brighter regions in Figure 2.8(c) have higher Euclidean distances than the darker regions. Theoretically, the solid voxel that has the greatest value of the Euclidean distance amongst its neighbors corresponds to the particle center since it is the farthest away from the void spaces. After obtaining the Euclidean distances of the voxels in the binarized tomography data, the voxels corresponding to local maxima of the Euclidean distances are located and marked as particle centers (represented by red dots in Figure 2.8(d)). Note that not all of the brightest regions in Figure 2.8(d) are marked as maxima since only a slice of the 3D tomography data is shown, and the other Euclidean distance maxima are located on the other slices.

Once the local Euclidean distance maxima are located, these are taken as starting points for the watershed segmentation algorithm (Beucher and Lantuejoul 1979) to obtain digital representations of the individual particles in the sample (shown in different colors in Figure 2.8(e)). All the voxels that belong to one particle are assigned a single unique integer value (also referred to as a label), which is different from every other particle in the sample. Often, after the application of the watershed algorithm, some particles may be over-segmented (shown in Figure 2.8(e) using white arrows).

Over-segmentation is caused by errors in the choice of local maxima of the Euclidean distance, and we correct this by identifying all particle pairs with unrealistically large contact areas and merging them [Figure 2.8(f)]. Two particles are merged if the area of contact between them [computed using spam (Stamati et al. 2020)] is larger than 0.64 times the cross-sectional area of the equivalent sphere of the smaller of the two touching particles (an equivalent sphere is a sphere with the same volume as that of the particle). The 0.64 threshold used to identify unrealistically large contacts was chosen based on a parametric study; this threshold value was found to correct over-segmentation in the XCT data without over-merging the segmented particles. We apply this procedure iteratively over the segmented XCT data until no unrealistically large contacts are left. After the over-segmentation is corrected, any particles with volume less than 1000 voxels^3 (equivalent volume of a cube with an edge length of 10 voxels) are removed because their size cannot be accurately assessed. For the scans analyzed in this research, removal of such small particles resulted in a solid volume loss of less than 0.5%.

After the 3D digital representations of the particles are obtained, the volume and size of the particles can be computed. The volume of a particle is the cumulative volume of all its voxels. The size of a particle can be quantified using different parameters (Al-Raoush and Papadopoulos 2010; Altuhafi et al. 2013; Andò 2013; Cil 2015; Druckrey 2016; Fonseca 2011; Fonseca et al. 2012, 2014; Hasan and Alshibli 2010). A reasonable approach to determine the most appropriate particle size parameter is to generate particle-size distribution curves using the different size parameters and compare them to the particle-size distribution curve from sieve analysis. The particle size parameter(s) that best capture the particle-size distribution from sieve analysis depends on the morphology of the sand particles (Fonseca et al. 2012).

For the test sands used in the present study, we considered five commonly used particle size parameters (Andò 2013; Fonseca et al. 2012; Ganju et al. 2020b): (1) equivalent sphere diameter (D_{eqsp}), (2) length along the major principal axis $D_{\mathrm{PA\text{-}max}}$, (3) length along the minor principal axis $D_{\mathrm{PA\text{-}min}}$, (4) maximum Feret diameter $D_{\mathrm{Feret\text{-}max}}$, and (5) minimum Feret diameter $D_{\mathrm{Feret\text{-}min}}$. We compared the particle-size distribution curves obtained using the five size parameters to the particle-size distribution curves from the sieve analysis of uncrushed sands. Figure 2.9 shows the particle-size distributions obtained using the five different particle size parameters in the analysis of XCT data, as well as the particle-size distributions obtained from sieve analysis of uncrushed 2QR, OGF, and OTC sands. As can be seen in Figure 2.9, for all three sands, the length along the minor principal axis $D_{\text{PA-min}}$ and the minimum Feret diameter $D_{\text{Feret-min}}$ were the particle size parameters that produced particle-size distribution curves closest to those from the sieve analyses. Consequently, all the particle-size distribution curves obtained from the analysis of XCT data used the $D_{\text{Feret-min}}$ as the particle size.

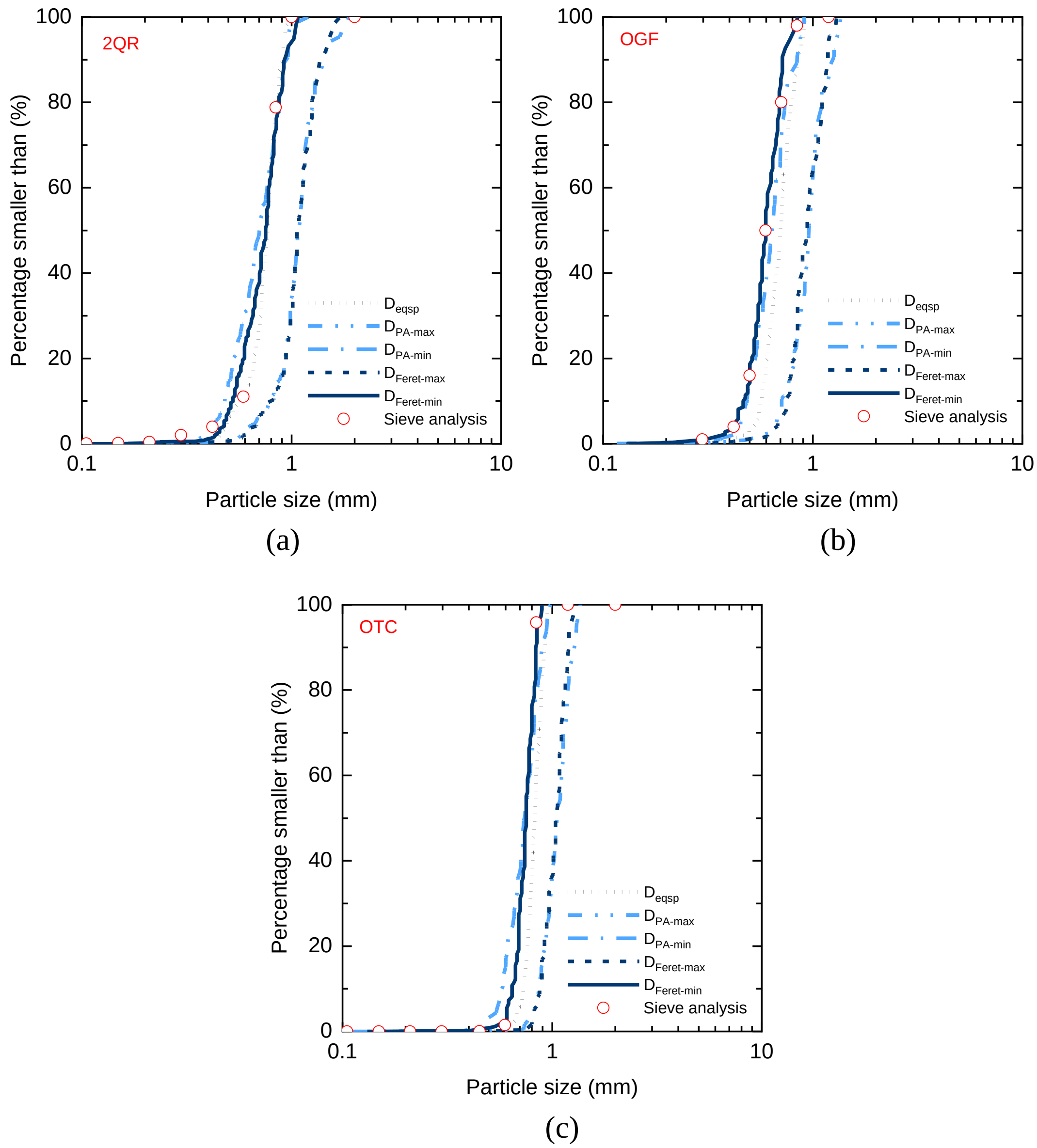

Figure 2.9 Comparison of particle size distributions obtained using different particle size parameters and the particle size distribution from sieve analysis of uncrushed (a) 2QR, (b) OGF, and (c) OTC sands.

With the analysis procedure established and the appropriate particle size parameter identified, the next step is the analysis of the tomography data of the sand samples at the different stress levels. However, the analysis of the entire XCT tomography data is time consuming and computationally expensive. Therefore, to assess the smallest subregion within the 3D tomography data that results in the same particle-size distribution and void ratio as the entire sample, we carried out a parametric study using subregions of different sizes extracted from within the tomography data (at the 0 MPa stress level) for each sample. For all the sands, the entire tomography data at the 0 MPa stress level was first binarized based on the measured sample density, and then cubical subregions of different sizes (1-7 D_{50} edge length) were extracted from the center of the binarized sample. The extracted subregions were then analyzed to obtain both the void ratios and the particle size distributions. Figure 2.10 shows the variation of void ratio with subregion size, and Figure 2.11 shows the change in the particle size distribution curves (using $D_{\text{Feret-min}}$ as the particle size) with subregion size for the four scanned samples. Also presented in Figure 2.11 are the results from sieve analyses of the uncrushed sands. From Figure 2.10 and Figure 2.11, we can see that a subregion size of 6 D_{50} is needed to capture the void ratios and particle size distributions for the dense samples, whereas a subregion size of 7 D_{50} is needed for the medium-dense sample. Similar approaches to compute minimum subregion size have been used in the literature (Al-Raoush and Papadopoulos 2010; Andò 2013; Karatza 2017).

Furthermore, in a subregion of size 6-7 D_{50}, the number of particles range from about 90 to 150. As the stresses increase, the number of particles within the subregion increases–due to particle crushing and densification of the sand sample (this was confirmed from the experimental results)–therefore, the subregion size selected for the lowest stress level is deemed adequate for all the other stress levels.

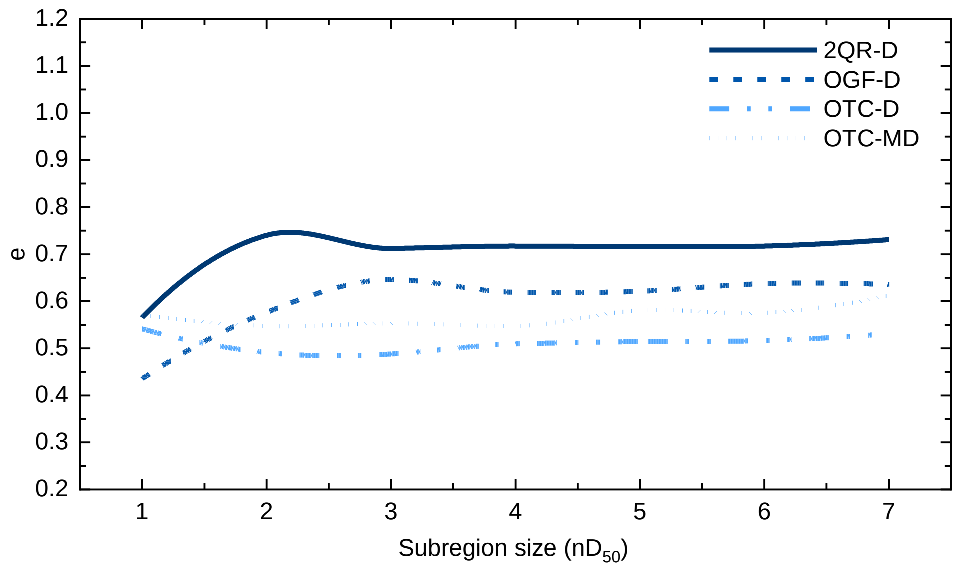

Figure 2.10 Selection of subregion size: variation of void ratio with subregion size for the dense OTC, OGF, and 2QR sand samples, and the medium-dense 2QR sample.

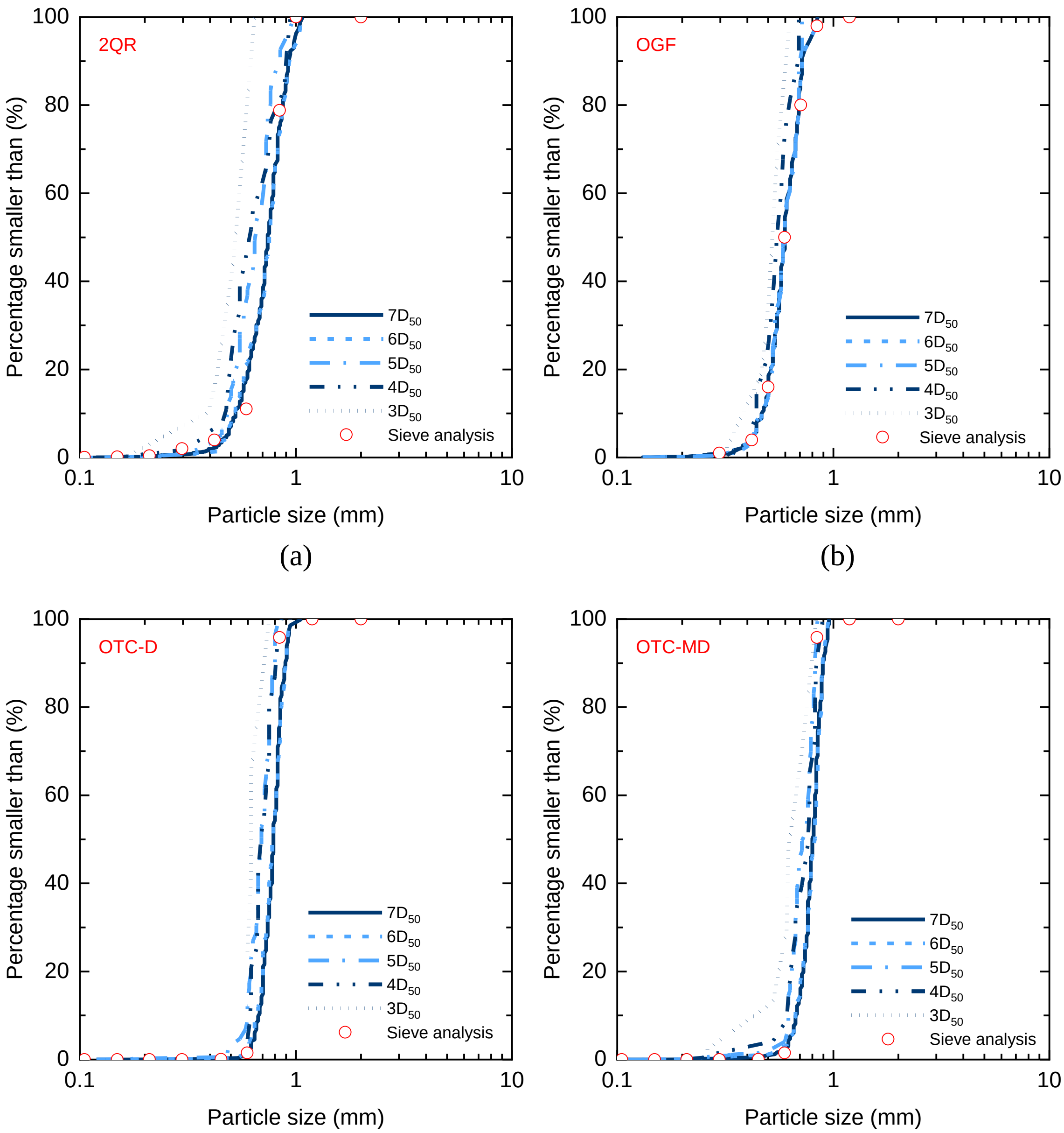

(c) (d)

Figure 2.11 Selection of subregion size: variation of particle size distribution curves with subregion size for the: (a) dense 2QR sample, (b) dense OGF sample, (c) dense OTC sample, and (d) medium-dense OTC sample.

2.3.3 Evolution of particle size and morphology with loading

2.3.3.1 Particle size

From the analysis of the 3D tomography data, the particle-size distribution curves of the dense 2QR, OGF, OTC sands and the medium-dense OTC sand were obtained at different stress levels. It is important to highlight at this point that to measure the size of a particle with reasonable accuracy, the number of voxels across the diameter of the particle should be greater than 10 (Wiebicke et al. 2017). In the tomography data of the dense 2QR, OGF and OTC sand samples at the 90 MPa stress level, a significant percentage of the particles (≥10% by mass) were observed to have less than 10 voxels across their diameters; as a result, the sizes of more than 10% of the particles could not be accurately assessed. XCT scans at a higher resolution could be carried out to overcome this limitation; however, higher resolution scans come at the cost of a significantly reduced scan window which was not suitable for our sample size. Therefore, to ensure reasonable accuracy in the measurements of particle sizes, we present results for dense samples for stress levels of up to 30 MPa.

Figure 2.12 shows the particle-size distribution curves for each sand sample compressed in the small mold, along with the 10-voxel threshold below which accuracy of particle size is low. Particle crushing in the sand samples, qualitatively observable in Figure 2.12, can be quantified using relative breakage parameters (B_r), two of which have gained wide acceptance: one proposed by Hardin (1985) and, the other, proposed by Einav (2007). Table 2.6 provides the values of Hardin (1985) and Einav (2007) relative breakage parameters for the particle-size distribution curves of the dense OGF and 2QR samples presented in Figure 2.12 (a) and (b). B_r values for the dense and medium-dense OTC sands samples were ≈ 0% at all stress levels up to 30 MPa, therefore, these are not included in Table 2.6.

In Figure 2.12(a), we see that there is not much change in the gradation of the dense 2QR sand sample for the stress levels less than 10 MPa. At 10 MPa, some amount of crushing is observed. From Table 2.6, we can see that the 2QR sample has a B_r value of 1% at 10 MPa. As the stress is increased to 30 MPa, more particles crushed, and the particle-size distribution curve shows a clear difference from the original. Furthermore, the B_r value increases to 6-7%. Visually, the crushing at 10 MPa appears to be mostly because of chipping of the sharp corners of the sand particles and, possibly, some splitting (see Figure 2.7(a)), whereas, at 30 MPa, clear splitting and disintegration of the particles can be observed in the XCT scans.

To assess if there is any variation in the amount of particle crushing in the dense 2QR sample, we analyzed two additional subregions–one close to the loading piston (top) and another close to the bottom of the compression mold (bottom). Figure 2.13 presents the particle-size distributions at the 0 MPa and 30 MPa stress levels for the dense 2QR sample obtained from the analyses of the subregions in the top, middle and bottom of the mold. As we can see from Figure 2.13, although there is a small variation in the particle size distribution between the three subregions at 0 MPa, the three particle size distributions at 30 MPa practically overlap.

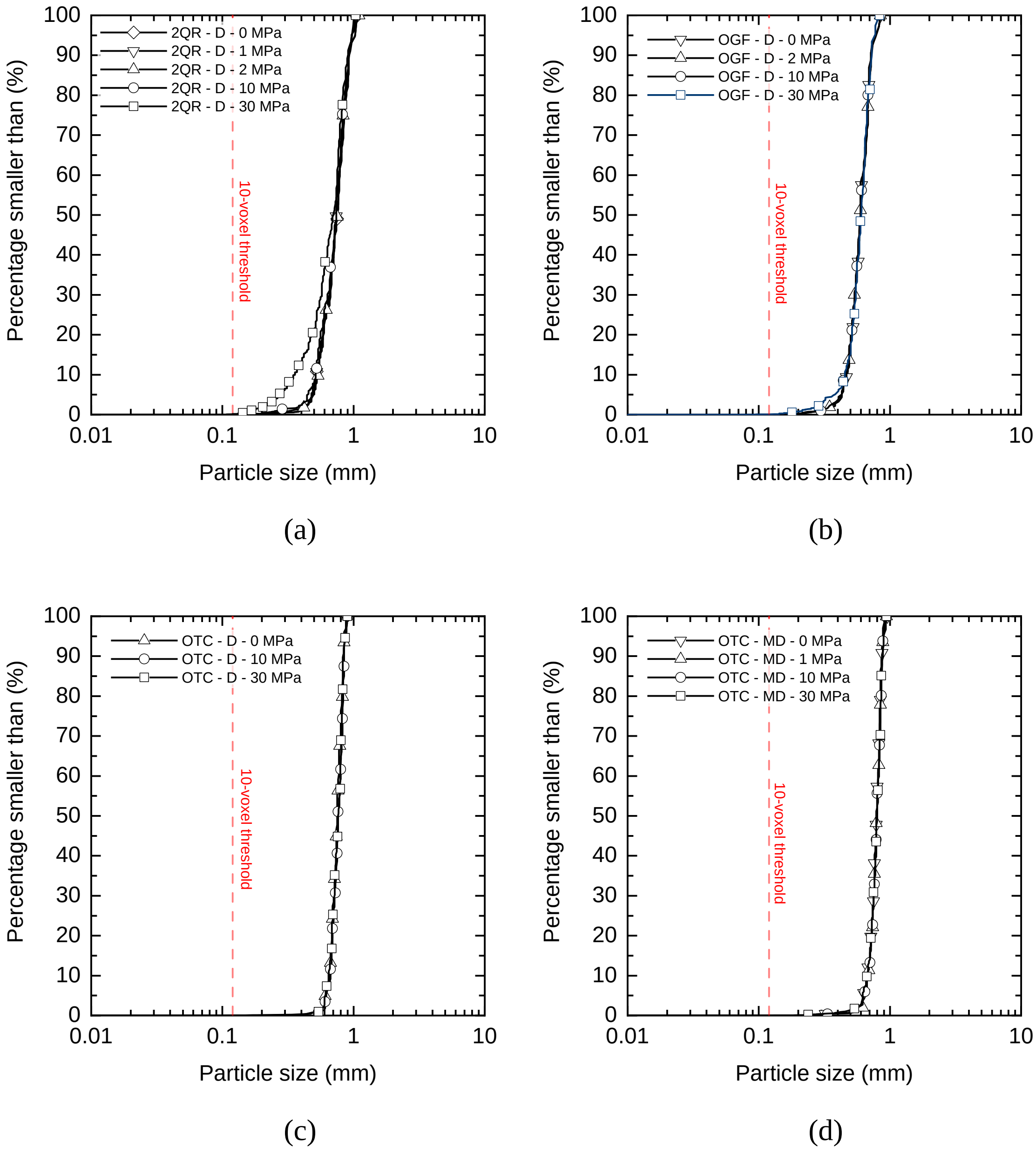

Figure 2.12 Particle-size distribution curves at different stress levels for: (a) dense 2QR sample, (b) dense OGF sample, (c) dense OTC sample, and (d) medium-dense OTC sample, along with the 10-voxel threshold below which accuracy of particle size is low.

Table 2.6 Relative breakage parameter (B_r) values from analysis of 3D tomography data.

Sand Sample	Stress (MPa)	Analysis of 3D tomography data	
		Einav (2007) B_r (%)	Hardin (1985) B_r (%)
2QR-D	1	0	0
	2	0	0
	10	1	1
	30	7	6
OGF-D	2	0	0
	10	0	0
	30	1	1

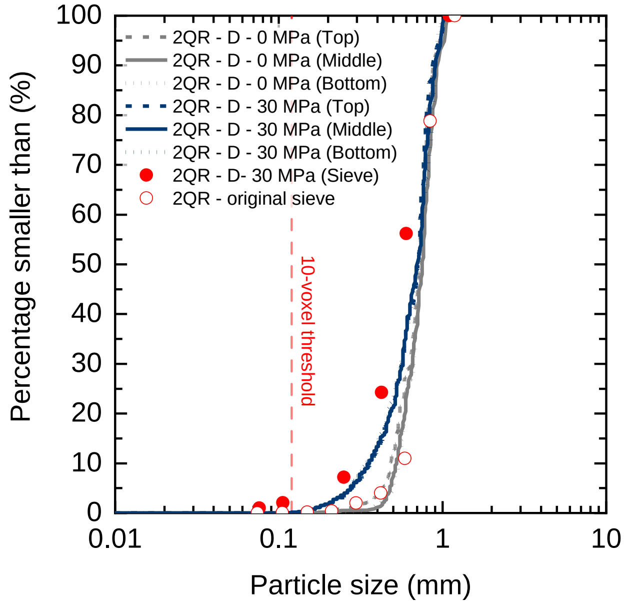

Figure 2.13 Variation in particle size distribution within the sample for dense 2QR sand obtained from analysis of XCT data, along with particle size distribution obtained from sieve analysis, along with the 10-voxel threshold below which accuracy of particle size is low.

Furthermore, to assess the accuracy of the particle size distribution curves of the crushed sand obtained from the analysis of the XCT data, we also present in Figure 2.13 results from sieve analyses of dense 2QR sand loaded to the 30 MPa stress level and of uncrushed 2QR sand. Since the original dense 2QR sand sample–which was scanned in the XRM–was loaded to a maximum stress of 90 MPa, we could not use the particle size distribution from the sieve analysis to compare with the particle size distribution from the XCT analysis (at 30 MPa). For this reason, we prepared another sample of the 2QR sand at the same initial D_R as the sample scanned in the XRM and loaded it in the same aluminum mold to 30 MPa. After unloading, we collected the sample and carefully sieved it. Because the samples being compared are different and the sieving process itself can cause some breakage of particles, the particle-size distributions cannot be expected to match perfectly. With that in mind, we can see in Figure 2.13 that the particle size distributions from the sieve analysis and those from the XCT analysis are in reasonable agreement. This also increases our confidence in the segmentation procedure followed to analyze the XCT data.

In the case of OGF sand, up until 10 MPa, no significant particle crushing can be observed from the CT scan (see Figure 2.7(b))–this is also reflected in the particle-size distribution curve presented in Figure 2.12(b). At 30 MPa, in Figure 2.7(b), we can observe some particle splitting and chipping. The particle-size distribution curve in Figure 2.12(b) reflects this in the form of an increase in the percentage of smaller particles in the 0.2-to-0.4 mm range. From Table 2.6, we can see that the B_r for the dense OGF sand reaches 1% at 30 MPa. For the OGF sand, we calculate $B_r \approx 1\%$ at 30 MPa stress level, while, for the 2QR sand, we calculate $B_r \approx 1\%$ at 10 MPa stress level. While some amount of particle breakage takes place in the samples at lower stress levels, the B_r values remain $\approx 0\%$. Therefore, in this research, we consider B_r value of $\approx 1\%$ to be a threshold above which particle crushing is significant enough to affect the particle size distribution. This B_r threshold can be further refined with XCT scans carried out at more closely spaced stress levels.

Figure 2.12(c) and (d) show the particle-size distribution curves of dense and medium-dense OTC sand samples, respectively. As previously mentioned, for the dense OTC sample, some crushing can be observed at 30 MPa (Figure 2.7(c)); however, the magnitude of this crushing is not high enough to be reflected in the particle-size distribution curve in Figure 2.12(c). The same holds true for the medium-dense OTC sample–almost no change in the particle size distribution is observable up to the stress level of 30 MPa. This is also reflected in the B_r values for the dense and medium-dense OTC sand samples, both of which have $B_r \approx 0\%$ at the 30 MPa stress level.

From the particle size distribution curves at different stress levels, we observe that, for a given initial D_R, the more angular the sand, the lower the stress level under uniaxial compression at which its constituent particles show signs of crushing in the XCT scans. We cannot precisely quantify the stress levels at which particle crushing initiates in the sand samples because XCT scan data are only available for discrete stress levels. These discrete data show that, $B_r \approx 1\%$ at stress levels of 10 MPa and 30 MPa for the dense 2QR and OGF sand samples, but $B_r \approx 0\%$ even for a stress of 30 MPa for the dense OTC sand.

2.3.3.2 Particle morphology

The 3D particle size parameters can also be used to assess the sphericity of the particles. In Table 2.1 we presented the value of S_{avg} for the three test sands based on the analysis of 2D images of the particles. The sphericity S was computed by fitting an ellipse to the 2D images of each particle and then taking the ratio of the short axis to the long axes of the fitted ellipse (Zheng and Hryciw 2015). To have an analogous measure of sphericity in 3D, we take the ratio of the length of the particle along the minor principal axes ($D_{PA\text{-}min}$) to the length along the major principal axis ($D_{PA\text{-}max}$). This approach gives, for all three sands, an average sphericity value (at 0 MPa stress level) close to the values obtained from the 2D image analyses. Figure 2.14 presents the evolution of the 3D sphericities S of the sand samples with loading.

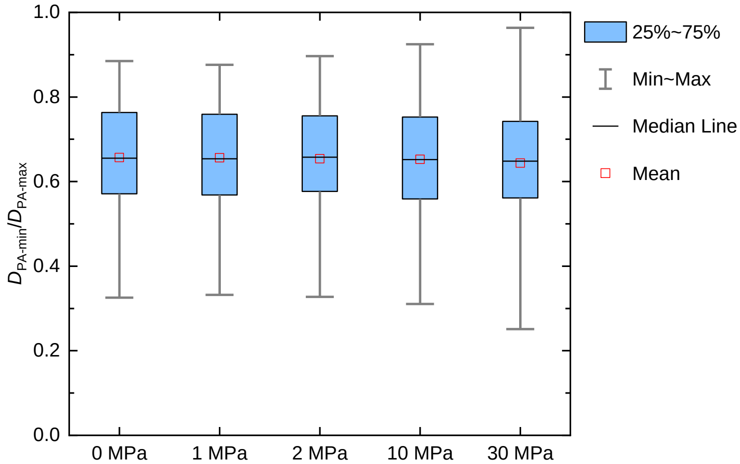

(a)

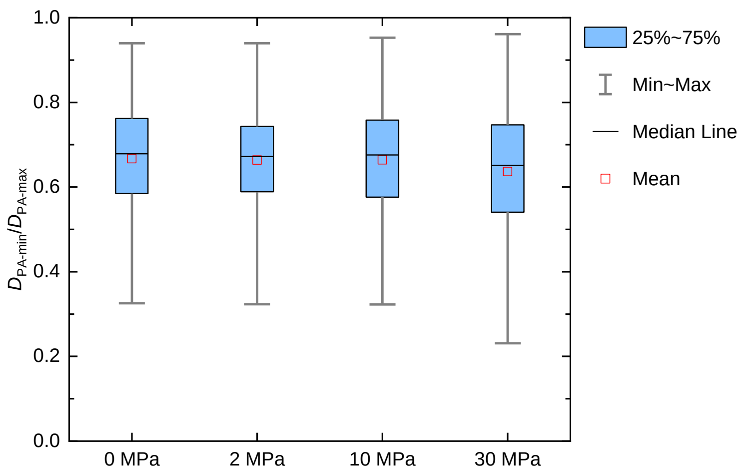

(b)

Figure 2.14 Change in 3D sphericity ($D_{PA\text{-}min}/D_{PA\text{-}max}$) with loading for: (a) dense 2QR sand sample, (b) dense OGF sand sample, (c) dense OTC sand sample and (d) medium-dense OTC sand.

Figure 2.14 continued

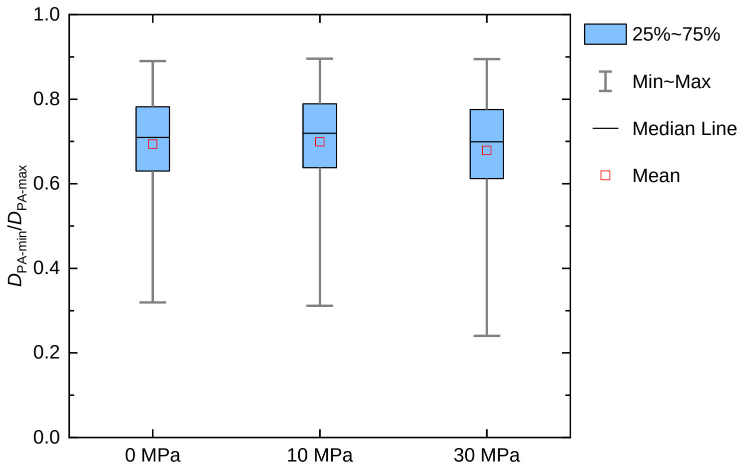

(c)

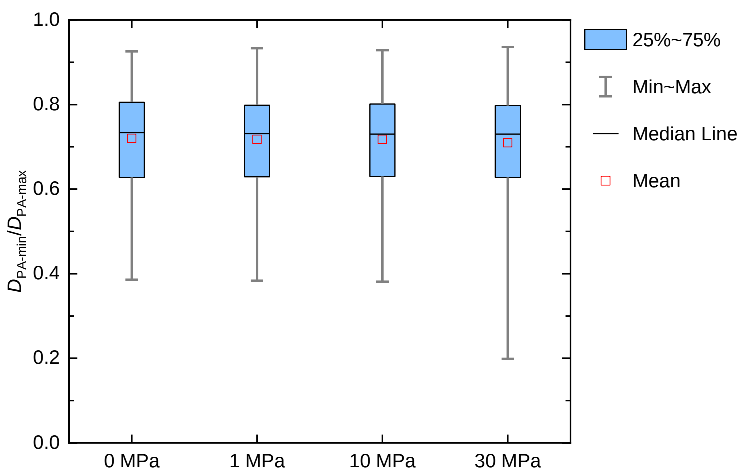

(d)

For 2QR, as loading increases, the distribution of sphericity of the particles remains relatively stable for stresses less than 10 MPa (Figure 2.14(a)). At and beyond the 10 MPa stress level, we observe a slight drop in the average sphericity, along with an increase in the range of values. The increase in the upper bound of the sphericities is explained by the fact that if crushing occurs as a result of particle chipping, the larger (parent) particle will have a more spherical shape (the smaller (child) particle may or may not be more spherical). The slight drop in average sphericity of 2QR with increasing uniaxial compressive stresses suggests that, on average, crushing of 2QR results in particles that are slightly less spherical than the original particles. Similar observations have been made by Seo et al. (2020) who reported a decrease in average sphericity of the 2QR particles with increase in applied stress under uniaxial compression.

For OGF, show in Figure 2.14(b), we observe a similar decrease in sphericity as the sample is loaded to 30 MPa, at which stress level we first observe crushing in the XCT scans. Interestingly, there is very little increase in the upper bound of sphericity, which can be attributed to the OGF's higher R_{avg}, with the particles crushing by splitting or fragmentation rather than by chipping.

For the dense and medium-dense OTC samples, shown in Figure 2.14(c) and (d), even though we observe minimal change in the particle size distributions, the minor particle damage reported in the previous sections does seems to affect the sphericity values. For the dense OTC sample, shown in Figure 2.14(c), as a result of the breakage of the particles, we see a drop in the lower bound of the sphericity values. In the case of the medium-dense OTC sand sample, shown in Figure 2.14(d), similar to the dense OTC sand, we do not see much variation in the sphericity values until a stress level of 10 MPa; however, at 30 MPa stress level we observe a drop in the lower bound of the sphericity values. It should be noted here that the dense and medium-dense

OTC sands have similar mean sphericity values at 0 MPa stress level, but different upper and lower bounds of sphericity. This can be explained by minor variations in the two samples.

2.3.4 Fabric from 3D tomography data

According to Oda (1977), the fabric of an aggregate of particles may be quantified in one of three ways: (1) based on the distribution of the orientation of the major principal axis of the particle in the aggregate; (2) based on the 3D distribution of the orientation of the contact normal between an arbitrary pair of contacting particles; and (3) based on the distribution of the coordination number (number of interparticle contacts per particle). For more spherical particles (with high values of S_{avg}), the orientation of the major principal axis is often ambiguous and hard to assess. The test sands used in the present study have a relatively high S_{avg}; therefore, to quantify sample fabric, we use the distribution of coordination number and the orientations of the contact normals between contacting particles.

To identify particle contacts, we use the random walker RW method which has been shown, at present, to produce the least error in the estimation of orientation of contact normals (Wiebicke et al. 2017, 2019, 2020b; a). The random walker RW method, implemented in *spam* (Stamati et al. 2020), was used for contact analyses. The RW method identifies particle contacts by locating the points in space by interpolation where the probability of belonging to either one of two particles in contact is 50%. The algorithm then fits a plane through all the points identified, and the normal to the fitted plane is taken as the contact normal for the two contacting particles.

According to Wiebicke et al. (2017), based on the analysis of high resolution scans and synthetics images, the mean error between the actual contact normal and the contact normal obtained from the RW algorithm depends on the morphology of the contacting particles and the resolution of the tomography data. For the scans of OGF and 2QR sands presented in this paper, this error is expected to be about 15°. This expected error value is based on the fact that the OGF and 2QR sands have a morphology similar to that of the Hostun sand tested by Wiebicke et al. Wiebicke et al. (2017), and that the Hostun sand has a mean error of approximately 15° at comparable scan resolutions. For the more rounded OTC sand, this error can be expected to be less than 15°, but more than 10° (the mean error for high-precision manufactured ruby spheres Wiebicke et al. (2017)). To be conservative, we adopt the mean error of 15° for the OTC sand as well. This mean error of 15° is taken into account when computing the values of the fabric tensor **N**, the deviatoric fabric tensor **F** and the anisotropy scalar $\boldsymbol{F}_{\mathrm{q}}$ defined by Kanatani (1984):

$$\mathbf{N} = \frac{1}{N_{\mathbf{c}}} \sum_{\boldsymbol{\alpha}=1}^{N_{\mathbf{c}}} n^{\alpha} \otimes n^{\alpha} \tag{2.3}$$

$$\mathbf{F} = \frac{15}{2}\left(N - \frac{1}{3}\mathrm{tr}(\mathbf{N})\mathbf{I} \right) \tag{2.4}$$

$$F_{\mathrm{q}} = \sqrt{\frac{3}{2}\mathbf{F} : \mathbf{F}} \tag{2.5}$$

where n^{α} is the contact normal vector for the contact α, and N_{c} is the total number of contacts in the sample. A high value of F_{q} indicates that the sample fabric is very anisotropic, and all the contacts are oriented mostly in one direction, and a very low value of F_{q} indicates that the contact normal is uniformly distributed with respect to its direction in space. As done for the particle size and void ratio, to save computation time, we investigated the effect of the subregion size on the computed F_{q} value through a parametric study. From the study, it was found that a subregion size of $6D_{50}$ is large enough to capture the fabric anisotropy of the sample. This size is the same size as that selected for the analyses of particle-size distribution and void ratio for the dense samples.

2.3.5 Evolution of fabric with loading

Figure 2.15 presents the cross sections of the 3D tomography data, the distribution of the coordination number, and the distribution of the interparticle contact orientation for the dense 2QR, OGF and OTC samples and for the medium-dense OTC sample at multiple stress levels. When computing the distribution of the coordination numbers, only whole particles are considered. Particles that are cut by the edge of the subregion must not be considered in the distribution because their inclusion causes an underestimation of the average coordination number (and unrealistic values of coordination numbers, such as 1s and 0s, for the particles cut by the subregion edge). Therefore, in the distribution of coordination numbers shown in Figure 2.15, particles that are cut by the boundaries of the subregion are not included. Figure 2.15 shows the values of F_q as a function of the stress applied on the four sand samples.

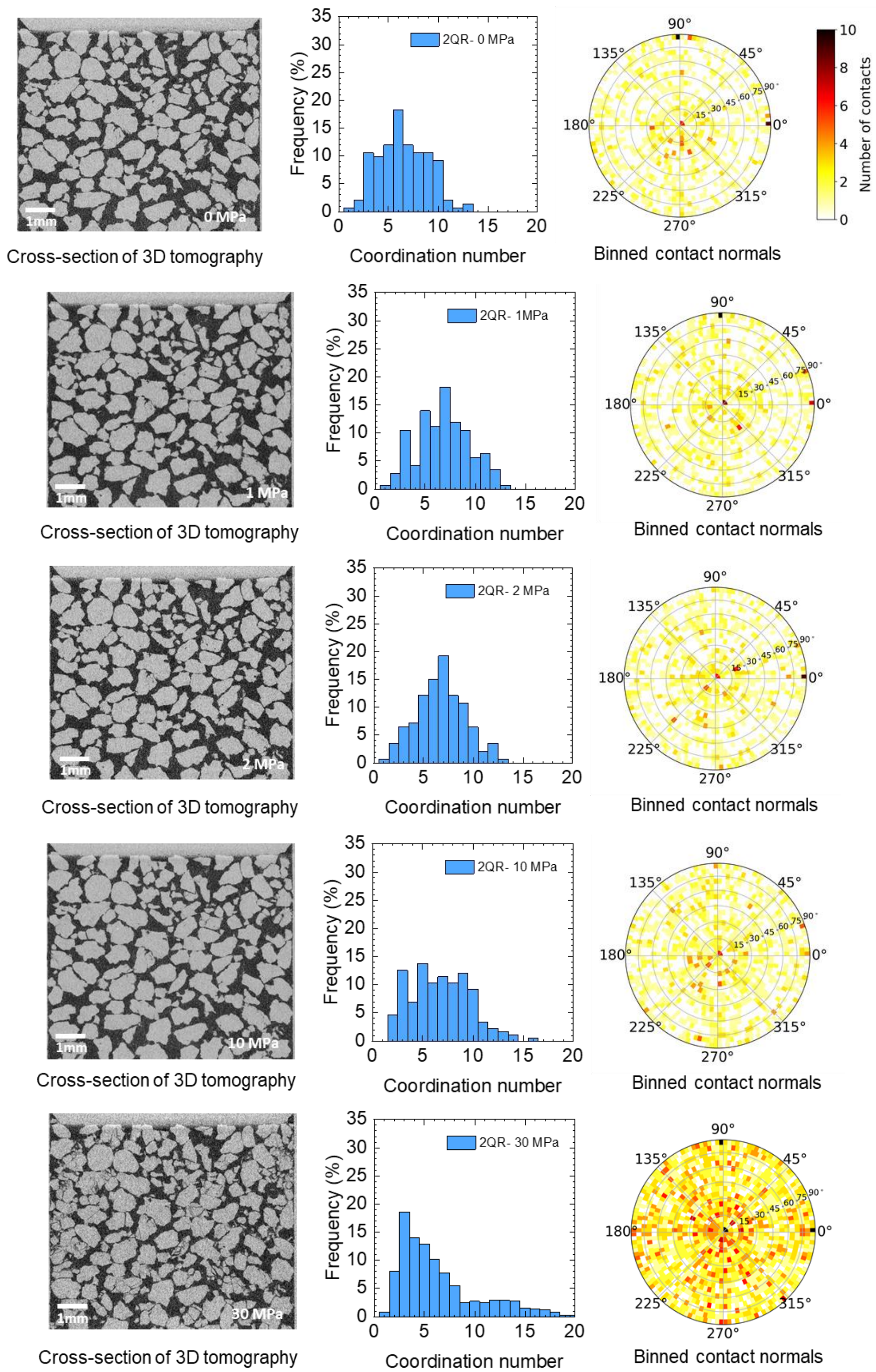

(a)

Figure 2.15 Distribution of coordination numbers and interparticle contact orientations under uniaxial compression for (a) dense 2QR sample at 0 MPa, 1MPa, 2 MPa, 10 MPa, and 30 MPa stress levels, (b) dense OGF sample at 0 MPa, 2 MPa, 10 MPa, and 30 MPa stress levels, (c) dense OTC sample at 0 MPa, 10 MPa, and 30 MPa stress levels, and (d) medium-dense OTC sample at 0 MPa, 1 MPa, 10 MPa, and 30 MPa stress levels.

Figure 2.15 continued

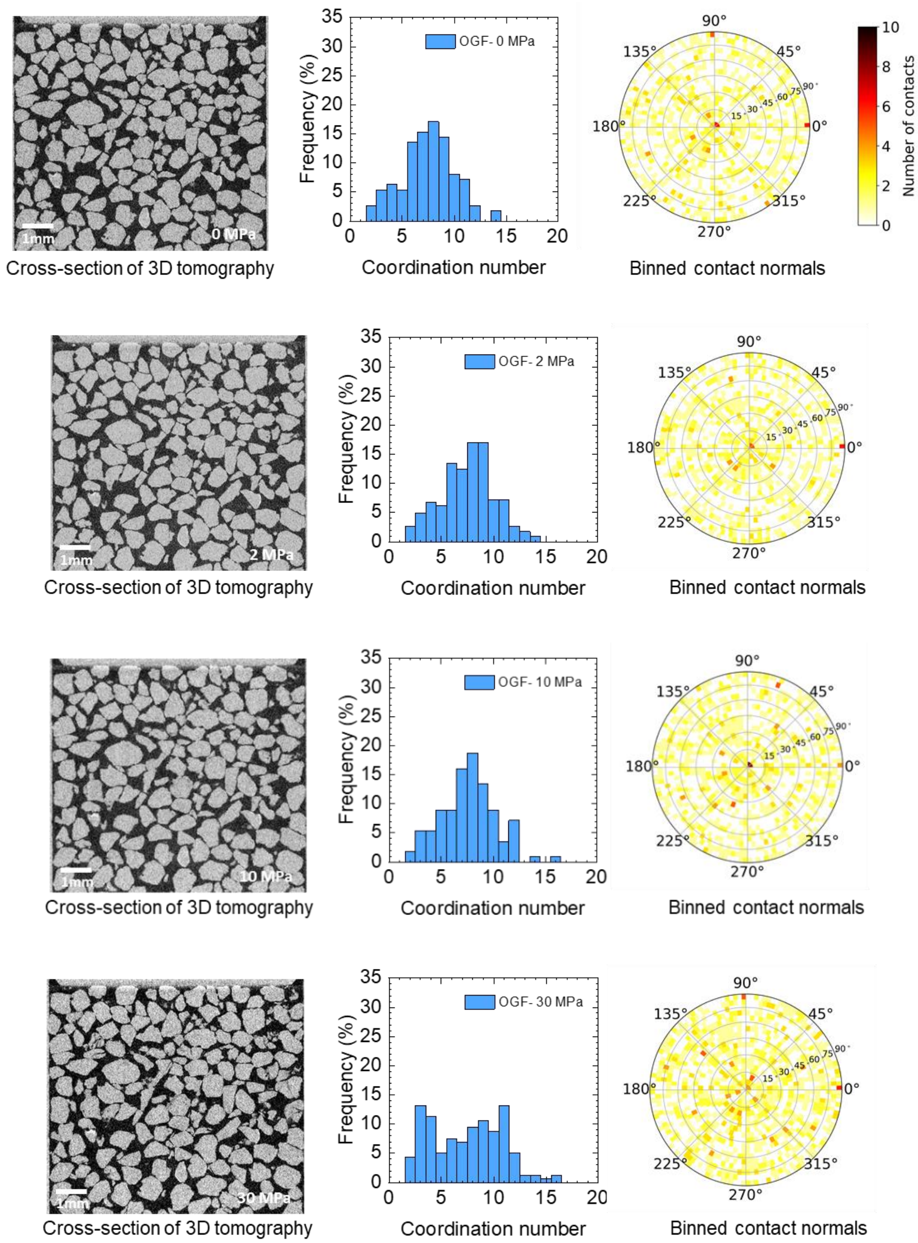

(b)

Figure 2.15 continued

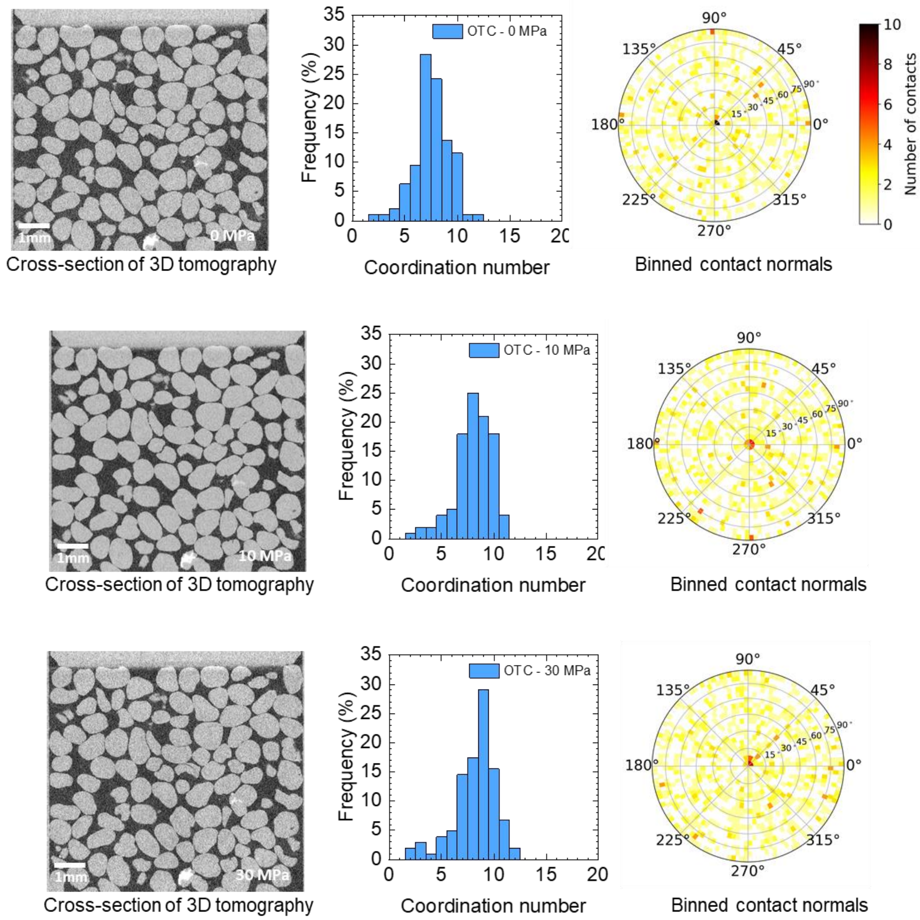

(c)

Figure 2.15 continued

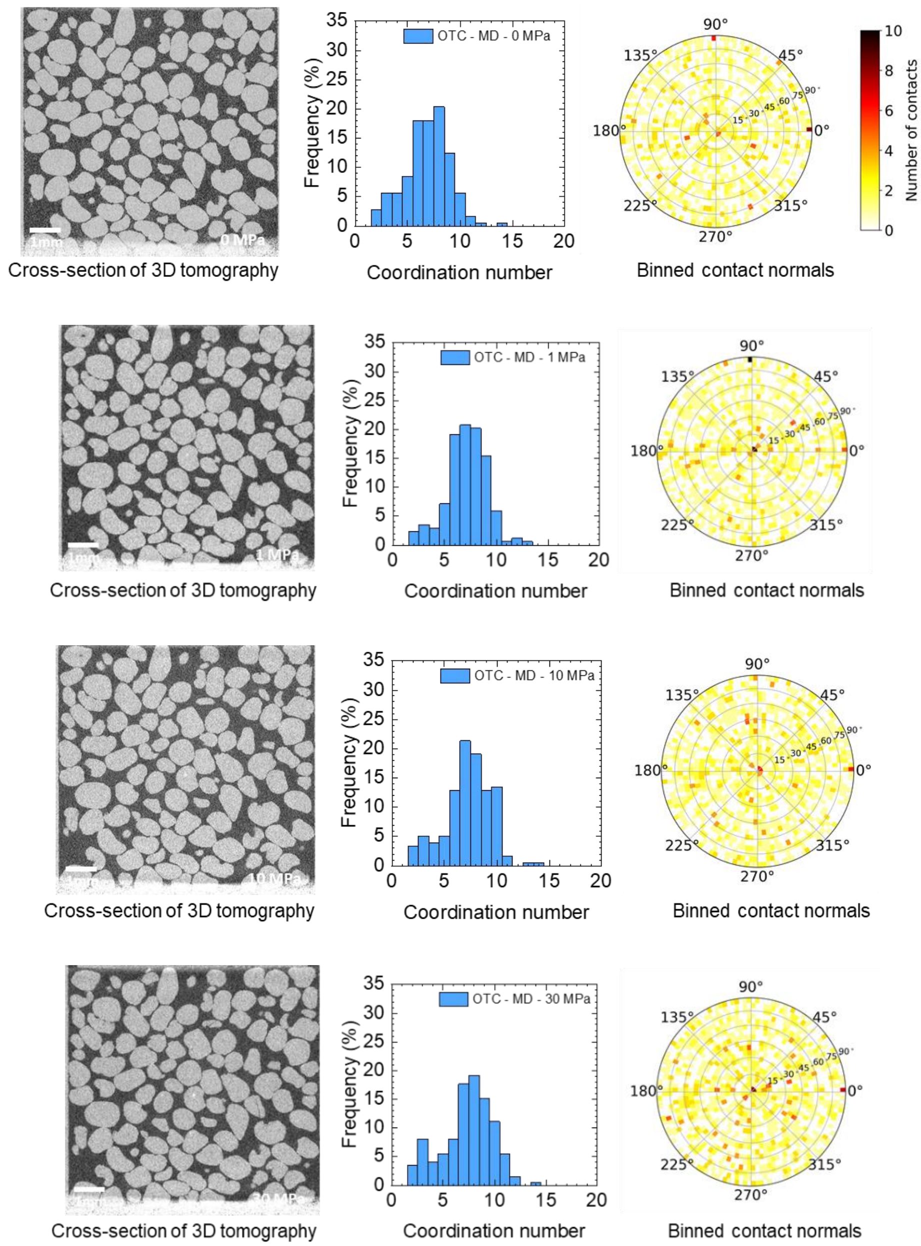

(d)

The distributions of the interparticle contact normal in Figure 2.15 are presented using binned Lambert projection plots (Andò 2013). For the binned Lambert projections, we are plotting one vector for each contact and projecting the southern hemisphere to the northern hemisphere. If we visualize a contact normal as a unit vector normal to the plane of contact between two particles in space, and if we translate all contact normals in the sample such that their tails are located at the origin, then the tip of all the translated contact normals would lie on the surface of a unit sphere. Lambert projection plots allow us to visualize this 3D spherical distribution of contact normals as a 2D circular projection following an equal-area projection mapping rule. For example, in a Lambert projection plot, a contact normal pointing in the vertical direction in 3D (along the direction of loading in our case) will be plotted as a point at the center of the 2D circular projection, whereas a contact normal pointing in the horizontal direction in 3D will be plotted as a point on the circumference of the 2D circular projection. Therefore, if the majority of the contact normals in the sample point in the vertical (or horizontal) direction, indicating an anisotropic sample fabric, a larger number of points will be observed close to the center (or the circumference) of the projection. On the other hand, if the contact normals within a sample are randomly oriented in space, indicating an isotropic sample fabric, the points on the Lambert projection will be more homogeneously distributed through the area of projection. Grouping of the projection points creates a binned Lambert projection plot (Figure 2.15), which allows us to visually identify dominant orientations of the contact normals within the sample. The grouping is done on the basis of the angle made by the contact normal with respect to the vertical axis (which ranges from 0° to 90°), and the angle made by the projection of the contact normal on the horizontal plane with respect to one of the horizontal axes (which ranges from 0° to 360°).

Results for the 2QR sample [see Figure 2.15(a) and Figure 2.16(a)] show that the sample fabric remains relatively stable until a stress equal to 2 MPa. From Figure 2.15(a), we see that the distributions of the coordination numbers and the Lambert projections of the contact normals remain about the same. The distribution of the coordination numbers appears to be approximately normal, with a mean ranging from 6.5 at 0 MPa to 6.8 at 2 MPa. The mean coordination number value at 0 MPa is consistent with the findings of Fei and Narsilio (2020). Based on XCT analyses of sands with different morphologies, Fei and Narsilio (2020) reported values of average coordination numbers of about 6.5 for angular sands similar to the 2QR sand used in this research.

As the stress on the dense 2QR sand sample increases to 10 MPa, we observe an increase in the number of particles with coordination numbers in the range of 2-3 [see Figure 2.15(a)]. Crushing of particles generates smaller particles which have lower coordination numbers because these newly created smaller particles are in contact with only a few larger particles. On the other hand, the coordination number of large particles in the sample increases due to the appearance of small, crushed particles in their surroundings [as also observed by Alam et al. (2018)]. These trends continue as the stress increases to 30 MPa, at which stage particles with coordination numbers in the range of 3-4 become more prevalent. The number of interparticle contacts increases from approximately 900 at 0 MPa to approximately 2700 at 30 MPa (as qualitatively observable from the binned Lambert projection plots).

From Figure 2.16(a), we can see an increase in F_q from about 0.70 at the 0 MPa stress level to about 0.78 at the 2 MPa stress level, indicating a slight increase in interparticle contact anisotropy of the dense 2QR sample with loading. However, upon further loading to higher stress levels, the value of F_q drops to 0.66 at 10 MPa and to 0.44 at 30 MPa. For the dense 2QR sample,

F_q values near the top and bottom of the sample [shown in Figure 2.16(a) for the 0 MPa and 30 MPa stress levels] agree reasonably well with the values in the middle of the sample.

The same features are observed in the evolution of the fabric of the dense OGF sand sample with loading, as shown in Figure 2.15(b) and Figure 2.16(b). From Figure 2.15(b), we can see that the distribution of contact normals and the shape of the distribution of the coordination numbers remain relatively stable until 10 MPa. At the 30 MPa stress level, the distribution of coordination numbers still appears to be normal, with more particles having coordination number in the 3-4 range. The average coordination number ranges from 7.5 at 0 MPa to 7.6 at 30 MPa; these values are slightly higher than those for the more angular 2QR sand sample at the same stress levels. The number of interparticle contacts increases from approximately 850 at 0 MPa to approximately 1200 at 30 MPa. From Fig. 16(b), we can see that, similarly to what was observed for the dense 2QR samples, the dense OGF sand experiences a slight increase in the F_q values from 0.51 at 0 MPa to 0.57 at 10 MPa, but then drops to 0.47 at 30 MPa.

The evolution of the fabric of the dense OTC sample with loading is presented in Figure 2.15(c) and Figure 2.16(c). From Figure 2.15(c) we can see that for the dense OTC sample the shape of the distribution of the coordination numbers does not change appreciably with loading and the orientations of the contact normals also remain relatively stable. The average coordination number ranges from 7.6 at the 0 MPa stress level [this value is similar to the average value of 7.2 reported by Fei and Narsilio (2020)] to 8.2 at the 30 MPa stress level. Furthermore, from Figure 2.16(c) we can see that the F_q value increases slightly from 0.41 at 0 MPa to 0.44 at 30 MPa.

From Figure 2.15(d) we can see that for the medium-dense OTC sample, the distribution of coordination numbers follows the same trend as that in the dense OTC sample. The mean coordination number for the medium-dense OTC sand sample increases from 6.9 at 0 MPa to 7.4

at 30 MPa (these values are lower–as expected–than the coordination numbers of the dense OTC sand). From Figure 2.16(d) we see that the value of F_q also increases from 0.37 at 0 MPa stress level to a little above 0.51 at the 30 MPa stress level, indicating a greater increase in the interparticle contact anisotropy in comparison to the dense OTC sample.

The results presented above indicate that, in uniaxial compression, the value of F_q initially tends to increase as the applied stress increases. However, this increase in F_q with the applied stress is limited by particle crushing. For example, in the case of the dense 2QR and OGF sands, we first observe a drop in F_q at stress levels of 10 MPa and 30 MPa, respectively. These are the same stress levels at which we first observe a $B_r \approx 1\%$ for the two sands.

Furthermore, for the dense and medium-dense OTC sand samples, we observe a similar increase in F_q as the stress increases. However, for both the dense and the medium-dense OTC samples, at the 30 MPa stress level, we see no drop in the F_q and a $B_r \approx 0\%$. Therefore, the data presented here suggests that, as long as $B_r \approx 0\%$, F_q tends to increase with increasing stress. However, as B_r increases towards and beyond 1%, interparticle contacts become more randomly oriented, leading to a decrease in the value of F_q. This points to a clear link between the anisotropy of the interparticle contacts (F_q) and the breakage (B_r) in sand samples loaded under uniaxial compression. Further research, however, is needed to better understand and quantify this link.

2.4 Conclusions

In this paper, we presented the results of uniaxial compression experiments carried out on three silica sands. The sands were fully characterized prior to the uniaxial compression experiments to quantify the particle-size distributions, particle morphologies, packing densities, average particle fracture stresses and critical-state friction angles. The uniaxial compression experiments were carried out in a special loading frame placed inside a high-resolution X-ray Microscope (XRM) to obtain 3D tomography data of the sand samples at multiple stress levels during loading. Analysis of the 3D tomography data was done to obtain the distribution of particle sizes, and interparticle contact normals (used to quantify sample fabric) within the samples with loading.

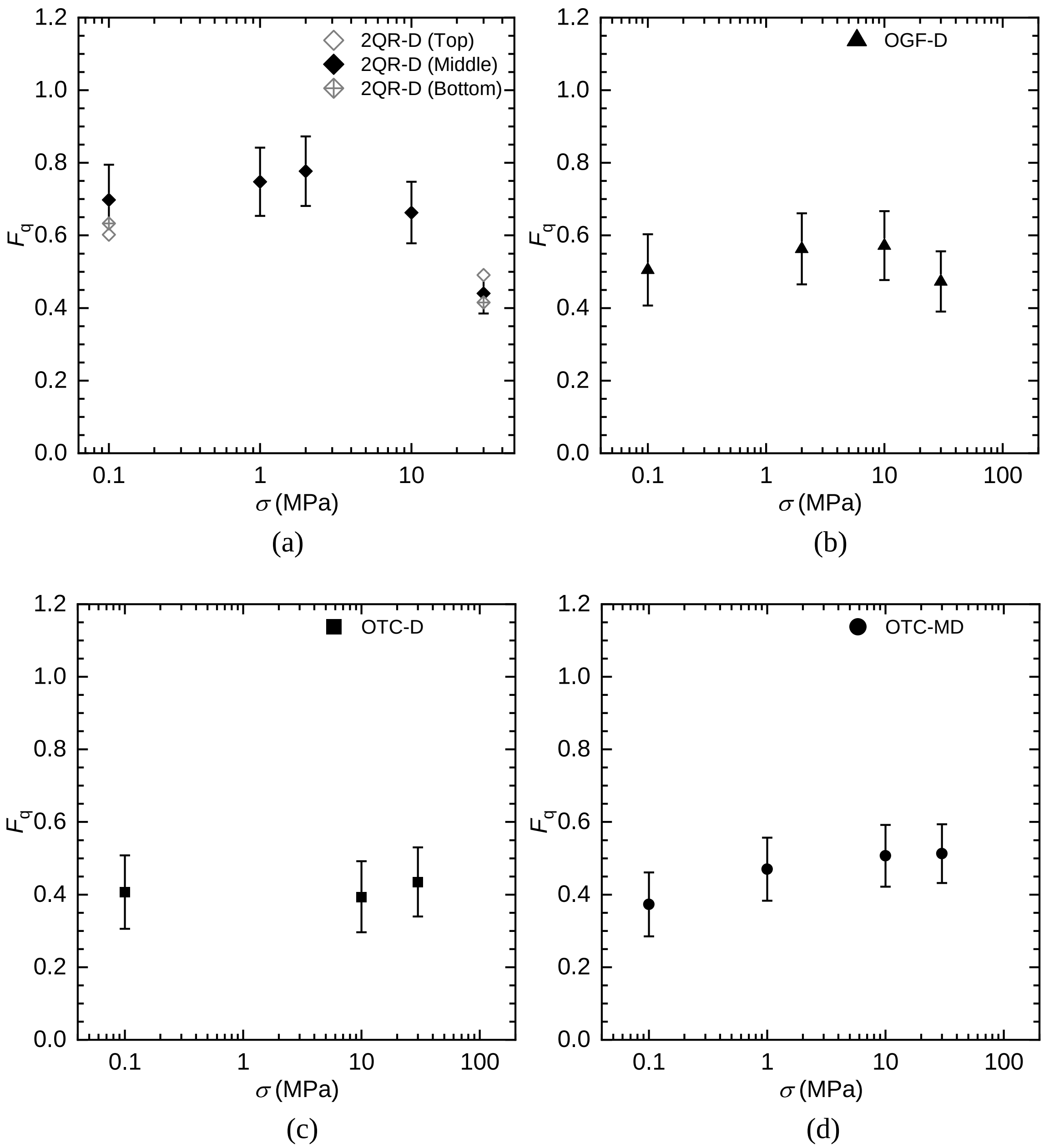

Figure 2.16 Variation of the anisotropy scalar (F_q) with stress (σ) for (a) dense 2QR sample, (b) dense OGF sample, (c) dense OTC sample and (d) medium-dense OTC sample.

The main findings are as follows.

(1) The average particle fracture stress ($\sigma_{f,avg}$) correlates well with the average particle roundness (R_{avg}). Sands consisting of particles with lower R_{avg} tend to have lower $\sigma_{f,avg}$. The lower $\sigma_{f,avg}$ can be explained by the crushing of surface asperities observed in the particles with low R_{avg}; these asperities become stress concentration points when the particles are loaded under compression. In addition to the R_{avg}, the $\sigma_{f,avg}$ is also affected by the presence of internal defects in the sand particles; occurrence of more internal defects results in a decrease in the $\sigma_{f,avg}$.

(2) R_{avg} also affects the macroscopic behavior of the sands. Sands with lower R_{avg} tend to have comparatively lower packing densities (higher e_{min} and e_{max}), higher critical state friction angles (ϕ_c), and lower yield stresses (σ_{yield}) in uniaxial compression (for the same initial relative density D_R). The higher e_{min}, e_{max}, and ϕ_c can be attributed to the interlocking of the surface asperities of the particles at lower stresses, whereas the lower σ_{yield} can be attributed to the crushing of those asperities at higher stresses.

(3) The average sphericity (S_{avg}) of the sample tends to decrease with particle crushing; however, the range of particle sphericities (S) observed in the sample as the loading progresses depends on the initial morphology of the particles. Sands with lower initial R_{avg} tend to produce, upon crushing, particles with both higher and lower S than the original, uncrushed sand. On the other hand, sands with higher initial R_{avg}, tend to produce, upon crushing, particles with generally lower S than the original, uncrushed sand.

(4) The anisotropy scalar F_q increases as the axial stress increases for samples loaded under uniaxial compression, indicating an increase in the anisotropy of interparticle contact

normals with increasing loading. This increase in F_q is however reversed by the occurrence of particle crushing. For the samples tested in the current research, as long as $B_r \approx 0\%$, increases in axial stress tend to generally increase the interparticle contact anisotropy; however, by the time $B_r \approx 1\%$, the interparticle contact orientations have become more randomly oriented and F_q has dropped. This clearly indicates a link between the anisotropy of the interparticle contacts and the breakage in sand samples loaded under uniaxial compression.

The data on the link between the crushing of the particles and the change in particle morphology and interparticle contact distribution (sand fabric) offers some insight on the impact of crushing on mechanical response, under what conditions it starts and how to consider it, at least for one-dimensional compression. The data presented here linking microscopic properties of sand particles to the macroscopic response of the sands to uniaxial loading is relevant to researchers working on multiscale modeling of crushable granular materials.

3 DISPLACEMENTS, STRAINS, AND SHEAR BANDS IN DEEP AND SHALLOW PENETRATION PROCESSES

This chapter has been accepted for publication as a paper in the Journal of Geotechnical and Geoenvironmental Engineering (DOI: 10.1061/(ASCE)GT.1943-5606.0002631).

3.1 Introduction

Efforts to theoretically model the penetration problem in geomechanics have traditionally framed it as a bearing capacity problem (Durgunoglu and Mitchell 1973; Terzaghi 1943; Vesic 1963), partly as a cavity expansion problem (Carter et al. 2009; Collins et al. 1992; Collins and Yu 1996; Cudmani and Osinov 2001; Salgado et al. 1997b; Salgado and Prezzi 2007; Salgado and Randolph 2001; Schnaid and Houlsby 1991; Vesic 1972; Yu and Houlsby 1991), or as a steady-state flow problem (Baligh 2008; Teh and Houlsby 1991; Yu et al. 2000). More recent research efforts have modeled the penetration process using variations of the finite element or material point methods (Ceccato et al. 2016; Huang et al. 2004; Kouretzis et al. 2014; Loukidis and Salgado 2011; Susila and Hryciw 2003; Wang et al. 2015; Woo and Salgado 2018; Zhang et al. 2013).

To visualize the deformation and strain fields in the soil surrounding a penetrometer, researchers have used soil samples excavated from load tests (BCP Committee 1971; Kuwajima et al. 2009), X-ray radiographs of lead shots embedded in the soil around penetrometers (Chen and Bassett 1988; Francescon 1983; Kobayashi and Fukagawa 2003), optical analysis of penetration experiments in transparent soils (Allersma 1982; Chen et al. 2014; Guzman et al. 2020; Iskander 2010), digital image correlation (DIC) analysis of penetration experiments in large calibration chambers with observation windows (Arshad et al. 2014; White et al. 2003), and in situ X-ray computed tomography (CT) scans of penetration experiments carried out in small calibration chambers (Doreau-Malioche et al. 2018, 2019; Paniagua et al. 2013). Experiments that produce data on the displacement and strain fields around penetrometers pushed into soil are helpful in assessing the quality of approximate models for penetration resistance calculation and are essential for validation of penetration simulations carried out using realistic soil models.

While the general description of the strain and displacement fields in the soil domain–usually expressed using vectors or contour lines–is informative, it does not lend itself to a clear identification of the shear band pattern that develops around a penetrometer. Shear bands in granular materials have been studied through element-level experiments using a wide range of experimental techniques. These techniques include the tracking of density variations in a sand sample using X-ray radiography (Roscoe 1970), the analysis of displacement of grid points printed on sample membranes (Alshibli et al. 2003; Alshibli and Sture 1999; Desrues et al. 1985; Saada et al. 1999), the analysis of the displacement field in the soil sample captured using stereophotogrammetry (Desrues and Viggiani 2004; Finno et al. 1997; Mooney et al. 1998, 1997), the tracking of density variations and particle movement using X-ray Computed Tomography (XCT) (Desrues and Andò 2015), the XCT-based microstructural analysis of void space in epoxy-hardened sand specimens (Alshibli and Sture 1999; Jang and Frost 2000; Oda et al. 2004; Oda and Kazama 1998), and the tracking of displacement and strain discontinuities using DIC analysis (Rechenmacher 2006; Rechenmacher and Finno 2004). Each of these approaches has advantages and disadvantages. A thorough, in-depth comparison of these approaches is beyond the scope of this paper; the focus of the this paper is the study of the formation of shear bands in the soil domain using the concept of zero-extension lines (ZELs) (Roscoe 1970; Salgado 2008) and DIC analysis (Arshad et al. 2014; White et al. 2003).

Strictly speaking, in three-dimensional conditions, shear bands would not be lines, but surfaces, but we will use the term ZEL to apply to three dimensions as well, so ZELs will represent shear surfaces. For a soil element undergoing deformation, the ZELs are oriented along directions of zero normal strain. They separate rigid soil masses moving with respect to each other. The relative movement of sand on either side of the ZELs along its direction is associated with a shear strain. In realistic soil representations, the shear strain is not completely localized along a line with no thickness, but rather along a band.

Shear bands have in the past been studied experimentally, in simple problems, using the concept of ZELs (James 1965; Roscoe 1970). The orientations of the shear bands and ZELs were first shown to match in model experiments carried out on embankments walls and in plane–mass flow bunkers, in which X-ray radiography was used to obtain the location of both ZELs and shear bands in the soil domain (Bransby and Blair-Fish 1975; James and Bransby 1971; Roscoe 1970). Dense sands were used in these experiments; therefore, as the sands sheared and dilated, regions where shear bands developed achieved a lower density than their surroundings. These regions of lower density were captured in 2D X-ray radiographs of the soil domain. The ZELs in the soil domain were extracted from the displacement and strain fields obtained from the movement of embedded lead-shot markers, which were also tracked using the 2D X-ray radiographs. Furthermore, Mooney et al. (1997), using stereophotogrammetric analysis of plane strain experiments, also observed that the mechanism of shear band formation is that of simple shear, i.e., the shear band is inextensible along its length–suggesting that the shear bands can indeed be seen as ZELs. Currently, with sophisticated DIC algorithms, we can determine the displacement field in the soil domain with greater detail and use it to obtain the strain field in a much more accurate manner than was possible in the past.

The main aim of this paper is to investigate the development of shear band patterns during penetration processes occurring in deep and shallow environments. We explore a method for visualization of the shear bands based on the concept of zero-extension lines (ZELs). Because, at any point in the soil domain, there are always two possible orientations for a ZEL, we also propose an algorithm for the automatic identification of the dominant orientation of ZELs at the point. We then apply the proposed method to the results of deep and shallow penetration experiments performed in dense silica sand in which shear localization was observed. We carry out the penetration experiments in a special half-cylindrical calibration chamber with observation windows, which allow us to capture digital images of the sand samples during the penetration experiments. We then analyze these images using DIC to obtain the incremental displacement and strain fields in the soil domain for deep penetration, and at several stages of shallow penetration. The proposed method is then used to automatically extract sets of shear bands from the incremental strain fields.

3.2 Materials and methods

Ohio Gold Frac (OGF) sand, a silica sand, was used in the penetration experiments. A seventh of the sand by weight was colored black using an acrylic paint, dried and then mixed thoroughly with uncolored sand to give the sand the texture that is required for DIC analysis (Arshad 2014; Arshad et al. 2014; Tehrani 2014; Tehrani et al. 2017). Table 3.1 shows the properties of the OGF sand used in the calibration chamber experiments.

Table 3.1 Index properties of Ohio Gold Frac (OGF) sand (after Han et al. 2018).

Sand	D_{50} (mm)	C_U	C_C	e_{max}	e_{min}	R	S	ϕ_{TXC} (deg)	ϕ_{DS} (deg)
OGF	0.62	1.6	1	0.87	0.58	0.43	0.83	32.5	32.0

Notes:
1. D_{50} = mean particle size; C_U = coefficient of uniformity = D_{60}/D_{10}; C_C = coefficient of curvature = $(D_{30})^2/(D_{10}\times D_{60})$; e_{max}= maximum void ratio (ASTM D4254-16 2016); e_{min} = minimum void ratio (ASTM 2016).
2. R = roundness of particle defined as the ratio of the average radius of curvature of internal corners of a 2D projection of the particle to the radius of the largest inscribed circle for the same projection (Wadell 1932); S = sphericity of particle defined as the ratio of the diameter of the circle with the same area as the projected area of the particle to the diameter of the minimum circle circumscribed to the projected area of the particle. Both R and S are computed using the definition of Zheng and Hryciw (2015).
3. ϕ_{TXC} = critical state-friction angle of sand under triaxial compression; ϕ_{DS} = critical state-friction angle of sand under direct shear.

The sand samples were prepared by raining down the OGF sand into a half-cylindrical calibration chamber using a custom pluviator with diffuser sieves. The half-cylindrical calibration chamber is 1.68 m in diameter and 1.2 m in height and is equipped with three Polymethyl Methacrylate (PMMA) observation windows on its flat vertical face. The PMMA observation windows have a thickness of 76 mm and are reinforced with metal supports that limit the maximum deformation of the observation windows to less than 0.0945 mm for the surcharge level used in this paper (Arshad 2014). Thus, issues with observation window deformability are not present in our experiments. The pluviator used to prepare the sand samples allows control of the rate of particle deposition (controlling the sample density) and ensures sample homogeneity (Lee 2008; Lee et al. 2011; Miura and Toki 1982; Rad and Tumay 1987; Vaid and Negussey 1984). Further details of the design and operation of the calibration chamber and the pluviator are presented by Arshad (2014), Arshad et al.(2014) and Tehrani et al. (2016). As the sand was pluviated, small cylindrical samplers were placed inside the calibration chamber at three levels to allow the determination of the local *in situ* density. The sand samples were homogenous, with a relative density D_R of 90% ± 5%.

After the sand sample was prepared, the surface of the sand was flattened, and a vertical surcharge was applied using a pressure-plate assembly. The initial vertical pressure in the sand at the final penetrometer depth was measured directly using a contact pressure cell (Model No. 4800, GEOKON, New Hampshire, USA) placed in the sand sample. For the surcharge level used in this research, the initial vertical pressure in the sand at the final penetrometer depth was equal to 33 kPa.

A cone penetrometer and a model footing were used for the deep and shallow penetration experiments, respectively. The cone penetrometer used in the deep penetration experiment is a half-cylindrical penetrometer made of brass with a diameter d of 38 mm (radius r_p = 19 mm). The apex angle of the cone is 60°. The penetrometer is instrumented with a load cell at the tip. The model footing used in the shallow penetration experiment is a half-square footing made of aluminum with a width B of 90 mm. Figure 3.1 shows a schematic of the cone penetrometer and model footing, and a labeled picture of the test setup. The cone penetrometer was pushed into the dense sand sample at a rate of 1 mm/s (simulating a jacked pile or a CPT), while the model footing was pushed in at a rate of 0.03 mm/s (simulating a load test). Both the penetrometer and model footing were jacked into the sand sample using a hydraulic actuator positioned above the calibration chamber. The actuator was connected to the penetrometer and model footing through a load cell and moment-break assembly to prevent the transfer of any eccentric load and moment to them. During the experiments, we took load readings and captured digital grey-scale images of the sand and the advancing penetrometer and model footing using 12-Megapixel complementary metal-oxide semiconductor (CMOS) monochrome cameras (Model No. beA4000-62km, Basler, Ahrensburg, Germany) positioned in front of the observation windows.

3.3 Penetration resistance

Figure 3.2 shows penetration resistance vs. depth for the cone penetrometer and the model footing obtained using measurements from the load cells. The cone penetrometer was pre-embedded 50 mm into the sand sample to ensure alignment with the surface of the observation window; therefore, the penetration resistance curve in Figure 3.2(a) starts at a depth of 50 mm. Figure 3.2(a) shows that the penetration resistance q_c for the cone penetrometer (measured at the penetrometer tip) has a monotonic rise from 0 MPa to a final penetration resistance of 13.55 MPa at a depth of 408 mm.

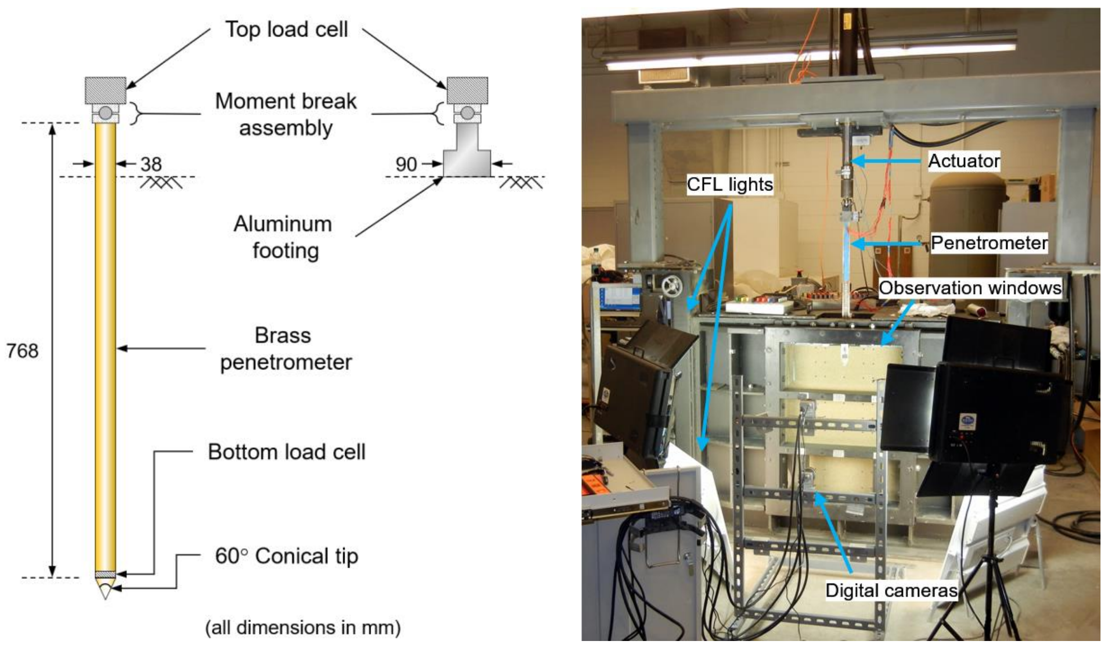

(a) (b)

Figure 3.1 Experimental setup: (a) cone penetrometer and model footing, and (b) labeled image of the half-cylindrical calibration chamber with three observation windows, and digital cameras positioned in front of it for image acquisition (after Ganju et al. 2020b).

The penetration resistance q_b for the model footing, in Figure 3.2(b), shows a monotonic rise up to a penetration resistance of 170 kPa (peak) at a depth of 7 mm, followed by a softening stage, and then a plunging stage after a penetration of 17 mm. The penetration resistance during the plunging stage was almost constant at 137 kPa. Also shown in Figure 3.2 are labels "C1" (Figure 3.2 (a)) and "F1" to "F4" (Figure 3.2 (b)), which mark the depths of penetration at which incremental DIC analysis was carried out for the cone penetrometer and the model footing, respectively.

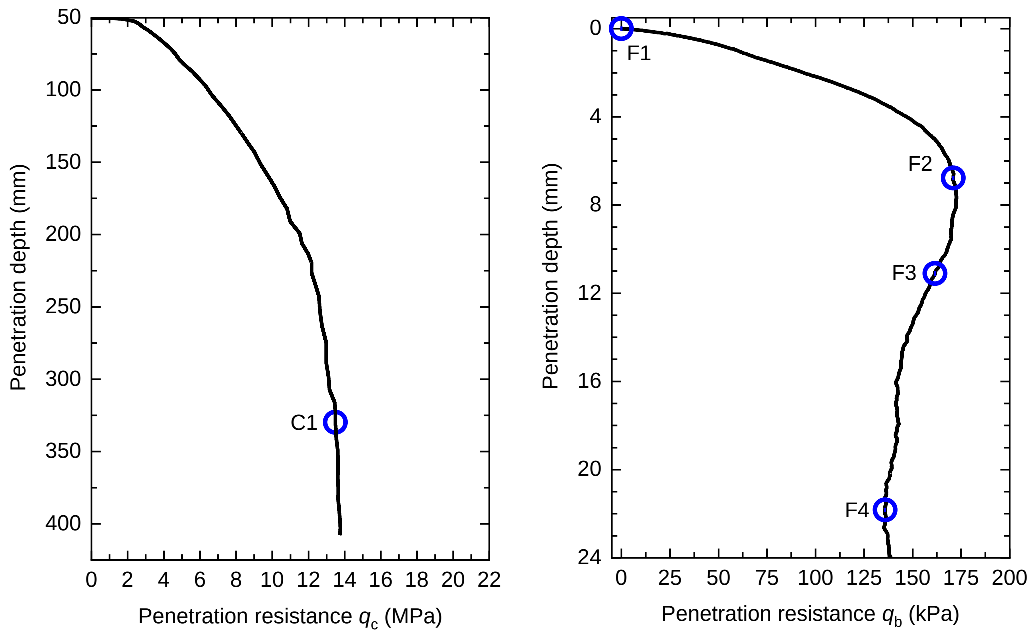

(a) (b)

Figure 3.2 Penetration resistance plots for (a) the cone penetrometer and (b) the model footing, with labels showing penetration depths at which digital image correlation (DIC) analysis was carried out.

3.4 Incremental displacement and strain fields in the soil domain

The incremental displacement field in the soil domain was computed for a 2 mm penetration increment. For the cone penetrometer, we analyzed the images starting from a penetration depth of 330 mm ("C1" in Figure 3.2(a)) until a penetration depth of 332 mm (both measured from the surface of the sand sample to the shoulder of the penetrometer; the shoulder is the point where the shaft of the penetrometer meets the inclined face of the cone). The q_c at 330 mm penetration, under a vertical confinement of 33 kPa, was 13.50 MPa. We chose the depth range to ensure that the cone penetrometer tip was sufficiently far from the top and bottom boundaries of the calibration chamber (to avoid any possible boundary effects) and to position the penetrometer tip in the upper half of the middle observation window, which allows an unobstructed view of the sand below the penetrometer tip for DIC analysis.

For the model footing, we analyzed the images for 2 mm penetration increments at 4 stages of penetration: at the start of penetration ("F1" on Figure 3.2 (b)), at peak resistance ("F2" on Figure 3.2 (b)), in the middle of the softening stage ("F3" on Figure 3.2 (b)) and upon plunging ("F4" on Figure 3.2 (b)). These were chosen to highlight important features in shear band formation in the soil domain.

3.4.1 Incremental displacement field from DIC analysis

DIC analysis, in general, is carried out on a sequence of images, one pair at a time, in the order in which they are captured. The DIC analysis procedure tracks the movement of a small square or rectangular area (the "subset") from the first image to the second image. This is done by comparing the grey-level pixel intensity of the subset in the first image (reference subset) with the grey-level pixel intensities of multiple subsets in the second image, and finding the best match according to a suitable matching criterion (Pan et al. 2009; Raffael et al. 2007; Sutton et al. 2009). After finding the best-matching subset (the optimal subset) in the second image, the displacement of the reference subset is calculated as the difference in the positions of the centers of the optimum and the reference subsets. The procedure is repeated for multiple subsets, separated by a fixed center-to-center distance, to get the displacement field in the entire domain of interest.

For the deep and shallow penetration experiments, we analyzed the sequence of images collected during the chosen penetration increments using the commercial software VIC-2D®, which is advantageous because it takes into account the deformation of subsets between the first and second images following the approach of affine transformation, as detailed by Sutton et al. (2009). We used the normalized sum of squared differences criterion for matching subsets because it can more efficiently handle minor changes in lighting conditions between the first and second images than other available methods (Arshad et al. 2014). For analysis of images captured during the cone penetration experiment, we used overlapped square subsets of size s_{sb} equal to 75 pixels, with a center-to-center distance s_{st} between adjacent subsets equal to 5 pixels (resulting in an overlap ratio of 93%). For the footing penetration experiment, we used overlapped square subsets of size s_{sb} equal to 51 pixels, with a center-to-center distance s_{st} of 5 pixels (resulting in an overlap ratio of 90%). The s_{sb} sizes were recommended by the VIC-2D® software based on the trackability of the texture of the colored sand and the lighting conditions. The computed displacements, in pixel units, were converted into length units using the calibration factor obtained using reference marks printed on the inner side of the observation windows. The calibration factor for the cone penetrometer experiment is 0.15059 mm/pixel, and for the model footing experiment, it is 0.12690 mm/pixel.

3.4.1.1 Incremental displacement field around the cone penetrometer

Figure 3.3(a) shows the incremental displacement vectors obtained from the DIC analysis for the cone penetrometer at the stage identified as "C1" on the penetration resistance curve. The horizontal axis of the figure is the radial distance r from the central axis of the penetrometer to the point of interest (center of subset), normalized by the radius of the penetrometer r_p; the vertical axis is the vertical distance h from the shoulder of the penetrometer to the center of subset, also normalized by the radius of the penetrometer r_p. The tail of each incremental displacement vector is located at the original undeformed position of the center of the subset. A region of thickness approximately equal to 6 mm (10 D_{50} or 0.3 r_p) right next to the penetrometer could not be tracked due to large displacement and rotation of soil elements there.

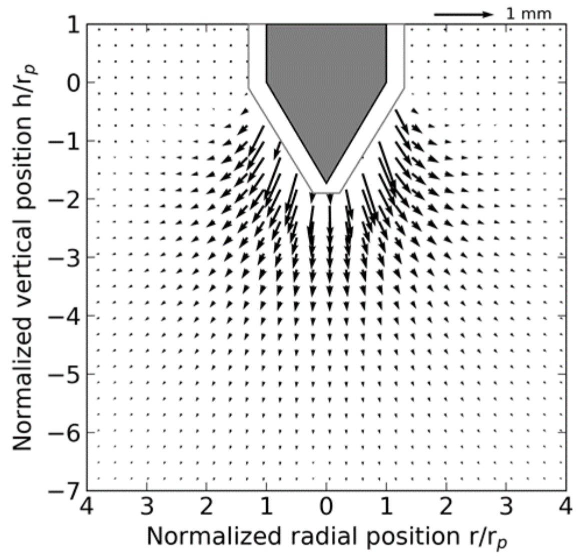

(a)

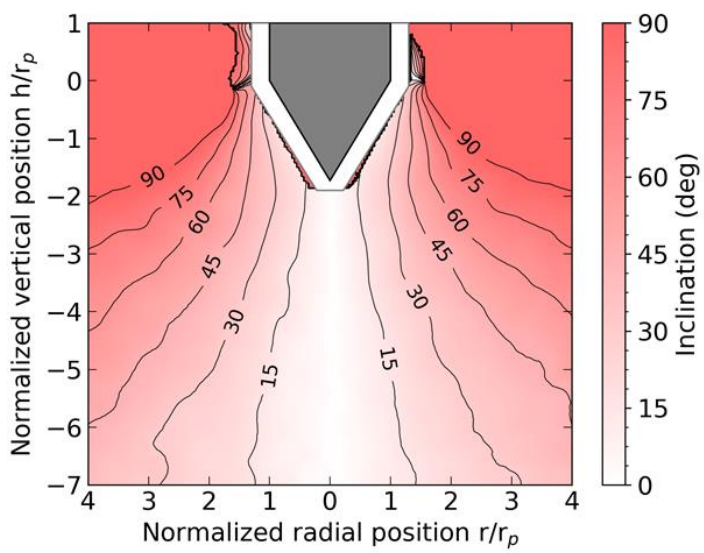

(b)

Figure 3.3 Displacement field around a cone penetrometer: (a) incremental displacement vectors and (b) heat map and contours of the magnitude of inclination of incremental displacement vectors (in degrees) with respect to the vertical direction for a vertical displacement increment of 2 mm of the cone penetrometer.

Figure 3.3 (b) shows the heatmap and contours of the magnitude of inclination (in degrees) of the incremental displacement vectors, shown in Figure 3.3(a), with respect to the vertical direction. Directly below the penetrometer tip, the displacement vectors are dominated by their vertical component; away from the centerline of the penetrometer, closer to the shoulder, displacement vectors are dominated by their horizontal component; between the tip and the shoulder, the displacement vectors transition from a vertical/sub-vertical to a horizontal orientation. Above the level of the penetrometer shoulder, the sand moves up, but only slightly. Similar observations have been reported by Arshad et al. (2014) using DIC analysis, by Allersma (1987) using optical analysis of photo-elastic material, and by Kobayashi and Fukagawa (2003) using X-ray radiographs of embedded lead shots.

Figure 3.4 and Figure 3.5 show the heat map and contour lines of the radial and vertical components, respectively, of the incremental displacement vectors shown in Figure 3.3. The incremental radial displacement du_r and the incremental vertical displacement du_z are plotted at the original, undeformed locations of the subsets. Radial displacements moving away from the centerline of the penetrometer, and vertical displacements moving upwards are both taken as positive. Displacements of subsets closest to the penetrometer surface are the largest. The radial displacement is greater closer to the shoulder of the penetrometer, whereas the vertical displacement is greater closer to the tip. The radial displacement dominates as the horizontal distance from the conical tip increases, whereas the vertical displacement dominates below the conical tip.

3.4.1.2 Incremental displacement field around the model footing

Figure 3.6 shows the incremental displacement vectors for the model footing corresponding to the four stages of penetration. The horizontal axis in the figures is the radial distance r from the central axis of the model footing to the center of the subset (or point) of interest normalized by the width *B* of the model footing; the vertical axis is the depth *z* from the free surface of the sand to the point of interest, also normalized by the width of the model footing *B*. The model footing is shown at the starting location of the penetration increment.

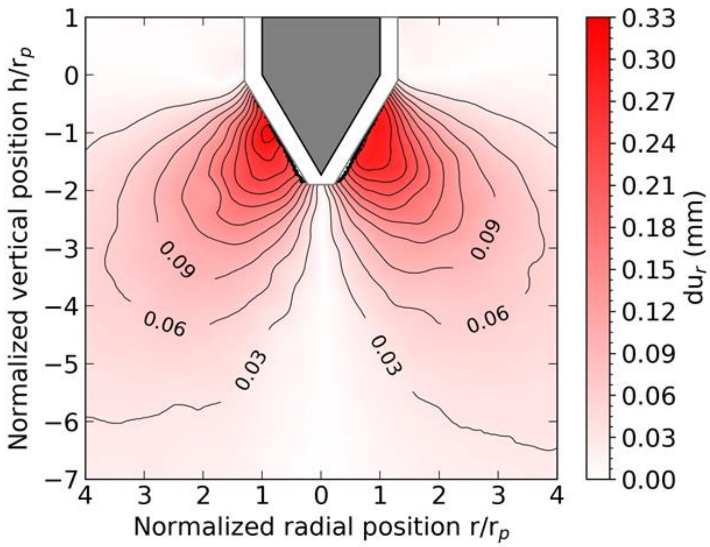

Figure 3.4 Heat map and contours of radial component du_r of the incremental displacement vectors in the soil domain for a vertical displacement increment of 2 mm of the cone penetrometer.

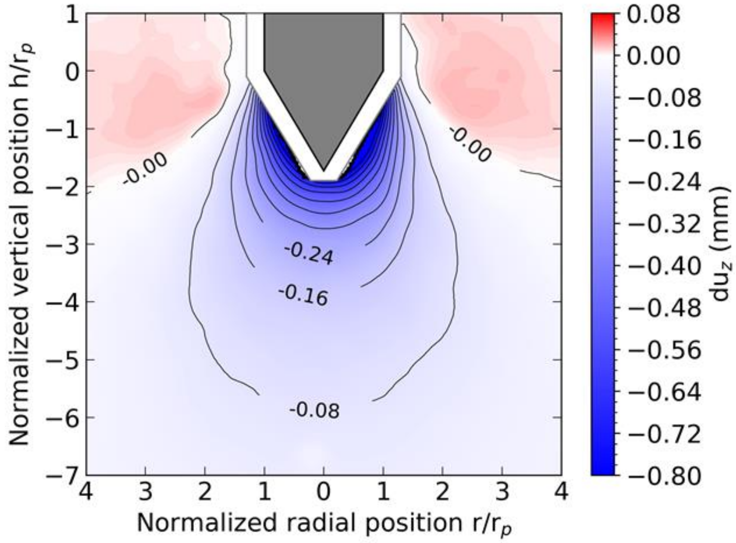

Figure 3.5 Heat map and contours of vertical component du_z of the incremental displacement vectors in the soil domain for a vertical displacement increment of 2 mm of the cone penetrometer.

At the start of penetration, represented by "F1" on Figure 3.2(b), the displacement vectors are dominated by their vertical component (see Figure 3.6(a)); as a result, the depth to which the sand "senses" the advancing penetrometer extends to ≈1.25B from the surface of the sample. However, as the model footing penetration proceeds, this depth of influence reduces from 1.25B to 0.75B at plunging. At the plunging stage ("F4" in Figure 3.2(b)), the displacement vectors are dominated by the radially outward and vertically upward directions close to and beyond the edges of the model footing (see Figure 3.6(d)).

Figure 3.7 shows the magnitude of inclination (in degrees) of the incremental displacement vectors with respect to the vertical direction for the model footing at the four stages of penetration. Like for the cone penetrometer, the incremental displacement vectors around the model footing have distinct orientations. For all the stages of penetration, close to the centerline and directly below the model footing, the displacement vectors are dominated by the vertical component; in the last stage of penetration, we can clearly see the formation of a "wedge" below the model footing. As we move closer to the edges of the model footing, the displacement vectors rotate, and the horizontal component of the displacement starts to dominate. Unlike the cone penetrometer, however, a significant upward movement of sand is observed close to and beyond the edges of the model footing. This is attributed to the lack of vertical confining pressure to suppress the upward motion of the sand (as would happen for deep penetration).

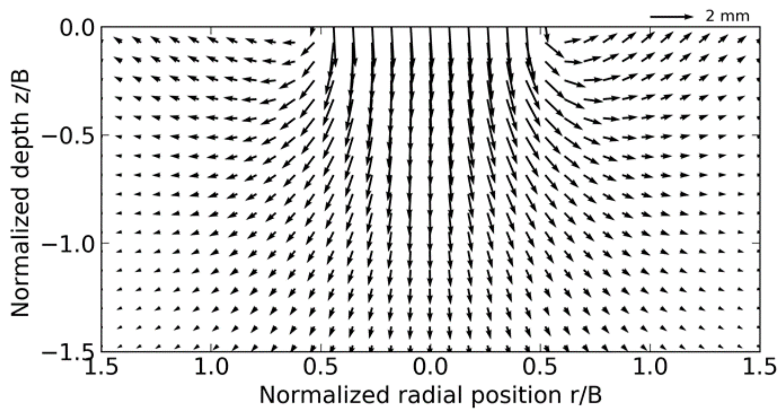

(a)

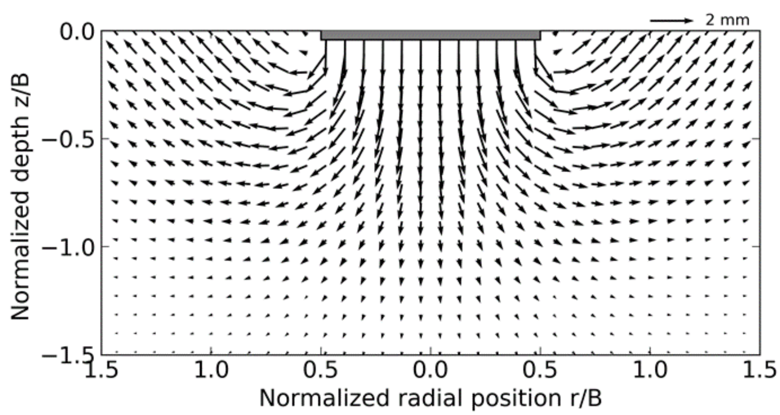

(b)

Figure 3.6 Incremental displacement vectors in the soil domain for a vertical displacement increment of 2 mm of the model footing at: (a) start of penetration (F1), (b) peak resistance (F2), (c) softening (F3), and (d) plunging (F4). The labels F1 through F4 can be seen on the penetration resistance curve in Figure 3.2(b).

Figure 3.6 continued

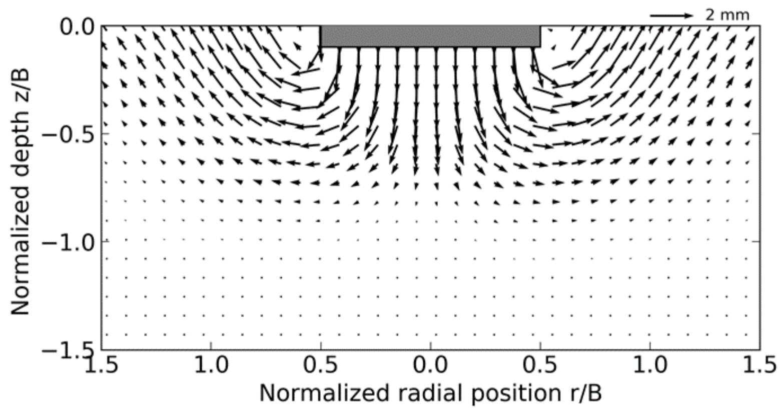

(c)

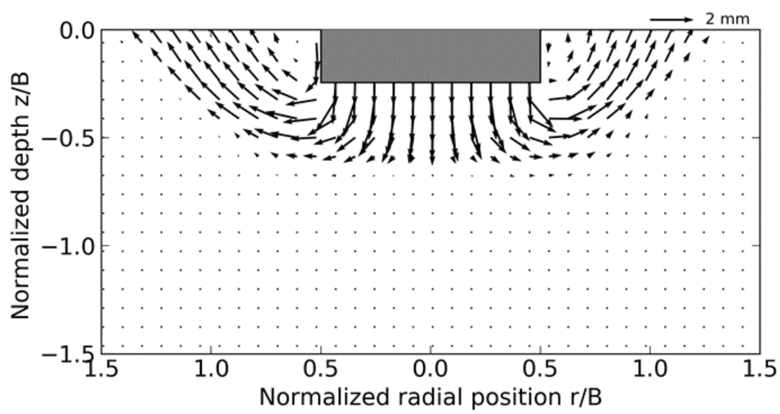

(d)

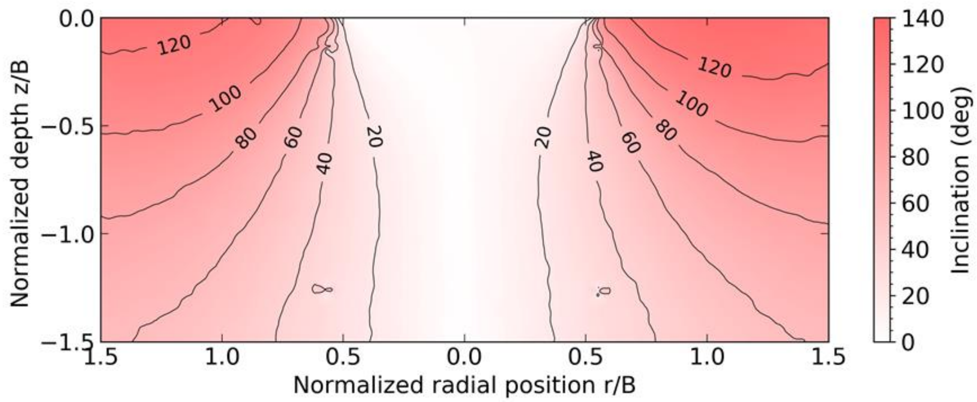

(a)

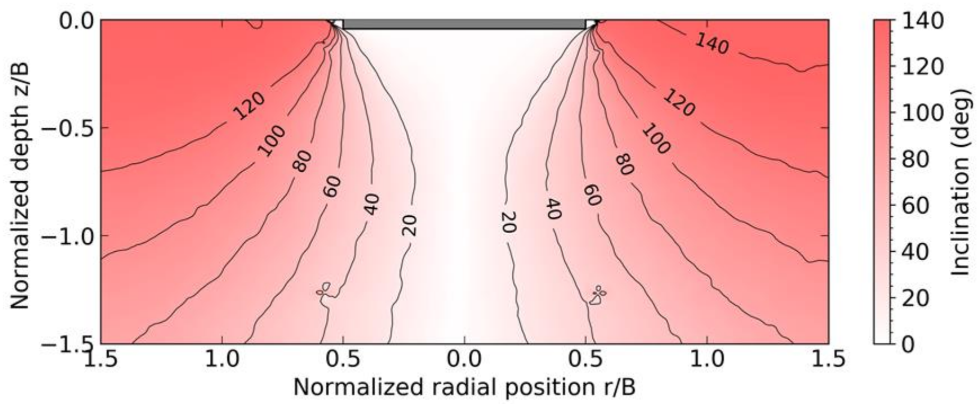

(b)

Figure 3.7 Heat map and contours of the magnitude of inclination (in degrees) of the incremental displacement vectors with respect to the vertical direction for a vertical displacement increment of 2 mm of the model footing at: (a) start of penetration (F1), (b) peak resistance (F2), (c) softening (F3), and (d) plunging (F4). The labels F1 through F4 can be seen on the penetration resistance curve in Figure 3.2(b).

Figure 3.7 continued

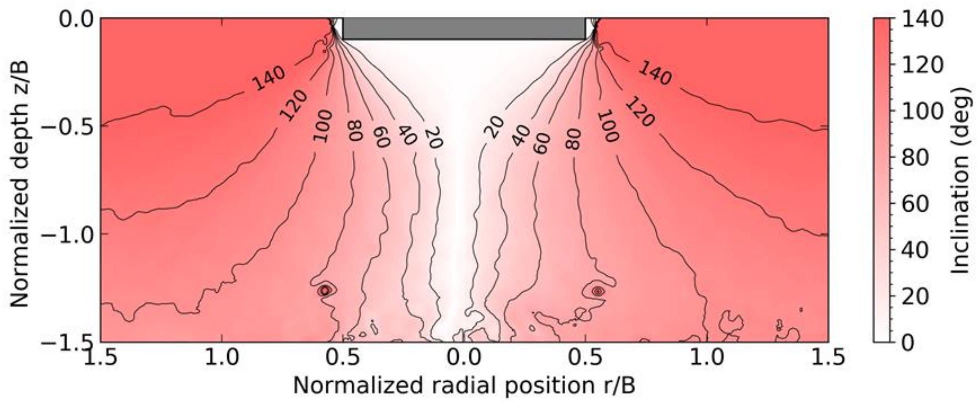

(c)

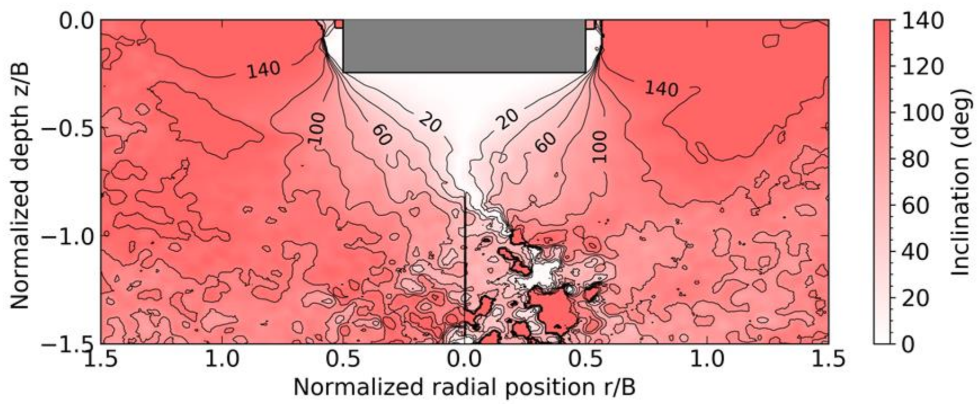

(d)

Error! Reference source not found. and Figure 3.9 show the heat map and contours of the radial and vertical components, respectively, of the displacement vectors shown in Figure 3.6. **Error! Reference source not found.**(a) shows the evolving localization of the radial displacement around the edges of the model footing as it advances. In both **Error! Reference source not found.** and Figure 3.9, we see the reduction in the depth of influence of the model footing from 1.25*B* at the start of penetration to less than 0.75*B* at the plunging stage.

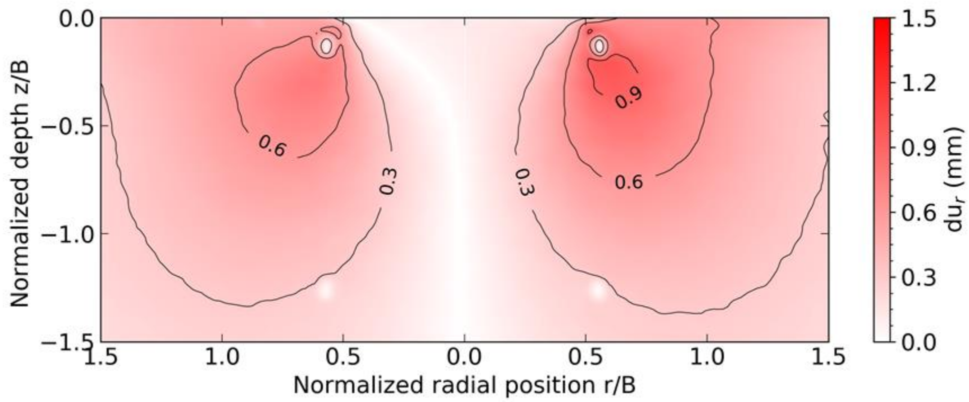

(a)

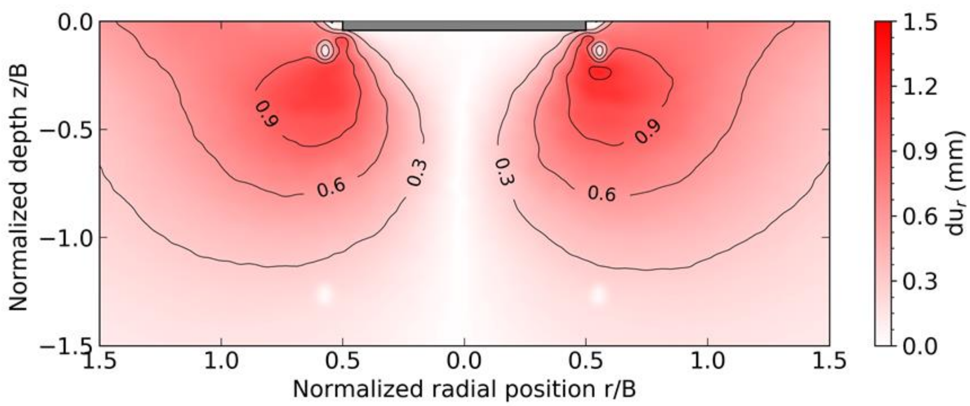

(b)

Figure 3.8 Heat map and contours of horizontal component du_r of the incremental displacement vectors in the soil domain for a vertical displacement increment of 2 mm of the model footing at (a) start of penetration (F1), (b) peak resistance (F2), (c) softening (F3), and (d) plunging (F4). The labels F1 through F4 can be seen on the penetration resistance curve in Figure 3.2 (b).

Figure 3.8 continued

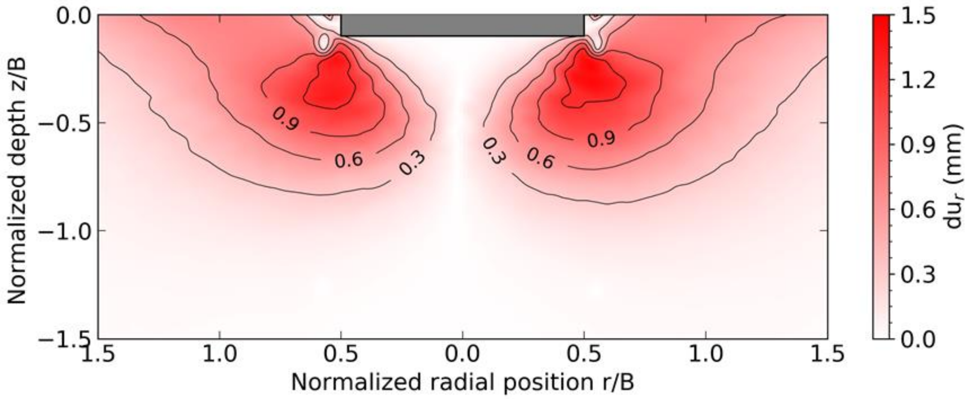

(c)

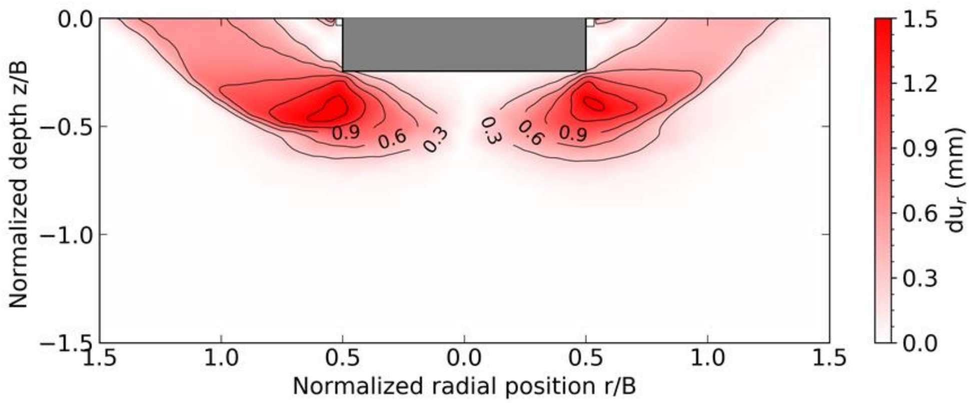

(d)

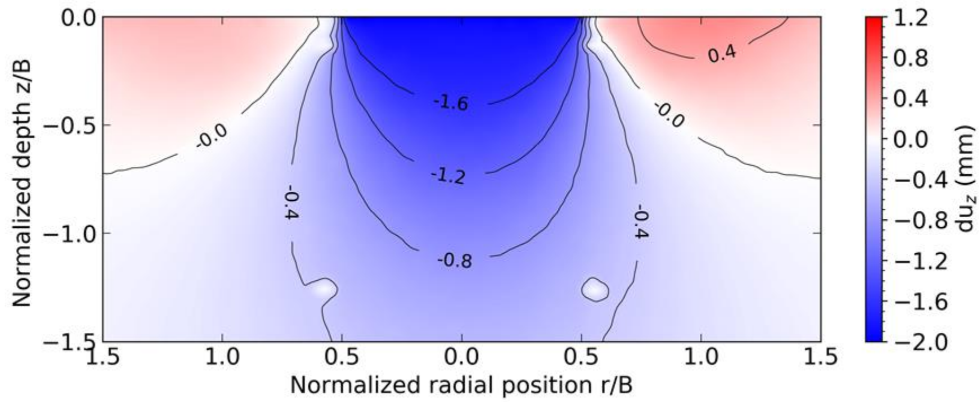

(a)

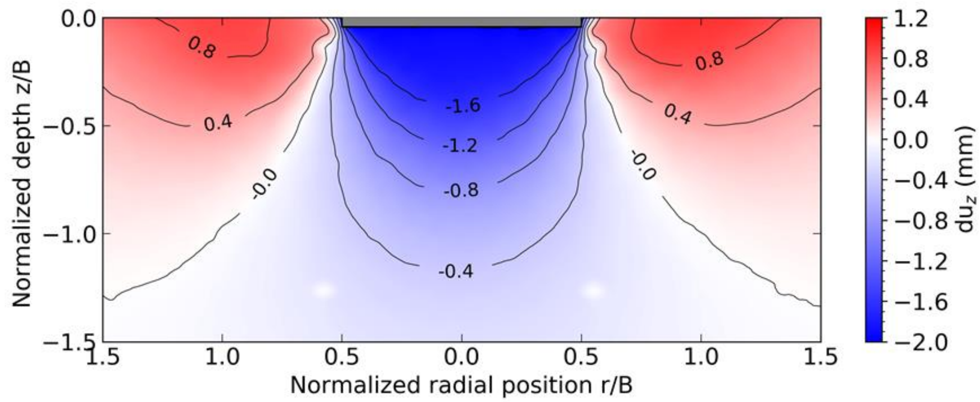

(b)

Figure 3.9 Heat map and contours of vertical component du_z of the incremental displacement vectors in the soil domain for a vertical displacement increment of 2 mm of the model footing at (a) start of penetration (F1), (b) peak resistance (F2), (c) softening (F3), and (d) plunging (F4). The labels F1 through F4 can be seen on the penetration resistance curve in Figure 3.2(b).

Figure 3.9 continued

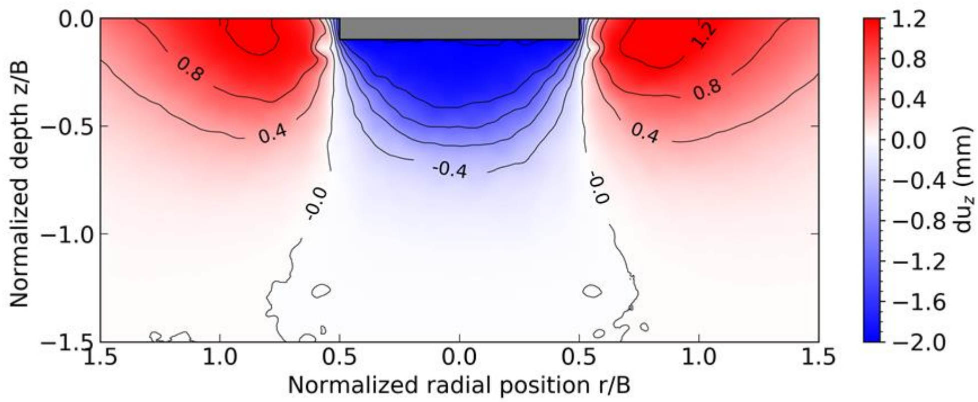

(c)

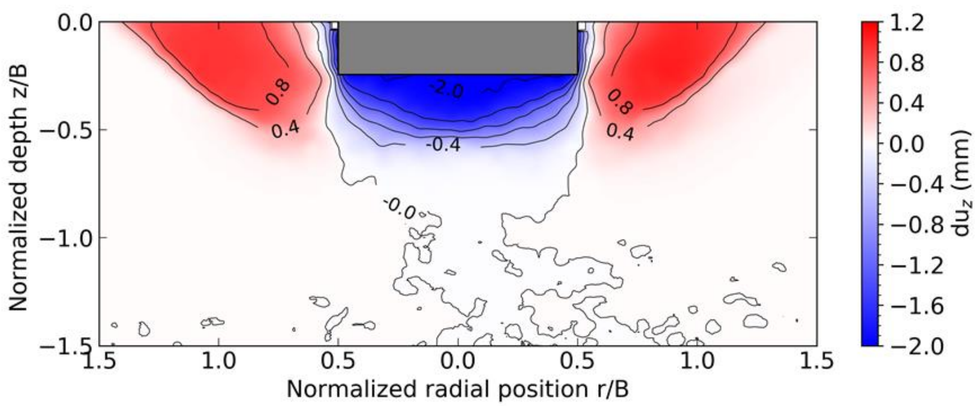

(d)

3.4.2 Incremental strain fields computed from the displacement field

The displacement field obtained from DIC analysis can be used to compute the strain field. We use the Green-St. Venant finite strain tensor to quantify the strains in the soil domain, computed using the built-in strain computation function in the VIC-2D® software. Other strain tensors (such as the Log strain or Biot strain tensors) produce similar results because we have followed an updated Lagrangian approach and were, in any case, interested in incremental strains. To compute the components of the strain tensor, VIC-2D® takes the original locations of the center of the subsets as nodes and generates a triangular mesh over the soil domain. For each linear triangular element, the incremental Lagrangian strain tensor dE_{ij} is computed as:

$$dE_{\mathrm{ij}} = \frac{1}{2}(u_{\mathrm{i,j}} + u_{\mathrm{j,i}} + u_{\mathrm{m,i}}u_{\mathrm{m,j}}) \tag{3.1}$$

with

$$u_{\mathrm{i,j}} = \frac{\partial u_{\mathrm{i}}}{\partial X_{\mathrm{j}}} \tag{3.2}$$

$$u_i = N_{\mathrm{A}}u_{\mathrm{i}}^{\mathrm{A}} + N_{\mathrm{B}}u_{\mathrm{i}}^{\mathrm{B}} + N_{\mathrm{C}}u_{\mathrm{i}}^{\mathrm{C}} \tag{3.3}$$

where u_{i} is a component of the displacement within the triangular element; $u_{\mathrm{i}}^{\mathrm{A}}$, $u_{\mathrm{i}}^{\mathrm{B}}$ and $u_{\mathrm{i}}^{\mathrm{C}}$ are the components of the displacement at the three element nodes A, B, and C, respectively; and N_{A}, N_{B}, and N_{C} are linear shape functions (Fish and Belytschko 2007; Sutton et al. 2009) for the triangular element. As each node is shared between multiple elements, the strain at the node is interpolated from the strains at the Gauss points of the elements sharing the node. After computing the strain at each node in the soil domain, a Gaussian filter of size 15 times the step size s_{st} ($15s_{\mathrm{st}} \approx 7.5$ mm) is applied to the strains to reduce noise (Correlated Solutions 2009).

3.4.2.1 Incremental strain fields around the cone penetrometer

Figure 3.10, Figure 3.11, and Figure 3.12 show the heatmap and contours of the incremental radial strain (dE_{rr}), the incremental vertical strain (dE_{zz}), and the magnitude ($|dE_{rz}|$) of the incremental in-plane shear strain in the soil domain around the cone penetrometer. The solid mechanics sign convention for strains is followed, with the vertical and radial strains being positive in extension and negative in compression. From Figure 3.10 and Figure 3.11, we see that the soil elements next to the cone penetrometer's shoulder are radially in compression and vertically in extension. Below the cone penetrometer's tip, the state of the soil is reversed, being vertically in compression and radially in extension. From the $|dE_{rz}|$ heat map and contours presented in Figure 3.12, we see that the in-plane shear strains are localized near the inclined surface of the penetrometer, with the largest shear strains observed closer to the shoulder.

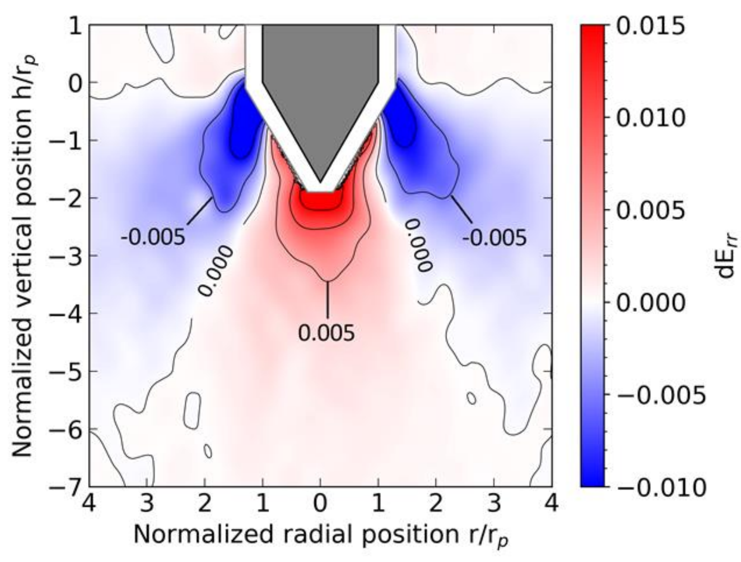

Figure 3.10 Heat map and contours of incremental radial strain dE_{rr} (strains positive in extension) in the soil domain for a vertical displacement increment of 2 mm of the cone penetrometer.

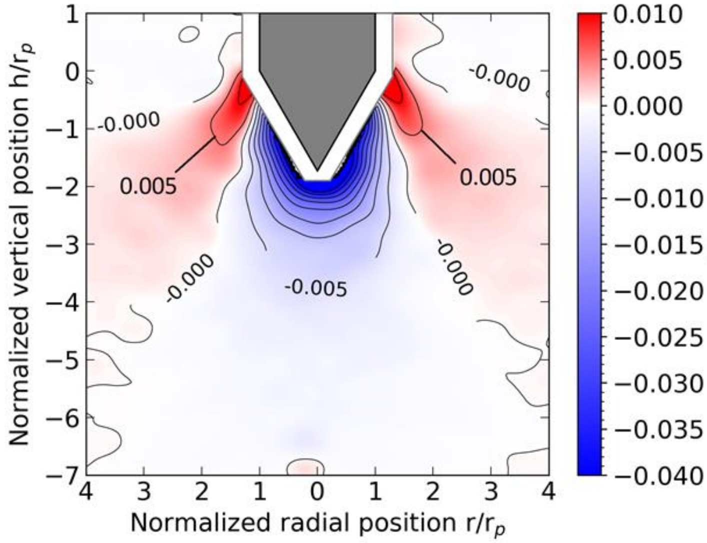

Figure 3.11 Heat map and contours of incremental radial strain dE_{zz} (strains positive in extension) in the soil domain for a vertical displacement increment of 2 mm of the cone penetrometer.

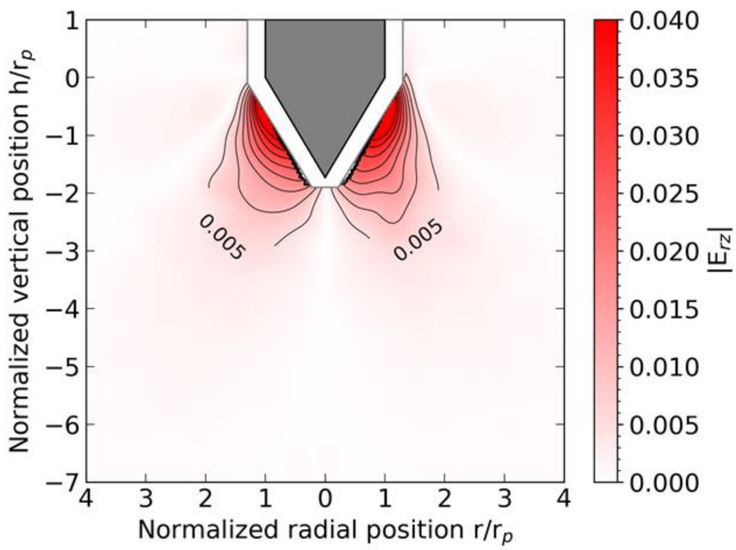

Figure 3.12 Heat map and contours of the magnitude |dE_{rz}| of incremental shear strain in the soil domain for a vertical displacement increment of 2 mm of the cone penetrometer.

3.4.2.2 Incremental strain fields around the model footing

Figure 3.13, Figure 3.14 and Figure 3.15 show the heat map and contours of dE_{rr}, dE_{zz} and $|dE_{rz}|$, respectively, for the model footing at different stages of penetration. The soil elements below the model footing are radially in extension and vertically in compression, and the elements beyond the edges of the model footing, away from the centerline, are radially in compression and vertically in extension. The magnitudes of these strains are much higher in the case of the model footing than the cone penetrometer. Furthermore, the strains are more diffused during the initial stages of penetration and become much more localized in the softening and plunging stages of penetration; however, the localization does not seem to be just close to the surface of the model footing – we also see shear localization away from the footing's surface.

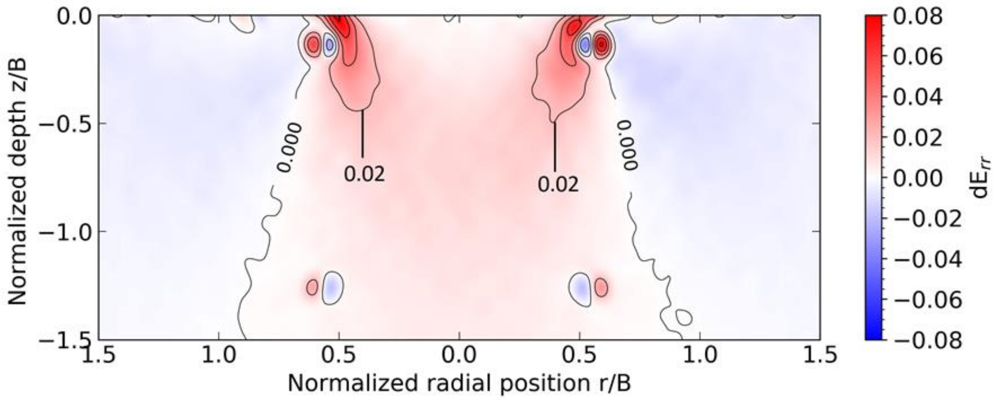

(a)

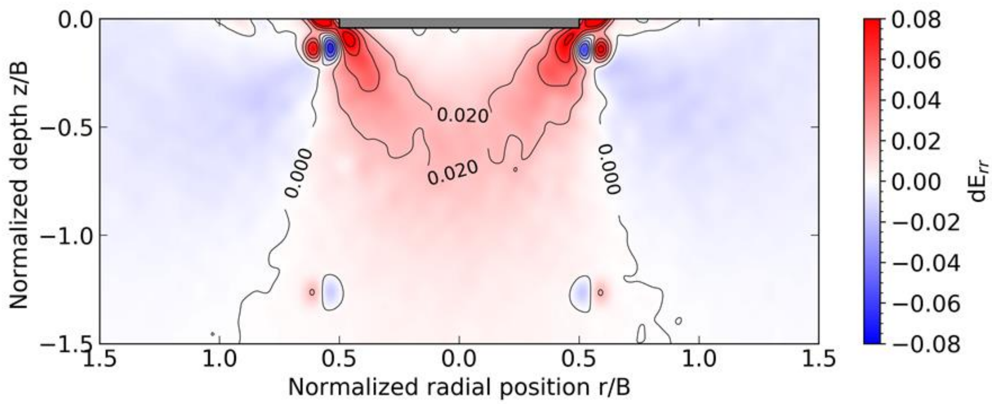

(b)

Figure 3.13 Heat map and contours of incremental radial strain dE_{rr} (strains positive in extension) in the soil domain for a vertical displacement increment of 2 mm of the model footing at (a) start of penetration (F1), (b) peak resistance (F2), (c) softening (F3), and (d) plunging (F4). The labels F1 through F4 can be seen on the penetration resistance curve in Figure 3.2 (b).

Figure 3.13 continued

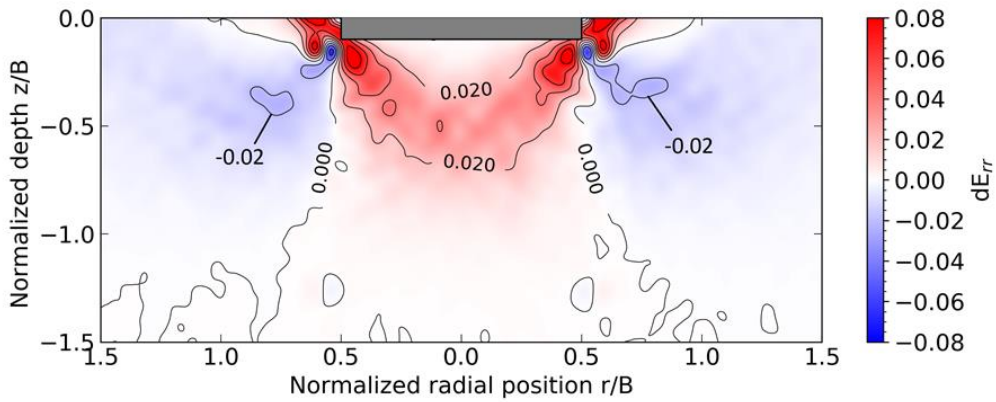

(c)

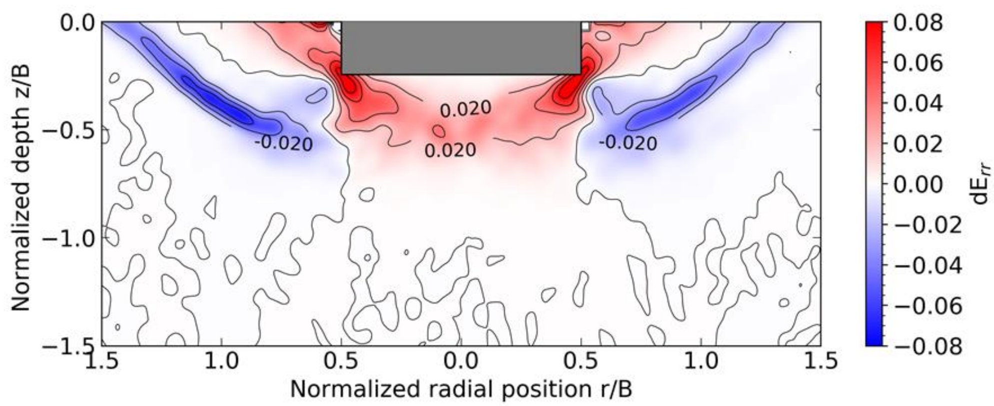

(d)

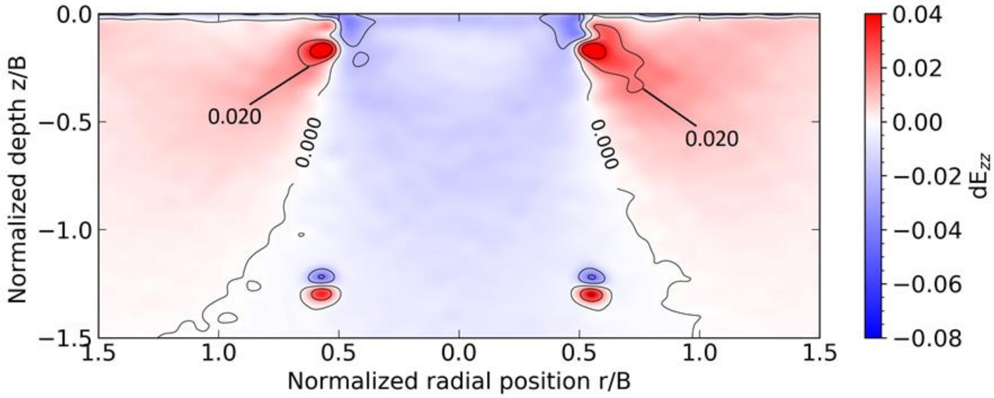

(a)

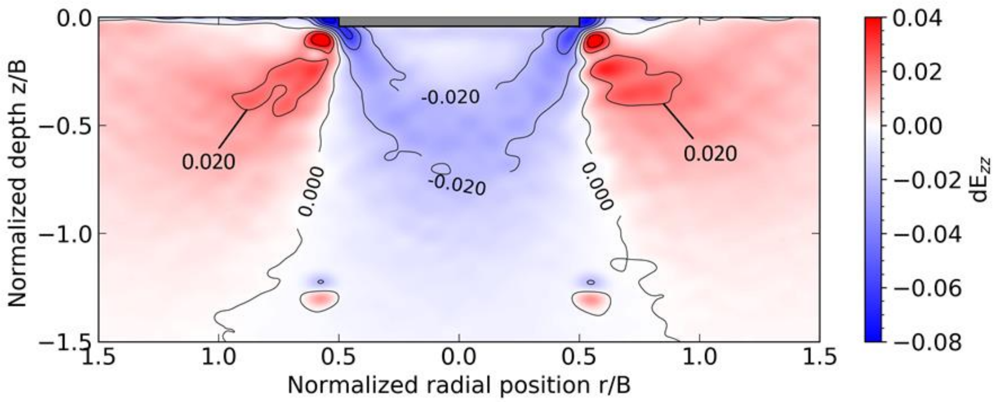

(b)

Figure 3.14 Heat map and contours of incremental vertical strain dE_{zz} (strains positive in extension) in the soil domain for a vertical displacement increment of 2 mm of the model footing at (a) start of penetration (F1), (b) peak resistance (F2), (c) softening (F3), and (d) plunging (F4). The labels F1 through F4 can be seen on the penetration resistance curve in Figure 3.2(b).

Figure 3.14 continued

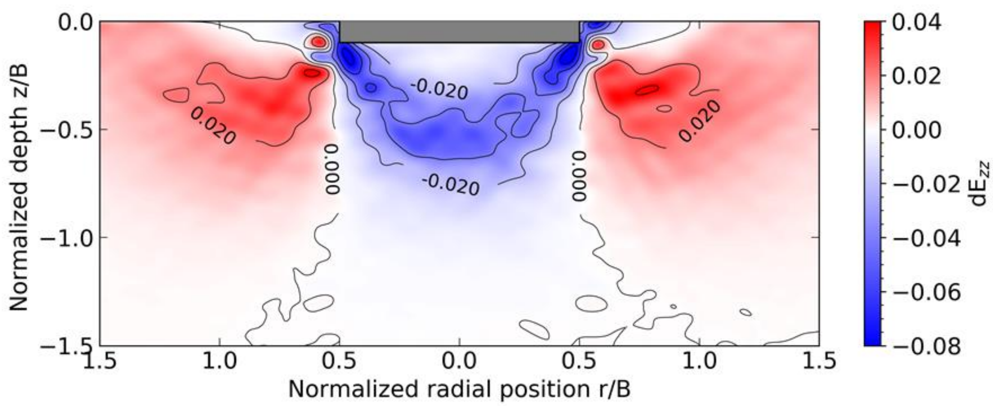

(c)

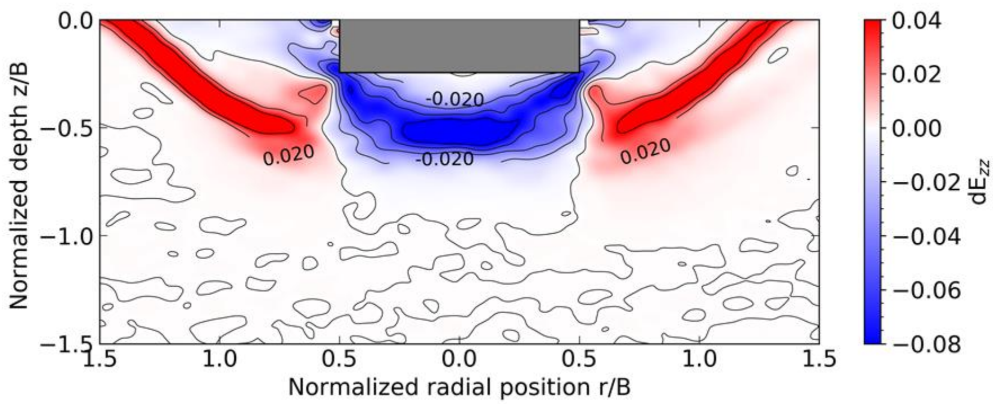

(d)

From the heat map and contours of $|dE_{rz}|$ presented in Figure 3.15, we see that the shear strains localize near the vertical faces of the model footing; this is consistent in all stages of penetration. At the plunging stage [see Figure 3.15(d)], in addition to the vertical faces of the model footing, we see the localization of shear strains at a depth of $0.5B$ and $0.25B$ from the surface of the sand.

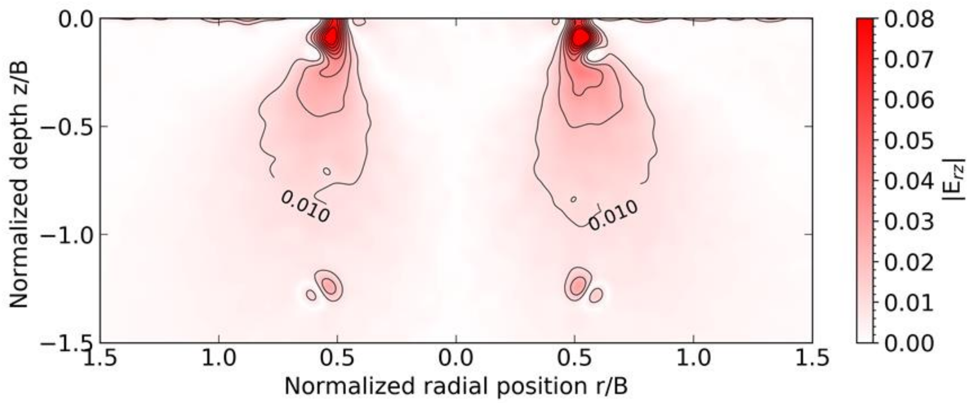

(a)

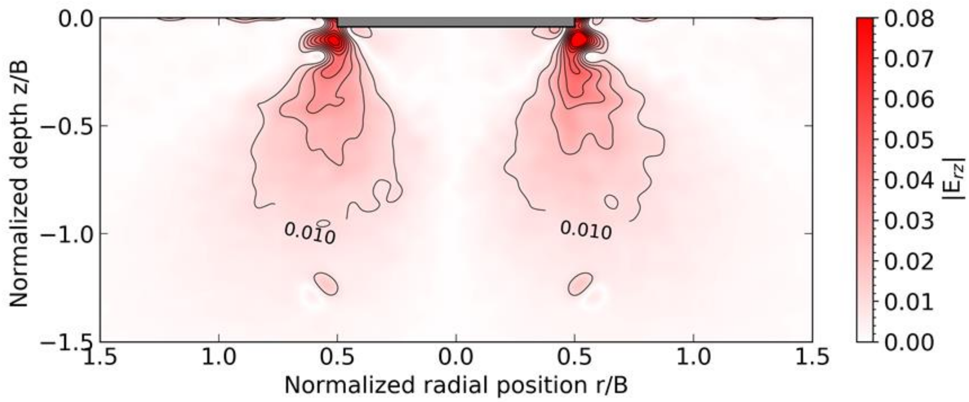

(b)

Figure 3.15 Heat map and contours of magnitude $|dE_{rz}|$ of incremental shear strain in the soil domain for a vertical displacement increment of 2 mm of the model footing at (a) start of penetration (F1), (b) peak resistance (F2), (c) softening (F3), and (d) plunging (F4). The labels F1 through F4 can be seen on the penetration resistance curve in Figure 3.2(b).

Figure 3.15 continued

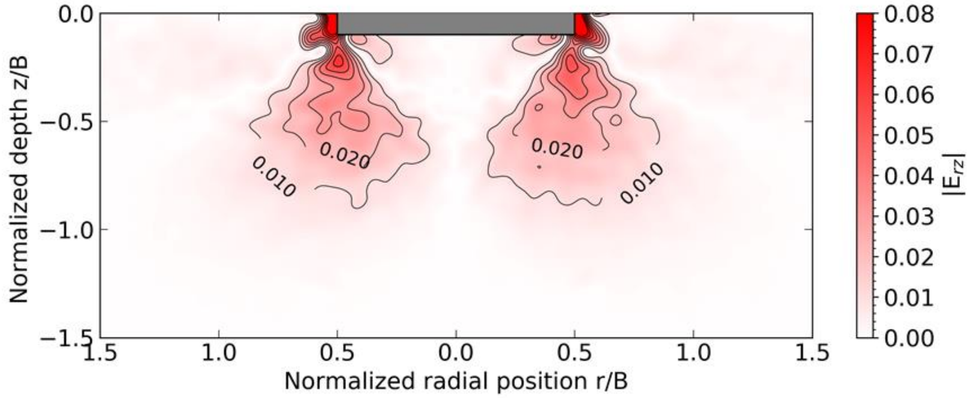

(c)

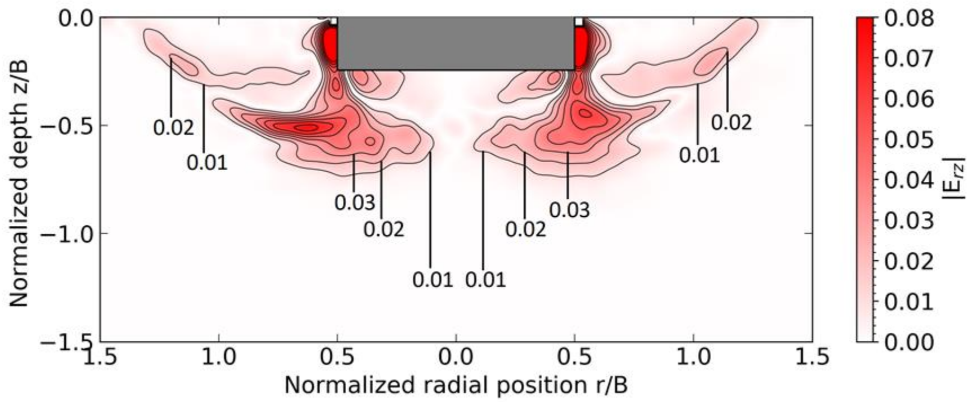

(d)

3.5 Orientation of strains in the soil domain

While the displacement vectors and the contour plots presented so far provide insights into the displacement and strain fields around the two advancing penetrometers, they do not provide an indication of the direction of shearing, which is of interest especially because the formation of shear bands is a key element in most analytical formulations of the penetration problem. These directions can be determined using the Mohr circle of strains.

3.5.1 Principal strain orientation

Using the pole method, the major and minor principal planes and the corresponding major and minor principal strains can be obtained from the Mohr circle of strains (Salgado 2008). Figure 3.16 and Figure 3.17 show the directions of the major and minor in-plane principal strains in the soil domain for the cone penetrometer and the model footing, respectively. We know from the heat map and contours of the radial and vertical strain that, below both penetrometers, the soil is in vertical compression and radial extension, with minimal shear strain, hence the major and minor principal strains are oriented horizontally and vertically, respectively. Moving from the region below the penetrometer to the region next to the penetrometer, the principal strain directions rotate. The soil there is in vertical extension and radial compression, hence the major and minor principal strains are oriented vertically and horizontally, respectively. Along the vertical surface of the two penetrometers, the principal strains make an angle approximately equal to ±45° with the horizontal axis, as also observed by Galvis-Castro et al. (2019) for the cone penetrometer. In addition to the orientation of the principal strains, we can also use the Mohr circle to obtain the orientation of the shear bands in the soil domain.

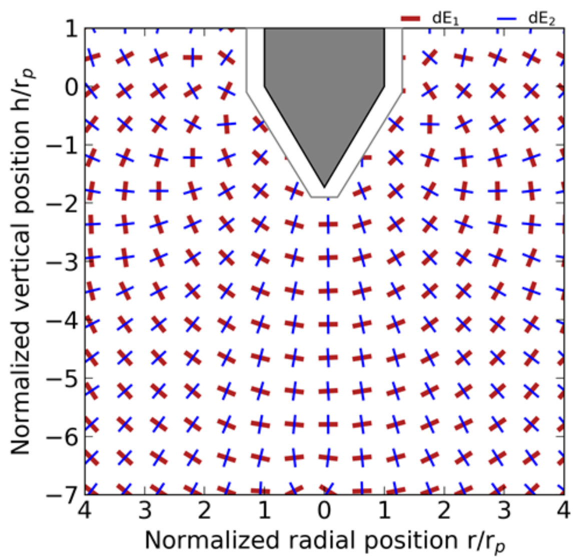

Figure 3.16 Direction of major (dE_1) and minor (dE_2) in-plane principal strains in the soil domain for a vertical displacement increment of 2 mm of the cone penetrometer (strains are positive in extension).

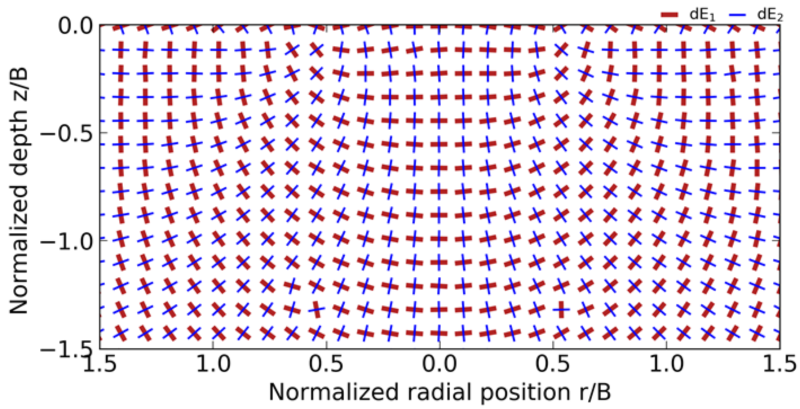

(a)

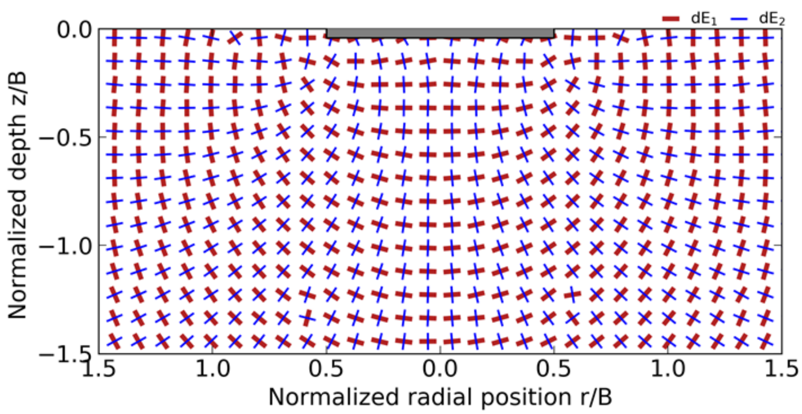

(b)

Figure 3.17 Direction of major (dE_1) and minor (dE_2) in-plane principal strains in the soil domain for a vertical displacement increment of 2 mm of the model footing at (a) start of penetration (F1), (b) peak resistance (F2), (c) softening (F3), and (d) plunging (F4). The labels F1 through F4 can be seen on the penetration resistance curve in Figure 3.2(b).

Figure 3.17 continued

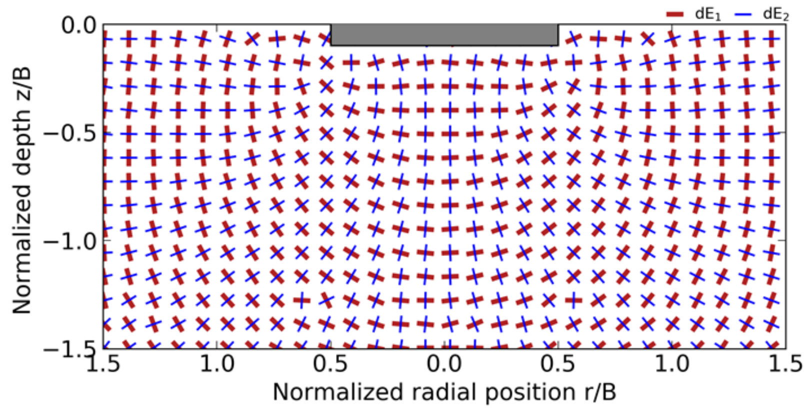

(c)

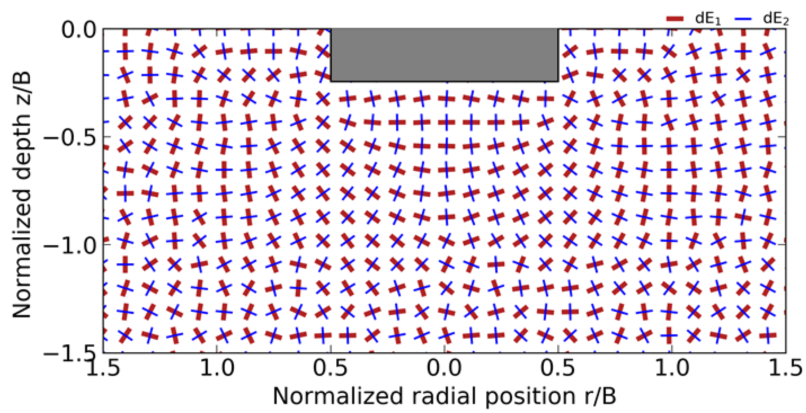

(d)

3.5.2 Zero-extension line (ZEL) and shear band orientation

The shear localizations that develop in a soil mass undergoing deformation are generally referred to as "slip surfaces." Conceptually, a slip surface develops when a mass of soil, behaving much like a rigid block, slides with respect to another rigid block without undergoing any deformation. In theory, the rigid blocks slide with respect to each other along a surface; in reality, however, a "slip surface" is a very thin zone or band of highly localized shear strain or "shear band." Figure 3.18 shows a schematic of the shear band conceptualized as a deformable soil element positioned in between two rigid soil elements that are on the verge of sliding past one another. The essential aspect of the concept of the shear band is that any elemental segment of it, being attached to rigid material on both sides, will experience zero stretch along it. The shear band is, therefore, a zero-extension line (ZEL) (Bardet 1990; Jahanandish and Ansaripour 2016; Roscoe 1970; Salgado 2008). In the schematic of Figure 3.18, the deformable element of the shear band (i.e., the ZEL) experiences distortion (shear) and expansion in the Y-direction but no elongation or shortening in the X-direction.

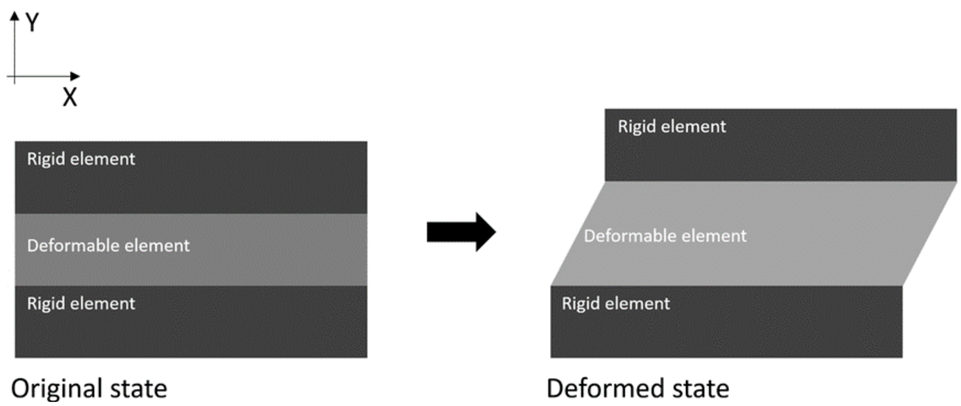

Figure 3.18 Schematic of the shear band represented by a deformable soil element bounded by two rigid soil elements on the verge of sliding past one another (after Salgado 2008).

The Mohr circle of strains can be used to determine the orientations of the shear bands around the penetrometers by using the relative orientation of the major principal plane and the planes of zero normal strain. In the Mohr circle of strains there are two points where the circle intercepts the y-axis. These points represent planes on which the normal incremental strain is zero; the angle between these two planes is bisected by the major principal plane. Consider the Mohr circle shown in Figure 3.19, the angle θ between the major principal plane and the plane of zero normal incremental strain can be computed from the angle 2θ between the lines connecting the points corresponding to these planes on the Mohr circle to the center of the Mohr circle. From the geometry of the Mohr circle, θ can be computed as follows:

$$\theta = \pm\frac{1}{2}\left(90 + \sin^{-1}\left(\frac{dE_1 + dE_2}{dE_1 - dE_2}\right)\right) \tag{3.4}$$

Knowing the values of the principal incremental strains, their orientations – shown in Figure 3.16 and Figure 3.17– and the angle θ between the major principal strain direction and the direction of zero normal incremental strain, we can compute the orientations of the two potential shear bands and the magnitude of shear strains along these orientations.

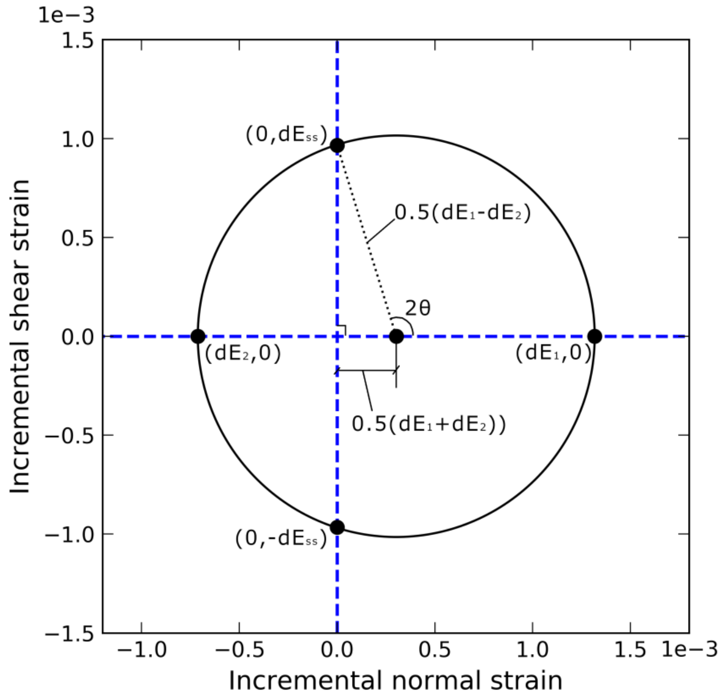

Figure 3.19 Mohr circle of strain showing the angle between the points representing the plane of zero normal strain (zero-extension plane) and the plane of zero shear strain (principal plane) on the circle.

3.5.2.1 Dominant shear bands around the cone penetrometer

Figure 3.20 shows the heat map and contours of the magnitude $|dE_{ss}|$ of incremental shear strain along the orientation of the shear band around the cone penetrometer. In the figure, we see that the regions next to the penetrometer surface have the largest magnitude of incremental shear strain, with $|dE_{ss}|$ ranging from 0 to 0.05. Just from the contours of $|dE_{ss}|$, however, the orientation of the shear bands cannot be judged.

Figure 3.21 shows the two sets of shear bands (corresponding to the two y-intercepts of the Mohr circle) as line segments scaled by $|dE_{ss}|$. The inclination of each line segment represents the orientation of the ZEL of the soil element, and the length of each segment represents the $|dE_{ss}|$ of the element. The location of the element is at the center of the line segment. At each soil element in Figure 3.21, there are two possible orientations along which the shear band can develop; the orientation of the shear band that dominates will depend on the orientation of the shear band in the neighboring soil elements and, ultimately, on the boundary conditions for the problem.

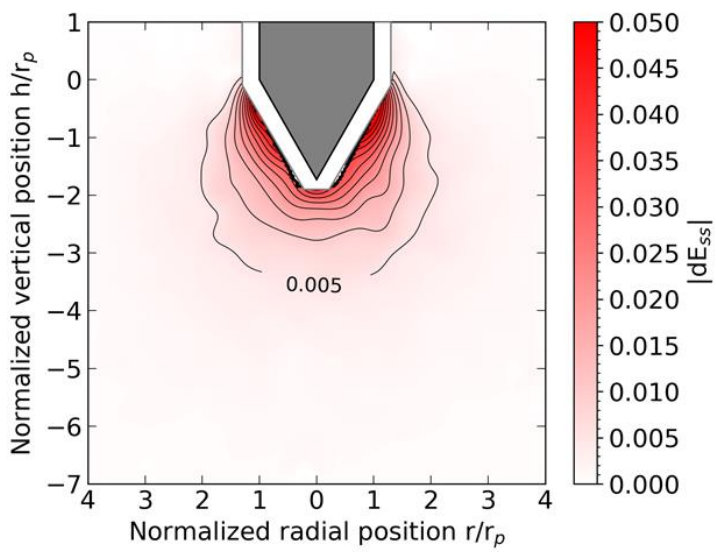

Figure 3.20 Heat map and contours of the magnitude $|dE_{ss}|$ of incremental shear strain along the directions of zero normal strain (zero extension) in the soil domain for a vertical displacement increment of 2 mm of the cone penetrometer.

To assess which of the two orientations is dominant, we first choose a location of interest in the soil domain (center of a subset) and define its neighborhood as a square area with an edge length of 9.3 mm (15 D_{50}). Then, for the two sets of shear bands (SB1 and SB2) within the defined neighborhood, we compute the coefficients of variation (CVs) of the inclination γ of the shear bands ($CV_{\gamma,SB1}$ and $CV_{\gamma,SB2}$). If $CV_{\gamma,SB1} < CV_{\gamma,SB2}$, then, at the location of interest, the shear band orientation corresponding to SB1 is taken as the dominant orientation; otherwise, the orientation corresponding to SB2 is taken as dominant. In cases where the CVs are within 5% of each other, we decline to choose a dominant shear band orientation. At such a location, there is possibly a region of diffused shearing.

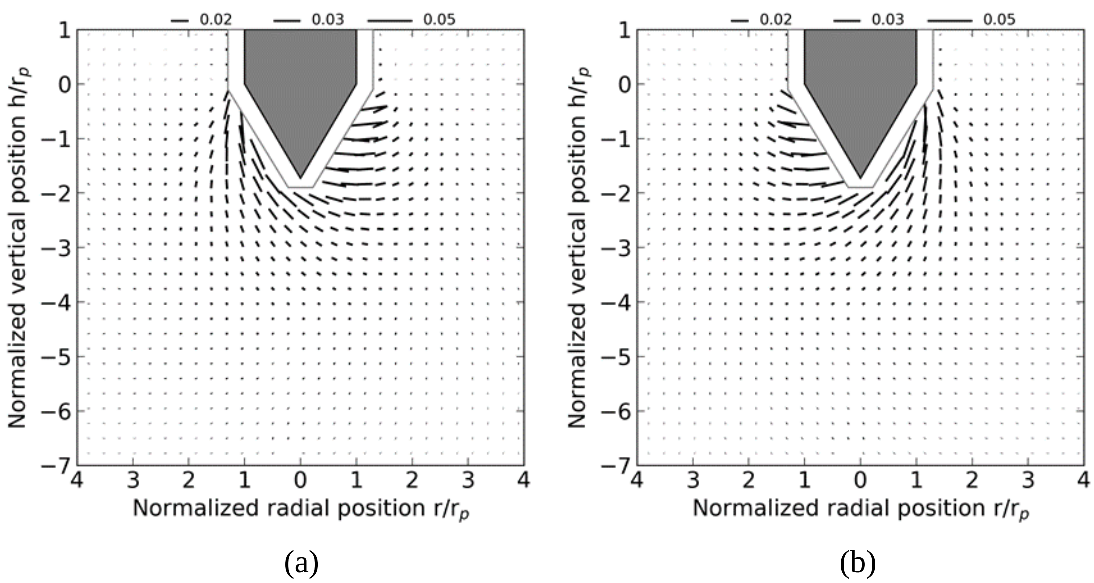

Figure 3.21 Orientation of the two potential sets of shear bands in the soil domain (corresponding to the two y-intercepts of the Mohr circle of strain), scaled by the magnitude $|dE_{ss}|$ of incremental shear strain along the zero-extension line for a vertical displacement increment of 2 mm of the cone penetrometer.

The choice of 5% CV threshold is a subjective one. Consider the different shear band patterns that emerge around the cone penetrometer as the CV threshold in the algorithm described above is changed from 3% to 15%, as show in Figure 3.22. In the figure, we can see that, as the CV increases, more regions around the cone fall into the category of "diffused shearing," as expected. However, this change does not happen uniformly around the cone. The regions most affected by the change in the CV threshold are those immediately below the cone tip. The regions least affected by the change in threshold are those near the shoulder of the penetrometer, along the inclined cone face. Since the shear band patterns that emerge assuming a 5% CV threshold are reasonably similar to the shear band patterns that emerge at higher CV thresholds, with limited loss in detail, we choose the 5% threshold of CV for the visualization of shear band patterns around the penetrometer.

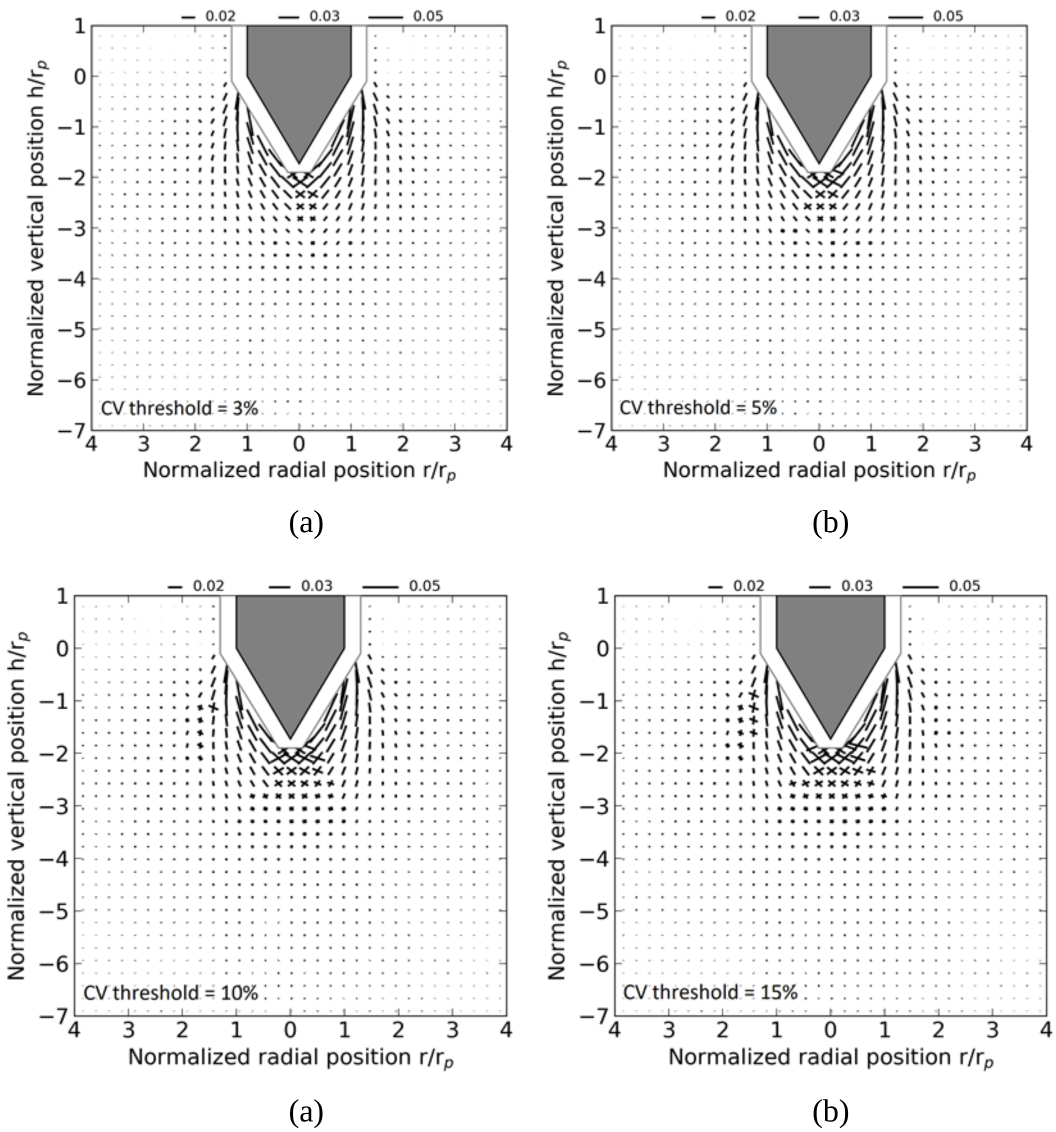

Figure 3.22 Orientation of dominant shear bands in the soil domain around the cone penetrometer for a CV threshold of (a) 3%, (b) 5%, (c) 10%, and (d) 15%.

In Figure 3.23(a), we show the dominant shear band orientations around the cone penetrometer. In general, the dominant shear bands localize near the penetrometer tip and orient themselves to be aligned with the inclined face of the penetrometer (pattern 1). Additionally, some shear bands localize near the penetrometer shoulder and are oriented downwards and away from the penetrometer surface (pattern 2). As the penetrometer advances, especially in sand, new shear bands tend to form around the penetrometer, and previously formed shear bands heal. The shear bands represented by pattern 1 are displaced by the advancing penetrometer tip; however, shear bands represented by pattern 2 may still be observable long after the penetrometer has passed. Paniagua et al. (2013), using CT analysis of cone penetration experiments performed in unsaturated silts, reported the presence of inclined "shear patterns" along the shaft of the penetrometer, like the ones represented by pattern 2.

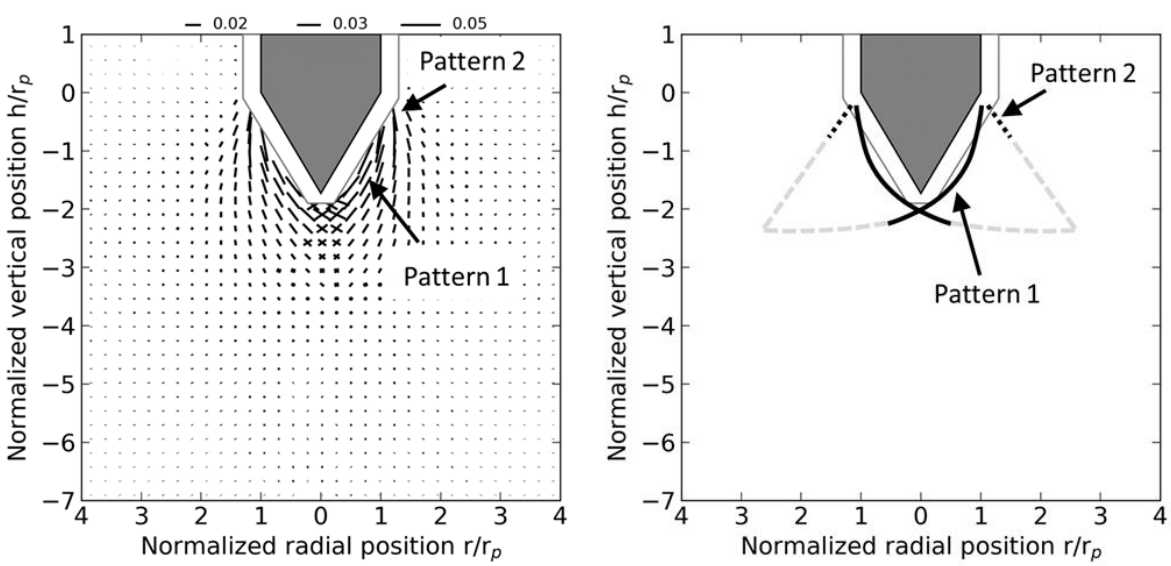

(a) (b)

Figure 3.23 Orientation of dominant shear bands in the soil domain: (a) shear bands oriented along the inclined face of the penetrometer (pattern 1) and shear bands emanating from the shoulder of the penetrometer (pattern 2), and (b) combined representation of the shear band patterns in the soil domain.

In Figure 3.23(b), we see a combination of the two shear band patterns, shown as solid and dotted black lines. The two patterns can be extended, shown by the dashed-grey lines in Figure 3.23(b), to form the traditional shear band ("slip surface") patterns reported in the literature for deep penetration. However, incremental shear strains in these extended portions of the shear bands are not large, and localization is, at best, incipient. As we can see from Figure 3.20 and Figure 3.23(a), the highly localized incremental shear strains around the penetrometer in a deep penetration environment and the continuous downward motion of the cone do not allow this extended pattern to develop.

3.5.2.2 Dominant shear bands around the model footing

Figure 3.24 shows the heat map and contour of |dE_{ss}| around the model footing at different stages of penetration; the magnitude |dE_{ss}| ranges from 0 to 0.07 in each stage.

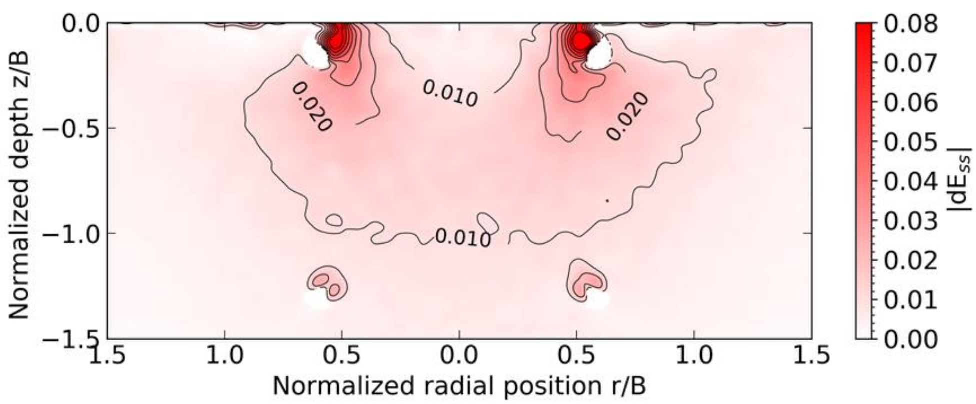

(a)

Figure 3.24 Heat map and contours of the magnitude |dE_{ss}| of incremental shear strain along directions of zero normal strain (zero extension) in the soil domain for a vertical displacement increment of 2 mm of the model footing at (a) start of penetration (F1), (b) peak resistance (F2), (c) softening (F3), and (d) plunging (F4). The labels F1 through F4 can be seen on the penetration resistance curve in Figure 3.2 (b).

Figure 3.24 continued

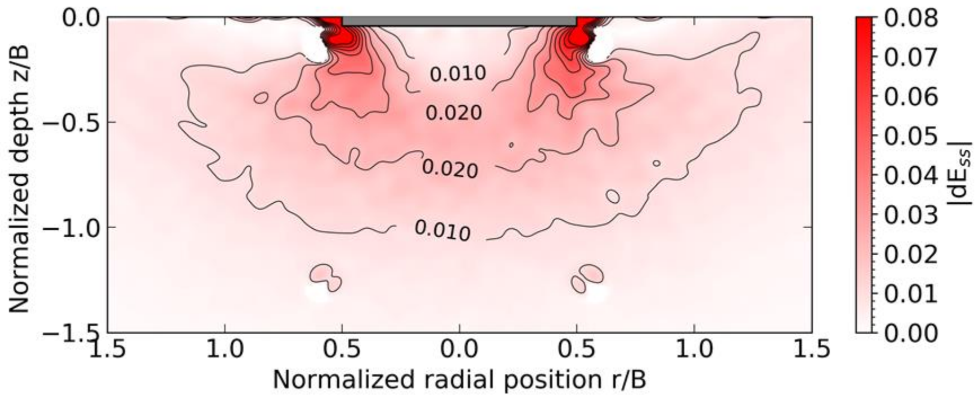

(b)

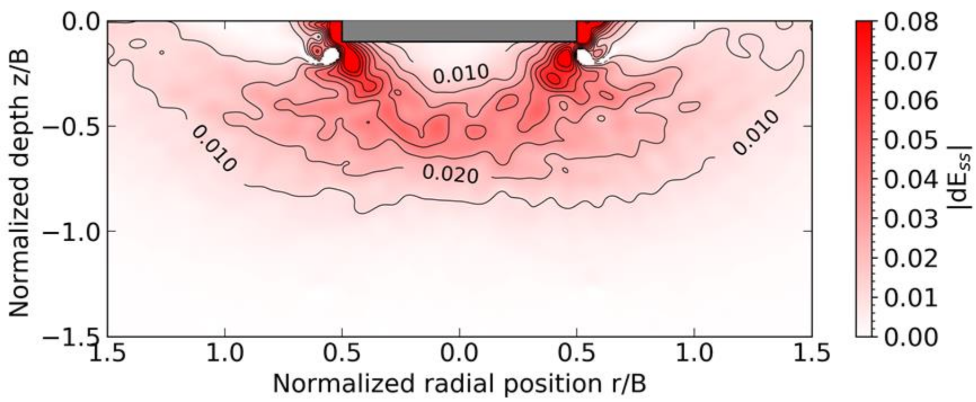

(c)

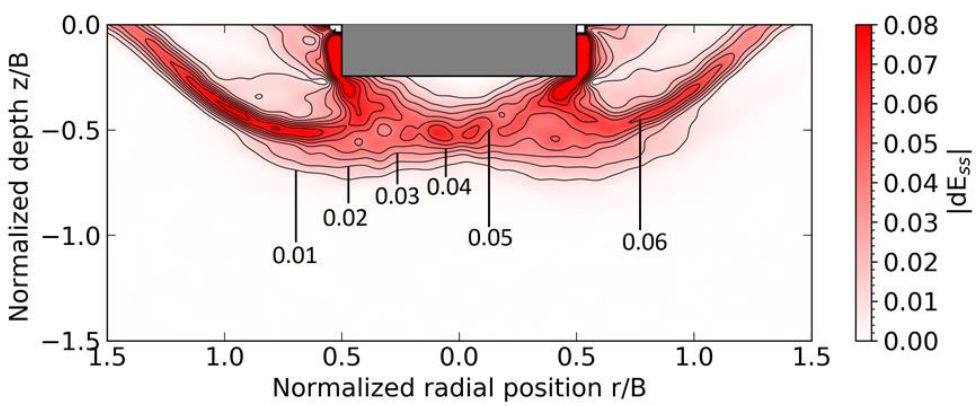

(d)

Figure 3.25 through Figure 3.28 show the orientations of the two sets of shear bands as line segments scaled by $|dE_{ss}|$ for each stage of penetration. At the start of penetration, the shear bands localize near the edges of the model footing (see Figure 3.25). As penetration progresses, we see hints of a "wedge" forming under the model footing (see Figure 3.26); this corresponds to the point of peak resistance in the penetration resistance curve (Figure 3.2(b)). In the softening stage of penetration, we see "fans" forming on either side of the previously developed "wedge" (see Figure 3.27). Finally, at the plunging stage, we see the persistence of the "wedge," albeit somewhat flattened, below the model footing, and the complete formation of "fans" on either side of the model footing (see Figure 3.28). Since quite a complete shear band pattern forms around the model footing in the plunging stage of penetration, we analyze the shear band orientations at plunging (as done for the cone penetrometer) and present the "dominant" shear band orientations in Figure 3.31(a).

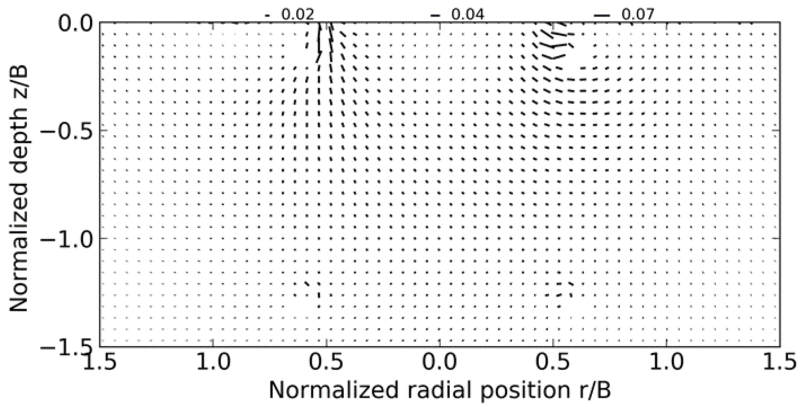

(a)

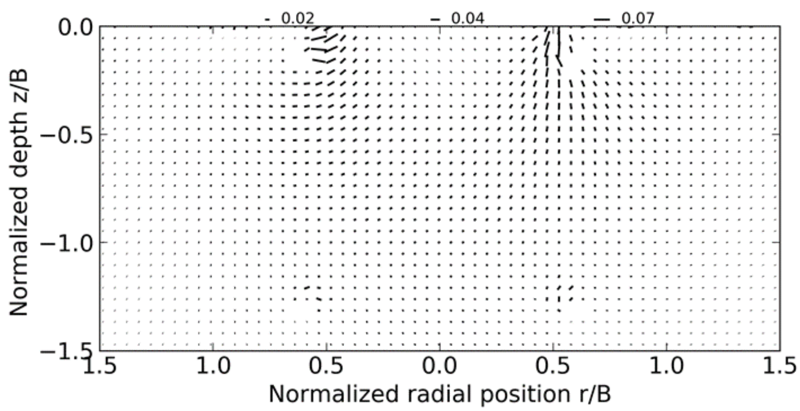

(b)

Figure 3.25 Orientation of the two potential sets of shear bands in the soil domain (corresponding to the two y-intercepts of the Mohr circle of strain), scaled by the magnitude $|dE_{ss}|$ of incremental shear strain along the zero-extension line for a vertical displacement of 2 mm of the model footing at the start of penetration (corresponding to label "F1" in the penetration resistance curve in Figure 3.2(b)).

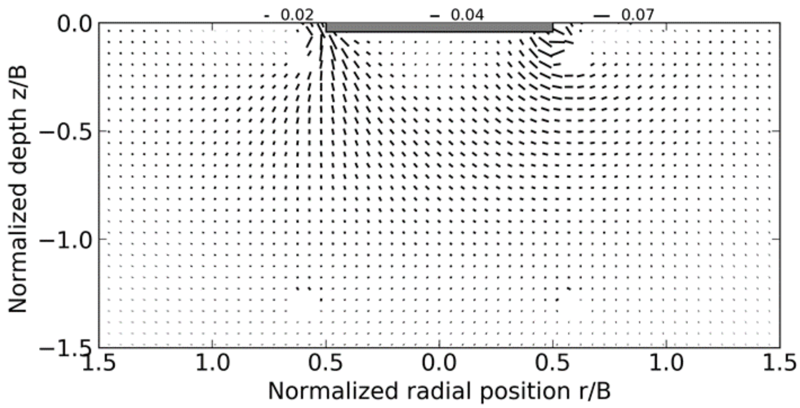

(a)

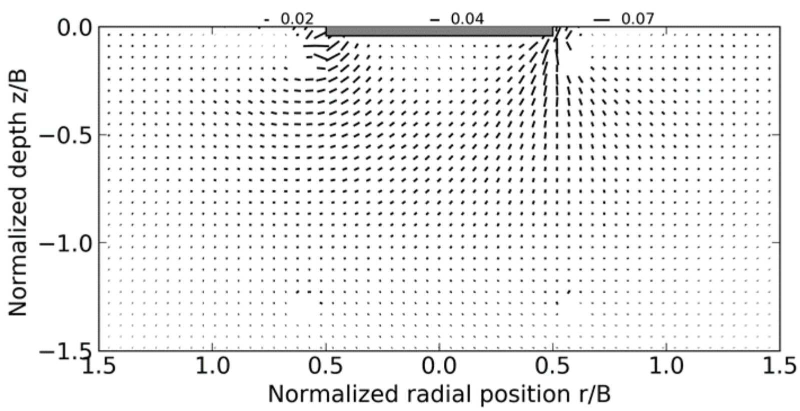

(b)

Figure 3.26 Orientation of the two potential sets of shear bands in the soil domain (corresponding to the two y-intercepts of the Mohr circle of strain), scaled by the magnitude $|dE_{ss}|$ of incremental shear strain along the zero-extension line for a vertical displacement of 2 mm of the model footing at peak resistance (corresponding to label "F2" in the penetration resistance curve in Figure 3.2 (b)).

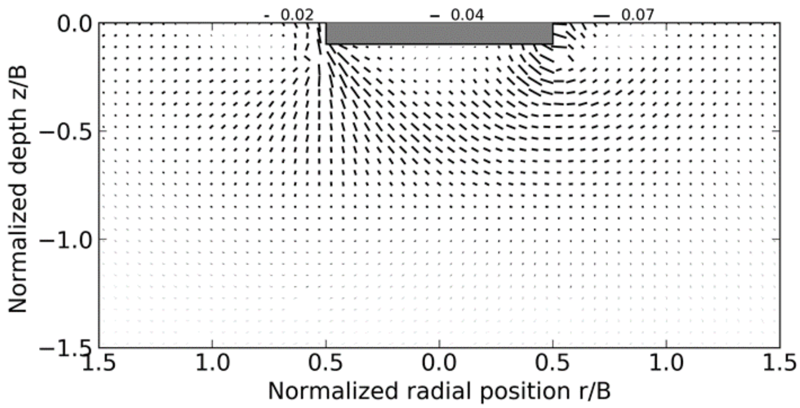

(a)

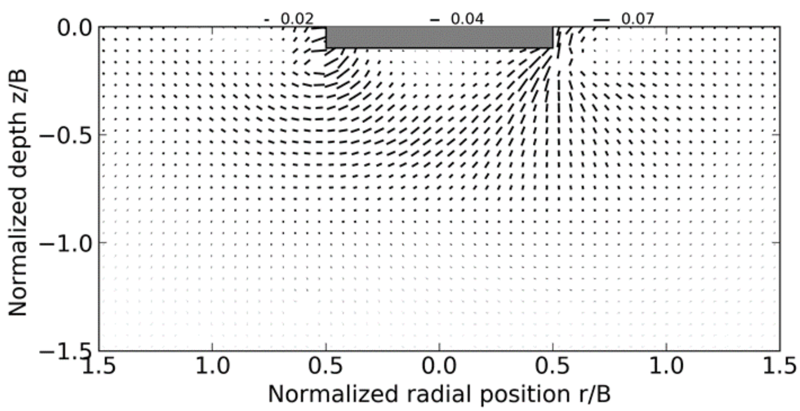

(b)

Figure 3.27 Orientation of the two potential sets of shear bands in the soil domain (corresponding to the two y-intercepts of the Mohr circle of strain), scaled by the magnitude $|dE_{ss}|$ of incremental shear strain along the zero-extension line for a vertical displacement of 2 mm of the model footing at softening (corresponding to label "F3" in the penetration resistance curve in Figure 3.2 (b)).

As done for the cone in Figure 3.22, we present in Figure 3.30 the different shear band patterns that emerge around the footing (at the plunging stage) as the CV threshold in the algorithm is changed from 3% to 15%. We can see from the figures that, as the CV threshold increases, the regions below the footing, at a depth of 0.5 *B*, start falling into the category of "diffused shearing." On the other hand, the dominant shear band orientations in the region 0.5 *B* below the surface and 0.5 *B* away from the centerline of the footing (right below the footing edge) tend to persist as the CV threshold is increased. As observed in cone penetration, the shear band patterns that emerge assuming a 5% CV threshold are reasonably similar to the shear band patterns that emerge at higher CV thresholds, with little loss in detail, and are therefore used for the visualization of shear band patterns around the footing.

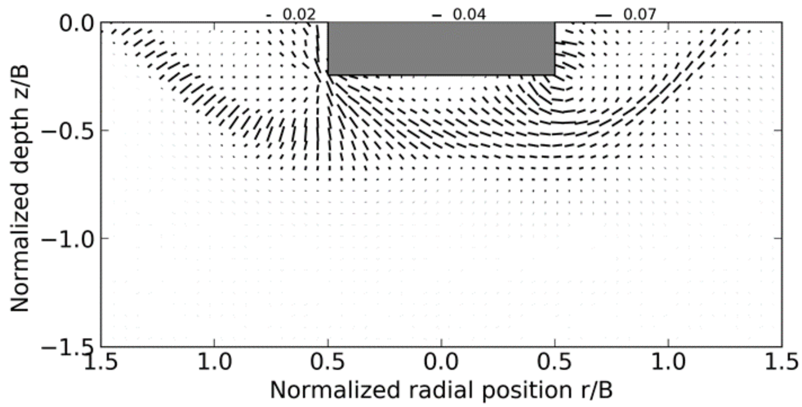

(a)

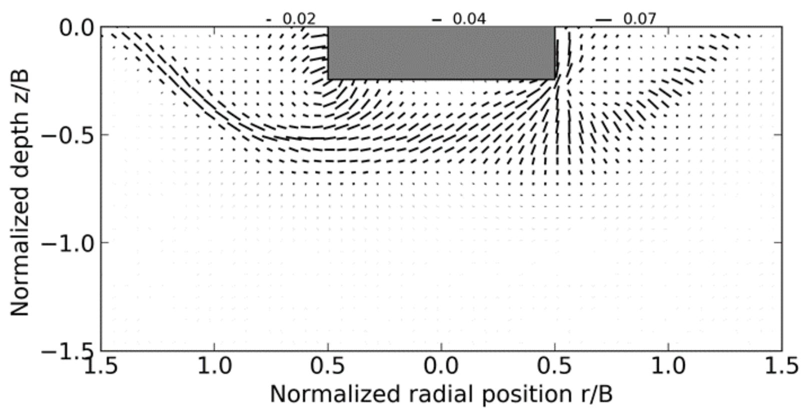

(b)

Figure 3.28 Orientation of the two potential sets of shear bands in the soil domain (corresponding to the two y-intercepts of the Mohr circle of strain), scaled by the magnitude $|dE_{ss}|$ of incremental shear strain along the zero-extension line for a vertical displacement of 2 mm of the model footing at plunging (corresponding to label "F4" in the penetration resistance curve in Figure 3.2 (b))

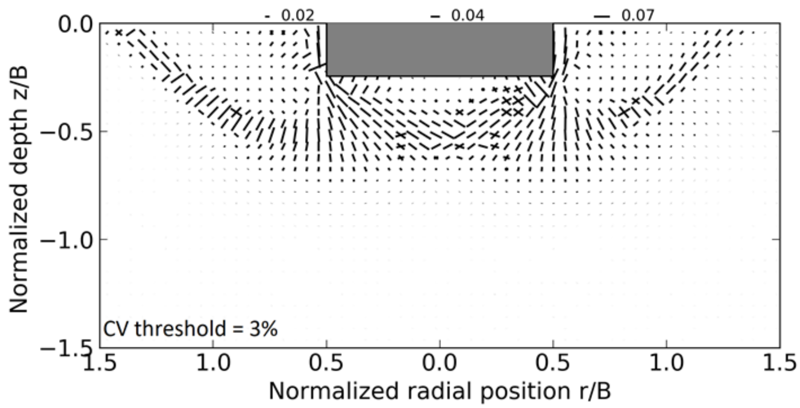

(a)

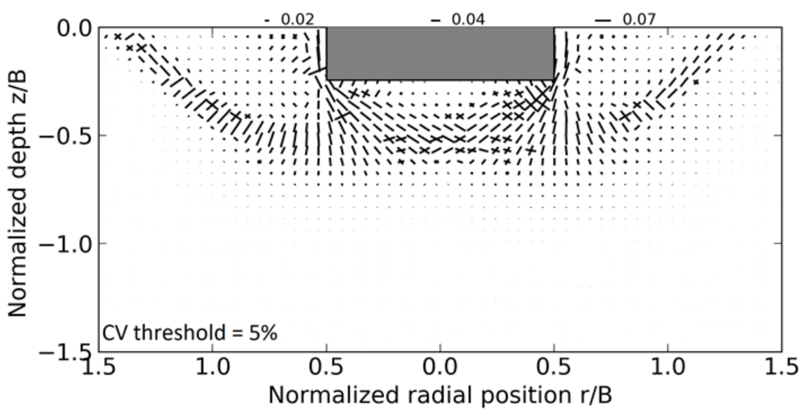

(b)

Figure 3.29 Orientation of dominant shear bands in the soil domain around the footing at plunging for a CV threshold of (a) 3%, (b) 5%, (c) 10%, and (d) 15%.

Figure 3.29 continued

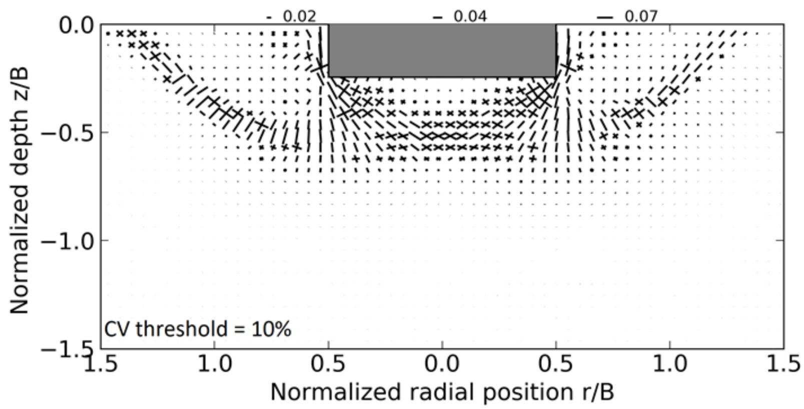

(c)

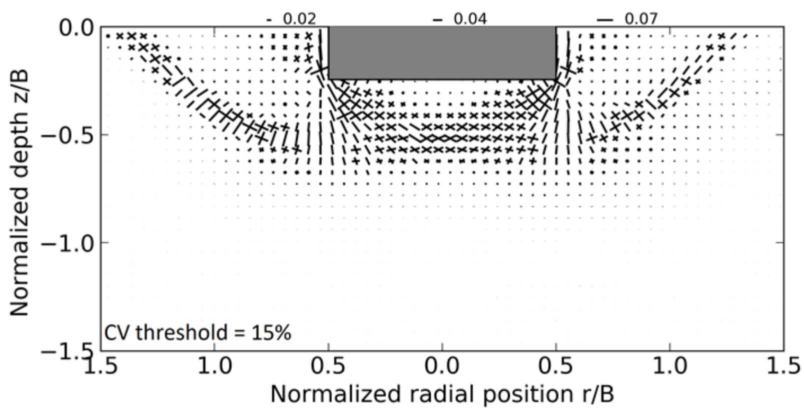

(d)

Figure 3.30 Orientation of dominant shear bands in the soil domain around the footing at plunging for a CV threshold of (a) 3%, (b) 5%, (c) 10%, and (d) 15%.

The first shear band pattern – the "wedge" – in Figure 3.31(a) has shear bands that originate from the edges of the model footing and point downwards and towards the centerline of the model footing. The second shear band pattern – the "fan" – starts at 1*B* from the center of the model footing at a depth of approximately 0.5*B* and reaches the surface of the sand sample at about 1.4 *B* from the center of the model footing. Rotation of the dominant shear bands takes place between the "wedge" and the "fan." Figure 3.31(b) shows the combined representation of the dominant shear band patterns observable in Figure 3.31(a); the solid lines represent the "wedge," the dotted lines represent the "fan," and the shaded areas represent the transition zone where the shear band orientation rotates between the "wedge" and the "fan." The "slip surface" mechanisms proposed in the literature tend to conform to the notion of rigid blocks sliding with respect to each other, with all shearing concentrated on discrete shear bands. However, from the dominant shear band pattern observed in Figure 3.31, we see that incipient or even fully developed shear bands tend to form even within these idealized "rigid blocks."

A simple alternative to the ZEL-based method of shear band determination would be to locate them based on identification of regions in the soil domain where maximum incremental shear strains exceed some threshold value. This approach is not based on a strict definition of shear band; instead, it is based on simply joining points at which the maximum shear strain is large with the expectation that, once these points are joined, the resulting area will characterize a shear band. The difficulty lies in determining the magnitude of incremental maximum shear strain to use to obtain these plots. In Figure 3.32(a), the shaded region around the cone penetrometer covers points with $|dE_{max}| > 2\%$. In Figure 3.32 (b), the shaded region around the footing covers points with a $|dE_{max}| > 3\%$. These shaded regions approximately match the shear band patterns around the cone and footing identified previously (see Figure 3.23and Figure 3.31).

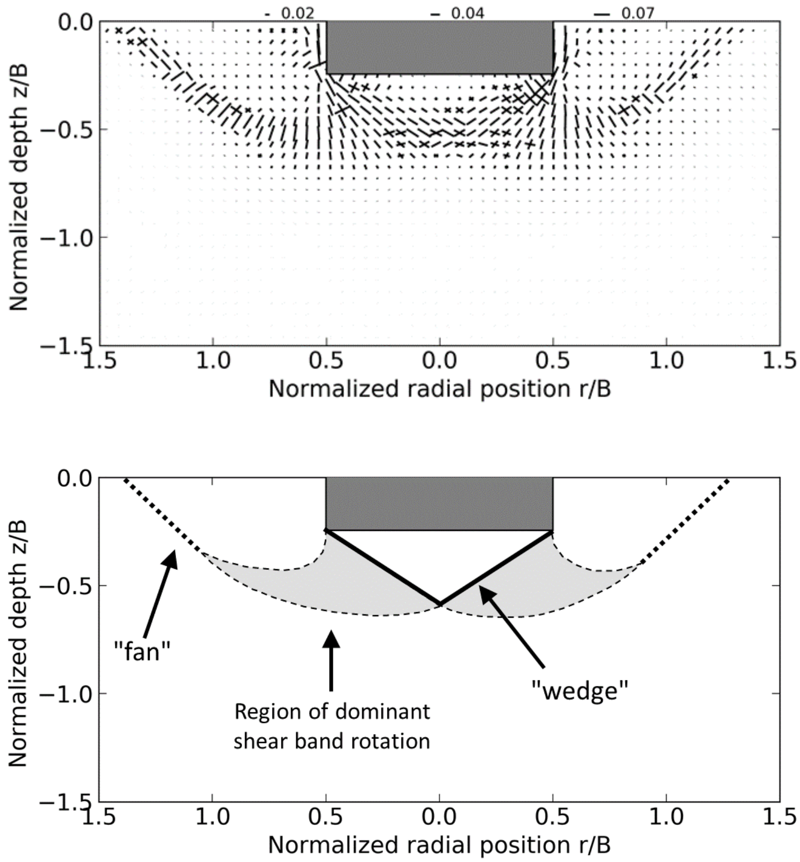

Figure 3.31 Strain localization around the model footing: (a) dominant shear bands around the model footing and (b) combined representation of the shear band patterns around the model footing: "wedge" under the model footing, "fan" on either side of it and a transition zone between the wedge and the fan.

The advantage of the ZEL method over this alternative method based on plotting zones in which the maximum shear strain increment exceeds some threshold value is that (1) it is based on the concept of a shear band and (2) it is automated. However, so long as a suitable threshold value of maximum shear strain increment is selected, a reasonable approximation for the shear band can be obtained.

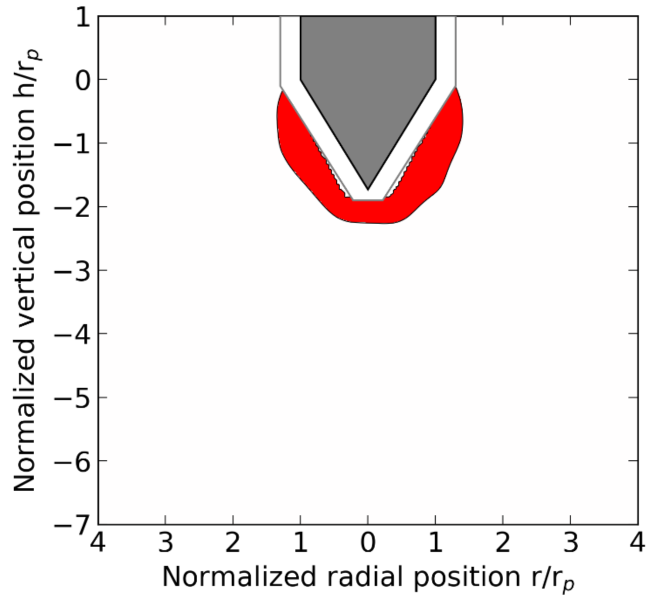

(a)

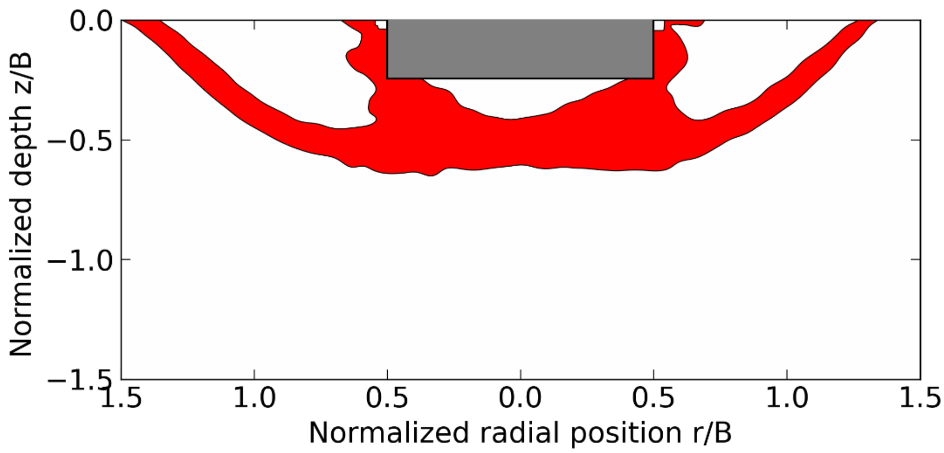

(b)

Figure 3.32 Regions in the soil domain with $|dE_{\max}|$ greater than a chosen threshold: (a) regions around cone penetrometer with $|dE_{\max}| > 2\%$, and (b) regions around footing at the plunging stage with $|dE_{\max}| > 3\%$.

3.6 Conclusions

In this paper, we presented results from deep and shallow penetration experiments in dense sands performed in a calibration chamber that allows image collection. The incremental displacement and strain fields around the penetrometer and model footing were obtained from DIC analysis of images collected during the penetration experiments. The shear band patterns were extracted from the incremental strain field using the concept of the zero-extension line. A method was proposed for automatic identification of the dominant shear bands for both deep and shallow penetration.

For the cone penetrometer, tested in a deep penetration environment, the shear band pattern was found to localize near the penetrometer tip. Two distinct shear band patterns were observed: one oriented with the inclined face of the penetrometer and the other emanating from the shoulder and oriented radially outwards and downwards. For the model footing in shallow penetration starting from the sand surface, the shear band pattern can be characterized as a combination of a "wedge" formed below the model footing and two "fans" on either side of the "wedge." The "wedge" developed near the peak in resistance, whereas the "fans" developed only once the plunging stage was reached. Rotation of the dominant shear band orientation was found to take place between the "wedge" and the "fan." The data and methodology presented here help us contrast the slip surface mechanisms that develop around penetrometers in deep and shallow penetration environments, aid us in the assessment of previous work attempting to model penetration in sands, and serve as a useful benchmark for validation of numerical simulations of the penetration process.

4 QUANTIFICATION OF PARTICLE CRUSHING AROUND CONE PENETROMETER

This chapter will be submitted as a paper to a peer-reviewed journal.

4.1 Introduction

Particle crushing occurs near the tip of an advancing penetrometer due to the large mean and shear stresses that develop in the soil domain during the penetration process (Kikumoto et al. 2010; Kuwajima et al. 2009; Xiao et al. 2016b; a; Yasufuku and Hyde 1995). Crushing of particles leads to change in the particle size distribution, which affects the stress-strain behavior of the soil (Einav 2007; Ghafghazi et al. 2014; Hardin 1985; McDowell and Bolton 2000; Xiao et al. 2014; Zhang et al. 2013). Crushing of the soil particles surrounding the penetrometer also results in contraction of the soil, which in turn results in stress relaxation and a drop in the mobilized cone resistance q_c (Cheng et al. 2004; Vallejo and Lobo-Guerrero 2005; Yao et al. 2008). Therefore, to better understand the q_c mobilization mechanism and its dependence on the crushing of the sand particles, quantification of crushing of soil near the penetrometer tip is important.

Particle crushing around penetrometers has been historically quantified using sieve/sedimentation-based analysis of soil samples collected around penetrometers after penetration experiments performed in calibration chambers (Kuwajima et al. 2009; Yasufuku and Hyde 1995); however, since both sieving and sedimentation require a minimum threshold of soil mass for the analysis, the inclusion of sand from a larger region than the region of interest around the penetrometer often becomes unavoidable. This issue is particularly evident around the tip of the penetrometer, where crushing tends to be localized in small regions near the penetrometer surface (Ganju et al. 2020b). To address this issue of sample size, researchers have used image-based analysis of smaller samples collected around the penetrometer to obtain the particle size distribution (Yang et al. 2010), but collection of such small samples at locations of interest around the penetrometer for subsequent particle size analysis is very challenging.

Penetration experiments performed in special calibration chambers equipped with observation windows allow the direct observation of the crushing of sand particles around the penetrometer (Arshad et al. 2014; White and Bolton 2004). However, the quantification of crushing from the images is hampered by the fine particles, which tend to fill the void between the larger particles and the window, blocking the line-of-sight from the cameras to these larger particles.

Researchers in the past decade or so have used X-ray-based Computed Tomographic (XCT) imaging to study, at the particle level, the soil behavior (Andò et al. 2013; Cil et al. 2017b; Guida et al. 2018; Hasan and Alshibli 2010; Kaestner et al. 2008; Otani et al. 2000) and soil response in small-scale boundary value problems (BVPs) (Chevalier et al. 2010; Chevalier and Otani 2011; Doreau-Malioche et al. 2019; Otani et al. 2005; Silva et al. 2013) in three dimensions. Such studies have employed miniature experimental set-ups which fit inside X-Ray scanners. While such experiments provide invaluable insights into soil behavior, their results are subject to scale and boundary effects due to their small size. However, with the use of sampling techniques that retain the in-situ soil particle arrangement, such as those developed by Emery et al. (1973), Jang et al. (1999), Palmer and Barton (1986), and Silva et al. (2013), samples can also be collected from larger-scale experiments and subsequently scanned using XCT scanners to study different BVPs.

To study crushing around a cone penetrometer, we performed a series of penetration experiments in dense samples of three different sands. The three test sands have similar particle size distributions; however, they differ in particle morphology and particle strengths. These differences allowed us to assess the effect of microscale particle characteristics on the macroscale penetration resistance. For each of the three test sands, three penetration experiments were performed under three different surcharge levels in a special half-cylindrical calibration chamber with Digital Image Correlation (DIC) capabilities. After each penetration experiment, minimally disturbed sand samples were collected from around the cone tip using a specially developed agar-impregnation technique. The agar-impregnated samples were scanned in an X-ray Microscope (XRM) to obtain the XCT data of the sand samples. The XCT data were further analyzed to obtain the particle size distributions at discrete locations around the penetrometer tip. The computed particle size distributions allowed us to quantify the amount and distribution of particle crushing around the penetrometer tip using the widely used relative breakage B_r parameter proposed by Hardin (1985) and Einav (2007).

4.2 Materials and methods

4.2.1 Test sands

Three silica sands were used for the cone penetration experiments: #2 Q-Rok (2QR), Ohio Gold Frac (OGF), and Ottawa 20-30 (OTC). Figure 4.1 shows the particle-size distribution curves for the three test sands (ASTM-D6913 2017), along with images of representative sand particles obtained using a microscope fitted with an 8-megapixel eye-piece camera. In Table 4.1 we show the values of average particle size (D_{50}), coefficient of uniformity (C_U), coefficient of curvature (C_C), and the USCS soil classification (ASTM D2487-17 2006) for the three test sands. The three test sands have similar particle size distributions; however, the particles of these sands differ in morphology and strength.

To quantify the difference in the particle morphologies of the three test sands, we captured over 90 2D images of the particles of each test sand. These images were subsequently analyzed using the MATLAB code by Zheng and Hryciw (2015) to obtain the distribution of morphology parameters–roundness (R) and sphericity (S)–for the three sands. R is defined as the ratio of the average radius of curvature of the corners of the particle to the radius of the largest circle that can be inscribed inside the particle boundaries (Wadell 1932), while S is defined as the ratio of the width of the particle to the length of the particle obtained by fitting an ellipse to a 2D image of the particle. Table 4.1 shows the values of average sphericity (S_{avg}) and average roundness (R_{avg}) for the test sands. All three sands have reasonably spherical particles with an S_{avg} in the range of 0.73-0.79. However, the three test sands have different R_{avg} values: the 2QR sand has the lowest R_{avg} value of 0.24, while the OTC sand has the highest R_{avg} of 0.74. The OGF sand has an intermediate R_{avg} value of 0.37. This difference in R_{avg}, affects the minimum and maximum packing density and the internal critical state friction angle ϕ_c of the three sands. From the values of minimum e_{min} and maximum e_{max} void ratios and ϕ_c shown in Table 4.1, we can see that the lower the R_{avg} is, the higher are the values of e_{min}, e_{max}, and ϕ_c. This may be attributed to the greater interlocking of particles caused by the angular surface asperities.

The three sands also differ in terms of their individual particle strengths. In Table 4.1, we also show a summary of the average particle fracture stresses ($\sigma_{f,avg}$) and the fitting parameters σ^* (applied stress level at which 37% of the loaded particles survive crushing) and the Weibull distribution's m (Weibull 1951) for the three test sands. These values were obtained from single particle loading experiments performed on over 50 particles for each test sand. The specifics of these single particle compression experiments are discussed in Chapter 2. From the data provided in Table 4.1 we can see that 2QR has the weakest particles with a $\sigma_{f,avg}$ of 22 MPa and σ^* of 23

MPa. OGF has stronger particles than 2QR, with a $\sigma_{f,avg}$ of 75 MPa and σ^* of 84 MPa. The OTC sand particles are the strongest, with a $\sigma_{f,avg}$ of 128 MPa and σ^* of 144 MPa. The values of m range from 1.15 (for 2QR) to 2.82 (for OTC), indicating that the weaker 2QR sand particles have greater variability in fracture stresses than the stronger OTC sand particles. Note that for the three test sands used in this research, the more angular the particles (the lower their R_{avg}), the lower $\sigma_{f,avg}$ they have. This trend runs counter to that of e_{min}, e_{max}, and ϕ_c, all of which were found to increase with decrease in R_{avg}. This observation will become relevant later in the paper when we discuss the penetration resistance values for the three sands.

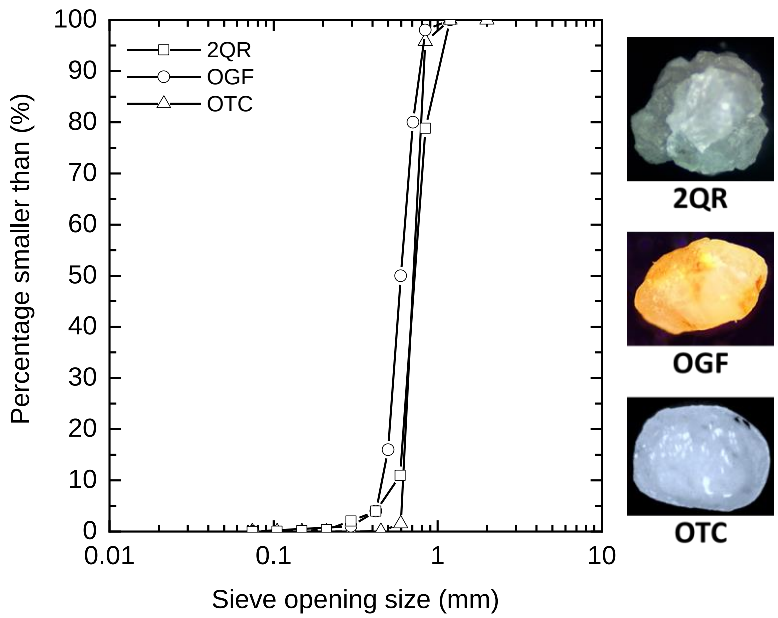

Figure 4.1 Particle size distribution of the three test sands: #2-Q-Rok (2QR), Ohio Gold Frac (OGF), and Ottawa 20-30 (OTC)

4.2.2 Half-cylindrical penetrometer and calibration chamber experiments

A total of nine cone penetration experiments were performed in dry air-pluviated dense samples of the three test sands. The sand samples were prepared in a half-cylindrical calibration chamber, which is 1.68 m in diameter and 1.2 m in height; Figure (a) shows a labeled image of the calibration chamber. This chamber is equipped with three 76 mm thick Polymethyl Methacrylate (PMMA) transparent observation windows on its flat vertical face. The windows of the chamber are reinforced with metal supports, which prevent deflections during the penetration experiments (Arshad 2014).

Table 4.1 Properties of test sands used in the calibration chamber experiments.

Sand	D_{50} (mm)	C_U	C_C	USCS	e_{min}	e_{max}	S_{avg}	R_{avg}	ϕ_c (°)	$\sigma_{f,avg}$ (MPa)	σ* (MPa)	m
2QR	0.73	1.4	1	SP	0.67	0.99	0.74	0.24	33.0	22	22.97	1.15
OGF	0.62	1.4	1	SP	0.61	0.89	0.73	0.37	32.5	75	84.13	1.59
OTC	0.72	1.4	1	SP	0.50	0.75	0.79	0.74	29.3	128	143.61	2.82

D_{50} is the particle size for which 50% of the particles by weight are smaller in size as obtained from sieve analysis following ASTM D6913-17 (2017); C_U and C_C are the coefficients of uniformity and curvature, respectively, for the particle size distribution curve obtain from sieve analysis; USCS is the type of the soil according type the unified soil classification system (ASTM D2487-17 2006) and SP stands for poorly graded sand; emin and emax are the minimum and maximum void ratios, respectively, determined following ASTM D4254-16 (2016); S and R are the average sphericity (aspect ratio) and Wadell (1932) roundness morphology parameters for the test sands obtained using the MATLAB code by Zheng and Hryciw (2015); $\sigma_{f,avg}$ is the average fracture stress of individual particles obtained using single particle uniaxial compression experiments; σ* and *m* are the Weibull (1951) fitting parameters for the single particle crushing experiments on the three sands; ϕ_c is the internal critical state friction angle of the three sands obtained from drained triaxial compression experiments.

The sand samples were formed inside this calibration chamber by raining the sand into the chamber using a special pluviator and diffuser-sieve arrangement. During the sample preparation, cylindrical plastic samplers were placed in the calibration chamber at different depths to assess the local variation of D_R of the sand; the D_R from the samplers for all the sand samples used in this research were found to be 90% ± 5%. Further details of the design and operation of the calibration chamber, the pluviator and diffuser-sieve arrangement, and the sample preparation procedures are discussed by Arshad (2014), Arshad et al.(2014) and Tehrani et al. (2016).

Figure (b) shows a schematic of the cone penetrometer used in the current research. The model penetrometer used for the penetration experiments is a smooth half-cylindrical brass penetrometer with a 60˚ conical tip and a diameter *B* of 38 mm. The surface of the penetrometer is smooth with an average centerline roughness R_a of 0.22 μm (Tovar-Valencia et al. 2018) and the penetrometer tip is instrumented with a load cell which allows us to measure the cone resistance q_c during the penetration experiments.

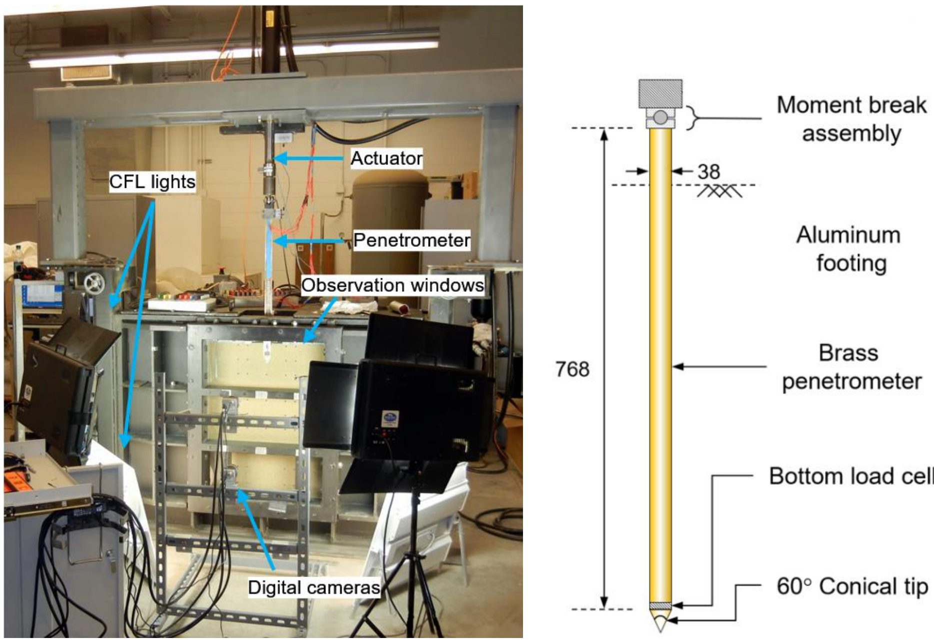

(a) (b)

Figure 4.2 Experimental setup: (a) labeled image of the half-cylindrical calibration chamber with three observation windows, and digital cameras positioned in front of it for image acquisition, and (b) cone penetrometer (all dimensions in mm), (modified after Ganju et al. 2020c).

After the sand sample was prepared, the surface of the sand was flattened, and a vertical surcharge was applied using a pressure-plate assembly. The initial vertical pressure in the sand at the final penetrometer depth was measured directly using a contact pressure cell (Model No. 4800, GEOKON, New Hampshire, USA) placed in the sand sample. For the three surcharge levels used in this research, the initial vertical pressures in the sand at the final penetrometer depth were equal to 17 kPa, 33 kPa and 57 kPa.

After application of the surcharge, the penetrometer was monotonically jacked into the sand sample at a rate of 1mm/s using a high-precision hydraulic actuator connected to the top of the penetrometer via a moment-break assembly. All penetration experiments were performed to a final depth of approximately 380 mm or 10 *B* (measured from the shoulder of the penetrometer to the sand surface). Table 4.2 shows a summary of the penetration experiments.

Table 4.2 Summary of cone penetration experiments performed in dense samples of the three tests sands, under different vertical pressures.

S no.	Experiment ID	Sand	Relative density (%)	Vertical pressure (kPa)
1	2QR-90%-17kPa	2QR	90±5	17
2	2QR-90%-33kPa	2QR	90±5	33
3	2QR-90%-57kPa	2QR	90±5	57
4	OGF-90%-17kPa	OGF	90±5	17
5	OGF -90%-33kPa	OGF	90±5	33
6	OGF -90%-57kPa	OGF	90±5	57
7	OTC-90%-17kPa	OTC	90±5	17
8	OTC -90%-33kPa	OTC	90±5	33
9	OTC -90%-57kPa	OTC	90±5	57

During each penetration experiment, a sequence of images of the soil and the penetrometer was captured at a rate of 2 images/second using 12 Megapixel complementary metal oxide semiconductor (CMOS) monochrome cameras (Model No. beA4000-62km, Basler, Ahrensburg, Germany) positioned in front of the observation windows. The collected images were analyzed using Digital Image Correlation (DIC) (Raffel et al. 2013; Sutton et al. 2009) to obtain the displacement field in the soil domain.

After the completion of each penetration experiment listed in Table 4.2, a minimally disturbed agar-impregnated sand sample was collected around the penetrometer tip. Figure 4.3 shows the step-by-step procedure followed to collect the agar-impregnated sample. Figure 4.3(a) shows the cross-sectional view of the calibration chamber at the end of the penetration experiment with the penetrometer tip at the desired penetration depth (380 mm). At the end of the penetration experiment, the penetrometer was secured to the calibration chamber using clamps (to prevent it from moving during the sample collection process) and then the surcharge was removed [see Figure 4.3(b)]. Subsequently, the sand was carefully excavated to the level of the penetrometer tip, making sure not to move the penetrometer or disturb the sand near the penetrometer tip [see Figure 4.3(c)]. After excavating the sand to approximately 10 mm above the shoulder of the penetrometer, a thin-walled (wall thickness $\leq$ 1 mm) half-cylindrical metallic sampler with an internal diameter of approximately 75 mm was carefully inserted into the sand sample around the penetrometer and then a 0.42% water-based agar solution was poured around the penetrometer tip, inside the sampler [see Figure 4.3(d)]. The half-cylindrical metallic sampler ensured that the flow of the agar solution remained vertical and covered most of the sand around the tip.

Agar is a biopolymer obtained from seaweed that is commonly used as a culture substrate in biological research (Ganju et al. 2020b). Water-based agar solution has a low viscosity at high temperatures (65 ˚C to 90 ˚C) and forms a gel at room temperature (<30 ˚C), making it very useful for sampling of sand in both laboratory and field conditions (Frost 1989; Schneider et al. 1989; Sutterer et al. 1996). Furthermore, a water-based agar solution sets quickly (under 5 min) at room temperature and does not adhere to the penetrometer or glass after setting, allowing easy separation of the sand sample. Also, the X-ray attenuation coefficient (Als-Nielsen and McMorrow 2011) of the agar solution is lower than that of the sand particles, therefore, it can be distinguished from the particles in the XCT scans.

Once the agar solution set, which took approximately 5 minutes, the remaining sand was excavated, and the agar-impregnated sand sample and the adjoining sampler were carefully removed [see Figure 4.3(e)]. Since the metallic sampler would impede the XCT scans, the agar-impregnated sand sample was gently transferred to a half-cylindrical plastic tube with the same internal diameter as that of the metallic sampler. Figure 4.4 shows an image of an agar-impregnated sample in the half-cylindrical plastic tube collected after the OGF-90%-33kPa experiment (refer to Table 4.2).

4.2.3 X-ray Microscope (XRM)

The agar-impregnated sand samples (along with the half-cylindrical plastic tubes) were carefully wrapped in thin plastic sheets and then scanned in a Zeiss X-ray Microscope (XRM) (Model No. VERSA-510, Zeiss, Pleasanton, California) to obtain the 3D XCT data of the sand sample. Figure 4.5 shows the plastic wrapped agar-impregnated sand sample placed inside the Zeiss XRM ready to be scanned. The basic functionality of the XRM used to obtain the XCT data is discussed in Chapter 2.

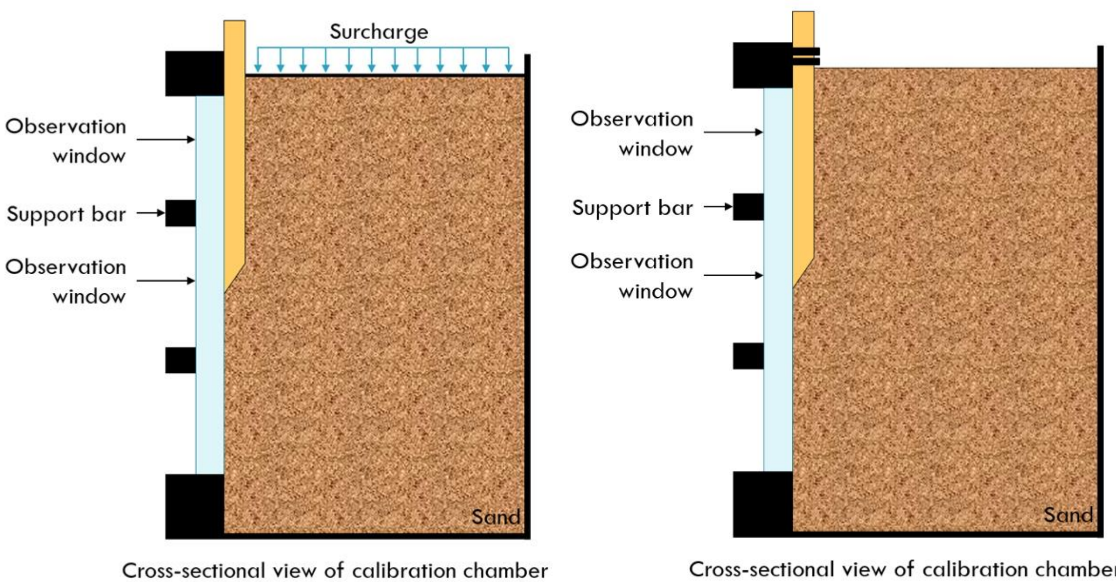

(a) (b)

Figure 4.3 Cross-sectional view of chamber showing the step-by-step procedure for collection of agar-impregnated sample around cone penetrometer: (a) completion of penetration experiment, (b) removal of surcharge and securing of penetrometer to the chamber, (c) excavation of sand to level of penetrometer, (d) insertion of thin-walled sampler and pouring of agar solution, and (e) further excavation of sand for removal of agar-impregnated sand and thin walled sampler.

Figure 4.3 continued

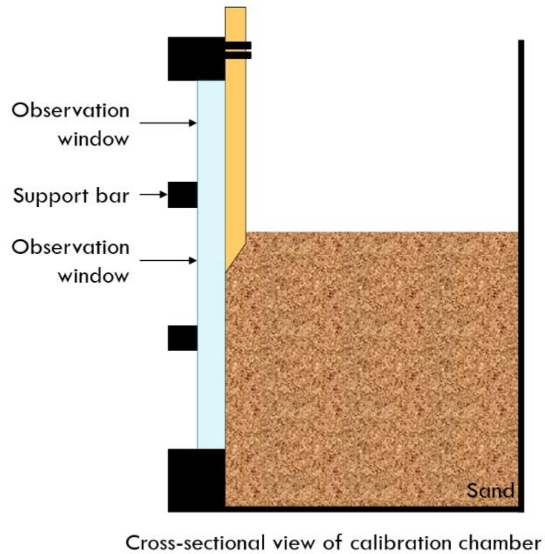

(c)

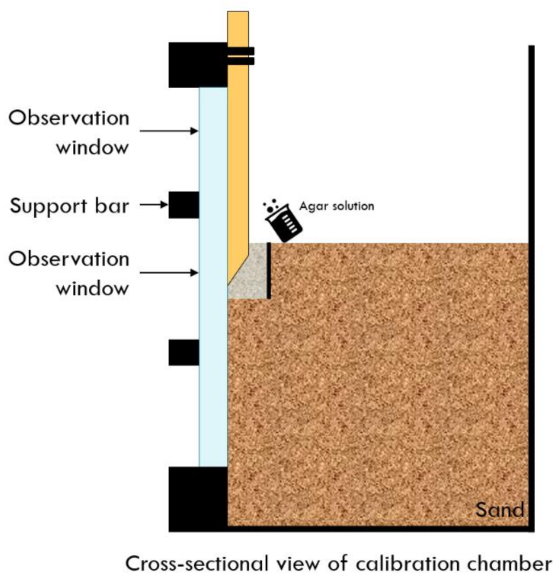

(d)

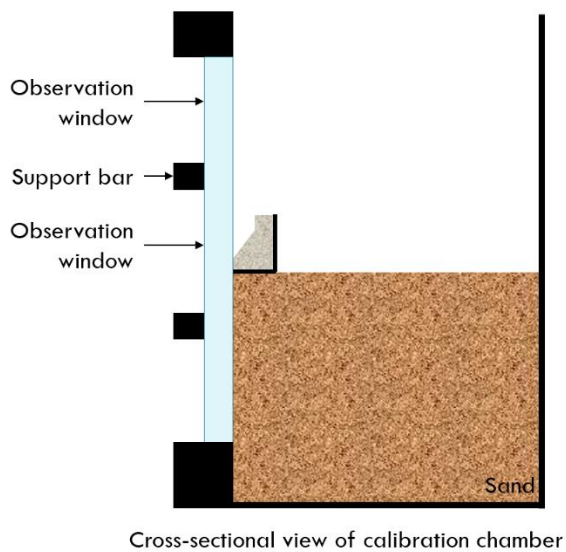

(e)

Figure 4.4 Agar-impregnated sand sample in plastic case collected using the agar-impregnation technique (shown in Figure 4.3) after the penetration experiment performed in dense OGF sand.

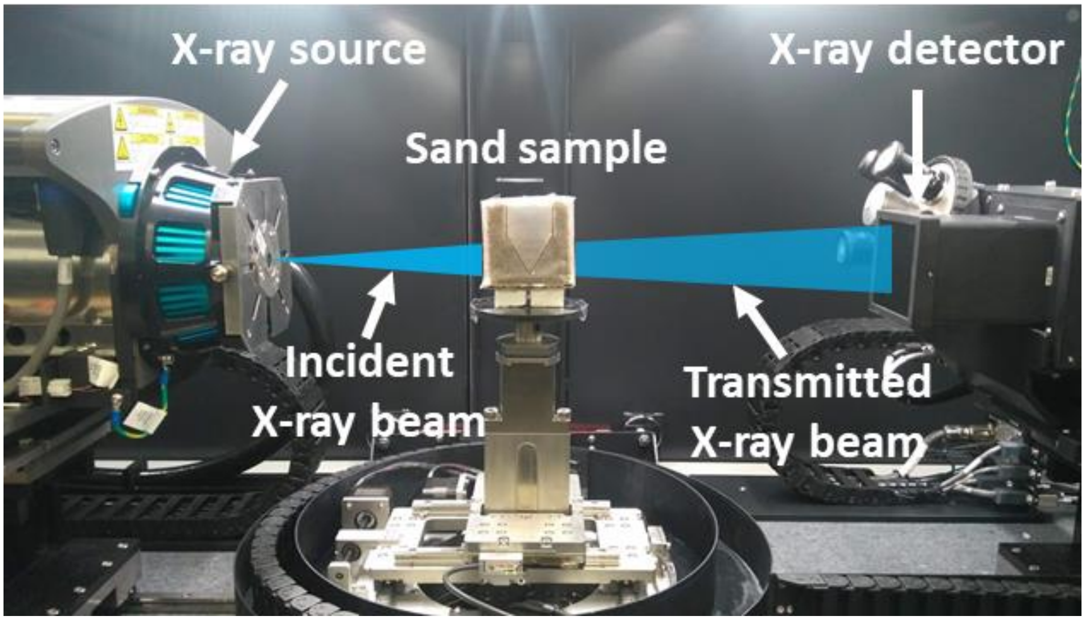

Figure 4.5 X-ray Computed Tomography XCT scan setup showing the X-ray source, sand sample being scanned and the X-ray detector.

In the XRM, each sand sample was scanned three times in three separate locations to capture the XCT data along the inclined face of the penetrometer. The scanned regions were cylindrical in shape with a diameter and a height of approximately 12.5 mm. The scans were performed at a resolution of 12.5 µm/voxel, which allows capture of the size of the particles around the penetrometer with reasonable accuracy (Wiebicke et al. 2017). Figure 4.6(a) shows the locations of the three scan regions around the penetrometer, while Figure 4.6(b) shows the dimensions of the cylindrical scan regions.

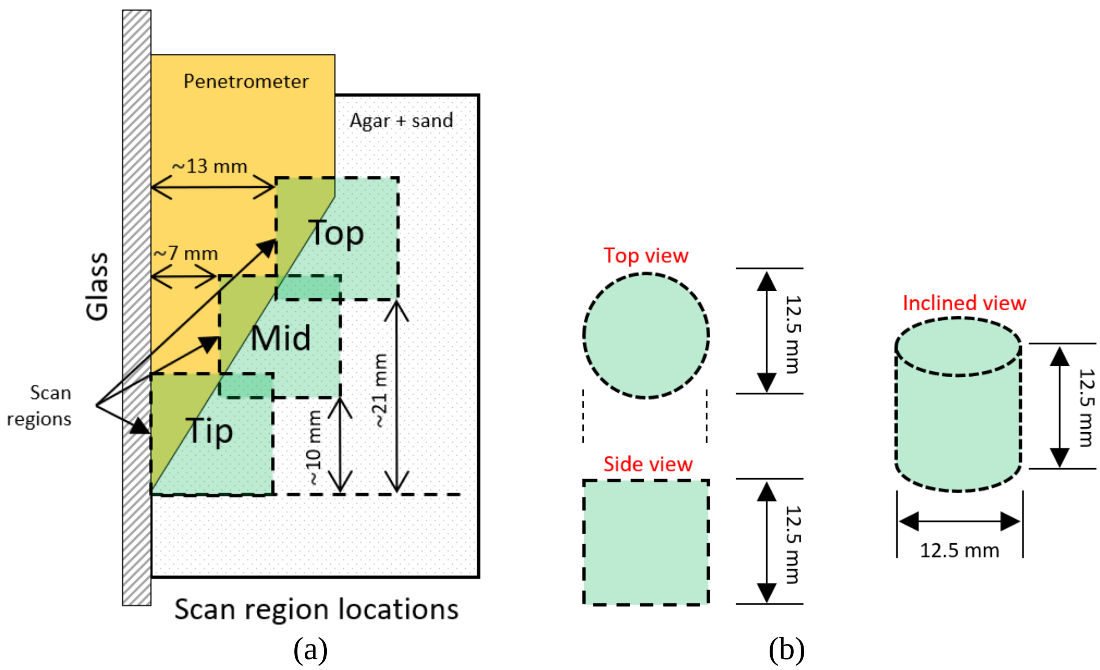

Figure 4.6 XCT scans of agar-impregnated sand samples: (a) location and XCT scan regions around the cone penetrometer tip and (b) dimensions of the cylindrical scan region.

From the three scan regions obtained for each penetration experiment, 30 cubical subregions of edge length $6D_{50}$, as discussed in Chapter 2, were extracted around the cone penetrometer. Based on a parametric study on XCT data of the same three test sands as that used in this research, In Chapter 2 we saw that in dense and uncrushed conditions, a subregion size of $6D_{50}$ contains approximately 100-200 particles of the test sands and this subregion size large enough to capture the particle size distribution of the sand. These extracted subregions were analyzed using the procedure outlined in Chapter 2 using open-source python libraries and an in-house code. The XCT analysis procedure is briefly discussed below.

Each XCT scan was first binarized using the binarization method proposed by Otsu (1979) to obtain the 3D binary map of the sample. Following the binarization, the Euclidean distance map of the binary map was computed and the local maxima in the Euclidean distance map were identified. Then, using these local maxima as seed points, the watershed segmentation algorithm (Beucher and Lantuejoul 1979) was applied to obtain the segmented XCT data. Any over segmentation was corrected by merging particle pairs with unrealistically large contact areas, and then any particles with volume less than 1000 voxels^3 were removed (to account for the resolution threshold).

After the completion of the segmentation step, the particle size distribution of the segmented data was obtained, assuming the minimum Feret diameter $D_{\text{Feret-min}}$ as the representative particle size. The choice of $D_{\text{Feret-min}}$ as the representative particle size was motivated by the findings reported in Chapter 2, where based on a parametric study we found that out of the commonly used particle size parameters available in the literature (Al-Raoush and Papadopoulos 2010; Altuhafi et al. 2013; Andò 2013; Cil 2015; Druckrey 2016; Fonseca 2011; Fonseca et al. 2012, 2014; Hasan and Alshibli 2010), for the three sands used in this research, the $D_{\text{Feret-min}}$ captures the particle size distribution from sieve analysis most closely.

It is important to note that the removal of small particles resulted in a percentage of solid volume loss p_{loss} in the range of 0-5%. To account for the volume loss, the particle size distribution was corrected. For each particle size in the particle size distribution, the updated percentage passing p_{update} was obtained by correcting the original percentage passing p_{original} with the p_{loss} as follows:

$$p_{\text{update}} = \frac{\left(p_{\text{original}} + p_{\text{loss}}\right)}{\left(100 + p_{\text{loss}}\right)} 100 \tag{4.1}$$

From the corrected particle size distributions, the relative breakage parameters B_r proposed by Hardin (1985) and Einav (2007) were computed for each of the 30 subregions corresponding to each of the nine cone penetration experiments. This allowed us to generate contours of both the Hardin (1985) and the Einav (2007) B_r around the cone penetrometer and visualize the spatial variation of crushing in the soil domain around the penetrometer.

4.3 Results and discussions

4.3.1 Penetration resistance

Figure 4.7 shows the cone resistance q_c measured during penetration experiments for the dense OTC, OGF, and 2QR sand samples. All penetration experiments were started with the cone at a pre-embedment depth of 50 mm–this allows us to minimize sand intrusion by ensuring good contact between the flat surface of the penetrometer and the observation window. This is the reason why the penetration plots in Figure 4.7 start from 50 mm instead of 0 mm. The penetration was performed at a rate of 1 mm/s to a final embedment depth of approximately 380 mm (measured from the shoulder of the penetrometer to the surface of the sand). The penetration resistance measured at the 380 mm penetration depth during each penetration experiment is given in Table 4.3.

For the dense 2QR sand [see Figure 4.7(a)] the measured q_c was 8.5 MPa, 11 MPa, and 14.5 MPa under the vertical confinements of 17 kPa, 33 kPa, and 57 kPa, respectively. For the dense OGF sand samples, shown in Figure 4.7(b), the measured q_c was 10.5 MPa under a vertical pressure of 17 kPa, 13.6 MPa under a vertical pressure of 33 kPa, and 18.5 MPa under a vertical pressure of 57 kPa. Whereas for the dense OTC sand samples, the measured q_c was 6.5 MPa under the 17 kPa vertical pressure, 10.5 MPa under the 33 kPa vertical pressure, and 14.5 MPa under the 57 kPa vertical pressure.

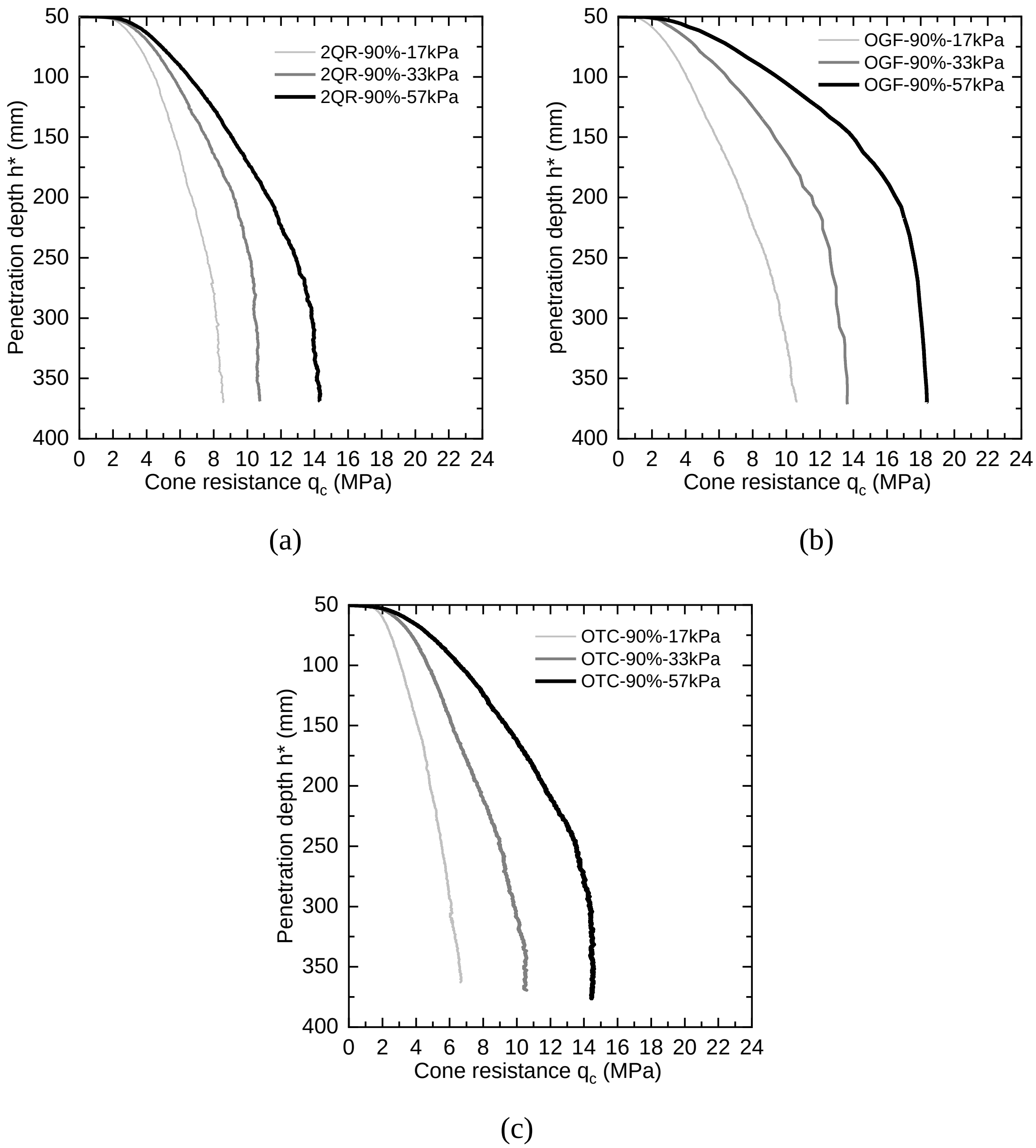

Figure 4.7 Penetration resistance in dense sand samples under vertical pressures of 17 kPa, 33 kPa, and 57 kPa for (a) 2QR sand, (b) OGF sand, (c) OTC sand.

For the penetration experiments performed under the 17 kPa vertical pressure, the OGF had the highest q_c with a value of 10.5 MPa, while the OTC sand had the lowest q_c with a value of 6.5 MPa. The angular 2QR sand has an intermediate q_c value, equal to approximately 8.5 MPa. The comparatively lower values of q_c for OTC sand are expected since OTC has a lower ϕ_c than both OGF and 2QR. As discussed previously, this lower ϕ_c of the OTC is a consequence of its more rounded particles (higher R_{avg}) compared to the 2QR and OGF sands.

Table 4.3 Cone penetration resistance q_c measured at end of penetration for penetration experiments performed in dense (D_R = 90%) samples of 2QR, OGF and OTC sands, under 17 kPa, 33 kPa, and 57 kPa vertical pressure.

Test ID	q_c (MPa)
2QR-90%-17kPa	8.5
2QR-90%-33kPa	11.0
2QR-90%-57kPa	14.5
OGF-90%-17kPa	10.5
OGF -90%-33kPa	13.6
OGF -90%-57kPa	18.5
OTC-90%-17kPa	6.5
OTC -90%-33kPa	10.5
OTC -90%-57kPa	14.5

However, when comparing OGF and 2QR, it can be observed that the OGF and 2QR have relatively similar properties, and yet 2QR has the lower q_c value. For all three vertical pressures, the q_c in the 2QR sand is approximately 80% of the q_c in the OGF sand. This may be explained by the lower $\sigma_{f,avg}$ for 2QR than for OGF. The more angular 2QR sand has weaker particles (see Table 4.1), and, as a result, has lower penetration resistance than the OGF sand.

In the penetration experiments performed under the 33 kPa vertical pressure, a similar trend is observed. The OGF sand has the highest q_c (=13.6 MPa), the OTC sand has the lowest q_c (=10.5

MPa), and the 2QR sand has an intermediate q_c (=11 MPa). However, the q_c for the 2QR sand is only slightly higher than the q_c in the OTC sand. At the 57 kPa vertical pressure, OGF still has the higher q_c (=18.5 MPa) in comparison to the other two sands; however, the q_c for the OTC sand now equals the q_c in the 2QR sand (=14.5 MPa). Therefore, from the q_c data for the narrowly graded test sands, it seems that for a given initial relative density, and a given confinement, the q_c depends on the angularity of the sands (which affects the ϕ_c) and on the strength of the particles ($\sigma_{f,avg}$) that constitute the sand. Under a given level of confinement, a sand with a larger ϕ_c will tend to mobilize a higher q_c (Salgado and Prezzi 2007); however, the mobilized q_c is limited by the crushing of the sand particles. It is known that, when crushing occurs, the sand tends to contract, resulting in a lower tip resistance (Cheng et al. 2004; Vallejo and Lobo-Guerrero 2005; Yao et al. 2008). This may be the reason for the comparable penetration resistances observed for the 2QR and the OTC sand samples at the 57 kPa vertical pressure.

Let us consider the correlation between the measured q_c vs the $\sigma_{f,avg}$ for all three sands under the three different vertical pressures [see Figure 4.8(a)]. For the 2QR and OGF sands–which have similar particle size distributions and similar friction angles (32.5˚ for OGF and 33˚ for 2QR)–we observe an increase in the measured q_c with the increase in the $\sigma_{f,avg}$. Even though the OTC sand has a higher $\sigma_{f,avg}$ than both OGF and 2QR, the measured q_c in it is generally lower than the OGF and 2QR sands because the OTC sand has a lower ϕ_c. However, if we correct the q_c in the OTC sand using the equation proposed by Salgado and Prezzi (2007) by assuming a ϕ_c for OTC comparable to that of OGF and 2QR (33˚), we get a trend that generally shows an increase in the q_c with increasing $\sigma_{f,avg}$ [see Figure 4.8(b)]. This clearly suggests that keeping all other variables the same, the q_c in the sand increases as $\sigma_{f,avg}$ increases.

4.3.2 Particle crushing around cone penetrometer

The penetration resistance data discussed in the previous section can be supplemented with data on the crushing around the cone penetrometer. XCT data from a total of 270 subregions around the penetrometer tip for the 9 cone penetration experiments (30 subregions ever penetration experiment) were analyzed following the procedure outlined in section 4.2.3 to obtain the particle size distributions. These particle size distributions were analyzed further to obtain the relative breakage B_r parameters proposed by Hardin (1985) and Einav (2007).

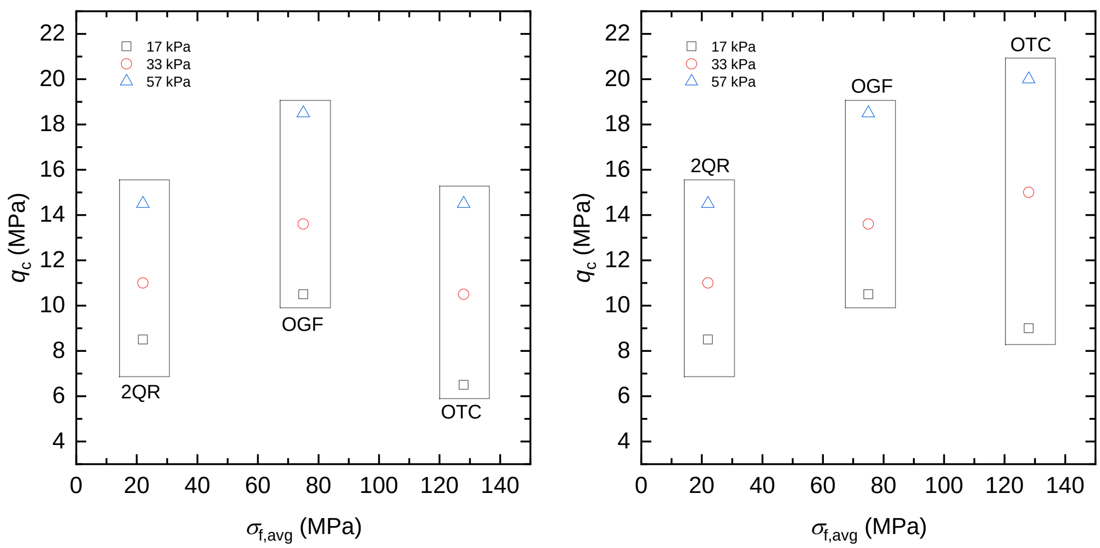

(a) (b)

Figure 4.8 Relation between cone resistance q_c and average fracture stress $\sigma_{f,avg}$: (a) using uncorrected q_c, as measured from the cone penetration experiments, and (b) using q_c for OTC corrected using the equation proposed by Salgado and Prezzi (2007) by assuming ϕ_c for OTC to be comparable (33˚) to that of OGF and 2QR.

Both Einav (2007) and Hardin (1985) define B_r as the ratio of the current breakage B_c to the potential breakage B_p. The current breakage B_c is defined as the area bounded by the current (crushed) particle size distribution and the original (uncrushed) particle size distribution, whereas the potential breakage B_p is defined as the area bounded by the ultimate particle size distribution and the original particle size distribution. All the particle size distributions are plotted on a semi-log graph (with the percentage passing on the linear axis and the particle size on the log axis).

The Einav (2007) and Hardin (1985) parameters differ mainly in the "fully crushed" particle size distribution reference used in their calculations. Hardin (1985) implicitly assumed that the crushing of particles could theoretically continue until the particles have fractured to a size smaller than 0.074 mm (sand-silt boundary). Therefore, a vertical line drawn at 0.074 mm in the particle size distribution may be chosen as the ultimate gradation. However, experimental data (McDowell and Bolton 1998; Sammis et al. 1987) seem to indicate that, for a poorly graded sands, such as the ones used in this research, the particle size distribution after extreme amounts of crushing tends approximately to a fractal distribution (Tsoungui et al. 1999; Turcotte 1986). Based on this observation, Einav (2007) proposed the ultimate particle size distribution as:

$$F_{\mathrm{u}} = \left(\frac{d}{d_{\max}} \right)^{3-\chi} \times 100 \tag{2}$$

where F_{u} is the percentage of the particles, by mass, smaller than the particle size d; $d_{\max}$ is the maximum particle size of the original uncrushed sand; and χ is the fractal dimension. Based on the previous findings of Sammis et al. (1987), Einav (2007) suggested a range of 2.5-2.6 for χ to compute the ultimate particle size distribution. For the B_{r} values calculated following Einav (2007) in this paper, we use χ=2.6 (Ganju et al. 2020b).

In some cases where extreme amount of particle crushing takes place, the largest particle size in the crushed sample may become smaller than that in the original uncrushed particle size distribution. In such cases, an example of which is shown in Figure 4.9 for a subregion close to the penetrometer shoulder in the penetration experiment 2QR-90%-57kPa, the $d_{\max}$ is shifted to the maximum particle size of the current particle size distribution to prevent the ultimate particle size distribution from falling below the current (crushed) particle size distribution. A similar approach was used by Zhang et al. (2013) to obtain the ultimate particle size distribution for sand samples collected around the cone penetrometer with extreme amounts of particle crushing. For the subregions analyzed in this research, this shift of d_{max} was less than 0.1 mm.

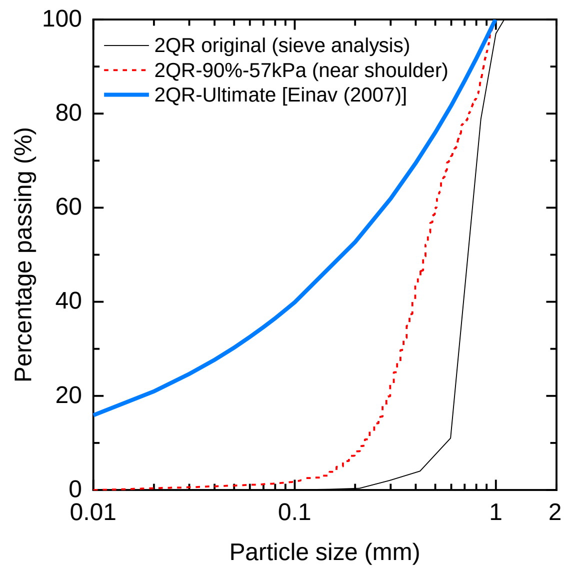

Figure 4.9 Crushing near the shoulder of penetrometer in test 2QR-90%-57kPa: largest particle size d_{max} in the sample reduces as a consequence of large amounts of particle crushing.

For the particle size distribution of a crushed sand sample, usually the Hardin (1985) B_r is smaller than the Einav (2007) B_r. For all the subregions analyzed in this paper, a comparison of the values of the Einav (2007) and Hardin (1985) B_r is shown in Figure 4.10. For penetration experiments with lower q_c values, the Einav (2007) and Hardin (1985) B_r are comparable; however, as the amount of crushing increases in experiments with greater measured q_c, the values of the Einav (2007) B_r become greater than that of the Hardin (1985) B_r. Similar observations on the comparatively higher values of Einav (2007) B_r in comparison to the Hardin (1985) B_r were reported by Einav (2007).

Figure 4.11 to Figure 4.16 show the heatmap of Einav (2007) and Hardin (1985) B_r values around the cone tip for the penetration experiments listed in Table 4.2. Additionally, the average μ and standard deviation σ of the Einav (2007) B_r and Hardin (1985) B_r are shown in Table 4.4 and Table 4.5, respectively. Also shown in Table 4.4 and Table 4.5 are the average μ and standard deviation σ of B_r for each scanned regions around the cone penetrometer (refer to Figure 4.6 for a schematic of the position of scan regions around the cone penetrometer).

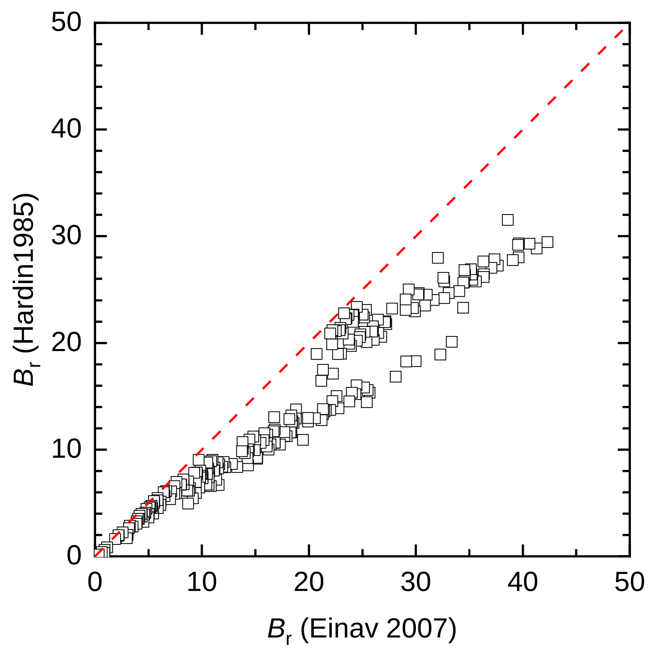

Figure 4.10 Comparison of the values of Einav (2007) and Hardin (1985) B_r for all the subregions analyzed for the penetration experiments listed in Table 4.2.

In Figure 4.11 and Figure 4.12 we show the heatmaps of Einav (2007) and Hardin (1985) B_r around the cone penetrometer for penetration experiments performed in the dense 2QR sand sample. Both the Einav (2007) and Hardin (1985) B_r are the highest for 2QR sand among the three sands tested in this research. This is reasonable since the particles of 2QR sand have the lowest $\sigma_{f,avg}$ (see Table 4.1).

For the penetration experiment performed under the vertical pressure of 17 kPa in the dense 2QR sand sample, the Hardin (1985) B_r values range from 18% to about 24% with an average value of 22% and a standard deviation of 1%. The Hardin (1985) B_r has an average value of 22% and a standard deviation of 1% in the scan region closest to the cone shoulder (see top scan region in Figure 4.6), an average value of 21% and a standard deviation of 1% in the scan region approximately in the middle of cone face (see mid scan region in Figure 4.6), and an average value of 21% and a standard deviation of 1% in the scan region closest to the tip of the penetrometer (see tip scan region in Figure 4.6). On the other hand, the Einav (2007) B_r values range from 20-29%, with an average value of 24% and a standard deviation of 2%. The Einav (2007) B_r has an average value of 24% and a standard deviation of 1% in the top scan region, an average value of 23% and standard deviation of 1% in the mid scan region and an average of 25% and a standard deviation of 2% in the tip scan region.

For the penetration experiments performed under a vertical pressure of 33 kPa in the dense 2QR sample, the Hardin (1985) B_r values range from 18% to 29% with an average of 24% and a standard deviation of 3%.The Hardin (1985) B_r has an average value of 24% and a standard deviation of 3% in the scan region closest to the cone shoulder (see top scan region in Figure 4.6), an average value of 26% and a standard deviation of 3% in the scan region approximately in the middle of cone face (see mid scan region in Figure 4.6), and an average value of 22% and a standard deviation of 3% in the scan region closest to the tip of the penetrometer (see tip scan region in Figure 4.6). On the other hand, the Einav (2007) B_r values range from 21-39%, with an average value of 31% and a standard deviation of 5%. The Einav (2007) B_r has an average value of 31% and a standard deviation of 6% in the top scan region, an average value of 33% and standard deviation of 6% in the mid scan region and an average of 27% and a standard deviation of 4% in the tip scan region.

For the penetration experiments performed under the vertical pressure of 57 kPa in the dense 2QR sample, the Hardin (1985) B_r values range from 19 to 32% with an average of 26% and a standard deviation of 3%. The Hardin (1985) B_r has an average value of 24% and a standard deviation of 4% in the scan region closest to the cone shoulder (see top scan region in Figure 4.6), an average value of 27% and a standard deviation of 2% in the scan region approximately in the middle of cone face (see mid scan region in Figure 4.6), and an average value of 26% and a standard deviation of 3% in the scan region closest to the tip of the penetrometer (see tip scan region in Figure 4.6). On the other hand, the Einav (2007) B_r values range from 22-42%, with an average value of 34% and a standard deviation of 5%. The Einav (2007) B_r has an average value of 32% and a standard deviation of 7% in the top scan region, an average value of 37% and standard deviation of 3% in the mid scan region and an average of 35% and a standard deviation of 3% in the tip scan region.

For the 2QR sand, at each vertical pressure level, the lowest value of B_r generally occurs closer to the conical tip of the penetrometer, whereas the highest B_r values occur approximately 0.5 r_p below the shoulder of the penetrometer, close to the penetrometer surface. Furthermore, the standard deviation of B_r generally increases with increasing crushing around the cone tip, indicating that crushing localizes in certain regions around the penetrometer (this is observable in Figure 4.11 and Figure 4.12). Given that the Einav (2007) and the Hardin (1985) B_r values show similar trends around the cone penetrometer, we limit ourselves in the discussions below to the values of the Einav (2007) B_r values, unless explicitly stated otherwise. Statistics for the Hardin

(1985) B_r around the cone penetrometer can be found in Table 4.5 for all the penetration experiments.

In Figure 4.13 and Figure 4.14, we show the heatmaps of Einav (2007) and Hardin (1985) B_r, respectively, around the cone penetrometer for penetration experiments performed in the dense OGF sand sample under different vertical pressures. Under the vertical pressure of 17 kPa, the Einav (2007) B_r values for OGF range from 6% to about 15% with an average value of 9% and a standard deviation of 2%. Under a vertical pressure of 33 kPa, the B_r values range from 5% to 25% with an average value of 14% and a standard deviation of 6%, whereas under a vertical pressure of 57 kPa, the B_r values range from 6% to 33% with an average value of 19% and a standard deviation of 7%. The values of B_r for OGF sand are lower than those for the 2QR sand at comparable vertical pressure levels; however, from Figure 4.13 and Figure 4.14 we see similar trends of localization of high B_r values near the shoulder of the penetrometer (0.5 r_p below the penetrometer shoulder), close to the penetrometer surface.

Figure 4.15 and Figure 4.16 show the heatmaps of Einav (2007) and Hardin (1985) B_r, respectively, around the cone penetrometer for penetration experiments performed in the dense OTC sand sample under different vertical pressure levels. OTC has the highest $\sigma_{f,avg}$ out of the three sands (see Table 4.1). Consistently with that, values of B_r around the cone penetrometer are lower than the other two sands. For the penetration experiment performed under the vertical pressure of 17 kPa, the Einav (2007) B_r values for OTC range from 0% to about 6%, with an average value of 4% and a standard deviation of 2%. Under a vertical pressure of 33 kPa, the B_r values range from 3% to 19% with an average value of 11% and a standard deviation of 5%, whereas under a vertical pressure of 57 kPa, the B_r values range from 10% to 32% with an average value of 19% and a standard deviation of 6%. The localization of the high B_r values near the penetrometer surface, close to the penetrometer shoulder is also evident here.

From the data, we clearly see that the crushing has considerable spatial variability around the penetrometer tip. Yang et al. (2010), based on sieve/optical analysis of sand samples collected after penetration experiments performed in a cylindrical calibration chamber, suggested three distinct "zones" of crushing around the penetrometer tip (identified as Zone 1, Zone 2, and Zone 3). According to Yang et al. (2010), Zone 1 is the closest to the penetrometer surface with an approximate thickness of 2.4 D_{50}, and it consists mostly of sand which has undergone "extreme" amounts of particle crushing. Zones 2 and 3 are farther away from the penetrometer surface and have comparatively lower amounts of particle crushing. Similarly to Yang et al. (2010), we observe that regions closer to the penetrometer have higher magnitudes of B_r than regions farther away from the penetrometer surface.

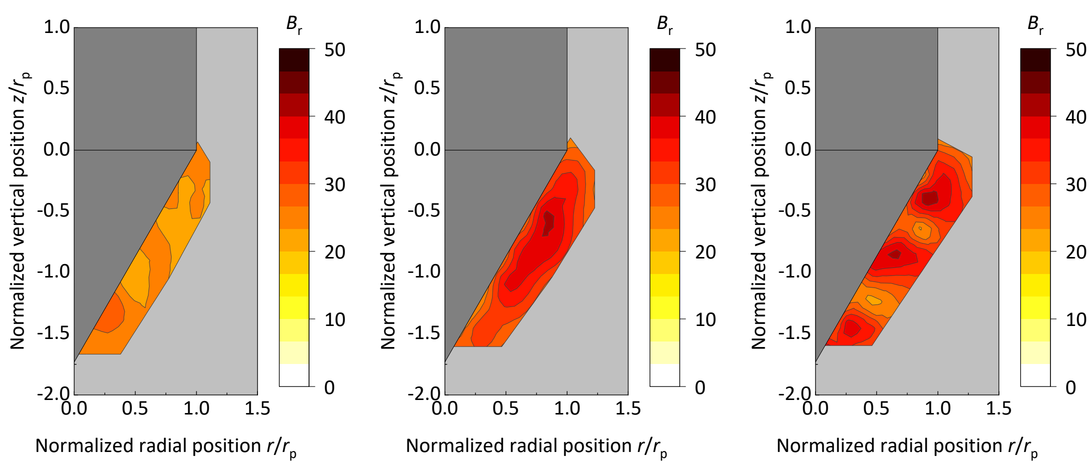

(a) (b) (c)

Figure 4.11 Einav (2007) B_r contours around cone penetrometer for the dense 2QR sand samples at (a) q_c = 8.5 MPa (vertical pressure = 17 kPa), (b) q_c = 11.0 MPa (vertical pressure = 33 kPa), and (c) q_c = 14.5 MPa (vertical pressure = 57 kPa)

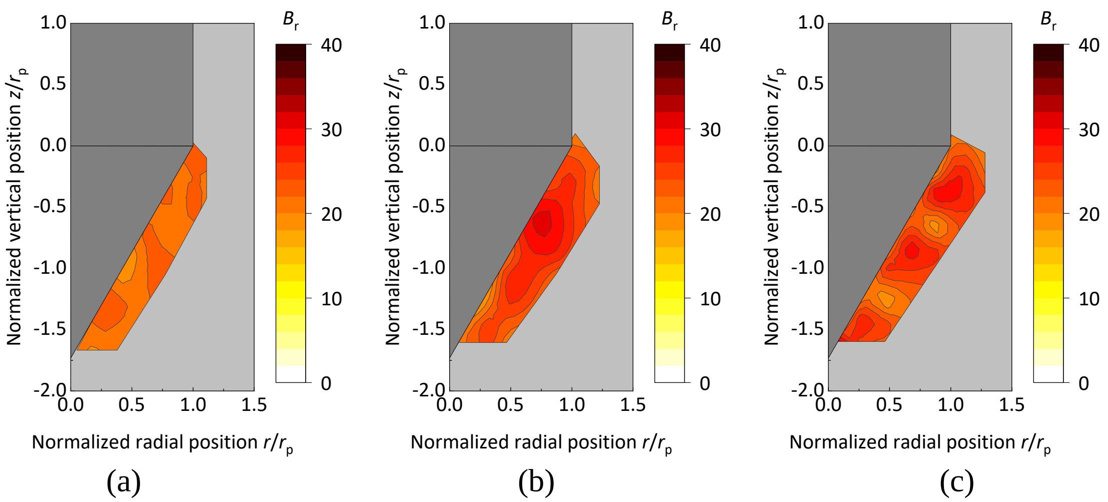

Figure 4.12 Hardin (1985) B_r contours around cone penetrometer for the dense 2QR sand samples at (a) q_c = 8.5 MPa (vertical pressure = 17 kPa), (b) q_c = 11.0 MPa (vertical pressure = 33 kPa), and (c) q_c = 14.5 MPa (vertical pressure = 57 kPa)

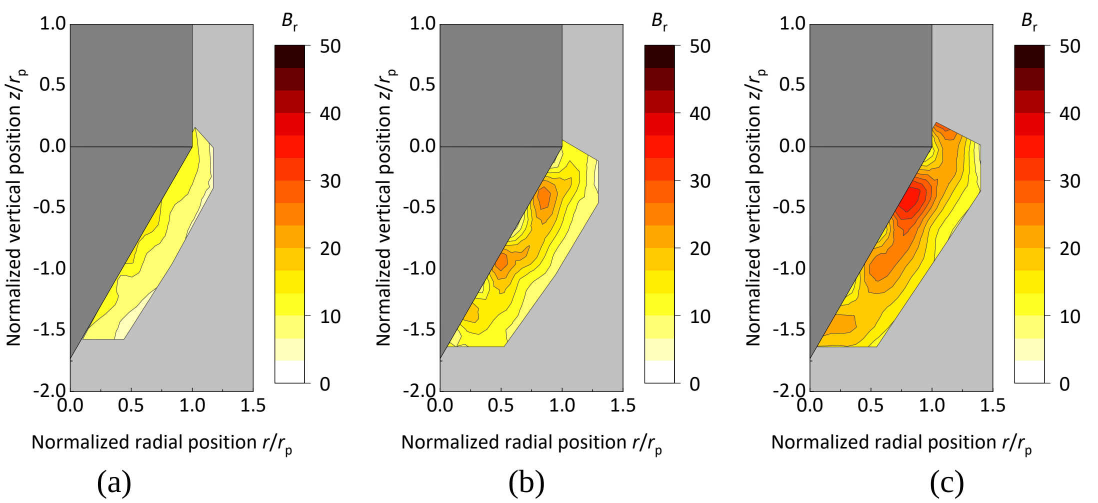

Figure 4.13 Einav (2007) B_r contours around cone penetrometer for the dense OGF sand samples at (a) q_c = 10.5 MPa (vertical pressure = 17 kPa), (b) q_c = 13.6 MPa (vertical pressure = 33 kPa), and (c) q_c = 18.5 MPa (vertical pressure = 57 kPa)

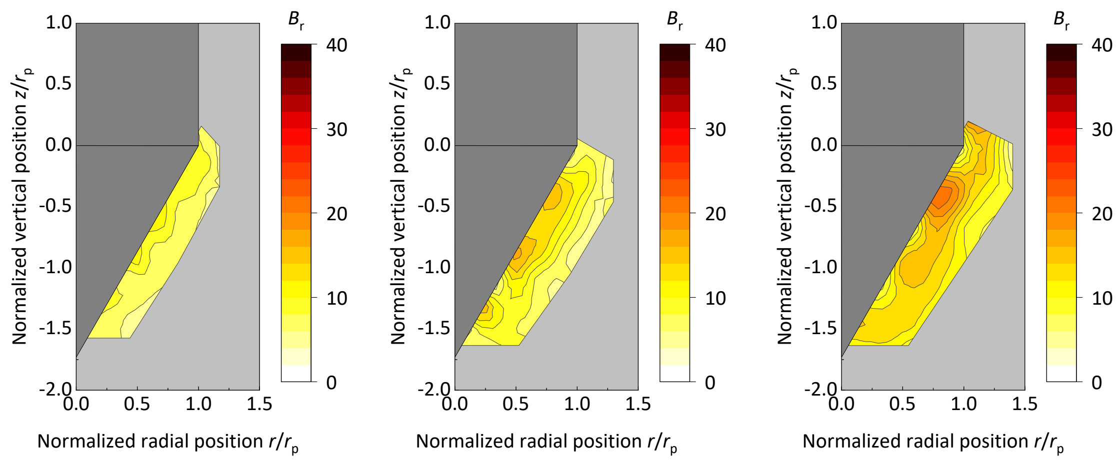

(a) (b) (c)

Figure 4.14 Hardin (1985) B_r contours around cone penetrometer for the dense OGF sand samples at (a) q_c = 10.5 MPa (vertical pressure = 17 kPa), (b) q_c = 13.6 MPa (vertical pressure = 33 kPa), and (c) q_c = 18.5 MPa (vertical pressure = 57 kPa)

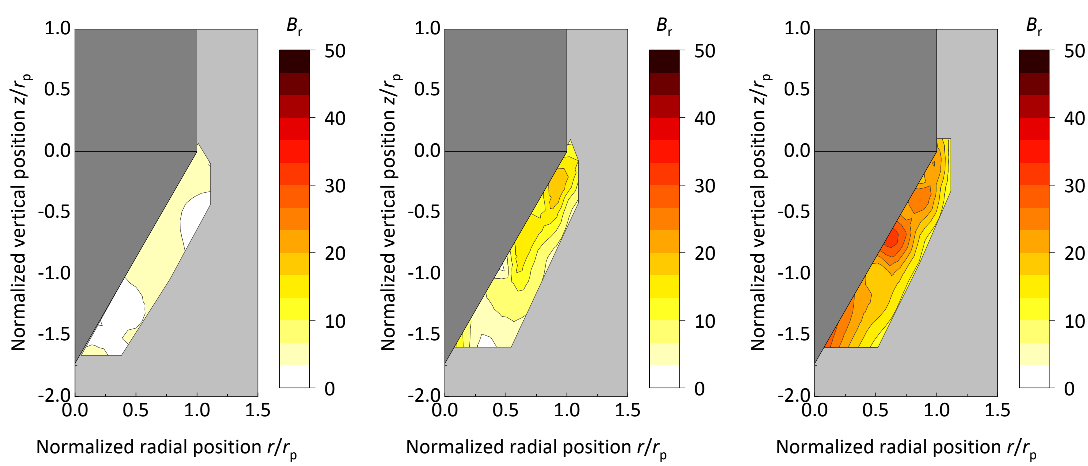

(a) (b) (c)

Figure 4.15 Einav (2007) B_r contours around cone penetrometer for the dense OTC sand samples at (a) q_c = 6.5 MPa (vertical pressure = 17 kPa), (b) q_c = 10.5 MPa (vertical pressure = 33 kPa), and (c) q_c = 14.5 MPa (vertical pressure = 57 kPa)

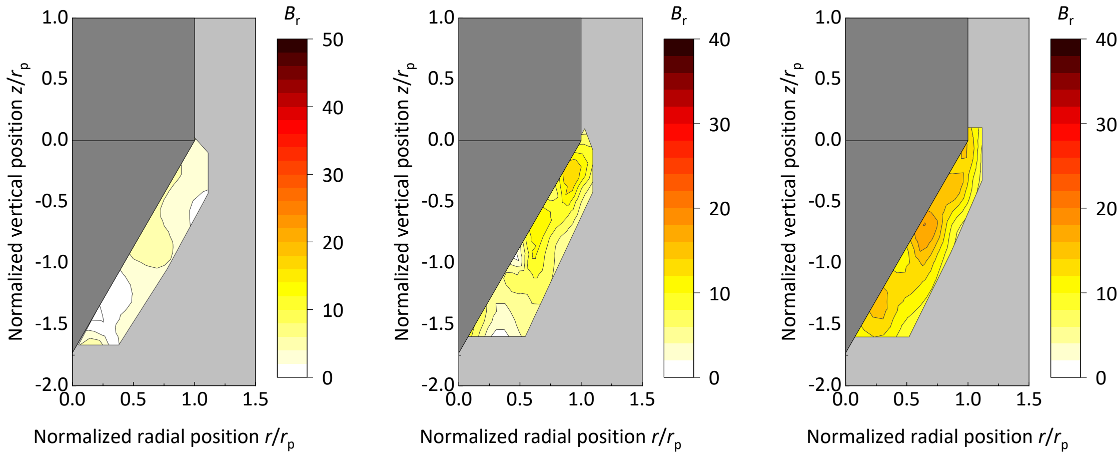

Figure 4.16 Hardin (1985) B_r contours around cone penetrometer for the dense OTC sand samples at (a) q_c = 6.5 MPa (vertical pressure = 17 kPa), (b) q_c = 10.5 MPa (vertical pressure = 33 kPa), and (c) q_c = 14.5 MPa (vertical pressure = 57 kPa)

In Figure 4.17(a), we show the variation of the average Einav (2007) B_r vs. the measured q_c for the nine penetration experiments listed in Table 4.2. We can see from the figure that, for all three sands, the average B_r around the penetrometer increases with increasing q_c. However, the three sands show three different trends. An important question that may be asked at this stage is this: keeping all other parameters the same (relative density, confinement, and sand friction angle), how does q_c vary with sand crushability? To assess the impact of particle crushability on q_c, a comparison of the q_c in sand samples that are similar in all other aspects except the particle strength $\sigma_{f,avg}$ of their constituent particles is needed. The 2QR and OGF sands used in this research meet these requirements, given their similar friction angle, while the OTC sand does not. However, following the discussion in section 4.3.1 and using the updated q_c values for the OTC sand shown in Figure 4.8, we can include the OTC sand in the analysis. In essence, the updated q_c for the OTC sand shown in Figure 4.8(b) would correspond to a sand that has friction angle of 33˚ (similar to the OGF and 2QR sands) and a $\sigma_{f,avg}$ of 128 MPa (higher than the $\sigma_{f,avg}$ of both OGF and 2QR).

Table 4.4 Values of average and standard deviation of Einav (2007) B_r for scan regions around the cone penetrometer for all the penetration experiments listed in Table 4.2 (for scan region locations, refer to Figure 4.6).

ID	All scan regions		Tip scan region		Mid scan region		Top scan region	
	μ	σ	μ	σ	μ	σ	μ	σ
2QR-90%-17kPa	24	2	25	2	23	1	24	1
2QR-90%-33kPa	31	5	27	4	33	6	31	5
2QR-90%-57kPa	34	5	35	3	37	3	32	7
OGF-90%-17kPa	9	2	8	2	11	3	9	3
OGF -90%-33kPa	14	6	13	4	16	6	14	7
OGF -90%-57kPa	19	7	17	4	21	6	18	10
OTC-90%-17kPa	4	2	2	2	5	1	4	1
OTC-90%-33kPa	11	5	7	4	12	3	13	5
OTC-90%-57kPa	19	6	19	5	22	6	18	6

Table 4.5 Values of average and standard deviation of Hardin (1985) B_r for scan regions around the cone penetrometer for all the penetration experiments listed in Table 4.2 (for scan region locations, refer to Figure 4.6).

ID	All scan regions		Tip scan region		Mid scan region		Top scan region	
	μ	σ	μ	σ	μ	σ	μ	σ
2QR-90%-17kPa	22	1	21	1	21	1	22	1
2QR-90%-33kPa	24	3	22	3	26	3	24	3
2QR-90%-57kPa	26	3	26	3	27	2	24	4
OGF-90%-17kPa	7	2	7	1	8	2	7	2
OGF -90%-33kPa	9	4	9	4	10	4	9	4
OGF -90%-57kPa	13	5	13	6	13	3	12	6
OTC-90%-17kPa	3	2	2	2	4	1	3	1
OTC -90%-33kPa	7	3	5	2	9	2	9	3
OTC -90%-57kPa	13	3	12	3	14	5	12	3

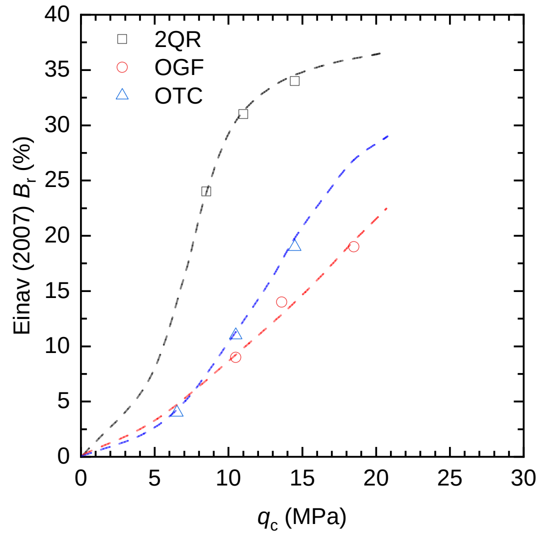

Figure 4.17 Variation of crushing with penetration resistance: correlation between Einav (2007) B_r values and q_c, for cone penetration experiments listed in Table 4.2

In Figure 4.18(a) we show, for the three vertical pressures, the ratio of q_c in the more crushable sands (OGF and 2QR) to the updated q_c in the less crushable sand (OTC sand) plotted against the ratio of the $\sigma_{f,avg}$ of the more crushable sands to the $\sigma_{f,avg}$ of the less crushable sand. In addition, a point is added for a hypothetical sand which has zero $\sigma_{f,avg}$, and therefore a zero value for the q_c ratio, and another point is plotted at (1,1), which corresponds to the reference sand.

From Figure 4.18(a) we can see that the q_c ratio vs $\sigma_{f,avg}$ ratio shows a clear trend. If we exclude the outliers corresponding to the 17 kPa vertical pressure – which we do on the basis that the equations proposed by Salgado and Prezzi (2007) used to update the q_c in the OTC sand were developed for vertical pressure levels starting approximately at 50 kPa–we can see that a power function [represented by the dashed-line in Figure 4.18(b)] accurately captures the relation between the q_c ratio and the $\sigma_{f,avg}$ ratio:

$$\frac{q_{c,\text{more crushable}}}{q_{c,\text{less crushable}}} = \left(\frac{\sigma_{f,\text{avg-more crushable}}}{\sigma_{f,\text{avg-less crushable}}} \right)^{0.18} \tag{4.3}$$

Figure 4.18(b) suggests that all other things (relative density, vertical pressure/penetration depth, and sand friction angle) being equal, q_c in a sand is a function of the $\sigma_{f,avg}$ of the sand.

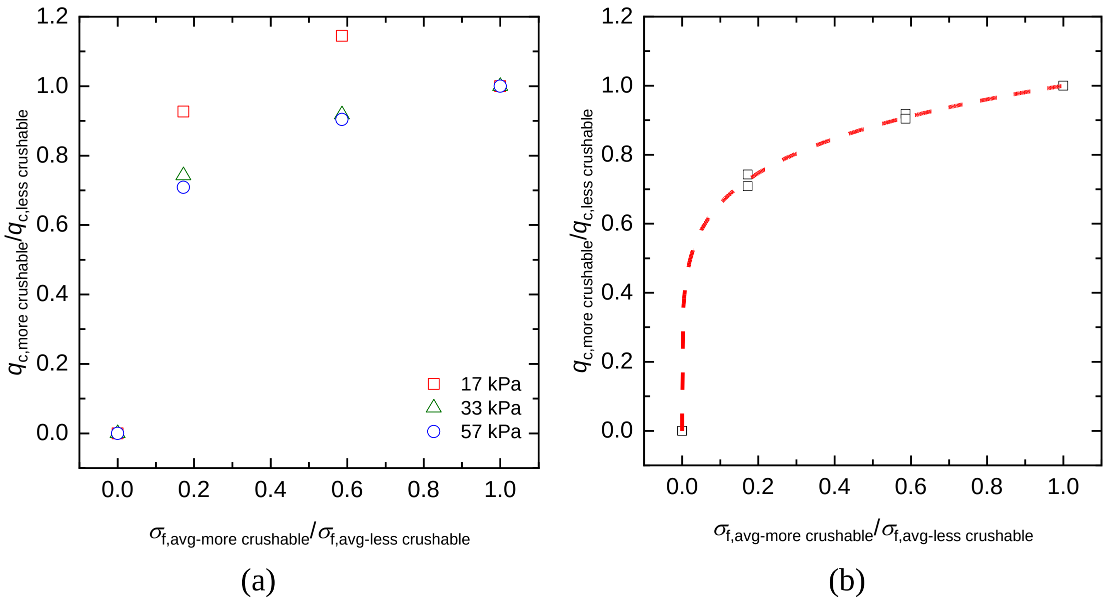

Figure 4.18 Effect of crushability on q_c: (a) for each srucharge level. the ratio of q_c in more crushable sands (OGF and 2QR) to q_c in less crushable sand (OTC) with the ratio of the $\sigma_{f,avg}$ of more crushable sands (OGF and 2QR) to the $\sigma_{f,avg}$ of less crushable sand (OTC) and (b) same plot with outliers removed and trendline added to remaining points

This provides us with an avenue for the development of a framework to compute the ratio of q_c in a more crushable sand to the q_c in a similar less crushable sand. Because the particle strength $\sigma_{f,avg}$ is not easy to measure, we further propose the development of correlations between B_r and $\sigma_{f,avg}$. B_r can be more easily measured, and such a correlation could then be used to obtain $\sigma_{f,avg}$ from uniaxial compression testing. For the three sands used in this research, an example of such a correlation is shown in Figure 4.19, which shows the variation of B_r with $\sigma_{f,avg}$ for dense samples of the three sands loaded to a stress level of 30 MPa. The data shown in Figure 4.19 was taken from Chapter 2.

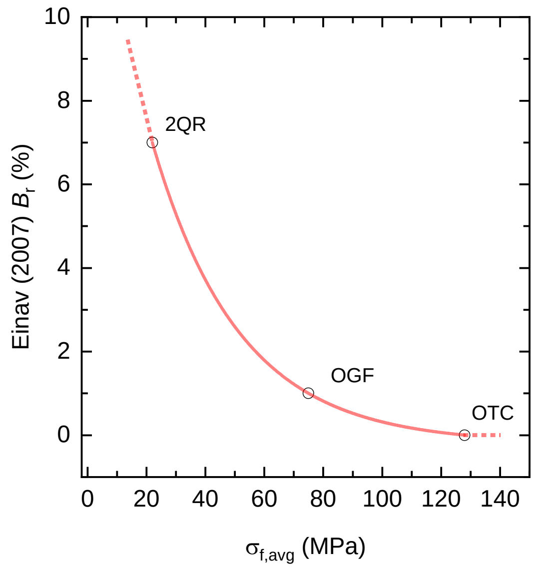

Figure 4.19 Variation of Einav (2007) B_r with the $\sigma_{f,avg}$ for dense samples of OTC, OGF and 2QR sand samples loaded under 1D compression to a stress level of 30 MPa

In Figure 4.20 we show the outline of the potential framework to obtain ratio of q_c in more crushable sand to the q_c in a less crushable sand. Within such a framework, a sample of the sand prepared at a fixed D_R would first be loaded under uniaxial compression to a fixed stress level [Figure 4.20(a)] and then from sieve analysis of the loaded samples, the B_r would be obtained [Figure 4.20(b)]. We propose a D_R of 90% as sand samples prepared at a higher D_R tend to be more homogenous than samples prepared at lower D_R. Furthermore, the stress level to which the sample is loaded may tentatively be fixed at 30MPa, since, for most silica sands, non-zero values of B_r can be achieved at a stress level of 30 MPa; this threshold may be refined with further testing. Using the B_r and correlations between the B_r and $\sigma_{f,avg}$ (such as the one shown in Figure 4.19) and an estimate of the $\sigma_{f,avg}$ of the sand will then be computed [Figure 4.20(c)]. This estimate of the $\sigma_{f,avg}$ will be used in correlations between the q_c ratio and $\sigma_{f,avg}$ ratio to obtain the ratio of the q_c in the more crushable sand to the q_c in the less crushable sand. This framework can be adapted, with sufficient data, to a CPT interpretation correlation such as that proposed by Salgado and Prezzi (2007).

Given the distribution of crushing around the cone penetrometer, another question that emerges is why does crushing localize at specific points around the cone penetrometer? The literature suggests that the magnitude of crushing in a given sand is affected by the mean stress and shear strain that the sand experiences (Cheng et al. 2003; Coop et al. 2004; Coop and Lee 1993; Ganju et al. 2020b; Hanley et al. 2015; Miao and Airey 2013). A larger mean stress results in higher interparticle contact forces, which lead to more severe particle crushing (Hardin 1985; Lade et al. 1996; Xiao et al. 2017), whereas shearing of the sand samples at a constant stress level results in occurrence of transient peaks in the inter-particle contact forces, which weakens the particles and also results in particle crushing (Coop et al. 2004; Hanley et al. 2015). The cone penetration process generates both large mean stresses and large shear stresses in the soil next to the cone, hence the significant crushing observed.

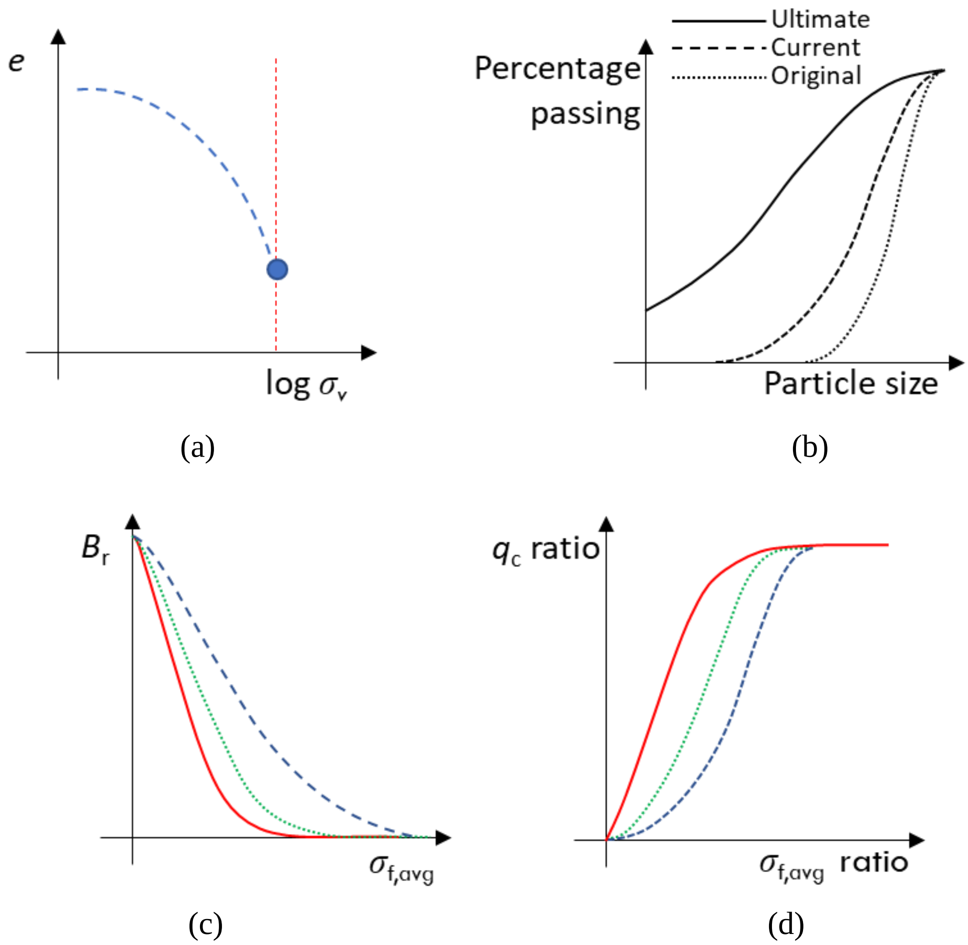

Figure 4.20 Potential framework to obtain the ratio of q_c in more crushable sands to q_c in less crushable sands: (a) load dense sample of the sand to a predetermined stress level under uniaxial compression, (b) perform particle size analysis of the sample loaded under uniaxial compression to obtain relative breakage B_r value, (c) use pre-established correlations between relative breakage B_r and average particle fracture stress $\sigma_{f,avg}$ to obtain an estimate of $\sigma_{f,avg}$, and (d) use the computed $\sigma_{f,avg}$ and pre-established correlation between ratio of q_c in more crushable sand to q_c in less crushable sand (q_c ratio) and the ratio of $\sigma_{f,avg}$ of more crushable sand to $\sigma_{f,avg}$ of less crushable sand ($\sigma_{f,avg}$ ratio) to obtain the ratio of q_c in more crushable sands to q_c in less crushable sands.

4.3.3 Strain fields around cone penetrometer

DIC analysis of the images collected during the penetration process provides us with the displacement fields that develop around the cone penetrometer. The DIC analyses were performed for a 2 mm penetration increment of the cone penetrometer at a penetration depth of about 380 mm for each of the nine penetration experiments listed in Table 4.2.

For each penetration experiment listed in Table 4.2, the sequence of images collected during the experiment was analyzed using DIC, one pair at a time, in the order in which they were captured. For each image pair, the movement of small square areas (termed "subsets") was tracked from the first image to the second image in the image pair. This was done by comparing the grey-level pixel intensity of the subset in the first image (reference subset) with the grey-level pixel intensities of multiple subsets in the second image. The best match was identified using the normalized sum of squared differences criterion for matching subsets because it can more efficiently handle minor changes in lighting conditions between the first and second images than other available methods (Arshad et al. 2014).

After finding the best-matching subset (the optimal subset) in the second image, the displacement of the reference subset was calculated as the difference in the positions of the centers of the optimum and the reference subsets. The procedure was repeated for multiple subsets (separated by a fixed center-to-center distance) to get the displacement field in the soil domain. For the DIC analyses, we used the commercial software VIC-2D® (Correlated Solutions, Irmo, South Carolina).

The displacement fields obtained from the DIC analysis were further analyzed to obtain the strain fields in the soil domain. Given that crushing depends on the shear strain and the mean stress in the sand, we focus on the heatmaps of the incremental maximum shear strain and the incremental volumetric strains dE_{vol} (which serves as a proxy for the mean stress in the soil domain) around the cone penetrometer.

In Figure 4.21, Figure 4.22, and Figure 4.23, we show the heatmaps of dE_{max} in the soil domain for the penetration experiments performed in the dense 2QR, OGF and OTC sands, respectively, under different vertical pressure levels. From these figures, we can see that for the penetration experiments performed in all three sands, the highest values of dE_{max} localize in a region closer to the penetrometer surface, approximately 0.5 r_{p} below the shoulder of the penetrometer. Furthermore, at higher vertical pressures, the region around the penetrometer with d$E_{\mathrm{max}} \geq 5\%$ increases. These regions of high dE_{max} coincide with the regions of high B_{r} values shown in the previous section.

These observations are consistent with previous experience: high shear strains lead to transient peaks in the inter-particle contact forces, which in turn can lead to particle crushing (Coop et al. 2004; Hanley et al. 2015). White and Bolton (2004) performed penetration experiments using a flat-ended penetrometer in a plane-strain calibration chamber and visually observed significant amount of particle crushing in similar regions right below the penetrometer tip, where a conical mechanism incorporating shear bands was identified; however, measurements of changes in particle size distribution were not reported.

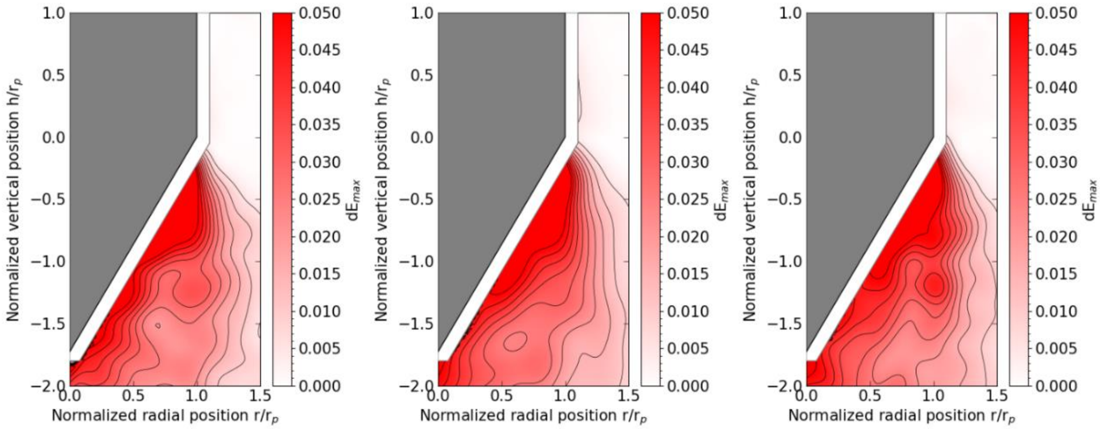

(a) (b) (c)

Figure 4.21 Incremental max shear strain contours around cone penetrometer for the dense 2QR sand samples at (a) 17 kPa, (b) 33 kPa, and (c) 57 kPa vertical pressures.

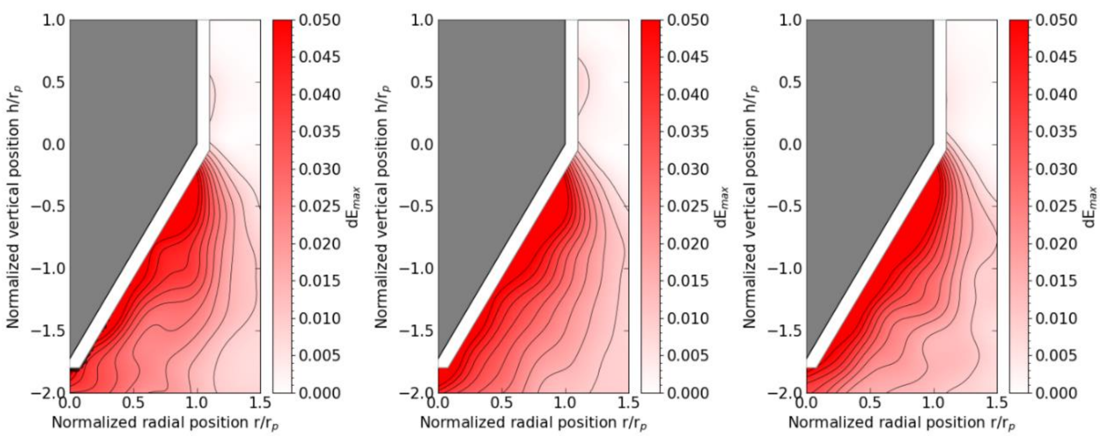

(a) (b) (c)

Figure 4.22 Incremental max shear strain contours around cone penetrometer for the dense OGF sand samples at (a) 17 kPa, (b) 33 kPa, and (c) 57 kPa vertical pressures.

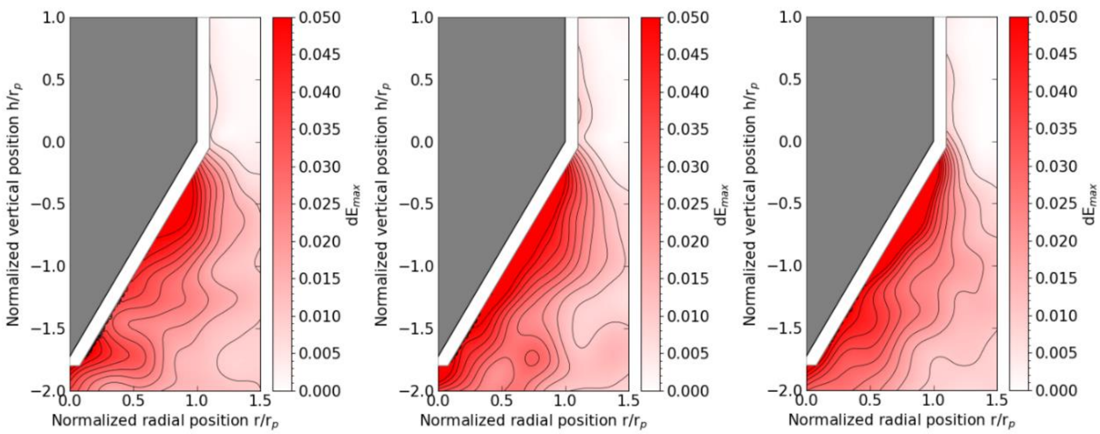

(a) (b) (c)

Figure 4.23 Incremental max shear strain contours around cone penetrometer for the dense OTC sand samples at (a) 17 kPa, (b) 33 kPa, and (c) 57 kPa vertical pressures.

In Figure 4.24, Figure 4.25, and Figure 4.26, we show the heatmaps of the incremental volumetric strain dE_{vol} in the soil domain for the penetration experiments performed in the dense 2QR, OGF and OTC sands, respectively, under the three different vertical pressure. The incremental volumetric strains are computed following the procedure outlined by Tehrani et al. (2018). Solid mechanics sign convention is followed: volumetric strains are positive for dilation and negative for contraction.

When dense sands are sheared, they tend to dilate; however, dilation is limited by crushing of the sand particles. Therefore, for a given level of confinement, sands with stronger particles, which are more resistant to crushing, will dilate more than sands with weaker particles, which are less resistant to crushing. From the DIC analysis, when crushing takes place in the soil, it appears as volumetric contraction. Note that contraction can also occur due to particle rearrangement due to slippage at the interparticle contacts with minimal crushing (Mesri and Vardhanabhuti 2009a); however, given that these are dense sands, with very limited void space, contraction caused by particle crushing is more prevalent.

Figure 4.24 through Figure 4.26 shows that the regions of sand undergoing contraction are located close to the surface of the penetrometer, near the penetrometer shoulder, while regions farther away from the penetrometer tend to undergo dilation. Similar observations regarding the relative positions of contractive and dilative zones around the penetrometer have been made by Paniagua et al. (2013) using 3D DIC analysis of XCT scans for penetrometer pushed into an unsaturated silt. Furthermore, the regions undergoing contraction are similarly positioned around the penetrometer as the regions where we see large B_r values in the sand.

From the dE_{vol} contours in the dense 2QR sand, shown in Figure 4.24, we observe that a larger region of the soil domain around the penetrometer tip is undergoing volumetric contraction, in contrast to the dE_{vol} contours of the OGF and OTC sands, for which the regions of contraction localize closer to the penetrometer shoulder and closer to the inclined face of the penetrometer. This more "diffused" volumetric contraction for the 2QR sand is reflected in the B_r contours shown in Figure 4.12 to Figure 4.16; the B_r contours of the 2QR sand are much more diffused than the B_r contours of the OGF and OTC sand. This alternating pattern of volumetric contraction and dilation in the dense 2QR sand suggests that the sand tend to dilate where particles can sustain the contact stresses; however, in regions where the stresses exceed the particle strengths, contraction takes place. Furthermore, comparing Figure 4.24 through Figure 4.26 to Figure 4.12 through Figure 4.16 we can see that, to some extent, regions of high B_r around the cone penetrometer tip can be approximately identified by the contours of the dE_{vol} (at least for the cone penetration experiments performed in dense sand samples).

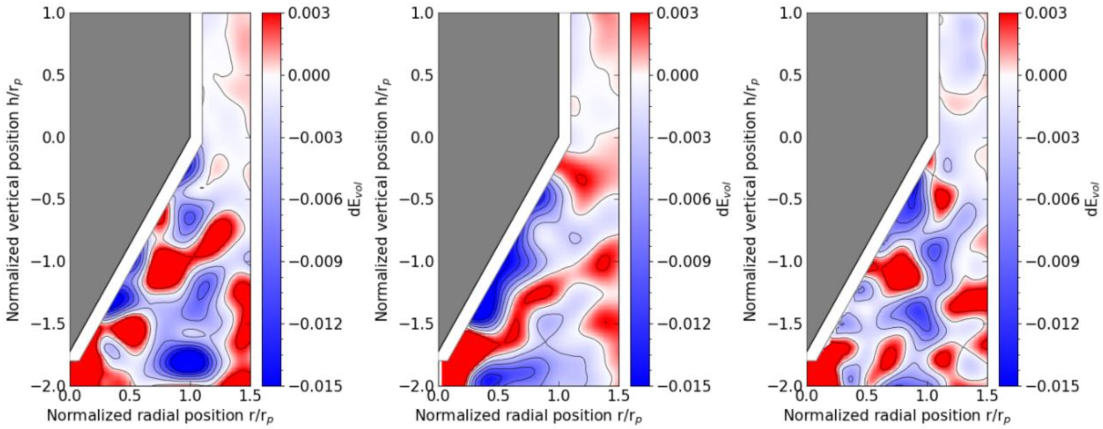

(a) (b) (c)

Figure 4.24 Incremental volumetric strain contours around cone penetrometer for the dense 2QR sand samples at (a) 17 kPa, (b) 33 kPa, and (c) 57 kPa vertical pressures.

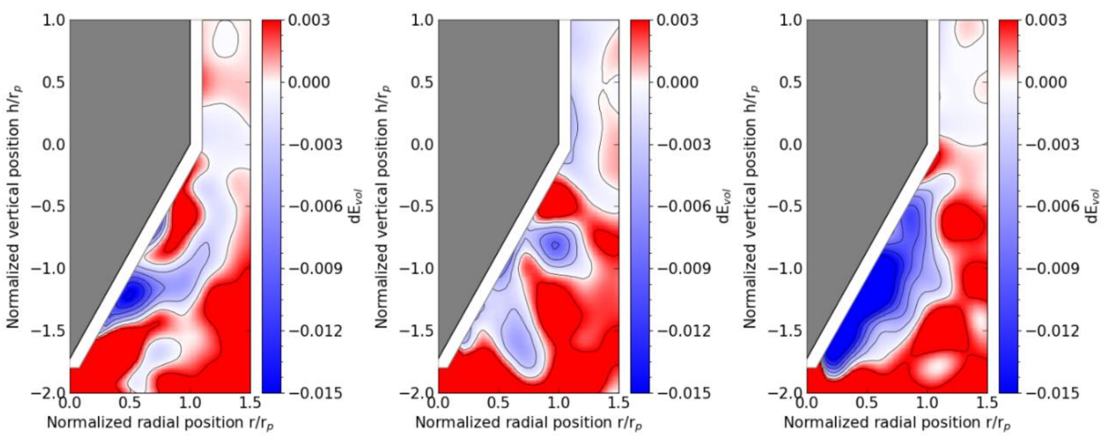

(a) (b) (c)

Figure 4.25 Incremental volumetric strain contours around cone penetrometer for the dense OGF sand samples at (a) 17 kPa, (b) 33 kPa, and (c) 57 kPa vertical pressures.

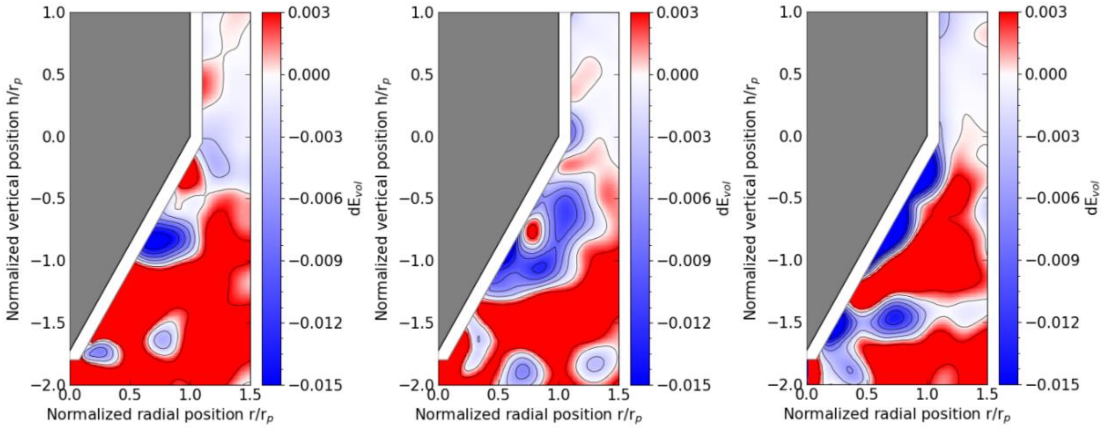

(a) (b) (c)

Figure 4.26 Incremental volumetric strain contours around cone penetrometer for the dense OTC sand samples at (a) 17 kPa, (b) 33 kPa, and (c) 57 kPa vertical pressures.

4.4 Conclusions

In this chapter, we provide data on the crushing of sand particles around the cone penetrometer. Cone penetration experiments were performed in dense samples of three silica sands under different surcharge levels in a half-cylindrical calibration chamber equipped with observation windows. During the penetration experiments, a sequence of images of the sand and penetrometer were captured using digital cameras placed in front of the observation windows. These images were later analyzed using DIC to obtain displacement and strain fields in the soil domain. After the penetration experiments, a novel agar-impregnation technique was used to collected minimally disturbed sand samples from around the penetrometer tip. The agar-impregnated sand samples were scanned in an X-ray Microscope to obtain 3D tomography data of the sand particles. The 3D tomography data were further analyzed to obtain particle size distributions and B_r values around the cone penetrometer. Furthermore, a potential framework was proposed to obtain the ratio of q_c in more crushable sands to q_c in less crushable sands.

The main findings from this research are summarized below:

(1) For a given initial relative density, and a given vertical pressure, q_c depends on the angularity of the sands and on the strength of the particles that constitute the sand.

(2) More angular sands tend to mobilize a higher q_c; however, the mobilized q_c is limited by the crushing of the sand particles.

(3) Keeping all other parameters (relative density, confinement, and sand friction angle) equal, the q_c in a sand is a function of the $\sigma_{f,avg}$ of the sand.

(4) For a given sample density, the amount of crushing around the cone penetrometer depends on the confinement and the morphological characteristics of the sand particles.

(5) The level of crushing is not uniform around the penetrometer tip: high B_r values tends to localize around the penetrometer closer to the surface of the penetrometer at approximately 0.5 r_p below the shoulder of the penetrometer.

(6) The regions with high B_r values around the cone penetrometer roughly overlap with regions of high dE_{max} and high dE_{vol}.

These results highlight the link between particle characteristics or "intrinsic" soil properties [in the sense of (Salgado et al. 1997b)] and penetration resistance. As clearly shown from the data in this paper, under a fixed vertical confinement, the penetration resistance not only depends on the particle friction angle but also on the particle crushing strengths. Sands with more angular particles may have a higher initial ϕ_c, however, under large mean stress and shear strains that develop around the cone penetrometer, these sands undergo crushing more readily, resulting in a lower penetration resistance. Therefore, estimation of soil intrinsic variables, including measures of particle crushability, will need to be added to CPT interpretation frameworks and pile design methods. The data in this paper is unique in the sense that it combines the potent techniques of

DIC and XCT to obtain not only the displacement and strain fields around the penetrometer, but also the distribution of particle crushing in the zone of influence around the cone. This data may potentially be useful to researchers working on multiscale modeling of penetration processes in sands.

5 QUANTIFICATION OF SAND FABRIC AROUND CONE PENETROMETER

This chapter will be submitted as a paper to a peer-reviewed journal.

5.1 Introduction

The fabric of a sand is defined by the arrangement of its particles and particle contacts within a sand mass (Mitchell and Soga 2005). According to Oda (1977), the fabric of the sand mass can be quantified in three main ways: (1) based on the distribution of the orientation of the major principal axis of the particles in the sand mass; (2) based on the 3D distribution of the orientation of the contact normal between arbitrary pairs of contacting particles; and (3) based on the distribution of the coordination number (number of interparticle contacts per particle).

For soils with non-spherical particles, such as silts or clays, quantification of fabric using the orientation of major principal axis of the particles is a reasonable approach. This approach has been used in the literature with some level of success (Fonseca et al. 2013; Paniagua et al. 2018; Tovey and Dadey 2002; Wilkinson 2011); however, for soils with more spherical, bulky particles, such as the sand used in the current research, this approach of using the orientation of the major principal axis of the particle is not optimal. Furthermore, the link between the orientation of interparticle contacts and the orientation of force chains in the soil make the choice of interparticle contacts as sample fabric descriptors more appealing (Fonseca et al. 2016). Therefore, we define fabric here as determined from the orientations of interparticle contacts within the sand sample.

Experimental studies have shown that fabric plays a major role in the mechanical behavior of sands (Kuwano and Jardine 2002; Murthy et al. 2007; Vaid and Sivathayalan 2000; Zlatovic and Ishihara 1997); however, due to the elusive nature of the fabric descriptors discussed above, accurate quantification of fabric has been–and continues to be–very challenging. Due to the difficulty in the assessment of fabric descriptors, many research studies in the past have inferred the change in sand fabric from macroscopic observations, such as the anisotropy of small-strain stiffness (Kuwano and Jardine 2002), and the dependence of material response on sample preparation method (Murthy et al. 2007; Vaid and Sivathayalan 2000; Zlatovic and Ishihara 1997). Research studies that focus on the direct measurements of fabric descriptors include those involving the loading of photo-elastic soil analogues (Oda et al. 1985; Oda and Konishi 1974), and, more recently, the analysis of 3D tomography data obtained from X-ray computed tomography (XCT) scans (Alam et al. 2018; Fonseca et al. 2013, 2016; Ganju et al. 2021; Wiebicke et al. 2020).

Oda and Konishi (1974) and Oda et al. (1985) were among the first to quantify the interparticle contact normal orientations in granular materials. They quantified the interparticle contact normal orientations using experiments carried out on transparent photo-elastic disks loaded under simple shear and biaxial loading conditions. Their findings indicated that, upon loading, the interparticle contact normals tend to orient in the direction of the major (compressive) principal stress increment, leading to a rise in interparticle contact normal anisotropy. In Chapter 2 we observed a similar rise in interparticle contact anisotropy; however, we also reported that this rise in contact anisotropy is limited by the crushing of the sand particles at higher stresses.

Fonseca et al. (2013) carried out multiple triaxial compression experiments on dense samples of Reigate sand, and injected epoxy resin into the sand samples at different stages of the compression experiments. The resin-impregnated sand samples were scanned using an XCT scanner to obtain the 3D tomography data of the sand. Based on the analysis of the interparticle contact normal orientations in the 3D tomography data, Fonseca et al. (2013) reported that the interparticle contact normals (both inside and outside the shear band) reoriented themselves in the direction of loading. Fonseca et al. (2013) further added that the contact normals of the large and stable contacts (as evidenced by their contact area) became parallel to the major (compressive) principal stress direction, confirming the findings of Oda and Konishi (1974) and Oda et al. (1985). Fonseca et al. (2016) extended further the findings of Fonseca et al. (2013) and reported that only 40 – 50% of the particles in the sample contribute to the force chains that support the applied loads.

Wiebicke et al. (2020) carried out *in situ* XCT scans of sand samples (Houston sand and Caicos ooids) as they were being loaded in a triaxial compression apparatus. From the analysis of the 3D tomography data obtained from the XCT scans, they investigated the evolution of interparticle contact orientations inside and outside the shear bands. Wiebicke et al. (2020) reported that the interparticle contact normals become more anisotropic and tend to align with the principal stress direction as loading progresses. After the start of shear localization in the sample, the contact density (distribution of coordination numbers) stabilizes outside the shear band; however, inside the shear band, the contact density decreases (as a result of reduction in void ratio caused by the sand dilation). With further loading, the interparticle contact anisotropy inside the shear band increases, reaches a peak, and then drops to a stable, steady state, and the interparticle contact normals inside the shear band align closely with the applied principal stress direction.

The research studies presented so far have shed significant light on fabric evolution in sands loaded under different loading conditions; however, these studies have mainly focused on the quantification of fabric in the sand sample in elemental loading experiments. In this paper, we investigate the evolution of interparticle contact normal orientations around a cone penetrometer advancing in a dense sand sample. We focus on a penetration experiment carried out in a dense air-pluviated sample of the Ottawa 20-30 (OTC) sand, under a vertical pressure of 33 kPa. The penetration experiment was performed in a half-cylindrical calibration chamber equipped with

Digital Image Correlation (DIC) capabilities. After the penetration experiments, a resin-impregnation technique was used to collect an undisturbed sand sample from around the penetrometer tip. The resin-impregnated sand sample was scanned in 5 different regions along the penetrometer tip using an X-ray Microscope (XRM) to obtain 3D tomography data of the sand. The 3D tomography data was analyzed to obtain the distribution of interparticle contact normal orientations around the cone penetrometer. The data on the distribution of interparticle contact normals is supplemented with data on the incremental displacement and strain fields around the penetrometer, obtained from DIC analysis of images collected during the penetration experiment.

5.2 Materials and methods

5.2.1 Test sand

The Ottawa 20-30 (OTC) sand was used in the penetration experiment carried out for this research. The OTC sand is a subrounded sand commonly employed as a reference sand in experimental geomechanics (ASTM C778-17 2017). Table 5.1 presents the index properties of the OTC sand. The OTC sand has a D_{50} of approximately 0.72 mm, a critical-state friction angle of 29.3˚, and an average Wadell (1935) roundness R_{avg} and average sphericity S_{avg} (breadth-to-length ratio) of 0.74 and 0.79, respectively. The particles of the OTC sand are very strong due to their high R_{avg} and the existence of minimal internal defects (Ganju et al. 2021; Druckrey 2016; Druckrey and Alshibli 2016). As a result, the OTC sand particles have an average fracture strength $\sigma_{f,avg}$ of 127.57 MPa (see Chapter 2). The distribution of fracture stresses for the OTC sand follows the Weibull (1951) distribution with σ^* value of 143.61 MPa (stress at which 37% of the loaded particles survive crushing) and Weibull (1951) modulus m of 2.82. Further details of the particle characteristics of the OTC sand can be found in Chapter 2.

Table 5.1 Properties of Ottawa 20-30 (OTC) sand used in the penetration experiment

Sand	D_{50}	C_U	C_C	USCS	S_{avg}	R_{avg}	e_{min}	e_{max}	$\sigma_{f,avg}$	σ^*	m	ϕ_c
OTC	0.72	1.4	1	SP	0.79	0.74	0.50	0.75	127.57	143.61	2.82	29.3

D_{50} is the particle size for which 50% of the particles by weight are smaller in size as obtained from sieve analysis following ASTM D6913-17 (2017); C_U and C_C are the coefficients of uniformity and curvature, respectively, for the particle size distribution curve obtain from sieve analysis; USCS is the type of the soil according type the unified soil classification system (ASTM D2487-17 2006) and SP stands for poorly graded sand; emin and emax are the minimum and maximum void ratios, respectively, determined following ASTM D4254-16 (2016); S_{avg} and R_{avg} are the average sphericity (aspect ratio) and Wadell (1932) roundness morphology parameters for the test sand obtained using the MATLAB code by Zheng and Hryciw (2015); $\sigma_{f,avg}$ is the average fracture stress of individual particles obtained using single particle uniaxial compression experiments; σ^* and m are the Weibull (1951) fitting parameters for the single particle crushing experiments; ϕ_c is the internal critical-state friction angle of the sand obtained from drained triaxial compression experiments.

5.2.2 Half cylindrical calibration chamber and cone penetrometer

For the penetration experiment, a dense air-pluviated sample of the OTC sand was prepared inside a half-cylindrical calibration chamber equipped with DIC capabilities. Figure 5.1 shows a labeled image of the calibration chamber, which is 1.68 m in diameter and has a height of 1.2 m. The dense OTC sand sample was prepared by air pluviation using a custom pluviator and diffuser sieve arrangement, which allowed us to control of the rate of particle deposition (controlling the sample density) and helped us ensure sample homogeneity (Lee 2008; Lee et al. 2011; Miura and Toki 1982; Rad and Tumay 1987; Vaid and Negussey 1984). As the sand was pluviated into the calibration chamber, we placed small cylindrical samplers inside the chamber at three levels to allow the determination of the local *in situ* density. The samplers revealed that the sand sample was homogenous, with a relative density D_R of 90% ± 5%.

As can be seen from Figure 5.1, the calibration chamber is equipped on its flat vertical surface with observation windows, which allow us to collect digital images of the sand and penetrometer during the penetration experiment. The observation windows are made of a 76-mm-thick (3 in) Polymethyl methacrylate (PMMA) sheet reinforced with metal supports that restrict the deflection of the windows during the penetration experiments. The metal supports limit the maximum deformation of the observation windows to less than 0.0945 mm for experiments performed under a similar vertical pressure as that used in the current experiment (Arshad 2014). Thus, issues with observation window deformability are not present in this experiment. Further details of the calibration chamber and the air-pluviation setup are discussed by Arshad (2014), Arshad et al. (2014) and Tehrani et al. (2018).

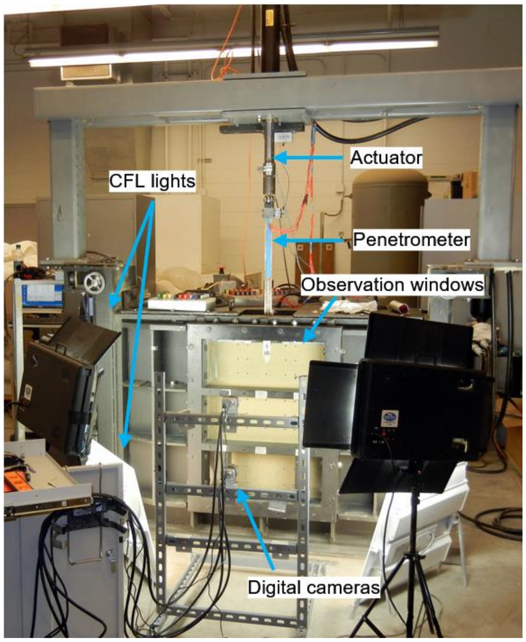

Figure 5.1 Labeled image showing the half-cylindrical calibration chamber with observation windows, the half-cylindrical penetrometer, the hydraulic actuator system used to push the penetrometer in the sand sample, and the digital cameras and illumination lights placed in front of the observation windows to collect digital images of the sand and penetrometer during the penetration process.

After the sand sample was prepared, the surface of the sand was flattened, and a vertical surcharge was applied using a pressure-plate assembly. The initial vertical pressure in the sand at the final penetrometer depth was measured directly using a contact pressure cell (Model No. 4800, GEOKON, New Hampshire, USA) placed in the sand sample. For the surcharge level used in this research, the initial vertical pressure in the sand at the final penetrometer depth was equal to 33 kPa.

Approximately 15 minutes after the application of the surcharge, the penetration experiment was carried out by pushing a special half-cylindrical Aluminum penetrometer into the dense sand sample at a steady penetration rate of 1mm/s using a high-precision hydraulic actuator system connected to the head of the penetrometer using a moment-break assembly. The cone penetrometer was pushed to a final embedment depth of approximately 380 mm (measured from the shoulder of the penetrometer to the sand surface). During the penetration experiment, images of the cone and the penetromer were captured using 12-megapixel CMOS cameras (Model No. beA4000-62km, Basler, Ahrensburg, Germany) placed in front of the observation windows. These images were later analyzed using DIC to obtain the incremental displacement and strain fields around the cone penetrometer.

Figure 5.2 presents a schematic of the cone penetrometer used for the penetration experiment. The penetrometer is a half-cylindrical solid Aluminum rod, approximately 762 mm in length, with an outer diameter of 38 mm and a 60˚ conical tip. Aluminum was chosen to make the penetrometer to facilitate X-ray imaging of the resin-impregnated sand sample with the penetrometer tip. The flat surface of the penetrometer is recessed by 3.2 mm to allow attachment of six plastic tubes (3 mm in diameter). These tubes are used to carry epoxy resin from the top of the penetrometer (which is accessible to us at all times) to the tip of the penetrometer (which is inaccessible at the end of penetration). The plastic tubes near the penetrometer tip bend away from the flat surface of the penetrometer and terminate at the penetrometer's curved surface, which is in contact with the sand. The six tubes do not extend beyond the curved surface of the penetrometer and therefore, they do not impede the flow of the sand around the penetrometer in any manner. Furthermore, prior to the penetration experiment, we insert flexible copper wires into each plastic tube, essentially blocking the plastic tubes to any sand ingress during the penetration experiment.

As can be seen in Figure 5.2, the penetrometer is designed in such a manner that the tip of the penetrometer is detachable from the upper part of the penetrometer. This allows us to re-use the upper part of the penetrometer with a new tip for future experiments. The design of the penetrometer and the arrangement of the tubes allow us to inject the epoxy resin into the sand without excavating the sand or removing the vertical confinement, minimizing disturbance of the fabric of the sand sample.

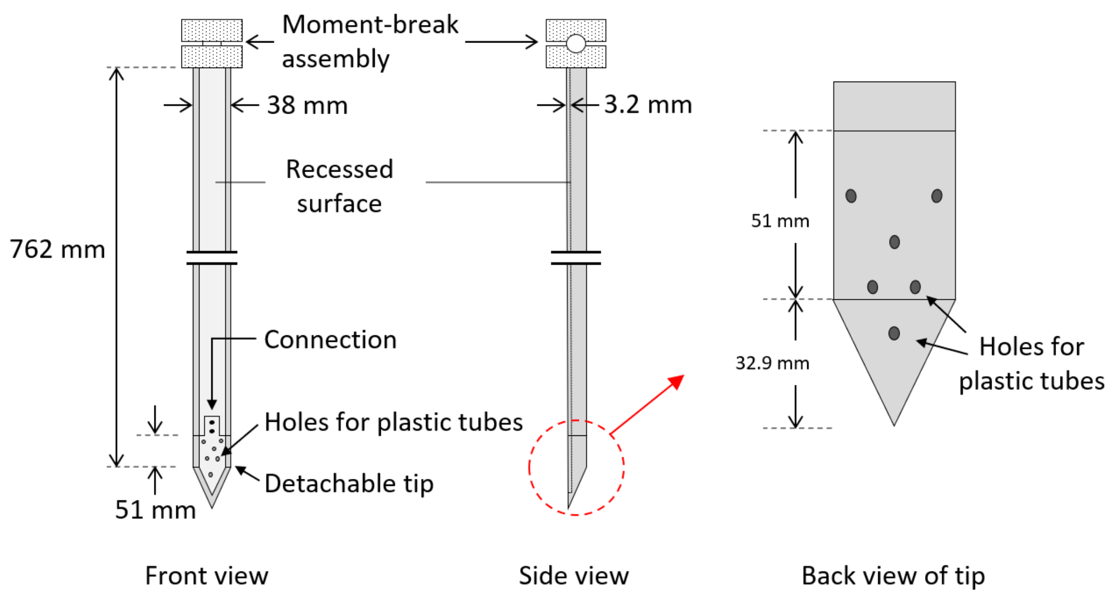

Figure 5.2 Schematic of the front and side view of the half-cylindrical penetrometer with the detachable tip, showing the dimensions of the penetrometer, and the holes and recessed inner surface for placement of plastic tubes.

After the penetration experiment was completed, and the tip was at the desired penetration depth (approximately 380 mm), the vertical confinement was maintained at 33 kPa at the level of the penetrometer tip and the copper wires blocking the plastic tubes were removed. Then a low-viscosity epoxy resin was slowly injected into the upper ends of the six plastic tubes using tapered plastic syringes. The epoxy resin used was EPOTEK 301 (EPOXY Technology, Billerica, MA), which is a two-part cold-setting epoxy resin.

EPOTEK 301 has been successfully used in previous research studies involving collection of sand samples (Doreau-Malioche et al. 2019; Fonseca et al. 2012; Palmer and Barton 1986). It has ideal properties for collection of sand samples: it has low viscosity (100 cP at 25˚C) and cures at room temperature. The curing time is approximately 12 hours, which allows the resin enough time to permeate the sand and cover a sufficient volume around the penetrometer. Additionally, the X-ray attenuation coefficient (Als-Nielsen and McMorrow 2011) of the epoxy resin is lower than that of sand; hence, it can be distinguished from the silica particles in X-ray scans.

After injecting the epoxy resin near the penetrometer tip, we allowed it to cure for a period of about 15 hours. During the curing time, the vertical pressure at the level of the penetrometer tip was maintained and the sand and penetrometer were tracked using DIC. No sand or penetrometer movement was observed over the period of 15 hours. Finally, at the end of the 15 hours, the confinement was removed, the sand was excavated to the level of the penetrometer tip, the tip of the penetrometer was detached from the rest of the penetrometer, and the resin-impregnated sand sample (along with the penetrometer tip) was retrieved. The entire resin sample was approximately 35 cm in length and was trimmed to a smaller size to ensure that it would fit inside the X-ray Microscope (XRM). Figure 5.3 shows images of the front and side views of the trimmed resin-impregnated sample, with annotations showing its dimensions.

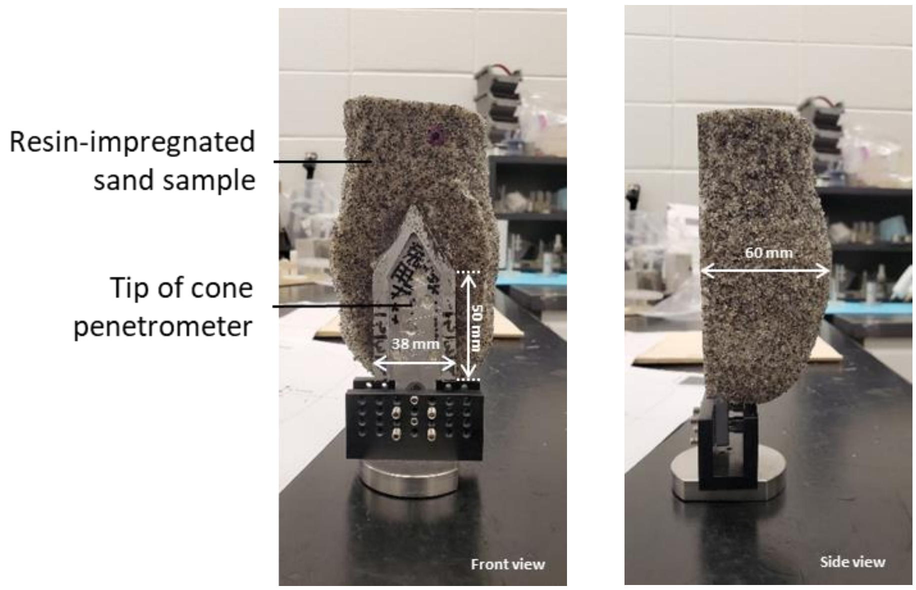

Figure 5.3 Front and side view of the trimmed resin-impregnated sand sample collected after penetration experiment was carried out in dense OTC sand under a vertical confinement of 33 kPa.

5.2.3 X-ray computed Tomography (XCT) scans

The trimmed resin-impregnated sand sample was scanned in an X-ray Microscope (XRM) (Model No. VERSA-510, Zeiss, Pleasanton, CA). The sample was scanned in five regions located around the cone penetrometer. Each of the five scan regions were cylindrical in shape, approximately 12.5 mm in diameter and 12.5 mm in height. The scans were carried out at a resolution of 0.012 mm/voxel, which corresponds to 60 voxels across the average particle diameter for the OTC sand (D_{50} = 0.72 mm). From previous experience and recommendations available in the literature (Wiebicke et al. 2019), this resolution was deemed high enough for us to capture the particle size and fabric around the cone penetrometer with reasonable accuracy. The five scan regions were positioned in such a manner so as to capture the evolution of the fabric around the cone. Figure 5.4 shows a schematic of a vertical cross-section of the resin-impregnated sand sample with the locations of the five scan regions around the cone penetrometer clearly marked.

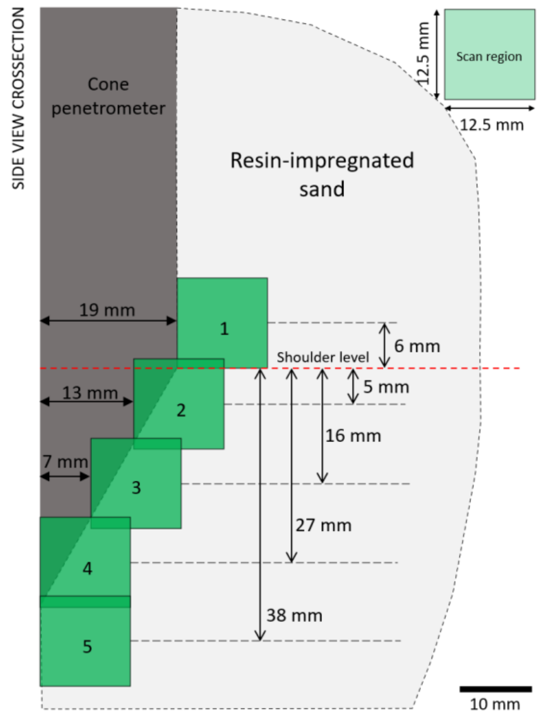

Figure 5.4 Schematic of the vertical cross-section of the resin-impregnated sand sample showing the locations of the scan regions around the cone penetrometer.

From Figure 5.4 we can see that the first scan region is located immediately above the shoulder of the penetrometer (the shoulder being the point where the inclined face of the penetrometer meets the vertical shaft of the penetrometer). The left edge of the first scan region is positioned right next to the penetrometer shaft, and the center of the scan region is approximately 6 mm above the shoulder of the penetrometer. The second scan region captures the sand around the shoulder of the penetrometer. This scan region is located below the first scan region; its left edge is 13 mm from the centerline of the penetrometer, and its center 5 mm below the shoulder. The third scan region is located roughly in the middle of the inclined face of the penetrometer, with the scan region's left edge approximately 7 mm from the centerline of the penetrometer, and its center 16 mm below the shoulder. The fourth scan region captures the sand near the tip of the penetrometer. The center of this scan region is located 27 mm below the cone shoulder, and the left edge of the scan region is at the centerline of the penetrometer. The last scan region captures the sand below the penetrometer tip. This subregion is located right below the fourth subregion, at a vertical distance of 38 mm below the shoulder of the penetrometer.

From within these scan regions, we extracted multiple cubical subregions of size $6D_{50}$ and analyzed the data from these subregions to obtain the orientation of interparticle contact normals. The subregion size of $6D_{50}$ was chosen based on the findings of the parametric study reported in Chapter 2. The subregions were analyzed following a similar procedure as that discussed in Chapter 2, and the analysis procedure is only briefly discussed below.

Due to the presence of the aluminum cone, some random noise was observed in the 3D tomography data. Therefore, first the 3D tomography data of the subregions were filtered using a non-local means filter (Buades et al. 2005) with a patch size of 5 pixels and a search size of 7 pixels. The non-local means filter is commonly used to filter 3D tomography data of granular materials such as sands because it prevents the erosion of particle edges, which are critical for assessing the interparticle contact orientations (Alam et al. 2018). After the filtration process, the data was binarized using the widely used binarization method proposed by Otsu (1979). After binarization, the Euclidean distance maps EDMs of the binarized XCT data were computed. Then the local maxima of the EDMs were identified and taken as starting points for the watershed segmentation algorithm (Beucher and Lantuejoul 1979). The segmented XCT data were checked for any over segmentation errors, and the over-segmented particles were merged following the procedure outlined in Chapter 2. Finally, any particles with volume smaller than 1000 voxels^3 were removed. This was done as the size and contact of any particle smaller than 10 voxels cannot be accurately captured (Wiebicke et al. 2017). Removal of the small particles resulted in only a 1% loss in solid volume for all the subregions analyzed. After these steps were taken, the segmented

XCT data were analyzed using the random walker algorithm [implemented in *spam* (Stamati et al. 2020)] to obtain the orientations of the interparticle contact normals around the cone penetrometer.

5.3 Results and discussions

5.3.1 Penetration resistance

Figure 5.5 presents a plot of cone resistance q_c vs. penetration depth z for the cone penetration experiment carried out in a dense (D_R = 90 %) sample of OTC sand under the vertical pressure of 33 kPa. The penetration experiment was started with the cone at a pre-embedment depth of 50 mm–this allows minimization of sand intrusion between the penetrometer and the observation window by ensuring good contact between the flat surface of the penetrometer and the observation window. This is the reason why the q_c vs. z plot shown in Figure 5.5 starts from 50 mm instead of 0 mm. The penetration was carried out at a rate of 1 mm/s to a final embedment depth of approximately 380 mm. The penetration resistance measured at the 380 mm penetration depth was approximately 10.5 MPa.

5.3.2 Fabric around cone penetrometer

From the 3D tomography data of the sand sample collected from the XCT scans, five representative subregions were selected to assess the orientations of the interparticle contact normals. Figure 5.6 presents the location of these subregions around the cone penetrometer, and Table 5.2 presents the normalized vertical distance (h/r_p) and the normalized radial distance (r/r_p) of these subregions with respect to the shoulder of the penetrometer and the centerline of the penetrometer, respectively. The radial distance r and vertical distance h are normalized by the radius r_p of the cone penetrometer (=19 mm). It is important to note that the five subregions chosen for analyses are located behind the penetrometer, instead of at the sand-glass interface; this is done to exclude any effect of the rigid boundary of the observation windows on the fabric of the sand.

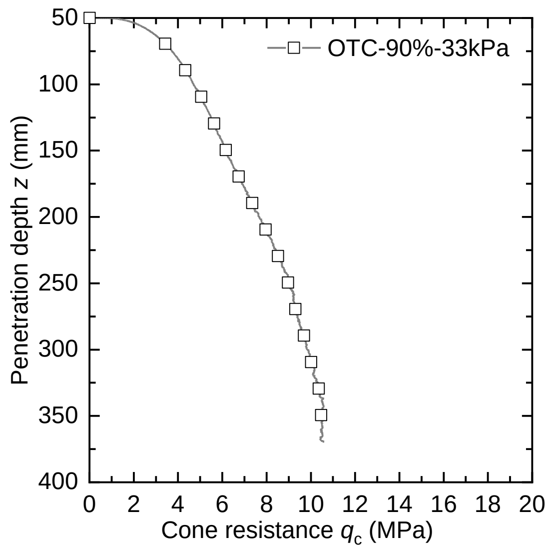

Figure 5.5 Plot of cone resistance q_c vs. the penetration depth z for the cone penetration experiment carried out in a dense (D_R = 90 %) sample of the Ottawa 20-30 (OTC) sand under a vertical confinement of 33 kPa.

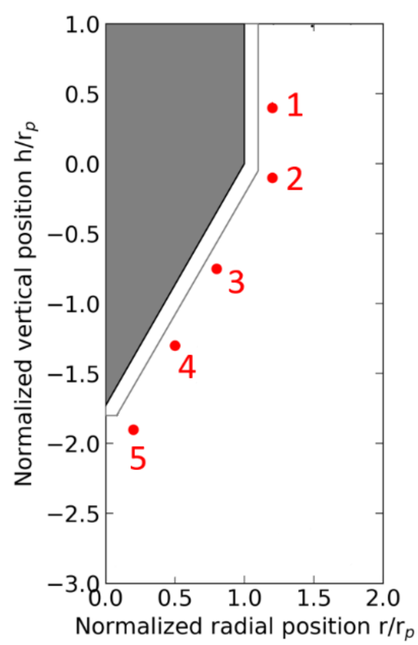

Figure 5.6 Location of five subregions around the cone penetrometer where the orientations of the interparticle contact normals were analyzed.

Table 5.2 Normalized vertical distance (h/r_p) and the normalized radial distance (r/r_p) of points with respect to the shoulder of the penetrometer and the centerline of the penetrometer.

Subregion ID	Normalized radial distance from center of penetrometer (r/r_p)	Normalized distance from shoulder of penetrometer (h/r_p)
1	1.20	0.40
2	1.20	-0.10
3	0.80	-0.75
4	0.50	-1.30
5	0.20	-1.90

Note: radial distances r moving away from the centerline of the cone penetrometer are positive; vertical distances h moving upwards from the shoulder of the penetrometer are positive; the distances are normalized by the radius r_p of the cone penetrometer (=19 mm).

The locations shown in Figure 5.6 and Table 5.2 were selected to highlight interesting features of interparticle contact normal orientations around the penetrometer and to help us visualize how the interparticle contact orientations evolve as the penetrometer advances through the sand. The subregion #1 is located right above the cone shoulder, subregion #2 is located right below the cone shoulder, subregion #3 is located at a third of the distance from the shoulder to the cone tip, subregion #4 is located at two-thirds the distance from the shoulder to the cone tip, and subregion #5 is located right below the cone tip. The analysis of the 3D tomography data from these subregions allows us to see how the interparticle contact orientations near the tip evolve as the penetrometer advances in the sand sample.

5.3.2.1 Interparticle contact normals and area of contacts

Fonseca et al. (2013) and Fonseca et al. (2016) have indicated that, as a sand sample is loaded, the force chains that develop in the sand mass tend to orient themselves towards the direction of loading, and that the force chains that develop tend to consist of larger particles. These larger particles have larger interparticle contact areas, which provide a stable support for transfer of loads. Therefore, if we want to assess the orientation of "force chains" in the sample, we should not include all the contacts in the sample in our analysis because not all contacts are involved in the "force network." Ideally, we would like to visualize the distribution of contacts that carry the largest loads; however, since we do not have measurement of interparticle contract forces, we instead need to rely on the contact areas corresponding to the contact normals to assess the orientation of the force chains in the sample. The reasoning for this is that normals corresponding to contacts with larger areas in the sample have a higher probability of belonging to a stable force chain; what constitutes a large or a small contact area within a sand sample will depend on the particle size and particle morphology.

To identify the interparticle contact normal orientations and to compute the interparticle contact areas, we use the *spam* code (Stamati et al. 2020). To identify particle contacts, we use the random walker RW method implemented in *spam*. Among the contact normal estimation methods available in literature, the RW method has been shown to produce the least error (Wiebicke et al. 2017, 2019, 2020b; a). For each contacting pair of particles, the RW method identifies particle contacts by locating the points in space by interpolation where the probability of belonging to either one of two particles in contact is 50%. The algorithm then fits a plane through all the points identified, and the normal to the fitted plane is taken as the contact normal for the two contacting particles. To calculate the area of the contact for each particle pair, *spam* dilates one of the particles in the pair and checks which voxels of the dilated particle overlap with the voxels of the undilated particle in the pair. The area is then calculated as the number of overlapping voxels multiplied by the area of the voxel face (10^{-4} mm^2).

In Figure 5.7 we present the interparticle contact area vs. the particle size for the five subregions around the cone penetrometer computed using *spam*. The interparticle contact areas in the 5 subregions around the cone penetrometer range from 10^{-4} mm^2 (lower threshold for area) to 0.07 mm^2. This range of interparticle contact areas agrees reasonably with the interparticle contact areas reported by Fonseca et al. (2016) for similarly sized sands. The average interparticle contact areas in the five subregions range from 0.012 mm^2 (for the subregion #5 located below the tip of the penetrometer) to 0.008 mm^2 (for the subregion #3 located 0.75 r_p below the shoulder of the penetrometer). In Chapter 4 we reported that for a penetration experiment carried out under similar conditions as those presented in this paper, the maximum crushing in the OTC sand is observed in the region approximately 0.5-1.0 r_p below shoulder of the penetrometer close to the penetrometer surface–in the same location as subregion #3 in the present study. This may explain, to some extent, the lower average interparticle contact area observed in the subregion #3 compared to other subregions.

Since each particle is in contact with multiple other particles, it has multiple interparticle contact areas associated with it. In general, the average interparticle contact area increases with the increase in particle size (as indicated by the dotted line for each subregion in Figure 5.7); however, as can be seen from the Figure 5.7, all particles, including the larger particles in the sample, tend to have some contacts with small contact areas. These contacts with smaller areas may not be contributing to the force network as described by Fonseca et al. (2013, 2016). Therefore, to assess the effect the area of contact has on the distribution of interparticle contact orientations around the cone penetrometer, it will be useful to investigate how the distribution of interparticle contact normals changes as we progressively remove contacts with the smallest contact areas from the distribution.

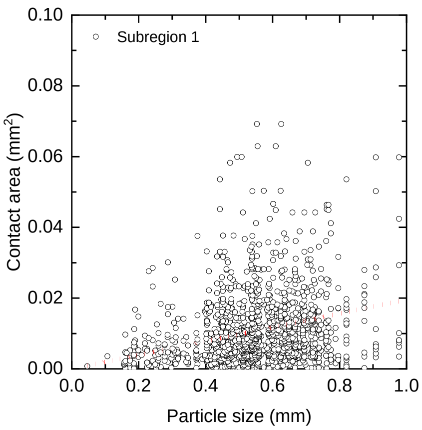

(a)

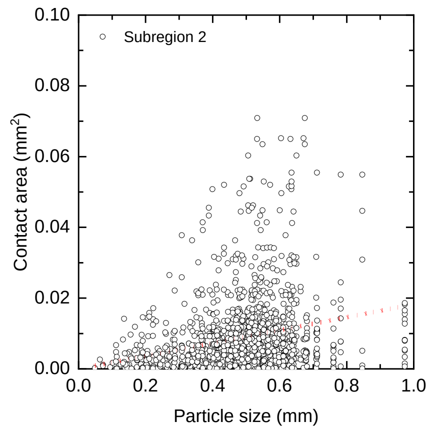

(b)

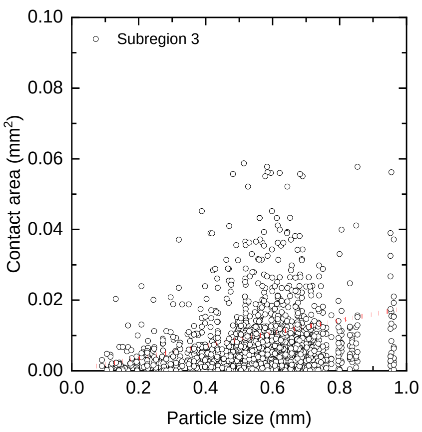

(c)

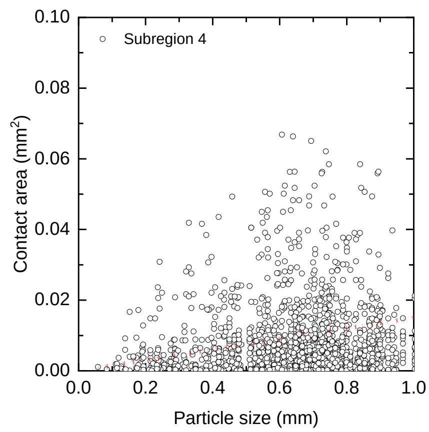

(d)

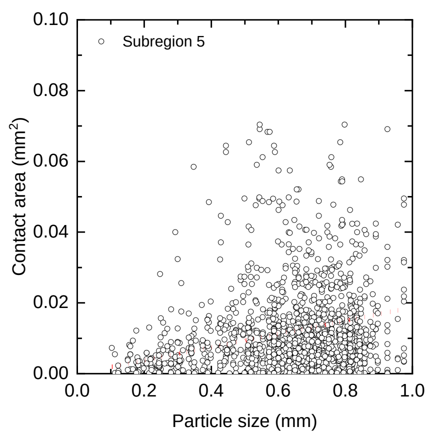

(d)

Figure 5.7 Interparticle contact area vs. particle size for the five subregions around the cone penetrometer presented in Figure 5.6 and Table 5.2 with dotted line showing a linear fit.

We use Rose diagrams to visualize the frequency of the orientations of the interparticle contact normals in the sand domain. Rose diagrams are generally used to show the distribution of 3D vectors projected on to a specific plane, which in our case is the vertical plane passing through the centerline of the penetrometer, perpendicular to the observation windows. Each contact normal is represented by a unit vector in space. To plot the Rose diagram, the contact vectors are put in bins (with a bin size of 15˚) and the percentages of contacts in each bin are computed. In Figure 5.8, we show how the contact normal orientations are presented in the Rose diagram by using as example three imaginary particle contacts around the penetrometer, identified using numbers 1, 2 and 3. The three contact normals we consider here are assumed to be contained in the vertical plane. The three contact normals make angles of 110˚(contact #1), 140˚ (contact #2), and 180˚ (contact #3), measured counterclockwise from the axis X pointing radially outwards from the centerline of the penetrometer. Since in the example shown in Figure 5.8 we only have three contacts, each bin has 33.3% of the contacts. Following this approach, we can obtain the distribution of contact normals for each of the five cubical subregions (shown in Figure 5.6) around the penetrometer. It should be noted that unlike the example shown in Figure 5.8, most interparticle contact normals do not exist in the vertical plane; for contact normals not in the vertical place, the projections of those contact normals on the vertical plane are used to plot the rose diagrams.

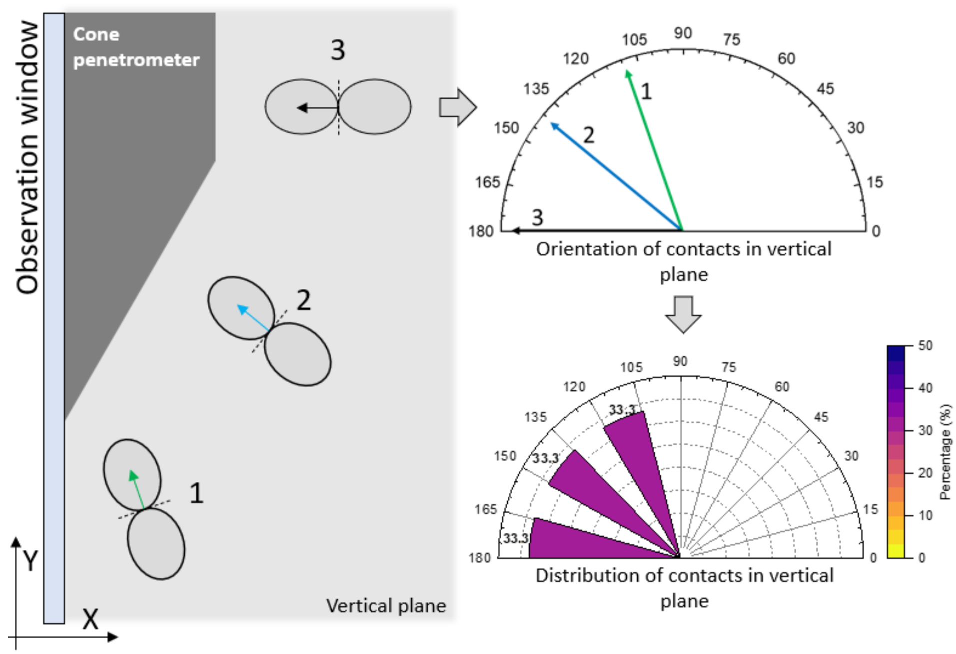

Figure 5.8 Plotting of Rose diagrams of interparticle contact normals orientations around the cone penetrometer: schematic showing the Rose diagrams of three imaginary contacts in the vertical plane passing through the centerline of the penetrometer, perpendicular to the observation window.

In Figure 5.9(a), we present the distribution of interparticle contact normal orientations for all the contacts within the subregion #1. This subregion is located slightly above the shoulder of the cone penetrometer (see Figure 5.6 and Table 5.2). The distribution presented in Figure 5.9(a) includes all the interparticle contacts in the subregion. From Figure 5.9(a) it can be seen that the contact normals appear to be uniformly distributed. 51% of the contact normals lie between 90˚ and 180˚, whereas 49% lie in the 0 to 90. Therefore, in this Rose diagram, it is not obvious if the contact normals have any clear directional bias.

In Figure 5.9(b) we show the distribution of contact normals excluding 10% of the contacts with the smallest contact areas. Exclusion of 10% of the contacts with the smallest areas results in a 2% increase in the percentage of the contact vectors in the 135˚-165˚ range; however, this is not a significant increase. With 10% of the smallest contacts excluded, 53% of the remaining contacts are oriented between 90˚ and 180˚, while 47% of the remaining contacts are oriented between 0˚

and 90˚. In Figure 5.9(c), we present the distribution of contact normals with 30% of the smallest contacts removed. Excluding 30% of the smallest contacts from the distribution results in a sharper bias towards the left half of the Rose diagram, towards the cone penetrometer: 56% of the remaining contacts are now oriented between 90˚ and 180˚.

As we continue excluding greater percentages of the smaller contacts, the remaining contact normals show a clear bias towards the cone penetrometer (between 90˚ and 180˚). For the Rose diagrams in which more than 50% of the smallest contacts are excluded, 56-59% of the remaining contacts are oriented between 90˚ and 180˚ with the increase in percentage of contact normals occurring mostly in the 105˚ to 135˚ range. This suggests that the contact normals of the contacts with smaller areas tend to be more randomly distributed, whereas the contact normals with larger areas (50% of the largest contacts) tend to be oriented towards the cone. We carry out analysis of the remaining subregions around the cone with 50% of the smallest contacts excluded. This results in the exclusion of contact normals with contact areas less than approximately 0.008 mm^2–these may be considered to be the small contacts that do not take part in the force network, as described by Fonseca et al. (2016).

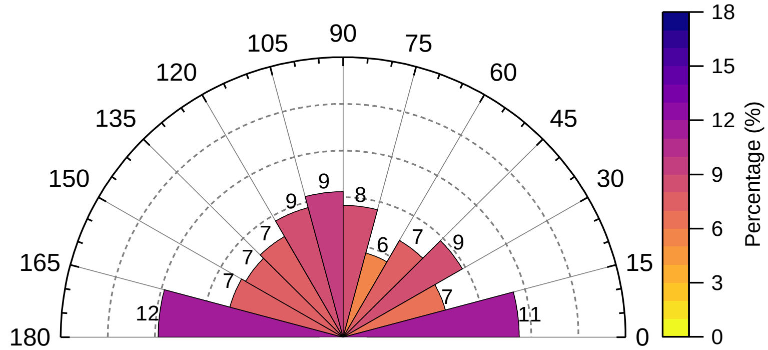

(a)

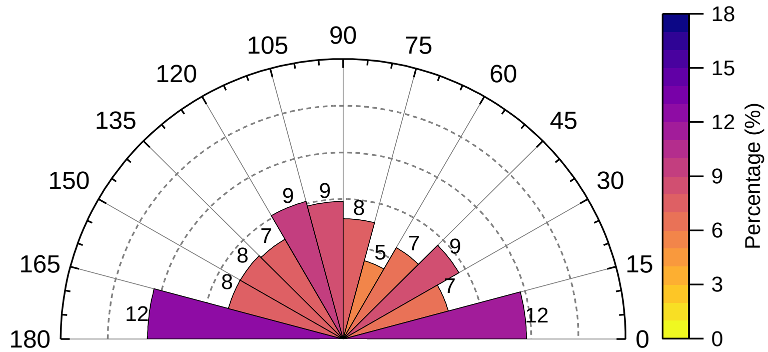

(b)

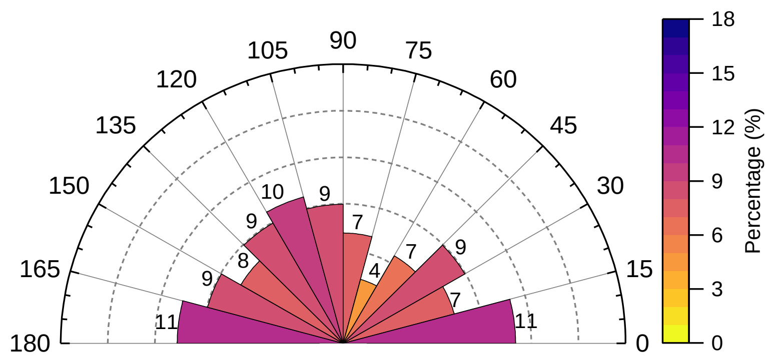

(c)

Figure 5.9 Rose diagram showing distribution of contact normal orientations for location #1 with (a) 0% of the contacts excluded, (b) 10% of the smallest contacts (by contact area) excluded, (c) 30% of the smallest contacts excluded, (d) 40% of the smallest contacts excluded, (e) 50% of the smallest contacts excluded, (f) 60% of the smallest contacts excluded, and (g) 70% of the smallest contacts excluded.

Figure 5.9 continued

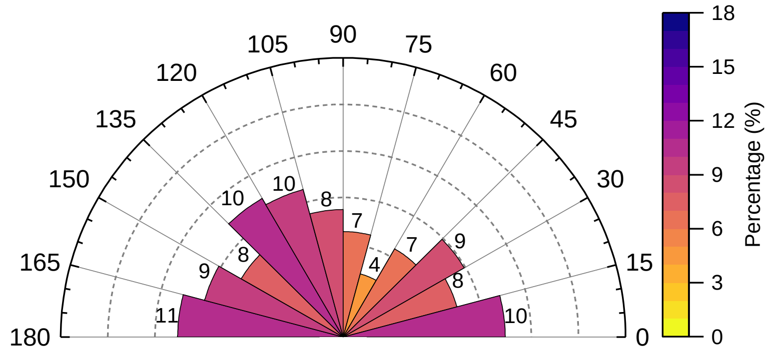

(d)

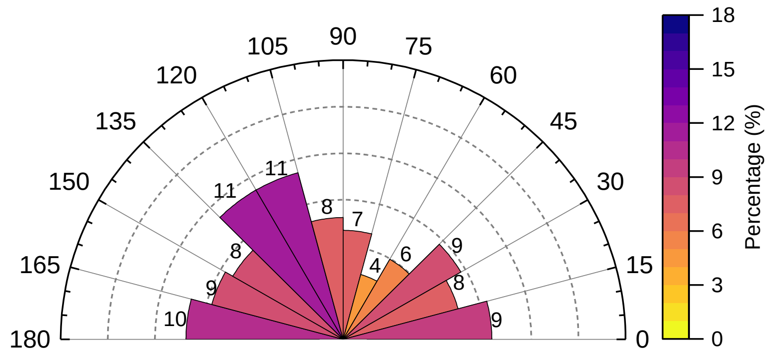

(e)

Figure 5.9 continued

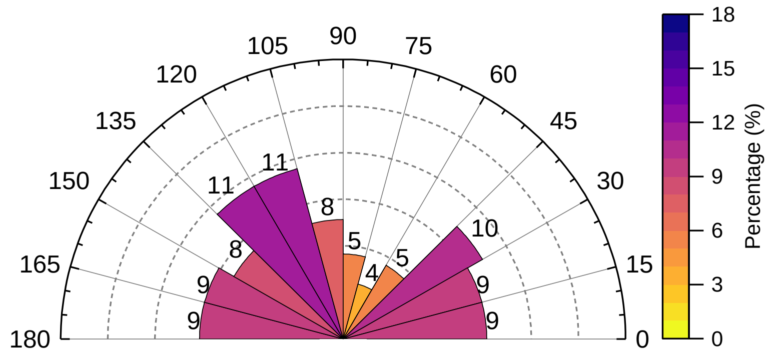

(f)

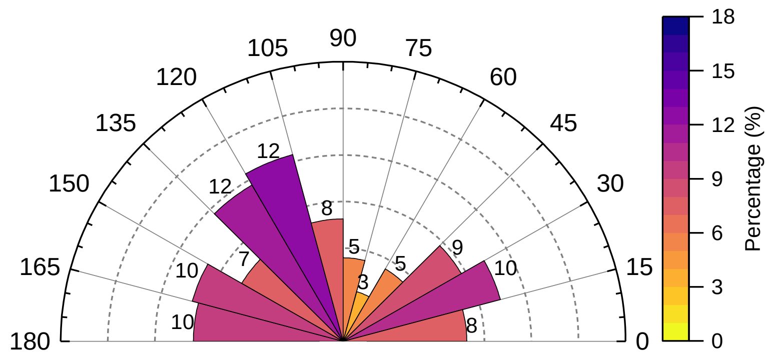

(g)

5.3.2.2 Distribution of interparticle contact normal orientations around penetrometer

To provide a point of reference for the results of the contact normals around a cone penetrometer, in Figure 5.10, we first present the Rose diagrams for an air-pluviated dense (D_R=85%) OTC sand sample. This sample has a very similar fabric to that of the air-pluviated sample used for the cone penetration experiment. From the figure, we can see that the orientations of the interparticle contact normals show a slight bias towards the vertical direction, which is the direction of pluviation. The Rose diagram presented in Figure 5.10 can serve as a reference to compare against the Rose diagrams of the contact normals of the subregions around the cone penetrometer.

Figure 5.11 shows the Rose diagrams for the contact normals of subregions around the cone penetrometer (with 50% of the smallest contacts excluded). Figure 5.11(a) shows contact orientations for subregion #1, which is located above the cone shoulder. We can see that 57% of the contact normals are located between 90˚ and 180˚, with 22% of the contact normals between 105˚ and 135˚. This general pattern of contact normal orientations continues for subregion #2, which is located immediately below the cone shoulder (see Figure 5.11(b)). For this subregion, 58% of the contacts are oriented between 90˚ and 180˚. Compared to the subregion #1, we see a 2% increase in the contacts in the horizontal direction (0˚-15˚ and 165˚-180˚) and also in the 120˚ to 150˚ range.

For subregions #3 and #4, shown in Figure 5.11(c) and (d), we see an increase in the percentage of the contact normal vectors in the 75˚-to-105˚ range. These subregions are located in the middle of the inclined face of the cone penetrometer–approximately one-third and two-thirds of the distance from the shoulder to the cone tip. The percentage of contact normal vectors in the 90˚ to 180˚ range are 60% and 58% for subregion #3 and subregion #4, respectively.

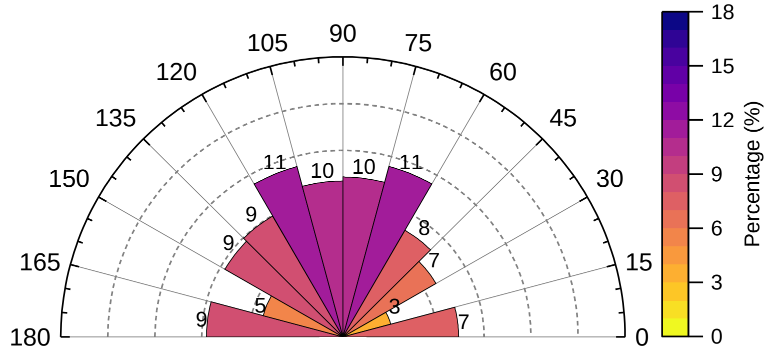

Figure 5.10 Rose diagram showing distribution of contact orientations for an air-pluviated dense (D_R=85%) OTC sand sample.

For the first four subregions, the contact normals have a bias towards the left half of the Rose diagram (i.e., in the 90˚–180˚ range), indicating that the force chains are oriented towards the cone. In Figure 5.11(e), we can see that below the cone the contact normals are oriented with a bias predominantly in the vertical direction. The percentage of contact normals in the 90˚-to-180˚ range drops to 53% for subregion #5 (compared to 60% and 58% for subregion #3 and subregion #4, respectively) and 44% of the contact normals occurs between 60˚ and 120˚(similar to the results of the air-pluviated sand sample shown in Figure 5.10).

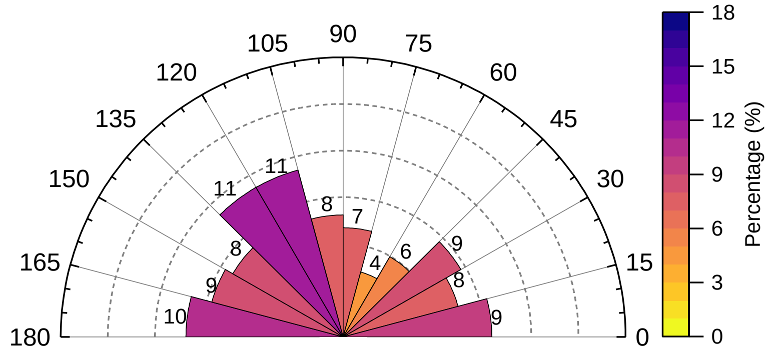

(a)

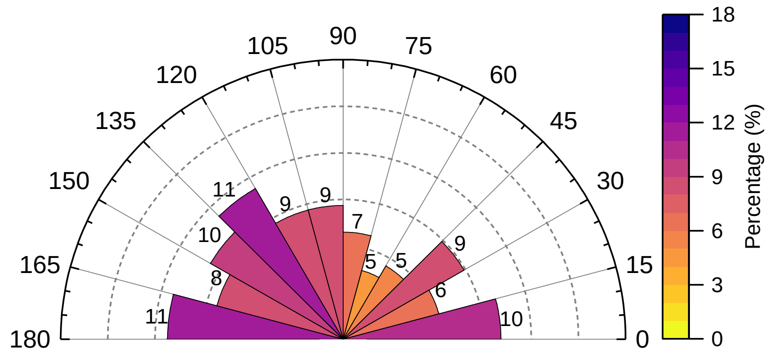

(b)

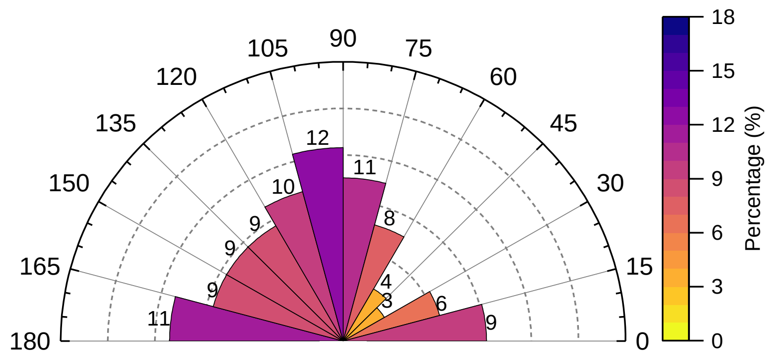

(c)

Figure 5.11 Rose diagram showing distribution of contact normal for (a) location #1, (b) location #2, (c) location #3, (d) location #4, and (e) location #5 around the cone penetrometer.

Figure 5.11 continued

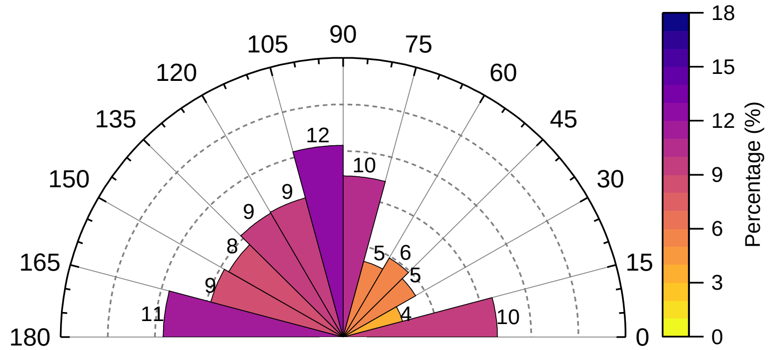

(d)

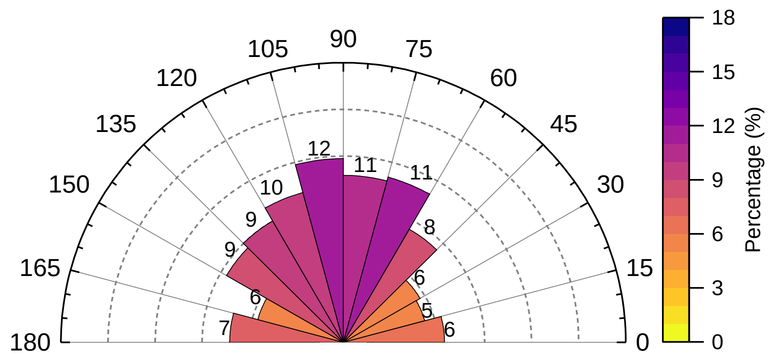

(e)

In Figure 5.11, we observe that the orientations of the contact normals stabilize when the contact normals with areas smaller than 50% of the contacts in the subregion are excluded, and from Figure 5.12 we see that the remaining contact normals orient in the direction of the cone penetrometer. Based on these two observations, it seems reasonable to assume that the orientations of the remaining contact normals (shown in Figure 5.12), to some extent, approximate the direction of the force chains in the sand. To express the orientation of the force chains statistically, we may use a fabric tensor **N** such as that proposed by Kanatani (1984). Using the contact normal orientations corresponding to contact normals with areas larger than 50% of the contacts in the sample, the fabric tensor **N**, the deviatoric fabric tensor **F**, and the anisotropy scalar $\boldsymbol{F}_q$ can be computed as follows:

$$\mathbf{N} = \frac{1}{N_{\mathbf{c}}} \sum_{\boldsymbol{\alpha}=1}^{N_{\mathbf{c}}} n^{\alpha} \otimes n^{\alpha} \tag{5.1}$$

$$\mathbf{F} = \frac{15}{2}\left(N - \frac{1}{3}\mathrm{tr}(\mathbf{N})\mathbf{I} \right) \tag{5.2}$$

$$F_q = \sqrt{\frac{3}{2}\mathbf{F} : \mathbf{F}} \tag{5.3}$$

where n^{α} is the contact normal vector for the contact α, and N_c is the total number of contacts in the sample. Figure 5.12 shows the values of **N**, **F**, and $\boldsymbol{F}_q$ for the five subregions around the cone penetrometer.

The X direction is taken radially outwards from the centerline of the penetrometer, the Y direction is the vertical direction (direction of penetration), and the Z direction is taken perpendicular to the plane of the cross section. In Figure 5.12 we can see that, as we progressively move from subregion #5 to subregion #1, the YY component of **N** increases from 0.37 in subregion #5 to 0.30 in subregion #1, indicating a reduction in the vertical component of the interparticle contact normals. On the other hand, the XX component of **N** increases from 0.28 in subregion #5 to 0.35 in subregion #1 – indicating an increase in the radial component of the interparticle contact normals. Due to the axis-symmetric nature of the penetration problem, the ZZ component of **N** remains stable as we move from subregion #5 to subregion #1. Furthermore, the anisotropy scalar, $\mathbf{F}_q$ remain in the range of 0.55-0.71, with higher values observed in the subregions #3 and #5.

5.3.3 Incremental displacement and strain fields around the cone penetrometer

For the penetration experiment in the dense OTC sand, we also carried out DIC analysis for a 2 mm penetration increment at a penetration depth of approximately 380 mm to obtain the incremental displacement and strain fields in the sand domain.

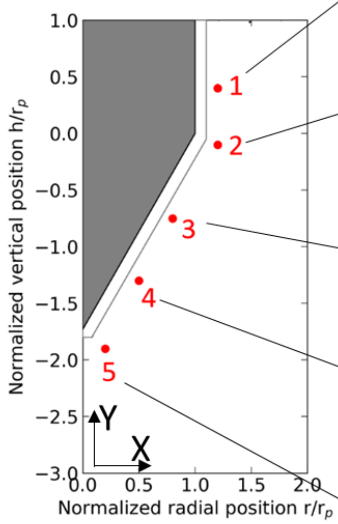

$$N = \begin{pmatrix} 0.35 & 0.04 & 0.00 \\ 0.04 & 0.30 & 0.00 \\ 0.00 & 0.00 & 0.34 \end{pmatrix} \quad F = \begin{pmatrix} 0.12 & 0.27 & -0.01 \\ 0.27 & -0.23 & 0 \\ -0.01 & 0 & 0.11 \end{pmatrix} \quad F_q = 0.59$$

$$N = \begin{pmatrix} 0.34 & 0.04 & 0.01 \\ 0.04 & 0.31 & 0.01 \\ 0.01 & 0.01 & 0.35 \end{pmatrix} \quad F = \begin{pmatrix} 0.08 & 0.27 & 0.09 \\ 0.27 & -0.17 & 0.08 \\ 0.09 & 0.06 & 0.09 \end{pmatrix} \quad F_q = 0.56$$

$$N = \begin{pmatrix} 0.30 & 0.45 & -0.01 \\ 0.45 & 0.35 & 0.00 \\ -0.01 & 0.00 & 0.35 \end{pmatrix} \quad F = \begin{pmatrix} -0.25 & 0.34 & -0.05 \\ 0.34 & 0.14 & 0.02 \\ -0.05 & 0.02 & 0.1 \end{pmatrix} \quad F_q = 0.71$$

$$N = \begin{pmatrix} 0.31 & 0.04 & 0.01 \\ 0.04 & 0.34 & 0.00 \\ 0.01 & 0.00 & 0.35 \end{pmatrix} \quad F = \begin{pmatrix} -0.18 & 0.33 & 0.04 \\ 0.33 & 0.07 & 0.03 \\ 0.04 & 0.03 & 0.11 \end{pmatrix} \quad F_q = 0.64$$

$$N = \begin{pmatrix} 0.28 & 0.01 & 0.01 \\ 0.01 & 0.37 & 0 \\ 0.01 & 0 & 0.35 \end{pmatrix} \quad F = \begin{pmatrix} -0.43 & 0.09 & 0.79 \\ 0.09 & 0.3 & -0.06 \\ 0.79 & -0.06 & 0.13 \end{pmatrix} \quad F_q = 0.71$$

Figure 5.12 Variation of fabric tensor **N**, the deviatoric fabric tensor **F**, and the anisotropy scalar $\boldsymbol{F}_q$ (Kanatani 1984) around the cone penetrometer.

DIC analysis, carried out on a pair of images at a time, allows us to track the movement of any arbitrary small square or rectangular area (a "subset") from the first image to the second image. This is done by comparing the grey-level pixel intensity of the subset in the first image (reference subset) with the grey-level pixel intensities of multiple subsets in the second image; for the DIC analysis of the images collected during the penetration experiment, we used the normalized sum of squared differences criterion for matching subsets, as it can handle minor variations in lighting conditions between images more effectively than other available methods (Arshad et al. 2014).

After finding the best-matching subset (the optimal subset) in the second image, the displacement of the reference subset is calculated as the difference in the positions of the centers of the optimum and the reference subsets. This procedure is repeated for multiple subsets, separated by a fixed center-to-center distance (called step size s_{st}), to get the displacement field in the entire sand domain. VIC-2D®, a commercial DIC analysis software, was used to analyze the sequence of images collected during the penetration experiment. For our DIC analysis, we used a subset size s_{sb} of 75 pixels with a center-to-center distance s_{st} between adjacent subsets equal to 5 pixels. The s_{sb} size was recommended by the VIC-2D® software based on the trackability of the texture of the colored sand and the lighting conditions. The incremental displacement field along with the radial and vertical components are presented in Figure 5.13. This incremental displacement field can be further analyzed to obtain the incremental strain field around the cone penetrometer. Figure 5.14 shows heatmaps of the incremental radial, vertical and shear strain around the penetrometer. The Green St. Venant strain tensor was used to compute the incremental strain field using the built-in strain computation functions in VIC-2D®.

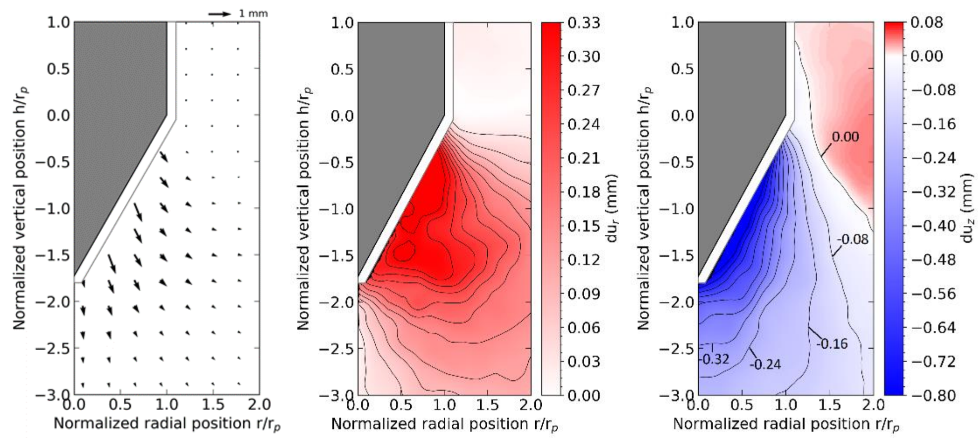

(a) (b) (c)

Figure 5.13 Incremental displacement field around the cone penetrometer: (a) incremental displacement vectors, (b) heatmap and contours of the radial component of the incremental displacement field, and (c) heatmap and contours of the vertical component of the incremental displacement field.

Force chains tend to align with the principal compressive stress direction (Fonseca et al. 2013; Oda et al. 1985; Oda and Konishi 1974). Given that the orientations of the principal compressive stress cannot be obtained directly from the DIC analysis, an appropriate proxy is needed. Experimental and numerical studies (Allersma 1987; Shi et al. 2020) have indicated that the principal stress and principal strain orientations tend to be approximately coaxial in space. Therefore, an estimate of the principal compressive stress orientation can be obtained from the orientation of the principal compressive strain. Using the pole method, the orientations of the principal planes and the orientations of the corresponding principal strains perpendicular to those planes can be obtained from the Mohr circle of strains (Salgado 2008, Ganju et al. 2021).

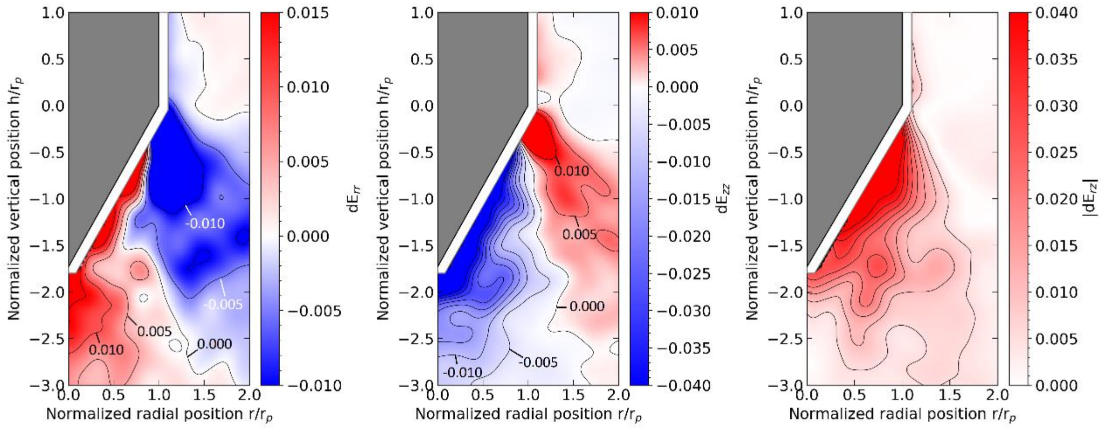

(a) (b) (c)

Figure 5.14 Incremental strain field around the cone penetrometer: (a) incremental radial strain, (b) incremental vertical strain, and (c) incremental shear strain.

In Figure 5.15 we show the incremental compressive principal strain orientations in the sand domain along with the distribution of contact normal orientations at the five subregions around the cone penetrometer. From Figure 5.15, the evolution of fabric around the cone penetrometer can be observed more clearly. Starting from below the cone penetrometer, for subregion #5, the contact normals point in the vertical direction and the orientations of the contact normals align with the orientation of the incremental principal strains, which have a strong vertical component and weak horizontal component.

Moving farther up to subregion #4, the contact normals still have a strong vertical component, but we also see an increase in the contacts in the horizontal direction. This again aligns with the incremental principal strain orientations, which in this location have an increased radial component compared to below the cone tip. A similar trend is observed in the subregion #3 to #1, in all of which we observe a progressive increase in the proportion of the radial component of the incremental principal strain orientation in comparison to the vertical component. In essence, we observe that the interparticle contact normals orient themselves to align with the incremental principal compressive strains as we move from the tip to the shoulder of the penetrometer.

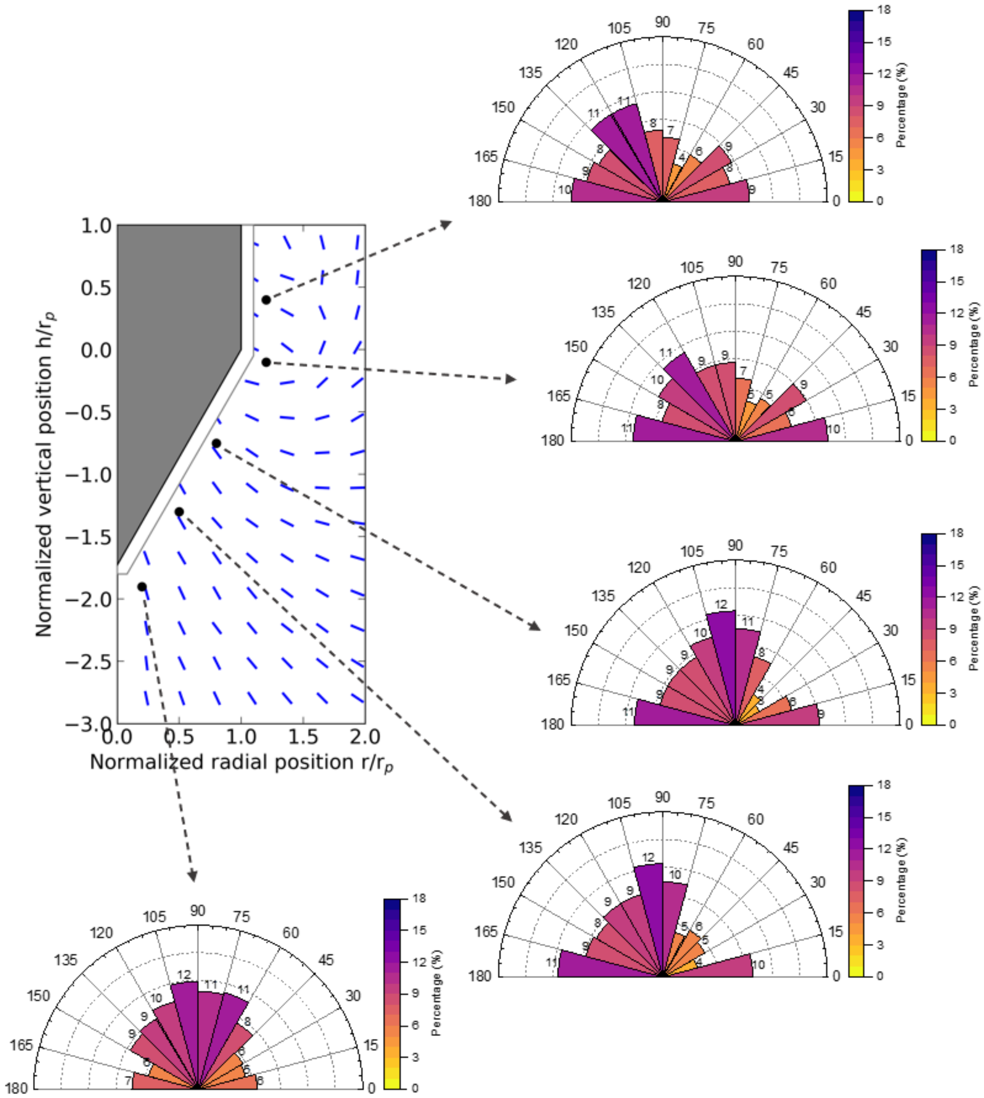

Figure 5.15 Incremental principal compressive strain orientations in the soil domain along with the distribution of contact normal orientations at the five subregions around the cone penetrometer.

5.4 Conclusions

In this paper, we presented data on the orientation of the interparticle contact normals around a cone penetrometer. A cone penetration experiment was performed in a dense air-pluviated sample of the subrounded OTC sand in a special half-cylindrical calibration chamber equipped with DIC capabilities. After the penetration experiment, a resin impregnation technique was used to collect an undisturbed sand sample from around the cone penetrometer. The resin-impregnated sample was scanned in an XRM to obtain the 3D tomography data of the sand particles around the penetrometer. The 3D tomography data was then analyzed to obtain the distribution of the interparticle contact normals at multiple locations around the penetrometer tip. The interparticle contact normal orientations were also used to compute the value of the fabric tensor **N**, the deviatoric fabric tensor **F**, and the anisotropy scalar $\boldsymbol{F}_q$. The data on the interparticle contact normals orientation was supplemented with the incremental displacement and strain fields around the cone penetrometer obtained from DIC analysis.

The main findings of the study are:

(1) In the five discrete subregions around the face of the cone penetrometer analyzed in this paper, the average interparticle contact areas generally increase increasing particle size; however, all particles, including the larger particles in the sample, tend to have some contacts with small contact areas. These smaller area contacts may not be contributing to the force network.

(2) Furthermore, in the five subregions, the interparticle contact normals with smaller areas tend to be more randomly distributed, whereas the contact normals of contacts with larger areas (contact areas greater than the contact areas of 50% of the interparticle contacts) tend to orient towards the cone.

(3) Below the cone penetrometer, where the incremental compressive principal strains have a strong vertical component, the contact normals tend to orient vertically upwards.

(4) Along the inclined face of the penetrometer, where the incremental principal strain orientations have both a vertical and horizontal component, the interparticle contact normal orientations align themselves along the incremental principal compressive strain orientations.

(5) Closer to the shoulder of the penetrometer, near the penetrometer shaft, the interparticle contact normals become more radially inclined to counter a larger proportion of the radial component of the incremental principal strain orientation.

The data clearly suggests that, in the sand domain, the interparticle contact normal orientations tend to align themselves with the principal strain increment orientation. Data presented here on the interparticle contact orientations, the fabric tensor and the incremental displacement and strain field orientations around the cone penetrometer can be very useful for researchers working on the multiscale modeling of penetration processes in granular materials.

6 SUMMARY AND CONCLUSIONS

Calibration chamber experiments, Digital Image Correlation (DIC) analysis, X-ray Computed Tomography (XCT) scans, and elemental laboratory experiments were used to study penetration processes in dense sands. For the purpose of this research, three test sands were selected: #2 Q-Rok (2QR), Ohio Gold Frac (OGF), Ottawa 20-30 (OTC). The three sands have similar particle size distributions; however, they differ in terms of their microscopic, particle-scale properties such as particle morphology and particle strength. These differences allowed us to study the effect of microscale properties of the sands on the macroscale response of the sand to quasi-static penetration processes.

Firstly, to study how the microscopic properties of the sand affect the macroscopic response of the sands to stresses high enough to cause crushing of its particles, dense and medium-dense cylindrical samples of the sand were loaded uniaxially in a compression mold. During the uniaxial compression experiments, the samples were scanned using an X-ray Microscope (XRM) to obtain 3D tomography data of the sand samples at different stress levels. The 3D tomography data were analyzed using open-source python libraries to obtain the particle size distribution and interparticle contact orientations. This allowed us to study the evolution of crushing and fabric in the sample during the penetration experiment. The results from this study gave us insights into the link between particle crushing and inter-particle contact orientations (fabric) of the sample. The main findings from the uniaxial compression experiments are as follows:

(1) The average particle fracture stress ($\sigma_{f,avg}$) correlates well with the average particle roundness (R_{avg}). Sands consisting of particles with lower R_{avg} tend to have lower $\sigma_{f,avg}$. The lower $\sigma_{f,avg}$ can be explained by the crushing of surface asperities observed in the particles with low R_{avg}; these asperities become stress concentration points when the

particles are loaded under compression. In addition to the R_{avg}, the $\sigma_{f,avg}$ is also affected by the presence of internal defects in the sand particles; occurrence of more internal defects results in a decrease in the $\sigma_{f,avg}$.

(2) R_{avg} also affects the macroscopic behavior of the sands. Sands with lower R_{avg} tend to have comparatively lower packing densities (higher e_{min} and e_{max}), higher critical state friction angles (ϕ_c), and lower yield stresses (σ_{yield}) in uniaxial compression (for the same initial relative density D_R). The higher e_{min}, e_{max}, and ϕ_c can be attributed to the interlocking of the surface asperities of the particles at lower stresses, whereas the lower σ_{yield} can be attributed to the crushing of those asperities at higher stresses.

(3) The average sphericity (S_{avg}) of the sample tends to decrease with particle crushing; however, the range of particle sphericities (S) observed in the sample as the loading progresses depends on the initial morphology of the particles. Sands with lower initial R_{avg} tend to produce, upon crushing, particles with both higher and lower S than the original, uncrushed sand. On the other hand, sands with higher initial R_{avg}, tend to produce, upon crushing, particles with generally lower S than the original, uncrushed sand.

(4) The anisotropy scalar F_q increases as the axial stress increases for samples loaded under uniaxial compression, indicating an increase in the anisotropy of interparticle contact normals with increasing loading. This increase in F_q is however reversed by the occurrence of particle crushing. For the samples tested in the current research, as long as $B_r \approx 0\%$, increases in axial stress tend to generally increase the interparticle contact anisotropy; however, by the time $B_r \approx 1\%$, the interparticle contact orientations have become more randomly oriented and F_q has dropped. This clearly indicates a link

between the anisotropy of the interparticle contacts and the breakage in sand samples loaded under uniaxial compression.

Next, cone penetration experiments were carried out in dense air-pluviated samples of the three sands. The dense sand samples were prepared in a special half-cylindrical calibration chamber equipped with observation windows, which allowed us to capture digital images of the sand and penetrometer during the penetration experiments. These images were analyzed using DIC to obtain the displacement field in the sand domain. The displacement field were further analyzed to obtain the strain fields and the strain localizations. A novel methodology was developed to automatically assess the patterns of dominant shear bands that develop around penetrometers in both shallow and deep penetration environments. The main findings from this study are as follows:

(1) For the cone penetrometer, tested in a deep penetration environment the shear band pattern was found to localize near the penetrometer tip.

(2) Around the cone, two distinct shear band patterns were observed: one oriented with the inclined face of the penetrometer and the other emanating from the shoulder and oriented radially outwards and downwards.

(3) For the model footing in shallow penetration starting from the sand surface, the shear band pattern can be characterized as a combination of a "wedge" formed below the model footing and two "fans" on either side of the "wedge."

(4) The "wedge" developed near the peak in resistance, whereas the "fans" developed only once the plunging stage was reached.

(5) Rotation of the dominant shear band orientation was found to take place between the "wedge" and the "fan."

After the cone penetration experiments, a specially developed agar-impregnation technique was used to obtain minimally disturbed sand samples from the around the cone penetrometer. These samples were scanned using an XRM to obtain 3D tomography data of the sand particles from around the cone tip. These 3D tomography data were analyzed to obtain particle size distributions around the cone penetrometer to quantify crushing around the penetrometer tip. The main findings from the analysis of the XCT data are as follows:

(1) For a given initial relative density, and a given vertical confinement, q_c depends on the angularity of the sands and on the strength of the particles that constitute the sand.

(2) More angular sands tend to mobilize a higher q_c; however, the mobilized q_c is limited by the crushing of the sand particles.

(3) Keeping all other parameters (relative density, confinement, and sand friction angle) equal, the q_c in a sand is a function of the $\sigma_{f,avg}$ of the sand.

(4) For a given sample density, the amount of crushing around the cone penetrometer depends on the vertical confinement and the morphological characteristics of the sand particles.

(5) The level of crushing is not uniform around the penetrometer tip: high B_r values tends to localize around the penetrometer closer to the surface of the penetrometer at approximately 0.5 -1.0 r_p below the shoulder of the penetrometer.

(6) The regions with high B_r values around the cone penetrometer roughly overlap with regions of high dE_{max} and high contractive dE_{vol}.

A shortcoming of the agar-impregnation technique was that to pour the agar solution into the sample, first the surcharge had to be removed and the sand needed to be excavated to the depth of the cone tip. This resulted in movement of the sand particles and caused some level of disturbance of the sand. While this did not affect the particle size, interparticle contacts were disturbed. To overcome this issue, a special resin-impregnation technique was developed to collect undisturbed sand samples from around the penetrometer. This new technique allowed us to collect resin-impregnated sand samples from around the penetrometer without disturbing the interparticle contacts of the sand. The collected sand sample was scanned in the XRM to obtain the 3D tomography data, which was further analyzed to obtain the interparticle contact orientations around the penetrometer tip. The main findings from the analysis of the 3D tomography data of the resin-impregnated sand sample are as follows:

(1) In the five discrete subregions analyzed around the face of the cone penetrometer, the average interparticle contact areas generally increase with increasing particle size; however, all particles, including the larger particles in the sample, tend to have some contacts with small contact areas. These smaller area contacts may not be contributing to the force network.

(2) Furthermore, in the five subregions, the interparticle contact normals with smaller areas tend to be more randomly distributed, whereas the contact normals of contacts with larger areas (contact areas greater than the contact areas of 50% of the interparticle contacts) tend to orient towards the cone.

(3) Below the cone penetrometer, where the incremental compressive principal strains have a strong vertical component, the contact normals tend to orient vertically upwards.

(4) Along the inclined face of the penetrometer, where the incremental principal strain orientations have both a vertical and horizontal component, the interparticle contact normal orientations align themselves along the incremental principal compressive strain orientations.

(5) Closer to the shoulder of the penetrometer, near the penetrometer shaft, the interparticle contact normals become more radially inclined to counter a larger proportion of the radial component of the incremental principal strain orientation.

The unique combination of calibration chamber experiments, DIC analysis, XCT scans and element laboratory experiment allowed us to investigate the dependence of macroscopic material behavior on microscopic sand properties and develop a data set of penetration experiments containing material properties of the test sands, penetration resistance values under different experimental conditions, displacement and strain fields in the sand domain, and the distribution of particle crushing and interparticle contact orientations around the cone penetrometer. The data presented in this dissertation allows us to assess the influence of microscopic sand properties on macroscopic response of the sand to the cone penetration process in dense sands. The data is aimed to be useful to researchers working on the multiscale modeling of penetration processes in granular materials.

REFERENCES

Al-Raoush, R., and Papadopoulos, A. (2010). "Representative elementary volume analysis of porous media using X-ray computed tomography." *Powder Technology*, Elsevier B.V., 200(1–2), 69–77.

Alam, M. F., Haque, A., and Ranjith, P. G. (2018). "A study of the particle-level fabric and morphology of granular soils under one-dimensional compression using insitu X-ray CT imaging." *Materials*, 11(6), 16–18.

Alikarami, R., Andò, E., Gkiousas-Kapnisis, M., Torabi, A., and Viggiani, G. (2014). "Strain localisation and grain breakage in sand under shearing at high mean stress: insights from in situ X-ray tomography." *Acta Geotechnica*, 10(1), 15–30.

Allersma, H. G. B. (1982). "Photoelastic investigation of the stress distribution during penetration." *Proceedings of the Second European Symposium on Penetraiton Testing*, Amsterdam, 411–418.

Allersma, H. G. B. (1987). "Optical analysis of stress and strain in photoelastic particle assemblies." TU Delft.

Allersma, H. G. B., and Broere, W. (2002). "Optical analysis of stress around a penetrating probe in granular material." *Physical Modelling in Geotechnics: Proceedings of the international Conference on Physical Modelling in Geotechnics*, (November), 149–154.

Als-Nielsen, J., and McMorrow, D. (2011). "Chapter 1 - X-rays and their interaction with matter." *Elements of Modern X-ray Physics*, 1–28.

Alshibli, K. A., Batiste, S. N., and Sture, S. (2003). "Strain localization in sand: plane strain versus triaxial compression." *Journal of Geotechnical and Geoenvironmental Engineering*, 129(6), 483–494.

Alshibli, K. A., and Reed, A. H. (Eds.). (2010). *Advances in Computed Tomography for Geomaterials*. John Wiley & Sons, Inc., Hoboken, NJ, USA.

Alshibli, K., and Cil, M. (2018). "Influence of Particle Morphology on the Friction and Dilatancy of Sand." *Journal of Geotechnical and Geoenvironmental Engineering*, 144(3), 04017118.

Alshibli, K., and Sture, S. (1999). "Sand Shear Band Thickness Measurements by Digital Imaging Techniques." *Journal of Computing in Civil Engineering*, 13(2), 103–109.

Altuhafi, F. N., Coop, M. R., and Georgiannou, V. N. (2016). "Effect of particle shape on the mechanical properties of natural sands." *Journal of Geotechnical and Geoenvironmental Engineering*, 142(07), 145.

Altuhafi, F., O'Sullivan, C., and Cavarretta, I. (2013). "Analysis of an Image-Based Method to Quantify the Size and Shape of Sand Particles." *Journal of Geotechnical and Geoenvironmental Engineering*, 139(8), 1290–1307.

Andò, E. (2013). "Experimental investigation of microstructural changes in deforming granular media using x-ray tomography." Dissertation, Universite de Grenoble.

Andò, E., Viggiani, G., and Desrues, J. (2020). "X-Ray Tomography Experiments on Sand at Different Scales." 1–20.

Andò, E., Viggiani, G., Hall, S. A., and Desrues, J. (2013). "Experimental micro-mechanics of granular media studied by x-ray tomography: recent results and challenges." *Géotechnique Letters*, 3(3), 142–146.

Arshad, M. (2014). "Experimental study of the displacements caused by cone penetration in sand." Purdue University.

Arshad, M. I., Tehrani, F. S., Prezzi, M., and Salgado, R. (2014). "Experimental study of cone penetration in silica sand using digital image correlation." *Géotechnique*, Thomas Telford Ltd, 64(7), 551–569.

ASTM. (2016). "Standard test method for minimum index density and unit weight of soils using a vibratory table (ASTM D4253-16)." *ASTM Standards*.

ASTM C778-17. (2017). "Standard specification for standard sand." *ASTM Standards.*

ASTM D2487-17. (2006). "Standard practice for classification of soils for engineering purposes (Unified Soil Classification System)." *ASTM Standards*.

ASTM D4253-16. (2016). "Standard Test Methods for Maximum Index Density and Unit Weight of Soils Using a." *ASTM Standards*, 00(Reapproved), 1–15.

ASTM D4254-16. (2016). "Standard test methods for minimum index density and unit weight of soils and calculation of relative density." *ASTM Standards*, 9.

ASTM D6913-17. (2017). "Standard Test Methods for Particle-Size Distribution (Gradation) of Soils Using Sieve Analysis." *ASTM*, 04(Reapproved 2009), 1–35.

Baligh, M. M. (2008). "Strain path method." *Journal of Geotechnical Engineering*, 111(9), 1108–1136.

Bardet, J. P. (1990). "A comprehensive review of strain localization in elastoplastic soils." *Computers and Geotechnics*, 10(3), 163–188.

Barr, A. D., Clarke, S. D., and Petkovski, M. (2019). "High-pressure compressibility and shear strength data for soils." *Canadian Geotechnical Journal*, 56(7), 1042–1048.

BCP Committee. (1971). "Field tests on piles in sand." *Soil and Foundations*, 11(2), 29–49.

Begemann, H. K. S. (1965). "The friction jacket cone as an aid in determining the soil profile." *Proceedings of the 6th International Conference on Soil Mechanics and Foundation Engineering*, ICSMFE, Montreal, 8–15.

Beucher, S., and Lantuejoul, C. (1979). "Use of watersheds in contour detection." *International Workshop on Image Processing: Real-time Edge and Motion Detection/Estimation*.

Bombasaro, E., and Kasper, T. (2016). "Evaluation of spatial soil variability in the Pearl River Estuary using CPTU data." *Soils and Foundations*, Elsevier, 56(3), 496–505.

Bransby, P. L., and Blair-Fish, P. M. (1975). "Deformations near rupture surfaces in flowing sand." *Geotechnique*, 25(2), 384–389.

Briaud, J.-L., Moore, B. H., and Mitchell, G. B. (1989). "Analysis of pile load tests at lock and dam 26." *Foundation Engineering: Current Principles and Practices*, ASCE, 925–942.

Buades, A., Coll, B., and Morel, J.-M. (2005). "A non-local algorithm for image denoising." *2005 IEEE Computer Society Conference on Computer Vision and Pattern Recognition (CVPR'05)*, IEEE, 60–65.

Cao, Z., Wang, Y., Au, S. K., and Cao, Z. (2010). "Bayesian approach for probabilistic characterization of sand friction angles." *Engineering Geology*, Elsevier B.V., 114(3–4), 354–363.

Carraro, J. A. H., Bandini, P., and Salgado, R. (2003). "Liquefaction Resistance of Clean and Nonplastic Silty Sands Based on Cone Penetration Resistance." *Journal of Geotechnical and Geoenvironmental Engineering*, 129(11), 965–976.

Carter, J. P., Booker, J. R., and Yeung, S. K. (2009). "Cavity expansion in cohesive frictional soils." *Géotechnique*, 36(3), 349–358.

Cavarretta, I., Coop, M., and O'Sullivan, C. (2010). "The influence of particle characteristics on the behaviour of coarse grained soils." *Géotechnique*, 60(6), 413–423.

Ceccato, F., Beuth, L., Vermeer, P. A., and Simonini, P. (2016). "Two-phase Material Point Method applied to the study of cone penetration." *Computers and Geotechnics*, Elsevier Ltd, 80, 440–452.

Chen, P. K., and Bassett, R. E. (1988). "The implications of observed deformations during cone penetration." *Proceedings of the geotechnology conference organized by the Institution of Civil Engineers*, Institution of Civil Engineers, ed., Birmingham.

Chen, Q., Wang, C., and Hsein Juang, C. (2015). "CPT-Based Evaluation of Liquefaction Potential Accounting for Soil Spatial Variability at Multiple Scales." *Journal of Geotechnical and Geoenvironmental Engineering*, 142(2), 04015077.

Chen, Z. (Chris), Omidvar, M., Iskander, M., and Bless, S. (2014). “Modelling of projectile penetration using transparent soils.” *International Journal of Physical Modelling in Geotechnics*, Thomas Telford Ltd, 14(3), 68–79.

Cheng, Y. . Y., Bolton, M. M. D., and Nakata, Y. (2004). “Crushing and plastic deformation of soils simulated using DEM.” *Geotechnique*, 54(2), 131–141.

Cheng, Y. P., Nakata, Y., and Bolton, M. D. (2003). “Discrete element simulation of crushable soil.” *Géotechnique*, 53(7), 633–641.

Chevalier, B., and Otani, J. (2011). “Arching observation in three-dimensional trapdoor problem with x-ray ct and discrete element method.” *Soils and Foundations*, 51(3), 459–469.

Chevalier, B., Takano, D., and Otani, J. (2010). “Comparison of X-ray CT and Discrete Element Method in the Evaluation of Tunnel Face Failure.” *Advances in Computed Tomography for Geomaterials*, 397–405.

Cil, M. (2015). “3D Kinematic and Strength Behavior of Granular Materials At the Particle-Level.”

Cil, M., and Alshibli, K. (2012). “3D assessment of fracture of sand particles using discrete element method.” *Géotechnique Letters*, 2(3), 161–166.

Cil, M., and Alshibli, K. A. (2014). “3D evolution of sand fracture under 1D compression.” *Géotechnique*, 64(5), 351–364.

Cil, M., Alshibli, K., and Kenesei, P. (2017a). “3D experimental measurement of lattice strain and fracture behavior of sand particles using synchrotron X-ray diffraction and tomography.” *Journal of Geotechnical and Geoenvironmental Engineering*, 143(9), 1–18.

Cil, M., Alshibli, K., and Kenesei, P. (2017b). “3D experimental measurement of lattice strain and fracture behavior of sand particles using synchrotron X-Ray diffraction and tomography.” *Journal of Geotechnical and Geoenvironmental Engineering*, 143(9), 1–18.

Collins, I. F., Pender, M. J., and Yan, W. (1992). “Cavity expansion in sands under drained loading conditions.” *International Journal for Numerical and Analytical Methods in Geomechanics*, 16(1), 3–23.

Collins, I. F., and Yu, H. S. (1996). “Undrained Cavity Expansions in Critical State Soils.” *International Journal for Numerical and Analytical Methods in Geomechanics*, 20(7), 489–516.

Coop, M. R., and Lee, I. K. (1993). “The behaviour of granular soils at elevated stresses.” *Predictive soil mechanics*, 186–198.

Coop, M. R., Sorensen, K. K., Freitas, T. B., and Georgoutsos, G. (2004). “Particle breakage during shearing of a carbonate sand.” *Geotechnique*, 54(3), 157–163.

Correlated Solutions. (2009). “VIC-2D.”

Cudmani, R., and Osinov, V. A. (2001). “The cavity expansion problem for the interpretation of cone penetration and pressuremeter tests.” *Canadian Geotechnical Journal*, 38(3), 622–638.

Desrues, J., and Andò, E. (2015). “Strain localisation in granular media.” *Comptes Rendus Physique*, Elsevier Masson SAS, 16(1), 26–36.

Desrues, J., Lanier, J., and Stutz, P. (1985). “Localization of the deformation in tests on sand sample.” *Engineering Fracture Mechanics*, 21(4), 909–921.

Desrues, J., and Viggiani, G. (2004). “Strain localization in sand: An overview of the experimental results obtained in Grenoble using stereophotogrammetry.” *International Journal for Numerical and Analytical Methods in Geomechanics*, John Wiley & Sons, Ltd., 28(4), 279–321.

Desrues, J., Viggiani, G., and Bésuelle, P. (2010). *Advances in X-ray Tomography for Geomaterials*. *Advances in X-ray Tomography for Geomaterials*.

Doreau-Malioche, J. (2018). “Imaging of sand-pile interface submitted to a high number of loading cycles.” *Physical Modelling in Geotechnics*, A. McNamara, S. Divall, R. Goodey, N. Taylor, S. Stallebrass, and J. Panchal, eds., CRC Press, London, United Kingdom, 841–846.

Doreau-Malioche, J., Combe, G., Viggiani, G., and Toni, J. B. (2018). “Shaft friction changes for cyclically loaded displacement piles: an x-ray investigation.” *Géotechnique Letters*, 8(1), 1–28.

Doreau-Malioche, J., Galvis-Castro, A., Tovar-Valencia, R., Viggiani, G., Combe, G., Prezzi, M., and Salgado, R. (2019). “Characterising processes at sand-pile interface using digital image analysis and X-ray CT.” *Géotechnique Letters*, 9(4), 254–262.

Douglas, B. J., and Olsen, R. S. (1981). “Soil classification using electric cone penetrometer.” *Symposium on cone penetration testing and experience*, Geotechnical Engineering Division ASCE, St. Louis.

Druckrey, A. (2016). “3D Multi-Scale Behavior of Granular Materials using Experimental and Numerical Techniques.” University of Tennessee, Knoxville.

Druckrey, A., and Alshibli, K. A. (2016). “3D finite element modeling of sand particle fracture based on in situ X-Ray synchrotron imaging.” *International Journal for Numerical and Analytical Methods in Geomechanics*, 40(1), 105–116.

Durgunoglu, H. T., and Mitchell, J. K. (1973). *Static penetration resistance of soils*. Berkeley, CA.

Einav, I. (2007). “Breakage mechanics—Part I: Theory.” *Journal of the Mechanics and Physics of Solids*, 55(6), 1274–1297.

Emery, J. J., Finn, W. D. L., and Lee, K. W. (1973). “Uniformity of saturated sand specimens.” *Evaluation of Relative Density and its Role in Geotechnical Projects Involving Cohesionless Soils, ASTM STP 523*, 506.

Fei, W., and Narsilio, G. A. (2020). "Impact of Three-Dimensional Sphericity and Roundness on Coordination Number." *Journal of Geotechnical and Geoenvironmental Engineering*, 146(12), 06020025.

Fenton, G. A. (1999). "Random field modeling of CPT data." *Journal Geotechnical and Geoenvironmental Engineering*, 125(6), 486–498.

Finno, R. J., Harris, W. W., Mooney, M. A., and Viggiani, G. (1997). "Shear bands in plane strain compression of loose sand." *Géotechnique*, Thomas Telford Ltd, 47(1), 149–165.

Firouzianbandpey, S., Ibsen, L. B., Griffiths, D. V., Vahdatirad, M. J., Andersen, L. V., and Sørensen, J. D. (2015). "Effect of Spatial Correlation Length on the Interpretation of Normalized CPT Data Using a Kriging Approach." *Journal of Geotechnical and Geoenvironmental Engineering*, 141(12), 04015052.

Fish, J., and Belytschko, T. (2007). *A first Course in FEM*. John Wiley & Sons Ltd.

Fonseca, J. (2011). "The evolution of morphology and fabric of a sand during shearing." *PhD Thesis*, (April).

Fonseca, J., Nadimi, S., Reyes-Aldasoro, C. C., O′Sullivan, C., and Coop, M. R. (2016). "Image-based investigation into the primary fabric of stress-transmitting particles in sand." *Soils and Foundations*, Elsevier, 56(5), 818–834.

Fonseca, J., O'Sullivan, C., Coop, M. R., and Lee, P. D. (2012). "Non-invasive characterization of particle morphology of natural sands." *Soils and Foundations*, Elsevier, 52(4), 712–722.

Fonseca, J., O'Sullivan, C., Coop, M. R., and Lee, P. D. (2013). "Quantifying the evolution of soil fabric during shearing using scalar parameters." *Geotechnique*, 63(10), 818–829.

Fonseca, J., Sim, W. W., Shire, T., and O'Sullivan, C. (2014). "Microstructural analysis of sands with varying degrees of internal stability." *Géotechnique*, 64(5), 405–411.

Francescon, M. (1983). "Model pile tests in clay: Stresses and displacements due to installation and axial loading." University of Cambridge.

Frost, J. D. (1989). "Studies on the monotonic and cyclic behavior of sands."

Fugro Engineers B. V. (2004). "Axial pile capacity design method for offshore driven piles in sand." *P-1003 API*, (3).

Galvis-Castro, A. C., Tovar-Valencia, R. D., Salgado, R., and Prezzi, M. (2019). "Effect of loading direction on the shaft resistance of jacked piles in dense sand." *Géotechnique*, 69(1), 16–28.

Ganju, E., Han, F., Prezzi, M., and Salgado, R. (2020a). "Static capacity of closed-ended pipe pile driven in gravelly sand." *Journal of Geotechnical and Geoenvironmental Engineering*, 146(4), 04020008.

Ganju, E., Han, F., Prezzi, M., Salgado, R., and Pereira, J. S. (2020b). "Quantification of displacement and particle crushing around a penetrometer tip." *Geoscience Frontiers*, Elsevier, 11(2), 389–399.

Ganju, E., Prezzi, M., and Salgado, R. (2017). "Algorithm for generation of stratigraphic profiles using cone penetration test data." *Computers and Geotechnics*, Elsevier Ltd, 90(10), 73–84.

Ganju, E., Salgado, R., and Prezzi, M. (2019). "Site Variability Characterization Using Cone Penetration Test Data." *Geotechnical Special Publication*.

Ghafghazi, M., Shuttle, D. A., and DeJong, J. T. (2014). "Particle breakage and the critical state of sand." *Soils and Foundations*, Elsevier, 54(3), 451–461.

Graham, J., Alfaro, M., and Ferris, G. (2004). "Compression and strength of dense sand at high pressures and elevated temperatures." *Canadian Geotechnical Journal*, 41(6), 1206–1212.

Guida, G., Casini, F., Viggiani, G. M. B., Andò, E., and Viggiani, G. (2018). "Breakage mechanisms of highly porous particles in 1D compression revealed by X-ray tomography." *Géotechnique Letters*, 8(2), 155–160.

Guzman, I. L., Iskander, M., and Bless, S. (2020). "A Comparison of Half and Quarter Space Penetration into Granular Media." *Geotechnical Testing Journal*, 43(4), 20190080.

Hagerty, M. M., Hite, D. R., Ullrich, C. R., and Hagerty, D. J. (1993). "One-dimensional high-pressure compression of granular media." *Journal of Geotechnical Engineering*, 119(1), 1–18.

Haimson, B. C., and Doe, T. W. (1983). "State of stress, permeability, and fractures in the Precambrian granite of northern Illinois (USA)." *Journal of Geophysical Research*, 88(B9), 7355–7371.

Han, F., Ganju, E., Salgado, R., and Prezzi, M. (2018). "Effects of interface roughness, particle geometry, and gradation on the sand–steel interface friction angle." *Journal of Geotechnical and Geoenvironmental Engineering*, 144(12), 04018096.

Han, F., Ganju, E., Salgado, R., and Prezzi, M. (2019). "Comparison of the load response of closed-ended and open-ended pipe piles driven in gravelly sand." *Acta Geotechnica*, 14(6), 1785–1803.

Hanley, K. J., Sullivan, C. O., and Huang, X. (2015). "Particle-scale mechanics of sand crushing in compression and shearing using DEM." *Soils and Foundations*, Elsevier, 55(5), 1100–1112.

Hardin, B. O. (1985). "Crushing of soil particles." *Journal of Geotechnical Engineering*, American Society of Civil Engineers, 111(10), 1177–1192.

Hasan, A., and Alshibli, K. (2010). "Experimental assessment of 3D particle-to-particle interaction within sheared sand using synchrotron microtomography." *Géotechnique*, 60(5), 369–379.

Hendron, A. (1963). *The behavior of sand in one-dimensional compression*.

Huang, A. (1991). *Calibration Chamber Testing*. *First International Symposium on Calibration*, Elsevier.

Huang, W., Sheng, D., Sloan, S. W., and Yu, H. S. (2004). "Finite element analysis of cone penetration in cohesionless soil." *Computers and Geotechnics*, 31(7), 517–528.

Iskander, M. (2010). *Modelling With Transparent Soils*. *Springer Series in Geomechanics and Geoengineering*.

Jahanandish, M., and Ansaripour, M. (2016). "Application of particle image velocimetry in establishing the field of zero extension lines in soils." *Iranian Journal of Science and Technology - Transactions of Civil Engineering*, Springer International Publishing, 40(4), 337–348.

James, R. (1965). "Stress and strain fields in sand." University of Cambridge.

James, R. G., and Bransby, P. L. (1971). "A Velocity Field for Some Passive Earth Pressure Problems." *Géotechnique*, 21(1), 61–83.

Jang, D.-J., Forst, J. D., and Park, J. Y. (1999). "Preparation of epoxy impregnated sandy soil specimens for image analysis." *Geotechnical Testing Journal*, 22(2), 147–158.

Jang, D. J., and Frost, J. D. (2000). "Use of image analysis to study the microstructure of a failed sand specimen." *Canadian Geotechnical Journal*, 37(5), 1141–1149.

Jardine, R., Chow, F., Overy, R., and Standing, J. (2005). *ICP design methods for driven piles in sand and clays*. Thomas Telford, London.

Jefferies, M. G., and Davis, M. P. (1991). "Soil classification by the cone penetration test: Discussion." *Canadian Geotechnical Journal*, 28(1), 1–178.

Kaestner, A., Lehmann, E., and Stampanoni, M. (2008). "Imaging and image processing in porous media research." *Advances in Water Resources*, 31(9), 1174–1187.

Kanatani, K.-I. (1984). "Distribution of directional data and fabric tensors." *International Journal of Engineering Science*, 22(2), 149–164.

Karatza, Z. (2017). "A study of temporal and spatial evolution of deformation and breakage of dry granular materials using x-ray computed tomography and the discrete element method."

Karatza, Z., Andò, E., Papanicolopulos, S.-A., Viggiani, G., and Ooi, J. Y. (2017). "Evolution of particle breakage studied using x-ray tomography and the discrete element method." *EPJ Web of Conferences*, (F. Radjai, S. Nezamabadi, S. Luding, and J. Y. Delenne, eds.), 140, 07013.

Karatza, Z., Andò, E., Papanicolopulos, S.-A., Viggiani, G., and Ooi, J. Y. (2019). "Effect of particle morphology and contacts on particle breakage in a granular assembly studied using X-ray tomography." *Granular Matter*, Springer Berlin Heidelberg, 21(3), 1–13.

Karatza, Z., Andò, E., Papanicolopulos, S., Ooi, J., and Viggiani, G. (2018). "Evolution of deformation and breakage in sand studied using X-ray tomography." *Géotechnique*, 68(2), 107–117.

Karlsrud, K., Clausen, C. J., Aas, P. M., and Karlsud, K. (2005). "Bearing capacity of driven piles in sand, the NGI approach." *Frontiers in Offshore Geotechnics*, Taylor & Francis, Perth, 667–681.

Kikumoto, M., Wood, D. M., and Russel, A. (2010). "Particle crushing and deformation behavior." *Soils and Foundations*, 50(4), 547–563.

Kobayashi, T., and Fukagawa, R. (2003). "Characterization of deformation process of CPT using X-ray TV imaging technique." *Deformational Characteristics of Geomaterial*, 43–47.

Kouretzis, G. P., Sheng, D., and Wang, D. (2014). "Numerical simulation of cone penetration testing using a new critical state constitutive model for sand." *Computers and Geotechnics*, Elsevier Ltd, 56, 50–60.

Krumbein, W. C., and Sloss, L. L. (1951). *Stratigraphy and sedimentation*. W. H. Freeman and Company, San Francisco, USA.

Kuwajima, K., Hyodo, M., and Hyde, A. F. (2009). "Pile bearing capacity factors and soil crushability." *Journal of Geotechnical and Geoenvironmental Engineering*, 135(7), 901–913.

Kuwano, R., and Jardine, R. J. (2002). "On the applicability of cross-anisotropic elasticity to granular materials at very small strains." *Geotechnique*, 52(10), 727–749.

Lade, P. V., Yamamuro, J. A., and Bopp, P. A. (1996). "Significance of Particle Crushing in Granular Materials." *Journal of Geotechnical Engineering*, American Society of Civil Engineers, 122(4), 309–316.

Lee, J. (2008). "Experimental investigation of the load response of model piles in sand." Purdue University.

Lee, J., Prezzi, M., and Salgado, R. (2011). "Experimental investigation of the combined load response of model piles driven in sand." *Geotechnical Testing Journal*, 34(6), 103269.

Lee, K. L., and Farhoomand, I. (1967). "Compressibility and crushing of granular soil in ansisotropic triaxial compression." *Canadian Geotechnical Journal*, 4(1), 68–86.

Lehane, B. M., Schneider, J. a., and Xu, X. (2005a). *A review of design methods for offshore driven piles in siliceous sand*.

Lehane, B. M., Schneider, J. A., and Xu, X. (2005b). “The UWA-05 method for prediction of axial capacity of driven piles in sand.” *Proceedings of the International Symposium on Frontiers in Offshore Geotechnics (IS-FOG 2005)*, M. Cassidy and S. Gourvenec, eds., Taylor & Francis, Perth, Australia.

Liao, C., Zhang, C., Wu, M., Ma, Y., and Ou, M. (2003). “Stress change near the Kunlun fault before and after the Ms 8.1 Kunlun earthquake.” *Geophysical Research Letters*, 30(20), 2003GL018106.

Loukidis, D., and Salgado, R. (2011). “Effect of relative density and stress level on the bearing capacity of footings on sand.” *Géotechnique*, 61(2), 107–119.

Lunne, T., Robertson, P. K., and Powell, J. J. M. (1997). *Cone penetration testing in geotechnical practice*. Routledge, New York, NY.

McDowell, G. R. (2002). “On the yielding and plastic compression of sand.” *Soils and foundations*, 42(1), 139–145.

McDowell, G. R., and Bolton, M. D. (1998). “On the micromechanics of crushable aggregates.” *Géotechnique*, 48(5), 667–679.

McDowell, G. R., and Bolton, M. D. (2000). “Effect of particle size distribution on pile tip resistance in calcareous sand in the geotechnical centrifuge.” *Granular Matter*, 2(4), 179–187.

McDowell, G. R., Bolton, M. D., and Robertson, D. (1996). “The fractal crushing of granular materials.” *Journal of the Mechanics and Physics of Solids*, 44(12), 2079–2101.

Mesri, G., and Vardhanabhuti, B. (2009a). “Compression of granular materials.” *Canadian Geotechnical Journal*, 46(4), 369–392.

Mesri, G., and Vardhanabhuti, B. (2009b). “Compression of granular materials.” *Canadian Geotechnical Journal*, 46(4), 369–392.

Miao, G., and Airey, D. (2013). “Breakage and ultimate states for a carbonate sand.” *Géotechnique*, 63(14), 1221–1229.

Mitchell, J. J. K., and Soga, K. (2005). *Fundamentals of soil behavior*. *Fundamentals of Soil Behavior*, Wiley John and Sons, New York.

Miura, S., and Toki, S. (1982). “A sample preparation method and its effect on static and cyclic deformation-strength properties of sand.” *Soils and foundations*, 22(1), 61–77.

Mooney, M. A., Viggiani, G., and Finno, R. J. (1997). “Undrained Shear Band Deformation in Granular Media.” *Journal of Engineering Mechanics*, 123(6), 577–585.

Mooney, M., Finno, R., and Viggiani, G. (1998). “A unique critical state for sand?” *Journal of Geotechnical and Geoenvironmental Engineering*, 124(11), 1100–1108.

Murthy, T. G., Carraro, J. A. H., Loukidis, D., Salgado, R., and Prezzi, M. (2007). "Undrained monotonic response of clean and silty sands." *Géotechnique*, 57(3), 273–288.

Nakata, Y., Hyodo, M., Hyde, A. f. L., Kato, Y., and Murata, H. (2001a). "Microscopic particle crushing of sand subjected to high pressure one-dimensional compression." *Soils and foundations*, 41(1), 69–82.

Nakata, Y., Kato, Y., Hyodo, M., Hyde, A. F. L., and Murata, H. (2001b). "One-dimensional compression behaviour of uniformly graded sand related to single particle crushing strength." *Soils and Foundations*, 41(2), 39–51.

Nardelli, V., and Coop, M. (2019). "The experimental contact behaviour of natural sands: Normal and tangential loading." *Géotechnique*, 69(8), 672–686.

Oda, M. (1977). "Co-Ordination Number and its Relation to Shear Strength of Granular Material." *Soils and Foundations*, 17(2), 29–42.

Oda, M., and Kazama, H. (1998). "Microstructure of shear bands and its relation to the mechanisms of dilatancy and failure of dense granular soils." *Geotechnique*, 48(4), 465–481.

Oda, M., and Konishi, J. (1974). "Microscopic Deformation Mechanism of Granular Material in Simple Shear." *Soils and Foundations*, 14(4), 25–38.

Oda, M., Nemat-nasser, S., and Konishi, J. (1985). "Stress-induced anisotropy in granular masses." *Soils and Foundations*, 25(3), 85–97.

Oda, M., Takemura, T., and Takahashi, M. (2004). "Microstructure in shear band observed by microfocus X-ray computed tomography." *Geotechnique*, 54(8), 539–542.

Okubadejo, O., Karatza, Z., Ando, E., Bonnaud, L., Mura, M. D., and Viggiani, G. (2017). "Identification and tracking of particles undergoing progressive breakage under stress with 3D + t image analysis." *3rd International Conference on Tomography of Materials and Structures*.

Olsen, R., and Mitchell, J. (1995). "CPT stress normalization and prediction of soil classification." *Proceedings of International Symposium on Cone Penetration Testing*, SGI, Linköping, Sweden.

Omidvar, M., Iskander, M., and Bless, S. (2012). "Stress-strain behavior of sand at high strain rates." *International Journal of Impact Engineering*, Elsevier Ltd, 49, 192–213.

Omidvar, M., Malioche, J. D., Chen, Z., Iskander, M., and Bless, S. (2015). "Visualizing kinematics of dynamic penetration in granular media using transparent soils." *Geotechnical Testing Journal*, 38(5), 656–672.

Otani, J., Mukunoki, T., and Obara, Y. (2000). "Application of X-ray CT method for characterization of failure in soils." *Soils and Foundations*, 40(2), 111–118.

Otani, J., Mukunoki, T., and Sugawara, K. (2005). "Evaluation of particle crushing in soils using X-ray CT data." *Soils and Foundations*, 45(1), 99–108.

Otsu, N. (1979). "A threshold selection method from gray-level histograms." *IEEE Transactions on Systems, Man, and Cybernetics*, 9(1), 62–66.

Palmer, S. N., and Barton, M. E. (1986). "Avoiding Microfabric Disruption During the Impregnation of Friable, Uncemented Sands with Dyed Epoxy." *Journal of Sedimentary Research*, 56(4).

Pan, B., Qian, K., Xie, H., and Asundi, A. (2009). "Two-dimensional digital image correlation for in-plane displacement and strain measurement: a review." *Measurement Science and Technology*, IOP Publishing, 20(6), 062001.

Paniagua, P., Andò, E., Silva, M., Emdal, A., Nordal, S., and Viggiani, G. (2013). "Soil deformation around a penetrating cone in silt." *Géotechnique Letters*, 3(4), 185–191.

Paniagua, P., Fonseca, J., Gylland, A., and Nordal, S. (2018). "Investigation of the change in soil fabric during cone penetration in silt using 2D measurements." *Acta Geotechnica*, Springer Berlin Heidelberg, 13(1), 135–148.

Paniagua, P., Fonseca, J., Gylland, A. S., and Nordal, S. (2014). "Microstructural study of the deformation zones during cone penetration in silt at variable penetration rates." *Canadian Geotechnical Journal*, 2098(September), 1–42.

Parab, N. D., Claus, B., Hudspeth, M. C., Black, J. T., Mondal, A., Sun, J., Fezzaa, K., Xiao, X., Luo, S. N., and Chen, W. (2014). "Experimental assessment of fracture of individual sand particles at different loading rates." *International Journal of Impact Engineering*, 68, 8–14.

Peng, Y., Ding, X., Xiao, Y., Deng, X., and Deng, W. (2020). "Detailed amount of particle breakage in nonuniformly graded sands under one-dimensional compression." *Canadian Geotechnical Journal*, 57(8), 1239–1246.

Pestana, J. M., and Whittle, A. J. (1995). "Compression model for cohesionless soils." *Géotechnique*, 45(4), 611–631.

Rad, N. S., and Tumay, M. T. (1987). "Factors affecting sand specimen preparation by raining." *Geotechnical Testing Journal*, 10(1), 31.

Raffael, M., Willert, C., Wereley, S. T., and Kompenhans, J. (2007). *Particle Image Velocimetry (the Third Edition)*.

Raffel, M., Willert, C. E., Wereley, S. T., and Kompenhans, J. (2013). "Particle Image Velocimetry: A Practicle Guide." *Climate Change 2013 - The Physical Science Basis*, Experimental Fluid Mechanics, Intergovernmental Panel on Climate Change, ed., Cambridge University Press, 460.

Ramsey, N. (2002). "A calibrated model for the interpretation of cone penetration tests (CPTs) in North Sea quaternary soils." *Offshore Site Investigation and Geotechnics' Diversity and Sustainability*, Society of Underwater Technology.

Rebaï, S., Philip, H., and Taboada, A. (1992). "Modern tectonic stress field in the Mediterranean region: evidence for variation in stress directions at different scales." *Geophysical Journal International*, 110(1), 106–140.

Rechenmacher, A. L. (2006). "Grain-scale processes governing shear band initiation and evolution in sands." *Journal of the Mechanics and Physics of Solids*, 54(1), 22–45.

Rechenmacher, A. L., and Finno, R. J. (2004). "Digital Image Correlation to Evaluate Shear Banding in Dilative Sands." *Geotechnical Testing Journal*, 27(1), 13–22.

Roberts, J. E., and de Souza, J. M. (1958). "The compressibility of sands." *Proceedings of the American Society of Testing Materials1*, ASCE, New York, NY, United States, 1269–1277.

Robertson, P. K. (1990). "Soil classification using the cone penetration test." *Canadian Geotechnical Journal*, 27(1), 151–158.

Robertson, P. K. (2009). "Interpretation of cone penetration tests — a unified approach." *Canadian Geotechnical Journal*, 46(11), 1337–1355.

Robertson, P. K. (2010). "Evaluation of Flow Liquefaction and Liquefied Strength Using the Cone Penetration Test." *Journal of Geotechnical and Geoenvironmental Engineering*, 136(6), 842–853.

Robertson, P. K., and Campanella, R. G. (1985). "Liquefaction Potential of Sands Using the CPT." *Journal of Geotechnical Engineering*, 111(3), 384–403.

Robertson, P. K., and Wride, C. E. (1998). "Evaluating cyclic liquefaction potential using the cone penetration test." *Canadian Geotechnical Journal*, 35(3), 442–459.

Roscoe, K. H. (1970). "The influence of strains in soil mechanics." *Géotechnique*, 20(2), 129–170.

Saada, A. S., Liang, L., Figueroa, J. L., and Cope, C. T. (1999). "Bifurcation and shear band propagation in sands." *Geotechnique*, 49(3), 367–385.

Salgado, R. (1993). "Analysis of penetration resistance in sands." University of California, Berkeley.

Salgado, R. (2008). *The engineering of foundations*. McGraw-Hill, New York.

Salgado, R. (2014). "Experimental Research on Cone Penetration Resistance." *Geo-Congress 2014 Keynote Lectures*, American Society of Civil Engineers, 140–163.

Salgado, R., Boulanger, R. W., and Mitchell, J. K. (1997a). "Lateral Stress Effects on CPT Liquefaction Resistance Correlations." *Journal of Geotechnical and Geoenvironmental Engineering*, American Society of Civil Engineers, 123(8), 726–735.

Salgado, R., Ganju, E., and Prezzi, M. (2019). "Site variability analysis using cone penetration test data." *Computers and Geotechnics*, Elsevier, 105(June 2018), 37–50.

Salgado, R., Mitchell, J. K., and Jamiolkowski, M. (1998). "Calibration Chamber Size Effects on Penetration Resistance in Sand." *Journal of Geotechnical and Geoenvironmental Engineering*, 124(9), 878–888.

Salgado, R., Mitchell, J. K., Jamiolkowski, M., Jamiolhowski, M., and Jamiolkowski, M. (1997b). "Cavity expansion and penetration resistance in sand." *Journal of Geotechnical and Geoenvironmental Engineering*, American Society of Civil Engineers, 123(4), 344–354.

Salgado, R., and Prezzi, M. (2007). "Computation of cavity expansion pressure and penetration resistance in sands." *International Journal of Geomechanics*, American Society of Civil Engineers, 7(4), 251–265.

Salgado, R., Prezzi, M., and Ganju, E. (2015). *Assessment of Site Variability from Analysis of Cone Penetration Test Data*.

Salgado, R., and Randolph, M. F. (2001). "Analysis of Cavity Expansion in Sand." *International Journal of Geomechanics*, 1(2), 175–192.

Sammis, C., King, G., and Biegel, R. (1987). "The kinematics of gouge deformation." *Pure and Applied Geophysics*, 125(5), 777–812.

Sanglerat, G., Nhim, T. V., Sejourne, M., and Andina, R. (1974). "Direct soil classification by static penetrometer with special friction sleeve." *Proceedings of the first European symposium on penetration testing*, 5–7.

Schnaid, F., and Houlsby, G. T. (1991). "An assessment of chamber size effects in the calibration of in situ tests in sand." *Géotechnique*, 41(3), 437–445.

Schneider, H. R., Chameau, J. Lou, and Leonards, G. A. (1989). "Chemical impregnation of cohesionless soils." *Geotechnical Testing Journal*, 12(3), 204–210.

Schneider, J. A., Hotstream, J. N., Mayne, P. W., and Randolph, M. F. (2012). "Comparing CPTU Q – F and Q – Δ u 2 /σ v0 ′soil classification charts." *Géotechnique Letters*, 2(4), 209–215.

Seo, D., Sohn, C., Cil, M., and Buscarnera, G. (2020). "Evolution of particle morphology and mode of fracture during the oedometric compression of sand." *Géotechnique,* 1–13.

Shi, D., Zheng, L., Xue, J., and Sun, J. (2016). "DEM Modeling of Particle Breakage in Silica Sands under One-Dimensional Compression." *Acta Mechanica Solida Sinica*, The Chinese Society of Theoretical and Applied Mechanics, 29(1), 78–94.

Shi, J., Guo, P., and Stolle, D. (2020). "Micromechanical analysis of non-coaxiality between stress and strain increment in granular materials." *Acta Geotechnica*, Springer Berlin Heidelberg, 15(9), 2559–2574.

Silva, I. M., Combe, G., Foray, P., Flin, F., and Lesaffre, B. (2013). "Postmortem analysis of sand grain crushing from pile interface using X-ray tomography." *AIP Conference Proceedings*, 297–300.

Stamati, O., Andò, E., Roubin, E., Cailletaud, R., Wiebicke, M., Pinzon, G., Couture, C., Hurley, R., Caulk, R., Caillerie, D., Matsushima, T., Bésuelle, P., Bertoni, F., Arnaud, T., Laborin, A., Rorato, R., Sun, Y., Tengattini, A., Okubadejo, O., Colliat, J.-B., Saadatfar, M., Garcia, F., Papazoglou, C., Vego, I., Brisard, S., Dijkstra, J., and Birmpilis, G. (2020). "spam: Software for Practical Analysis of Materials." *Journal of Open Source Software*, 5(51), 2286.

Stuedlein, A. W., Kramer, S. L., Arduino, P., and Holtz, R. D. (2012). "Geotechnical Characterization and Random Field Modeling of Desiccated Clay." *Journal of Geotechnical and Geoenvironmental Engineering*, 138(11), 1301–1313.

Suescun-Florez, E., Iskander, M., and Bless, S. (2020). "Evolution of particle damage of sand during axial compression via arrested tests." *Acta Geotechnica*, Springer, 15(1), 95–112.

Susila, E., and Hryciw, R. D. (2003). "Large displacement FEM modelling of the cone penetration test (CPT) in normally consolidated sand." *International Journal for Numerical and Analytical Methods in Geomechanics*, 27(7), 585–602.

Sutterer, K. G., Frost, J. D., and Chameau, J. A. (1996). "Polymer impregnation to assist undisturbed sampling of cohesionless soils." *Journal of geotechnical engineering*, 122(3), 209–215.

Sutton, M. A., Orteu, J.-J., and Schreier, H. W. (2009). *Image correlation for shape, motion and deformation measurements*. Springer Science & Business Media, New York, NY.

Teh, C. I., and Houlsby, G. T. (1991). "An analytical study of the cone penetration test in clay." *Géotechnique*, Thomas Telford Ltd , 41(1), 17–34.

Tehrani, F. S. (2014). "Study of the loading of piles using semi-analytical method and digital image correlaiton technique." Purdue University.

Tehrani, F. S., Arshad, M. I., Prezzi, M., and Salgado, R. (2018). "Physical modeling of cone penetration in layered sand." *Journal of Geotechnical and Geoenvironmental Engineering*, 144(1), 04017101.

Tehrani, F. S., Han, F., Salgado, R., and Prezzi, M. (2017). "Laboratory Study of the Effect of Pile Surface Roughness on the Response of Soil and Non-Displacement Piles." *Geotechnical Frontiers 2017*, American Society of Civil Engineers, Reston, VA, VA, 256–264.

Tehrani, F. S., Han, F., Salgado, R., Prezzi, M., Tovar, R. D., and Castro, A. G. (2016). “Effect of surface roughness on the shaft resistance of non-displacement piles embedded in sand.” *Géotechnique*, 66(5), 386–400.

Terzaghi, K. (1943). *Theoretical soil mechanics*. John Wiley & Sons, New York.

Terzaghi, K., and Peck, R. B. (1948). *Soil mechanics in engineering practice*. John Wiley & Sons.

Tovar-Valencia, R. D., Galvis-Castro, A., Salgado, R., and Prezzi, M. (2018). “Effect of Surface Roughness on the Shaft Resistance of Displacement Model Piles in Sand.” *Journal of Geotechnical and Geoenvironmental Engineering*, 144(3), 04017120.

Tovey, N. K., and Dadey, K. A. (2002). “Quantitative orientation and micro-porosity analysis of recent marine sediment microfabric.” *Quaternary International*, 92(1), 89–100.

Tsoungui, O., Vallet, D., and Charmet, J. C. (1999). “Numerical model of crushing of grains inside two-dimensional granular materials.” *Powder Technology*, 105(1–3), 190–198.

Tumay, M. T. (1985). *Field calibration of electric cone penetrometers in soft soils*. Baton Rouge.

Turcotte, D. L. (1986). “Fractals and fragmentation.” *Journal of Geophysical Research*, 91(B2), 1921–1926.

Uziellia, M., Vannucchi, G., and Phoon, K. (2005). “Random field characterisation of stress-normalised cone penetration testing parameters.” *Geotechnique*, 55(1), 3–20.

Vaid, Y. P., and Negussey, D. (1984). “Relative density of pluviated sand samples.” *Soils and Foundations*, 24(2), 101–105.

Vaid, Y. P., and Sivathayalan, S. (2000). “Fundamental factors affecting liquefaction susceptibility of sands.” *Canadian Geotechnical Journal*, 37(3), 592–606.

Vallejo, L. E., and Lobo-Guerrero, S. (2005). “DEM analysis of crushing around driven piles in granular materials.” *Géotechnique*, 55(8), 617–623.

Vesic, A. S. (1963). “Bearing Capacity of Deep Foundations in Sand.” *Highway Research Record*, 39, 112–153.

Vesic, A. S. (1972). “Expansion of cavities in infinite soil mass.” *Journal of Soil Mechanics & Foundations Divison*, 98(3), 265–290.

Viggiani, G., Andò, E., Takano, D., and Santamarina, J. C. (2015). “Laboratory X-ray tomography: A valuable experimental tool for revealing processes in soils.” *Geotechnical Testing Journal*, 38(1), 61–71.

Wadell, H. (1932). “Volume, shape, and roundness of rock particles.” *The Journal of Geology*, 40(5), 443–451.

Wadell, H. (1935). “Volume, shape, and roundness of quartz particles.” *The Journal of Geology*, 43(3), 250–280.

Wang, D., Bienen, B., Nazem, M., Tian, Y., Zheng, J., Pucker, T., and Randolph, M. F. (2015). “Large deformation finite element analyses in geotechnical engineering.” *Computers and Geotechnics*, Elsevier Ltd, 65, 104–114.

Wang, J., and Zhao, B. (2014). “Discrete-continuum analysis of monotonic pile penetration in crushable sands.” *Canadian Geotechnical Journal*, 51(10), 1095–1110.

Weibull, W. (1951). “A statistical distribution function of wide applicability.” *Journal of applied mechanics*, 103, 293–297.

White, D. J., and Bolton, M. D. (2004). “Displacement and strain paths during plane-strain model pile installation in sand.” *Géotechnique*, 54(6), 375–397.

White, D. J., Take, W. A., and Bolton, M. D. (2003). “Soil deformation measurement using particle image velocimetry (PIV) and photogrammetry.” *Geotechnique*, 53(7), 619–631.

Wiebicke, M., Ando, E., Herle, I., and Viggiani, G. (2017). “On the metrology of interparticle contacts in sand from x-ray tomography images.” *Measurement Science and Technology*, 28(12).

Wiebicke, M., Andò, E., Šmilauer, V., Herle, I., and Viggiani, G. (2019). “A benchmark strategy for the experimental measurement of contact fabric.” *Granular Matter*, Springer Berlin Heidelberg, 21(3), 54.

Wiebicke, M., Andò, E., Viggiani, G., and Herle, I. (2020a). “Measuring the evolution of contact fabric in shear bands with X-ray tomography.” *Acta Geotechnica*, Springer, 15(1), 79–93.

Wiebicke, M., Herle, I., Andò, E., and Viggiani, G. (2020b). “Measuring the fabric evolution of sand – application and challenges.” *geotechnik*, gete.202000019.

Wilkinson, S. (2011). “The microstructure of UK mudrocks.” University of London.

Woo, S. I. (2015). “Numerical simulation of penetration in sand.” Purdue University.

Woo, S. I., and Salgado, R. (2018). “Simulation of penetration of a foundation element in Tresca soil using the generalized interpolation material point method (GIMP).” *Computers and Geotechnics*, Elsevier Ltd, 94, 106–117.

Wu, M., Wang, J., and Zhao, B. (2021). “DEM modeling of the one-dimensional compression of sands incorporating a statistical particle fragmentation scheme.” *Canadian Geotechnical Journal*, (852), 1–48.

Xiao, T., Li, D.-Q., Cao, Z.-J., and Zhang, L.-M. (2018). “CPT-Based Probabilistic Characterization of Three-Dimensional Spatial Variability Using MLE.” *Journal of Geotechnical and Geoenvironmental Engineering*, 144(5), 04018023.

Xiao, Y., Desai, C. S., Daouadji, A., Stuedlein, A. W., Liu, H., and Abuel-Naga, H. (2020). "Grain crushing in geoscience materials–Key issues on crushing response, measurement and modeling: Review and preface." *Geoscience Frontiers*, Elsevier Ltd, (November).

Xiao, Y., Liu, H., Chen, Q., Ma, Q., Xiang, Y., and Zheng, Y. (2017). "Particle breakage and deformation of carbonate sands with wide range of densities during compression loading process." *Acta Geotechnica*, Springer Berlin Heidelberg, 12(5), 1177–1184.

Xiao, Y., Liu, H., Chen, Y., and Jiang, J. (2014). "Bounding Surface Model for Rockfill Materials Dependent on Density and Pressure under Triaxial Stress Conditions." *Journal of Engineering Mechanics*, 140(4), 04014002.

Xiao, Y., Liu, H., Desai, C. S., Sun, Y., and Liu, H. (2016a). "Effect of Intermediate Principal-Stress Ratio on Particle Breakage of Rockfill Material." *Journal of Geotechnical and Geoenvironmental Engineering*, 142(4), 06015017.

Xiao, Y., Liu, H., Ding, X., Chen, Y., Jiang, J., and Wengang Zhang. (2016b). "Influence of Particle Breakage on Critical State Line of Rockfill Material." *International Journal of Geomechanics*, 16(1), 04015031.

Yang, Z., Jardine, R., Guo, W., and Chow, F. (2016). "ZJU-ICL Database." *A Comprehensive Database of Tests on Axially Loaded Piles Driven in Sand*, Elsevier, London, England, 61–242.

Yang, Z., Liu, X., Guo, L., Cui, Y., Su, X., and Ling, X. (2021). "Soil Classification and Site Variability Analysis Based on CPT—A Case Study in the Yellow River Subaquatic Delta, China." *Journal of Marine Science and Engineering*, 9(4), 431.

Yang, Z. X., Jardine, R. J., Zhu, B. T., Foray, P., and Tsuha, C. H. C. (2010). "Sand grain crushing and interface shearing during displacement pile installation in sand." *Géotechnique*, 60(6), 469–482.

Yao, Y., Yamamoto, H., and Wang, N. (2008). "Constitutive model considering sand crushing." *Soils and foundations*, 48(4), 603–608.

Yasufuku, N., and Hyde, A. F. L. (1995). "Pile end-bearing capacity in crushable sands." *Geotechnique*, Thomas Telford, 45(4), 663–676.

Yu, F. (2019). "Particle breakage in granular soils: a review." *Particulate Science and Technology*, Taylor and Francis Inc., 1–10.

Yu, H. S., Herrmann, L. R., and Boulanger, R. W. (2000). "Analysis of Steady Cone Penetration in Clay." *Journal of Geotechnical and Geoenvironmental Engineering*, 126(7), 594–605.

Yu, H. S., and Houlsby, G. T. (1991). "Finite cavity expansion in dilatant soils: loading analysis." *Géotechnique*, 41(2), 173–183.

Zeiss. (2016). *ZEISS Xradia Versa User's Guide*.

Zhang, C., Nguyen, G. D., and Einav, I. (2013). "The end-bearing capacity of piles penetrating into crushable soils." *Géotechnique*, 63(5), 341–354.

Zhang, Z., and Tumay, M. T. (1999). "Statistical to Fuzzy Approach Toward CPT Soil Classification." *Journal of Geotechnical and Geoenvironmental Engineering*, American Society of Civil Engineers, 125(3), 179–186.

Zhao, B., Wang, J., Andò, E., Viggiani, G., and Coop, M. (2019). "An Investigation of Particle Breakage under One-Dimensional Compression of Sand Using X-ray Micro-Tomography." *Canadian Geotechnical Journal*, 9(June), 1–9.

Zhao, B., Wang, J., Coop, M. R., Viggiani, G., and Jiang, M. (2015). "An investigation of single sand particle fracture using x-ray micro-tomography." *Geotechnique*, 65(8), 625–641.

Zhao, J., Jiang, M., Soga, K., and Luding, S. (2016). "Micro origins for macro behavior in granular media." *Granular Matter*, Springer New York LLC.

Zheng, J., and Hryciw, R. D. (2015). "Traditional soil particle sphericity, roundness and surface roughness by computational geometry." *Géotechnique*, 65(6), 494–506.

Zheng, W., and Tannant, D. (2016). "Frac sand crushing characteristics and morphology changes under high compressive stress and implications for sand pack permeability." *Canadian Geotechnical Journal*, 53(9), 1412–1423.

Zlatovic, S., and Ishihara, K. (1997). "Normalized behavior of very loose non-plastic Soils: effects of fabric." *Soils and foundations*, 37(4), 47–56.

Zoback, M. D., and Healy, J. H. (1992). "In situ stress measurements to 3.5 km depth in the Cajon Pass scientific research borehole: implications for the mechanics of crustal faulting." *Journal of Geophysical Research*, 97(B4), 5039–5057.

Zoback, M. D., Tsukahara, H., and Hickman, S. (1980). "Stress measurements at depth in the vicinity of the San Andreas Fault: Implications for the magnitude of shear stress at depth." *Journal of Geophysical Research: Solid Earth*, 85(B11), 6157–6173.

APPENDIX A DISPLACEMENT AND STRAIN FIELDS AROUND THE CONE PENETROMETER

In this section, the incremental displacement and strain fields around the cone penetrometer are presented. These displacement and strain fields correspond to a penetration increment of 2 mm of the penetrometer at a penetration depth of approximately 380 mm under different vertical confinements. The data presented here is meant supplement the displacement and strain fields presented in Chapters 3-5. The DIC analysis procedure followed to obtain these are presented in Chapter 3. The volumetric and hoop strain around the cone penetrometer are obtained following the procedure outlined by Tehrani et al. (2018). For all the plots, the solid mechanics sign convention is followed (extension positive and compression negative).

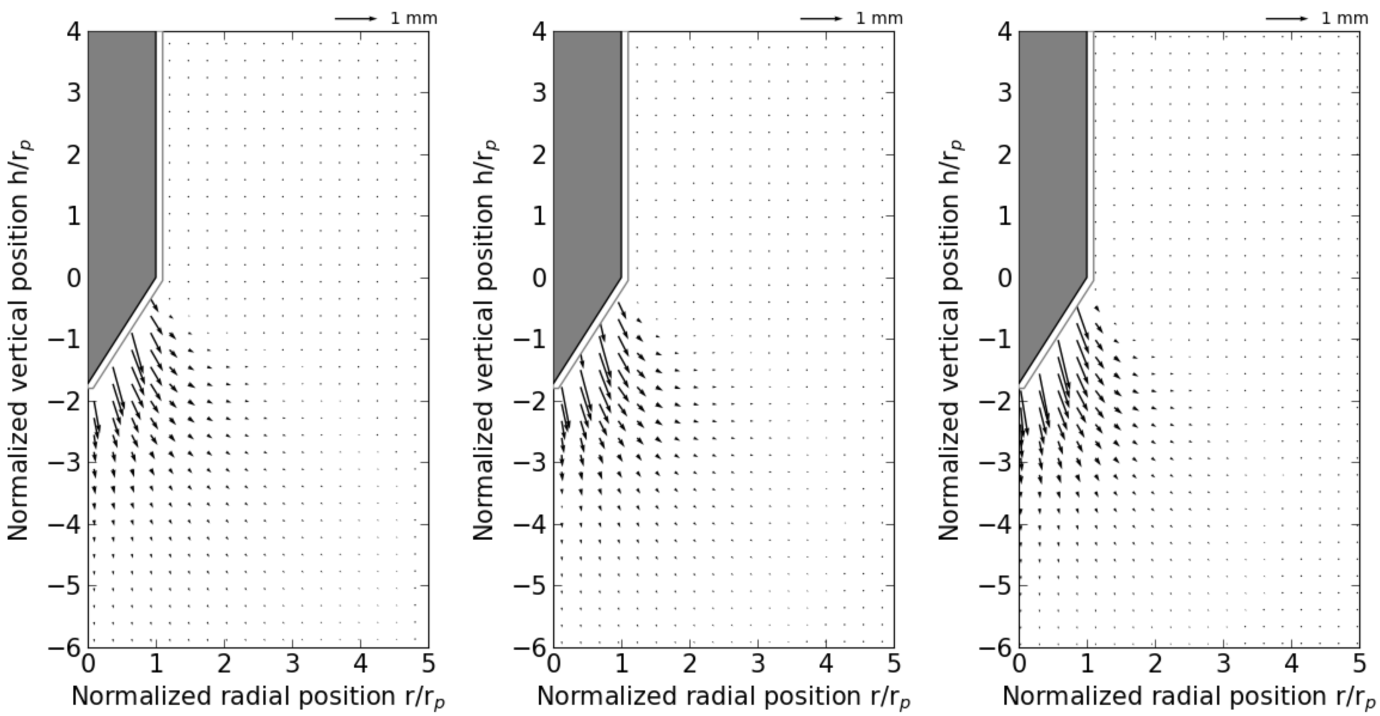

(a) (b) (c)

Figure A 1 Incremental displacement field around cone penetrometer for a 2 mm penetration increment in dense 2QR sand under a vertical pressure of (a) 17 kPa, (b) 33 kPa, and (c) 57 kPa.

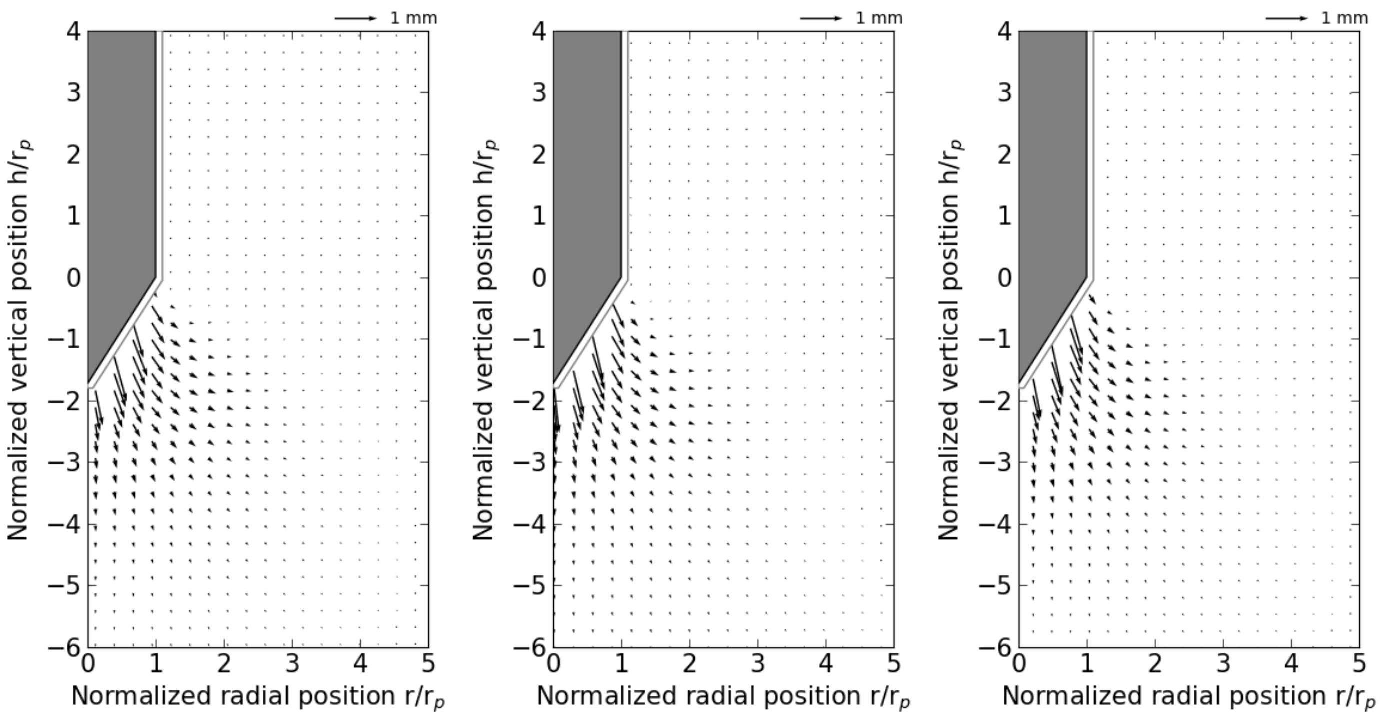

(a) (b) (c)

Figure A 2 Incremental displacement field around cone penetrometer for a 2 mm penetration increment in dense OGF sand under a vertical pressure of (a) 17 kPa, (b) 33 kPa, and (c) 57 kPa.

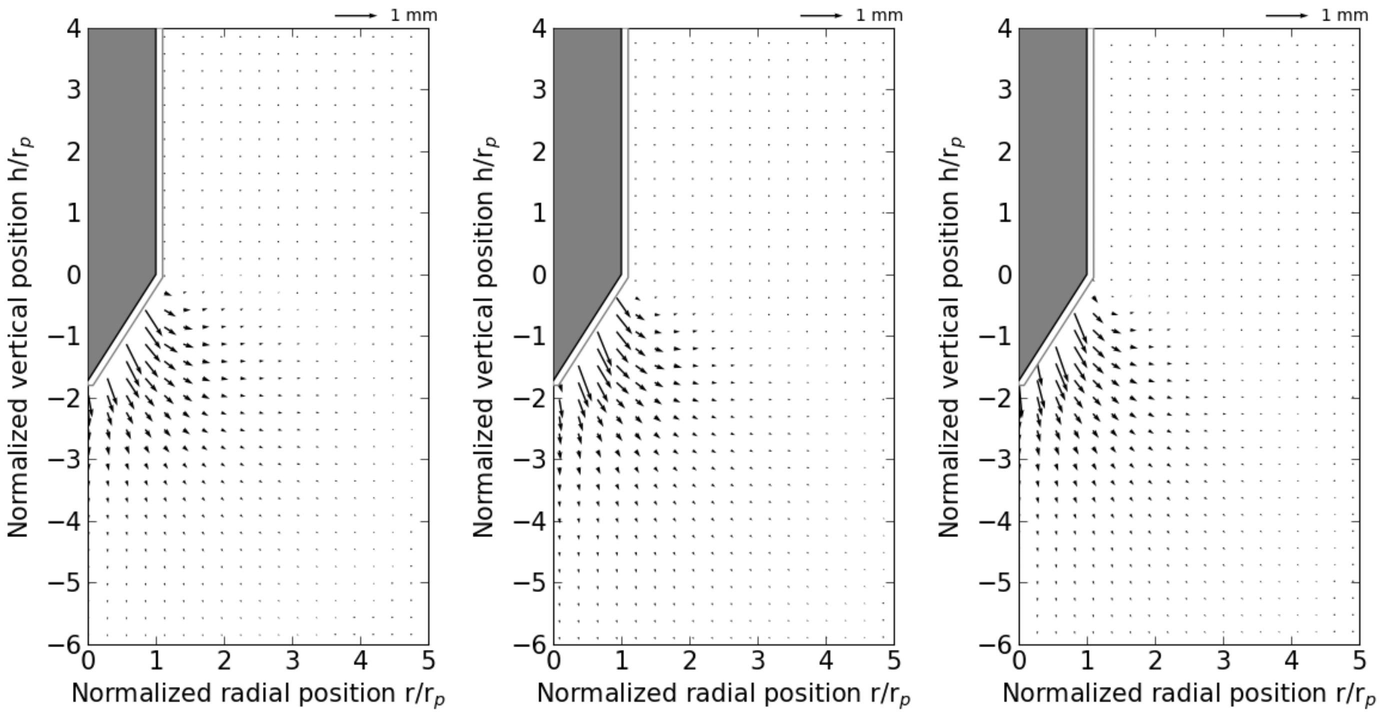

(a) (b) (c)

Figure A 3 Incremental displacement field around cone penetrometer for a 2 mm penetration increment in dense OTC sand under a vertical pressure of (a) 17 kPa, (b) 33 kPa, and (c) 57 kPa.

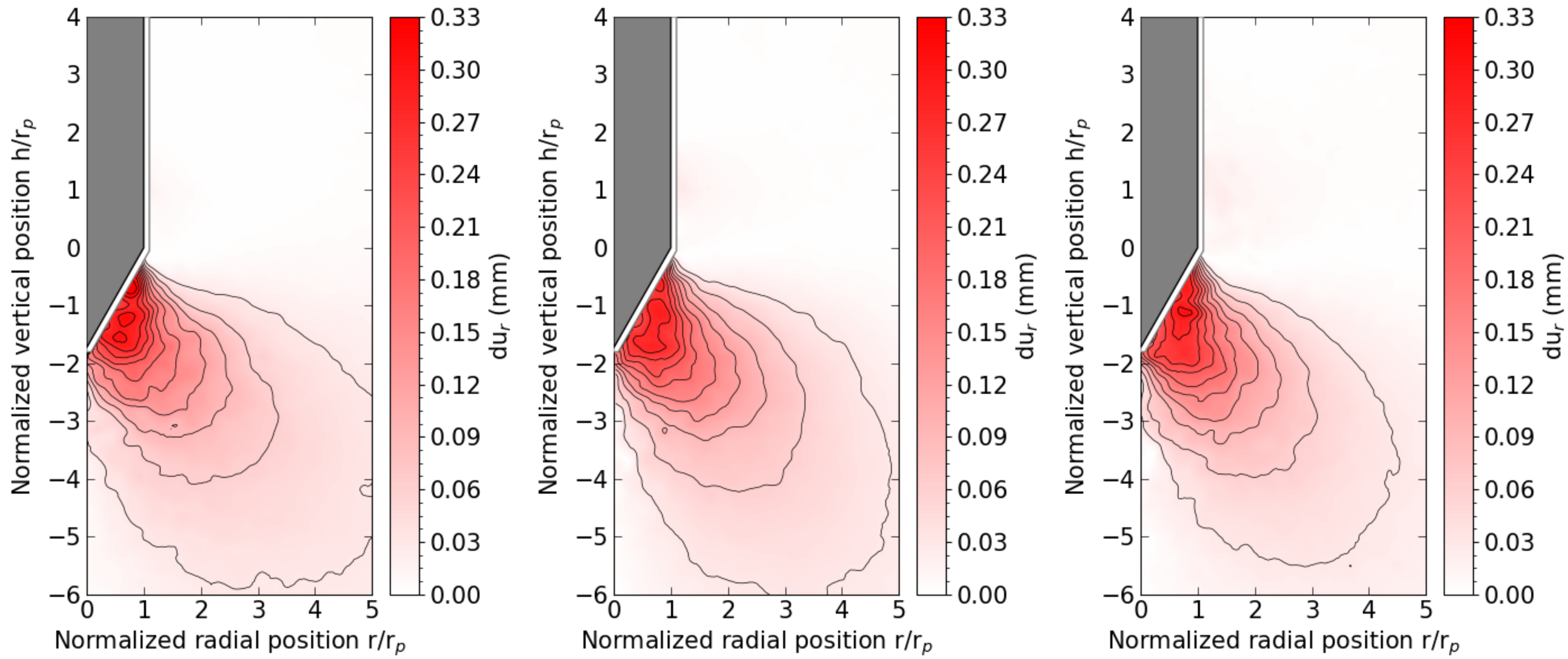

(a) (b) (c)

Figure A 4 Incremental radial displacement field around cone penetrometer for a 2 mm penetration increment in dense 2QR sand under a vertical pressure of (a) 17 kPa, (b) 33 kPa, and (c) 57 kPa.

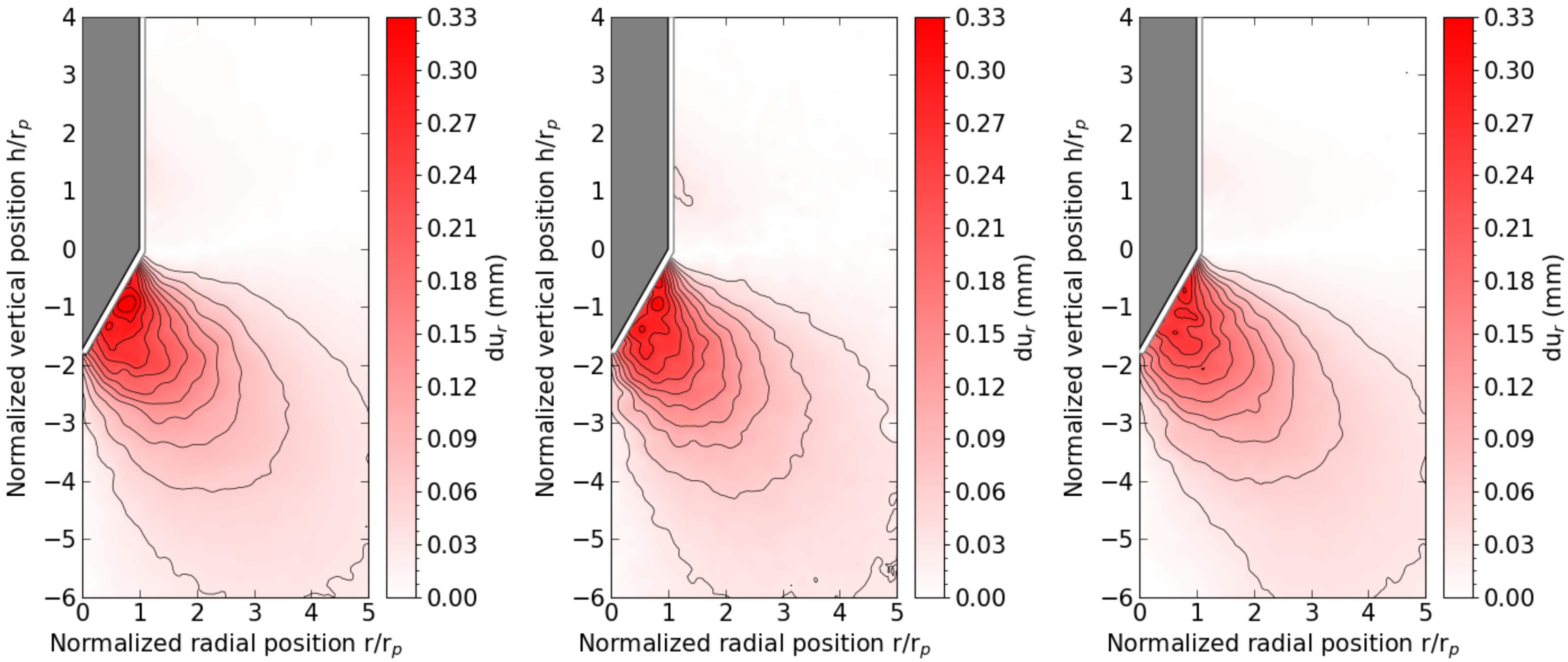

(a) (b) (c)

Figure A 5 Incremental radial displacement field around cone penetrometer for a 2 mm penetration increment in dense OGF sand under a vertical pressure of (a) 17 kPa, (b) 33 kPa, and (c) 57 kPa.

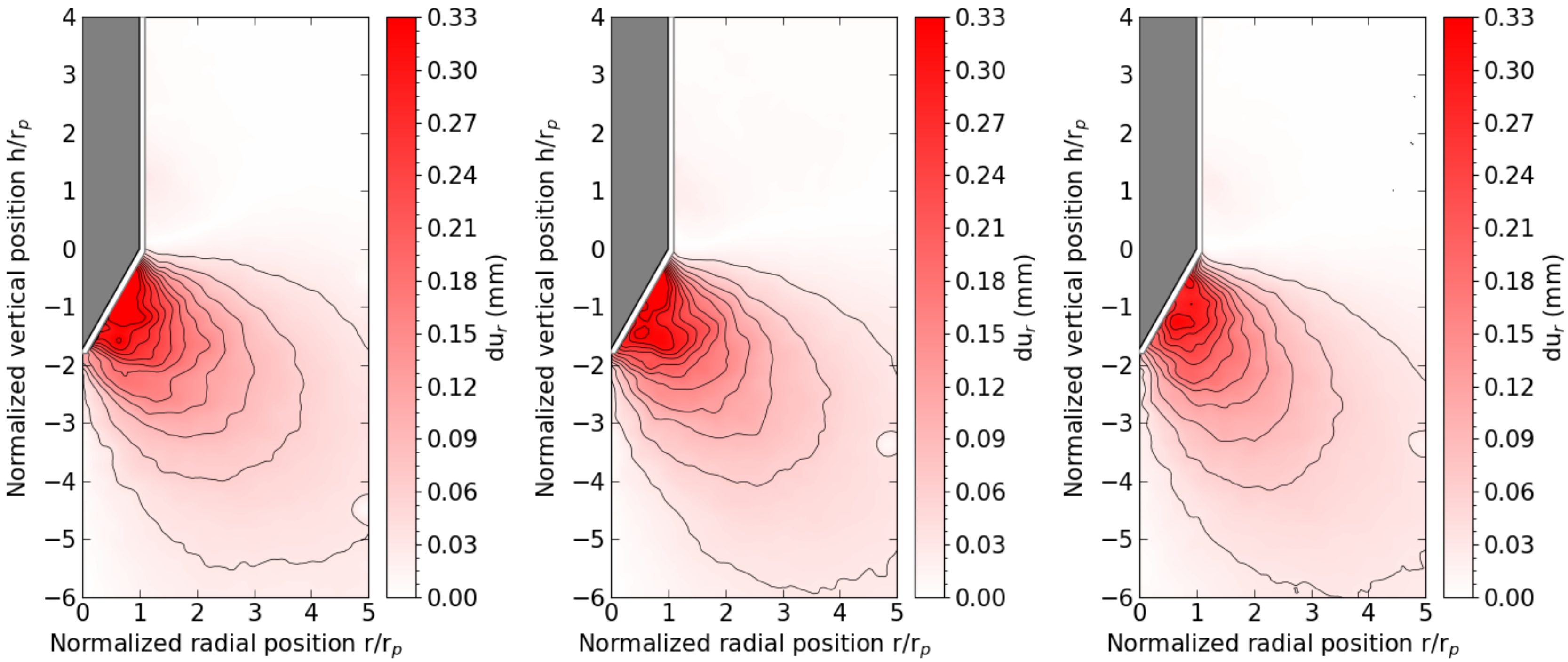

(a) (b) (c)

Figure A 6 Incremental radial displacement field around cone penetrometer for a 2 mm penetration increment in dense OTC sand under a vertical pressure of (a) 17 kPa, (b) 33 kPa, and (c) 57 kPa.

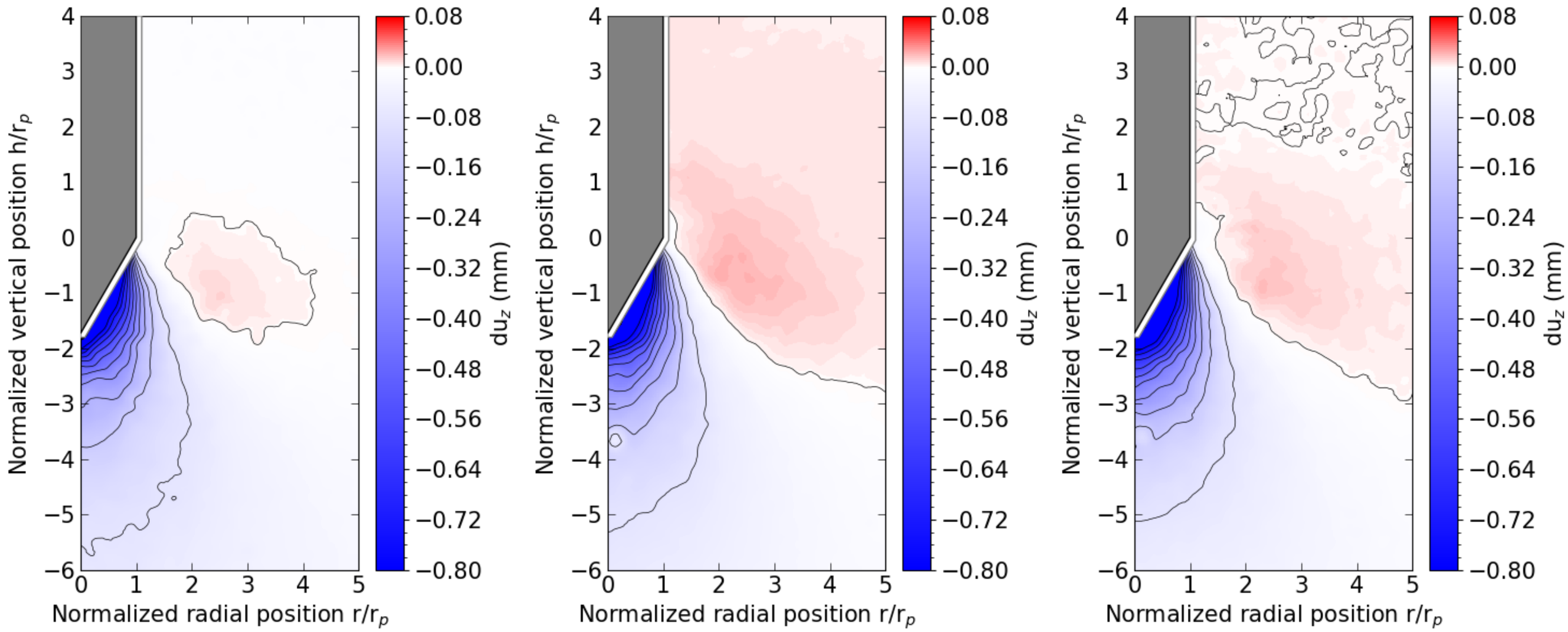

(a) (b) (c)

Figure A 7 Incremental vertical displacement field around cone penetrometer for a 2 mm penetration increment in dense 2QR sand under a vertical pressure of (a) 17 kPa, (b) 33 kPa, and (c) 57 kPa.

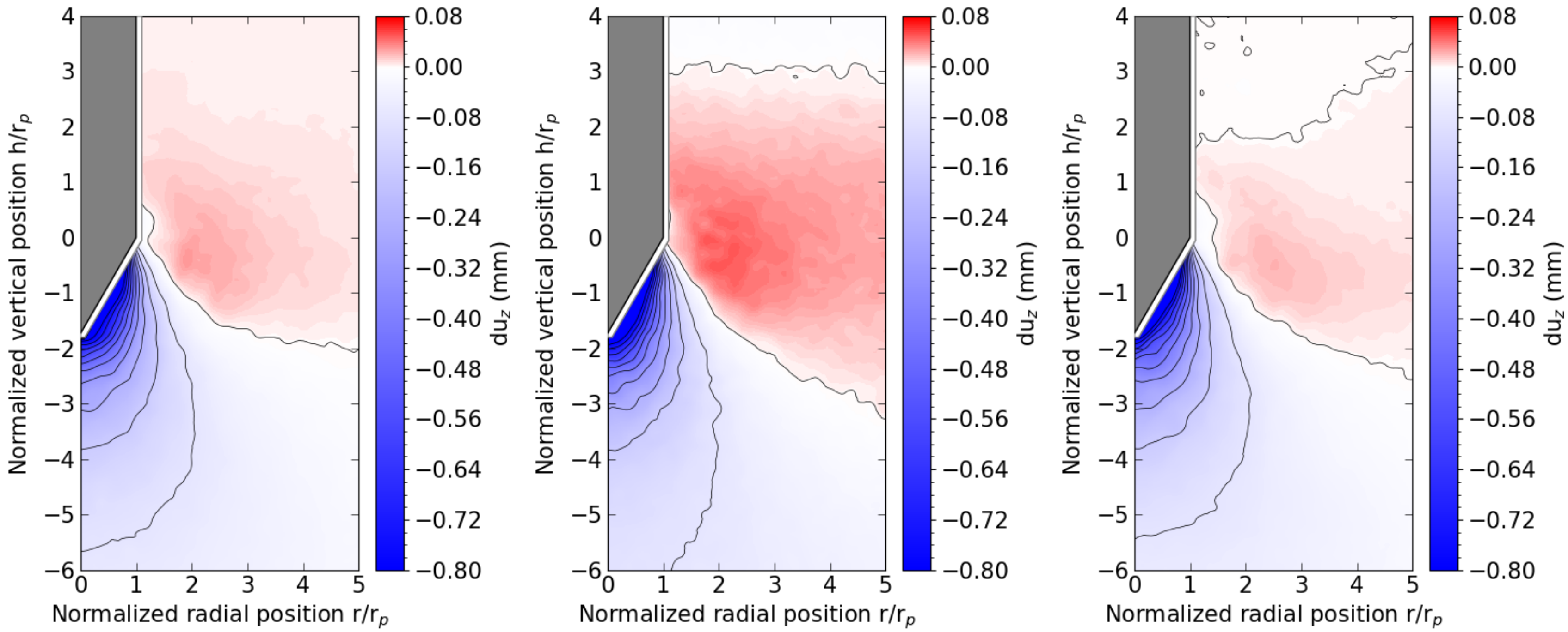

(a) (b) (c)

Figure A 8 Incremental vertical displacement field around cone penetrometer for a 2 mm penetration increment in dense OGF sand under a vertical pressure of (a) 17 kPa, (b) 33 kPa, and (c) 57 kPa.

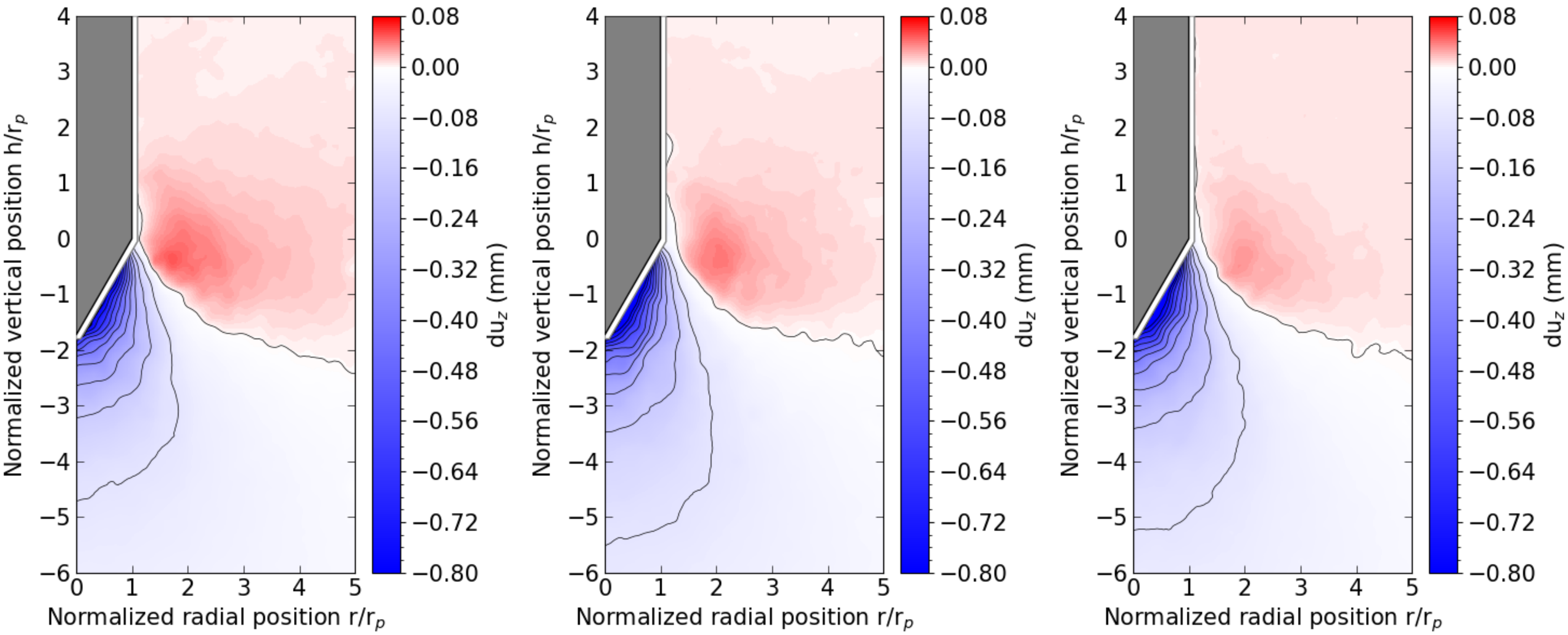

(a) (b) (c)

Figure A 9 Incremental vertical displacement field around cone penetrometer for a 2 mm penetration increment in dense OTC sand under a vertical pressure of (a) 17 kPa, (b) 33 kPa, and (c) 57 kPa.

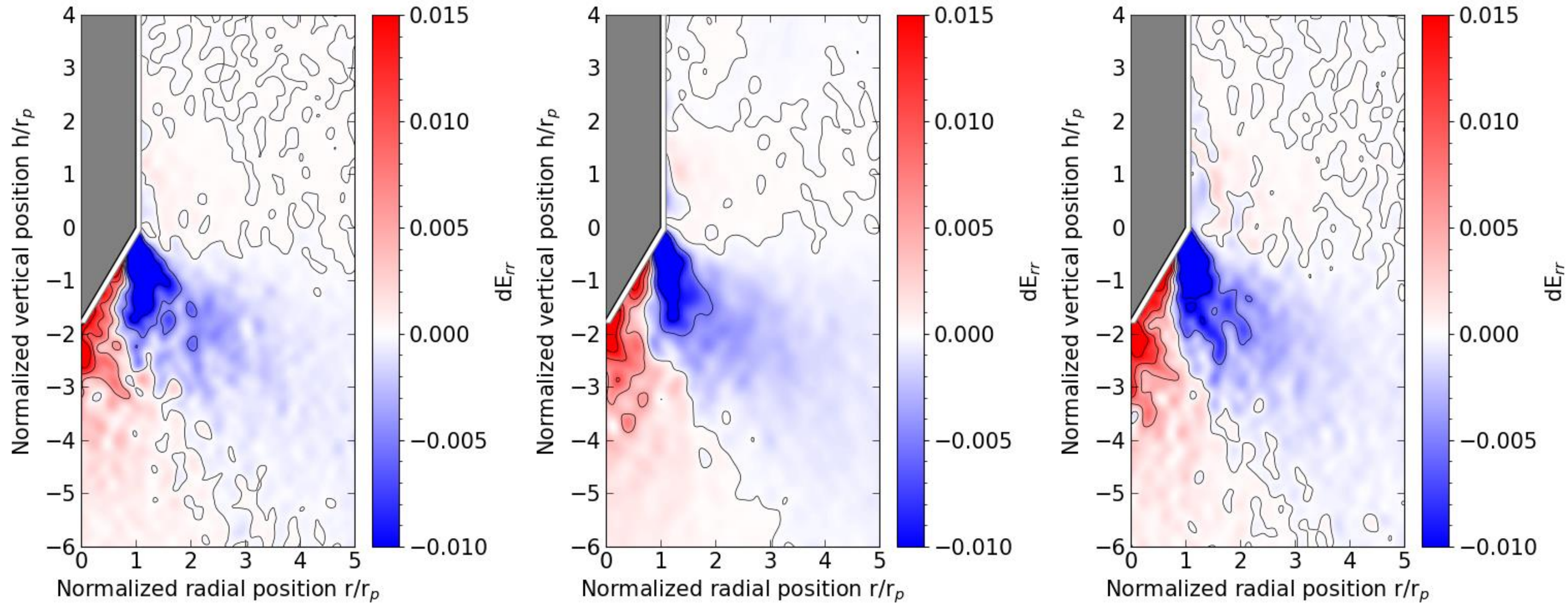

(a) (b) (c)

Figure A 10 Incremental radial strain field around cone penetrometer for a 2 mm penetration increment in dense 2QR sand under a vertical pressure of (a) 17 kPa, (b) 33 kPa, and (c) 57 kPa.

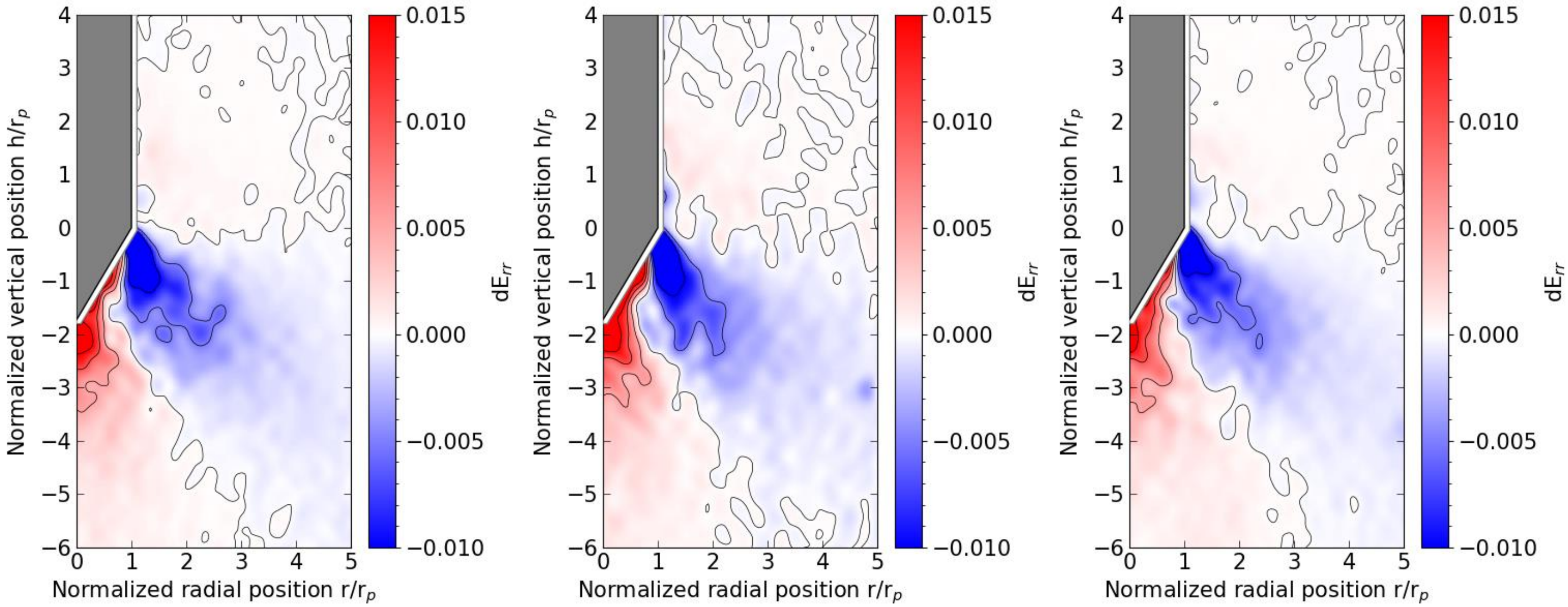

(a) (b) (c)

Figure A 11 Incremental radial strain field around cone penetrometer for a 2 mm penetration increment in dense OGF sand under a vertical pressure of (a) 17 kPa, (b) 33 kPa, and (c) 57 kPa.

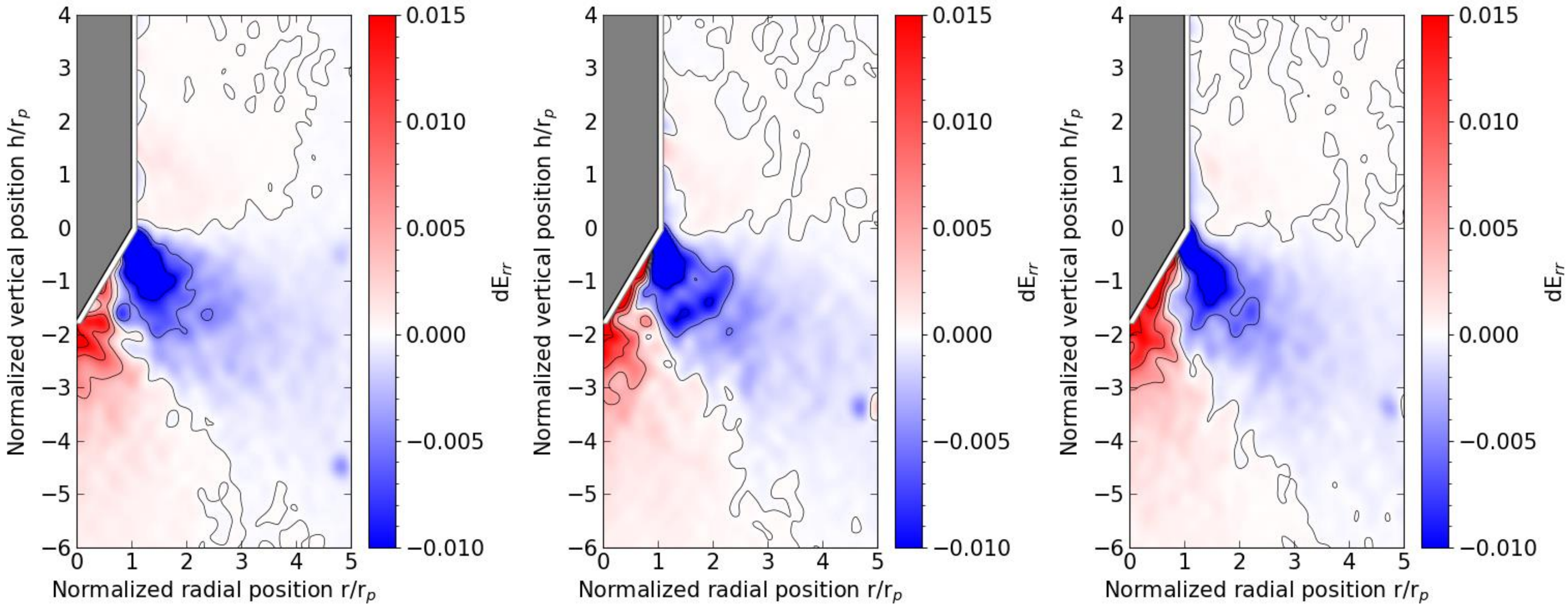

(a) (b) (c)

Figure A 12 Incremental radial strain field around cone penetrometer for a 2 mm penetration increment in dense OTC sand under a vertical pressure of (a) 17 kPa, (b) 33 kPa, and (c) 57 kPa.

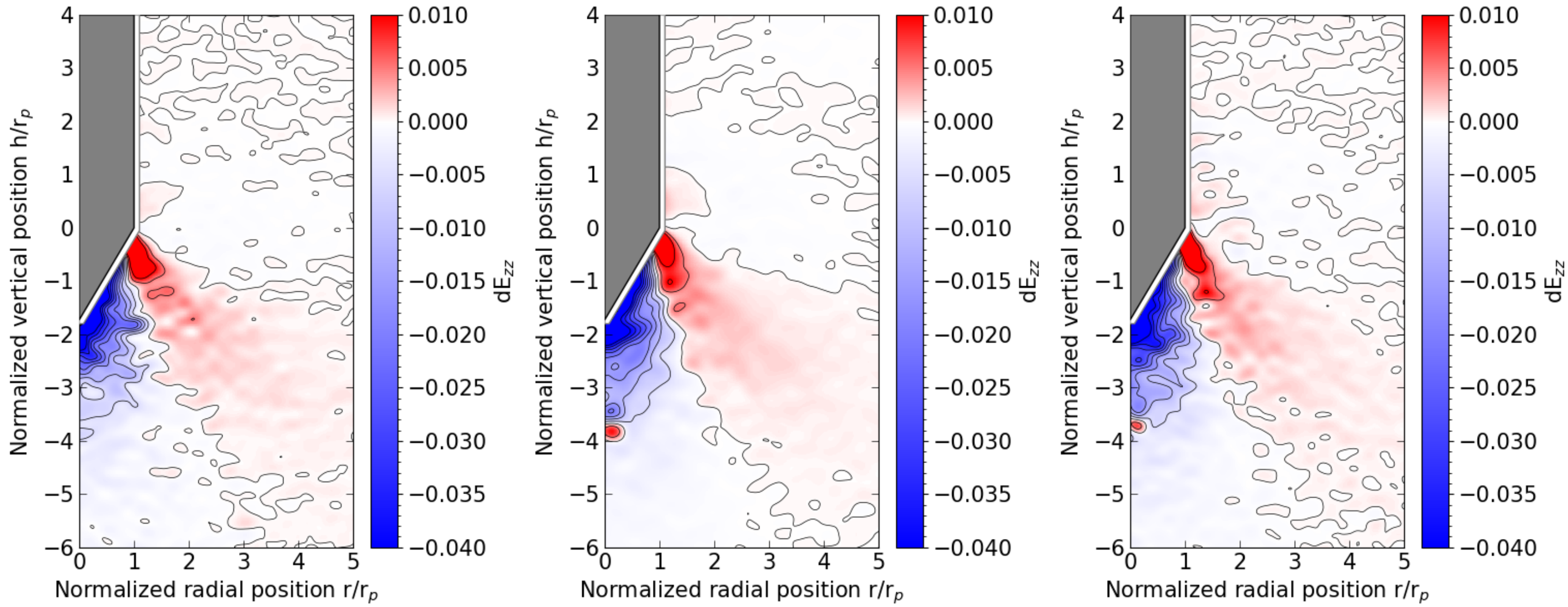

(a) (b) (c)

Figure A 13 Incremental vertical strain field around cone penetrometer for a 2 mm penetration increment in dense 2QR sand under a vertical pressure of (a) 17 kPa, (b) 33 kPa, and (c) 57 kPa.

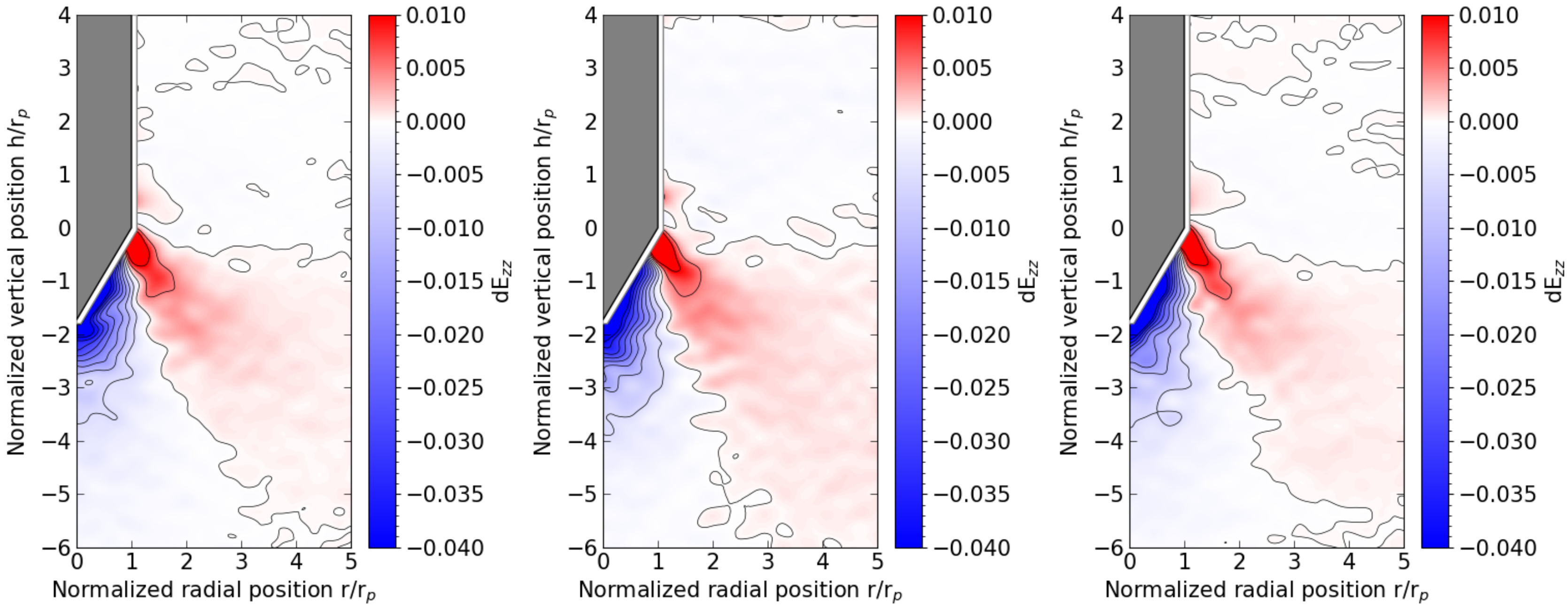

(a) (b) (c)

Figure A 14 Incremental vertical strain field around cone penetrometer for a 2 mm penetration increment in dense OGF sand under a vertical pressure of (a) 17 kPa, (b) 33 kPa, and (c) 57 kPa.

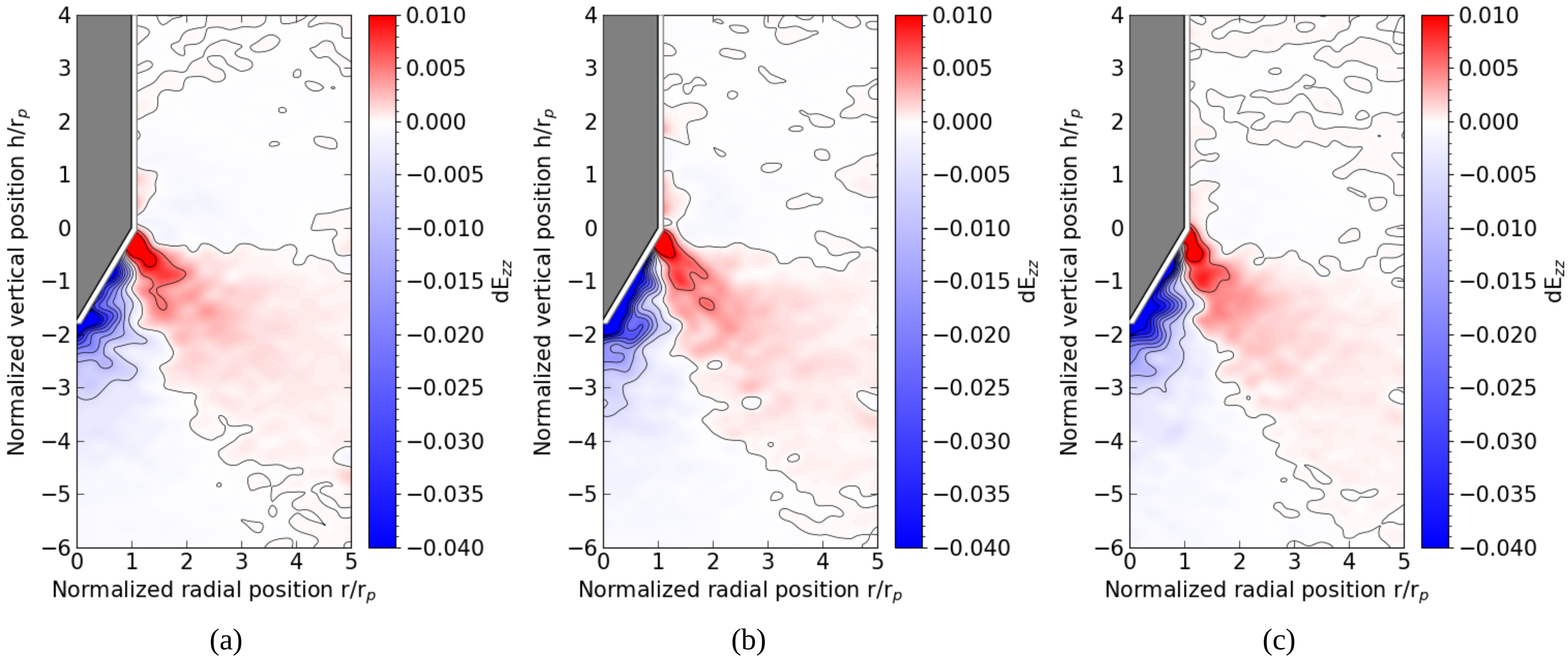

Figure A 15 Incremental vertical strain field around cone penetrometer for a 2 mm penetration increment in dense OTC sand under a vertical pressure of (a) 17 kPa, (b) 33 kPa, and (c) 57 kPa.

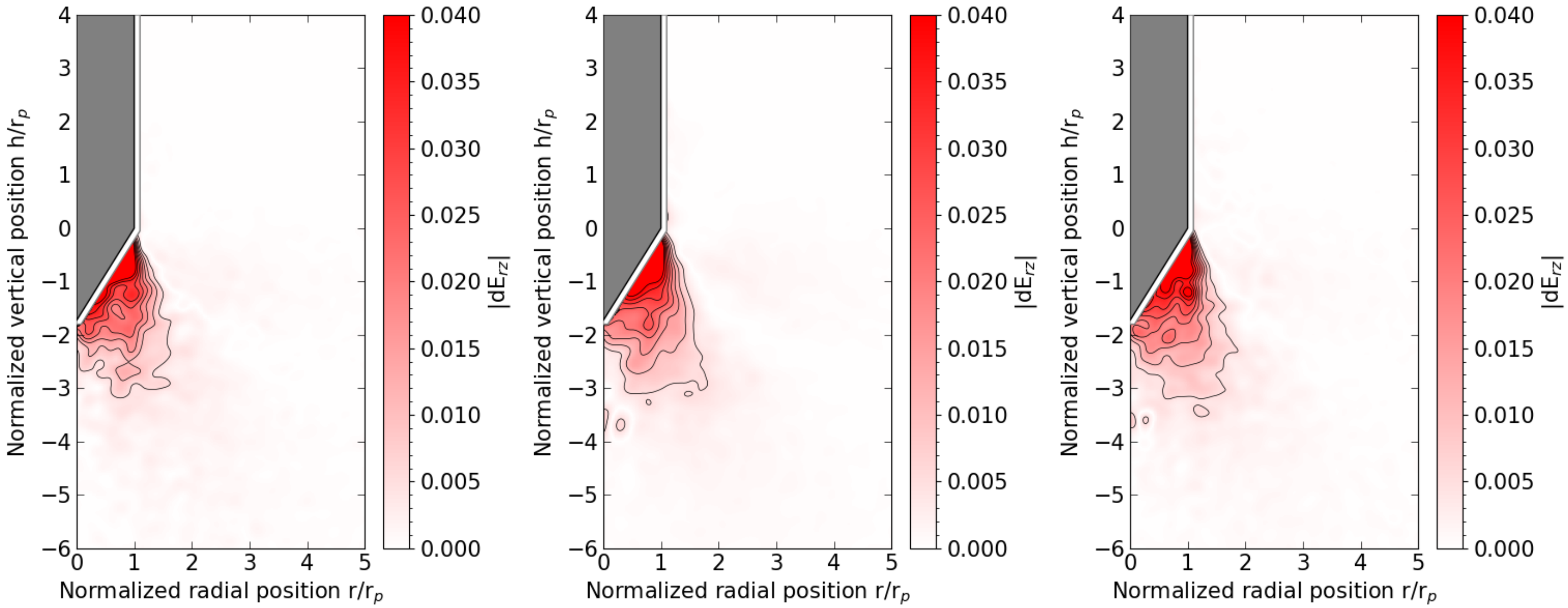

(a) (b) (c)

Figure A 16 Incremental shear strain field around cone penetrometer for a 2 mm penetration increment in dense 2QR sand under a vertical pressure of (a) 17 kPa, (b) 33 kPa, and (c) 57 kPa.

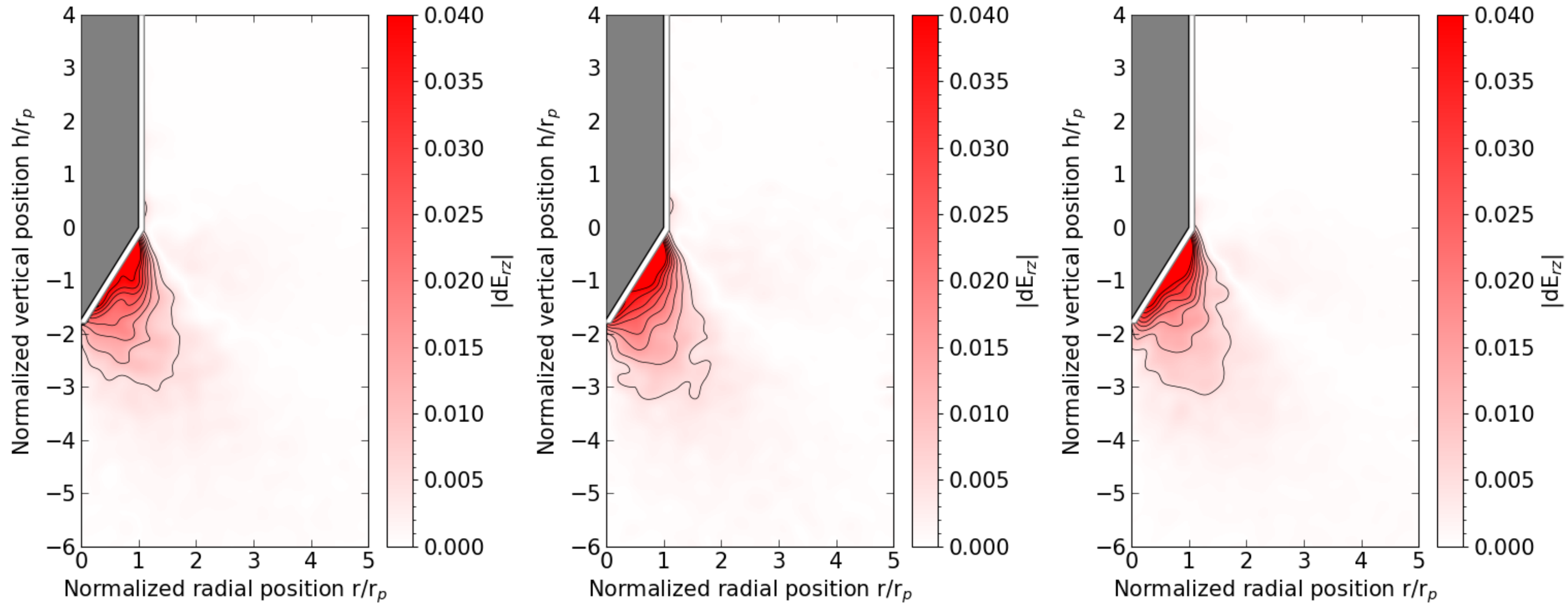

(a) (b) (c)

Figure A 17 Incremental shear strain field around cone penetrometer for a 2 mm penetration increment in dense OGF sand under a vertical pressure of (a) 17 kPa, (b) 33 kPa, and (c) 57 kPa.

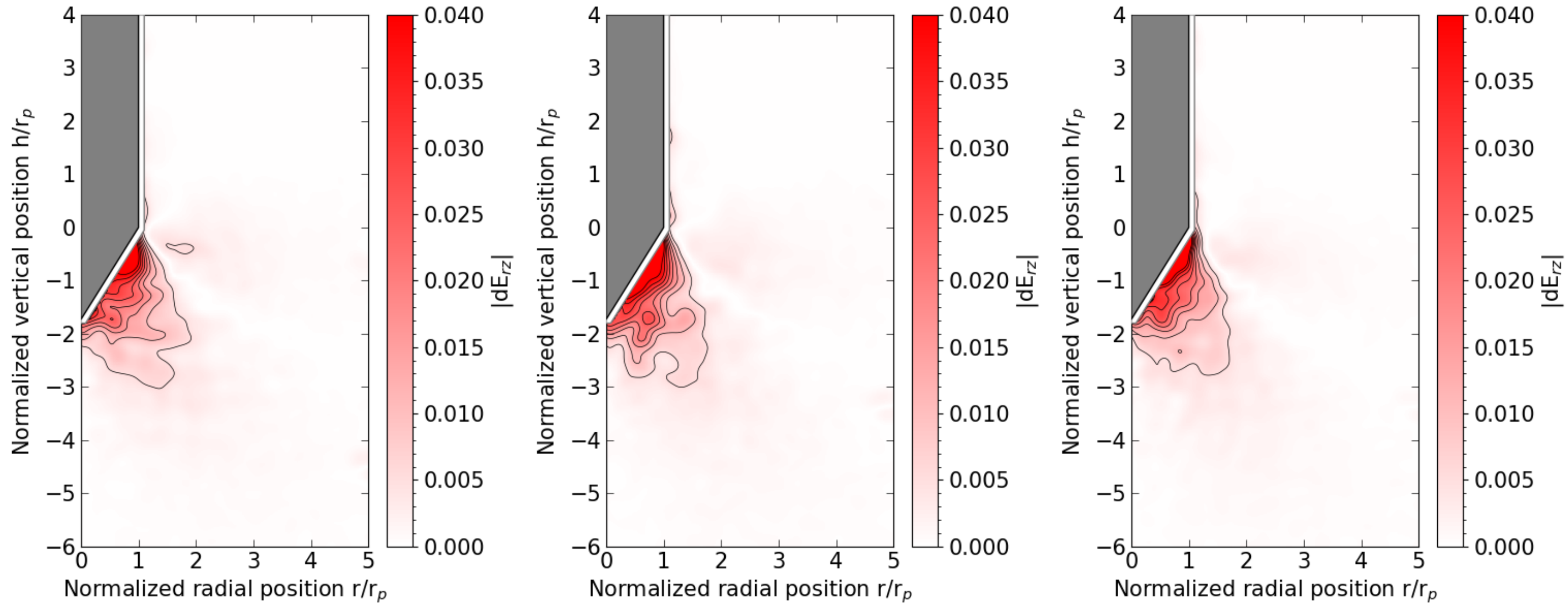

(a) (b) (c)

Figure A 18 Incremental shear strain field around cone penetrometer for a 2 mm penetration increment in dense OTC sand under a vertical pressure of (a) 17 kPa, (b) 33 kPa, and (c) 57 kPa.

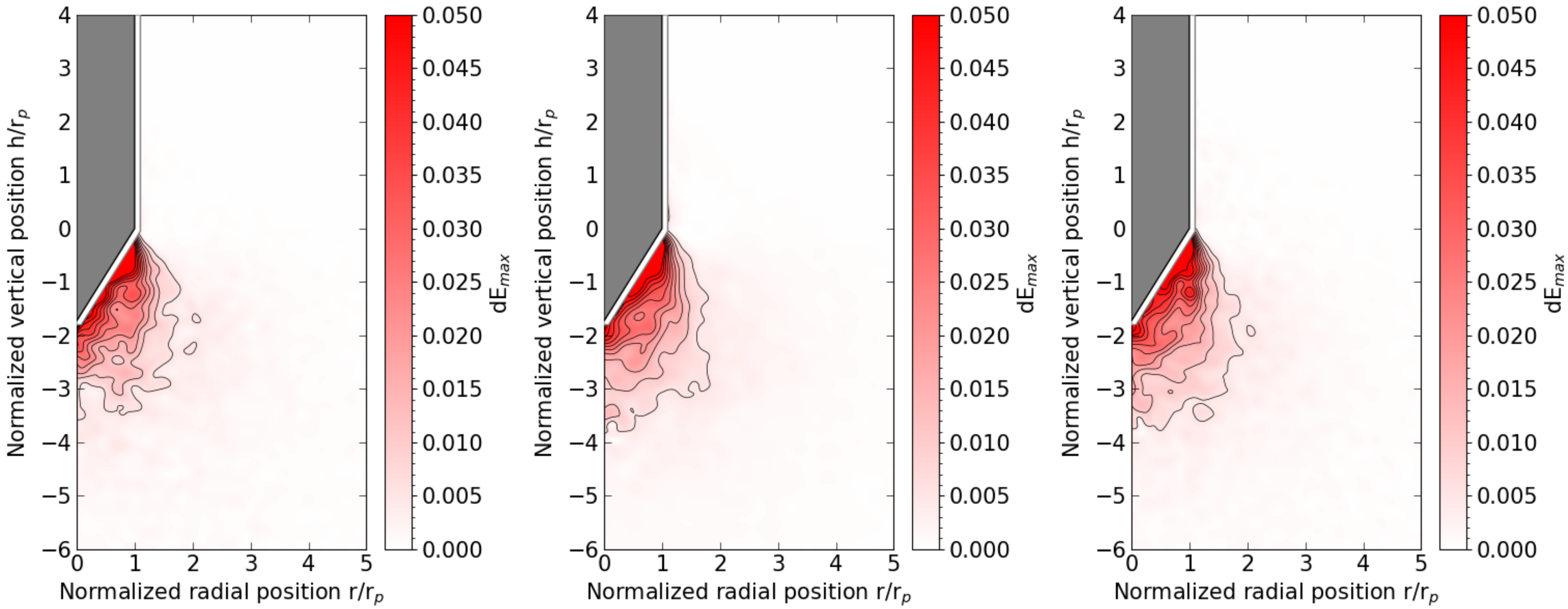

(a) (b) (c)

Figure A 19 Incremental max shear strain field around cone penetrometer for a 2 mm penetration increment in dense 2QR sand under a vertical pressure of (a) 17 kPa, (b) 33 kPa, and (c) 57 kPa.

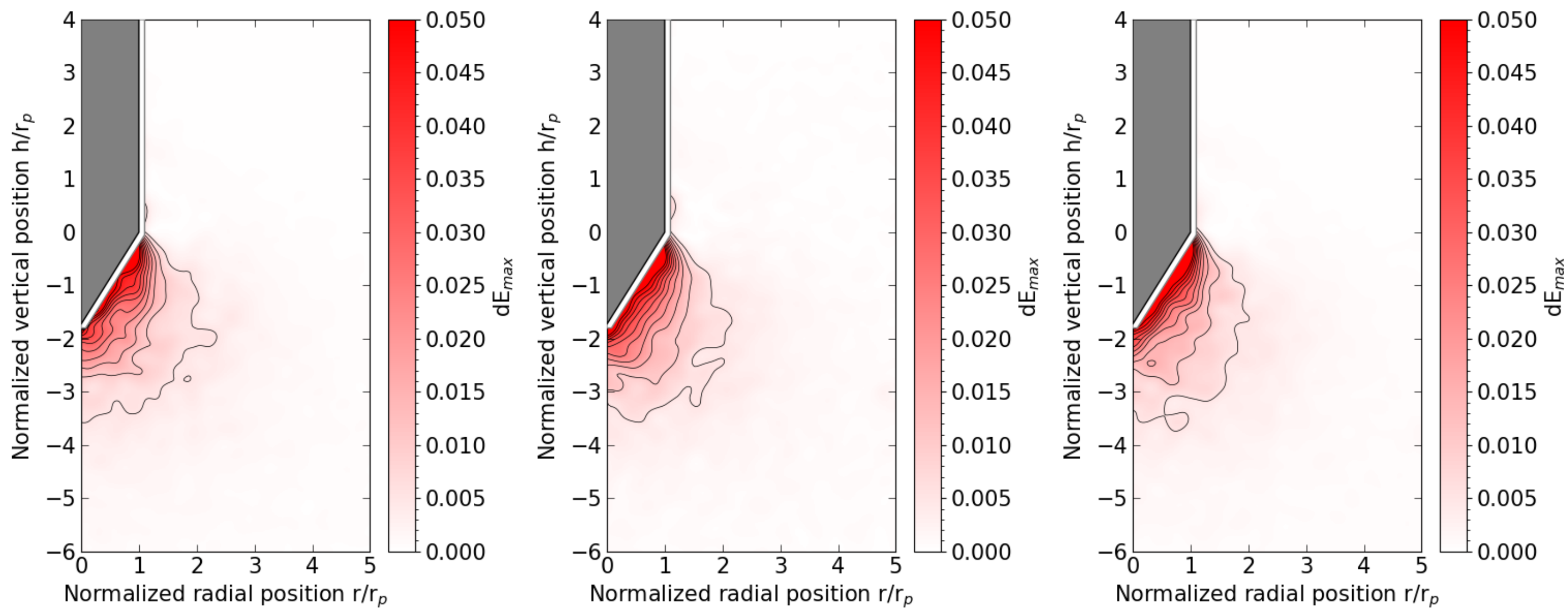

(a) (b) (c)

Figure A 20 Incremental max shear strain field around cone penetrometer for a 2 mm penetration increment in dense OGF sand under a vertical pressure of (a) 17 kPa, (b) 33 kPa, and (c) 57 kPa.

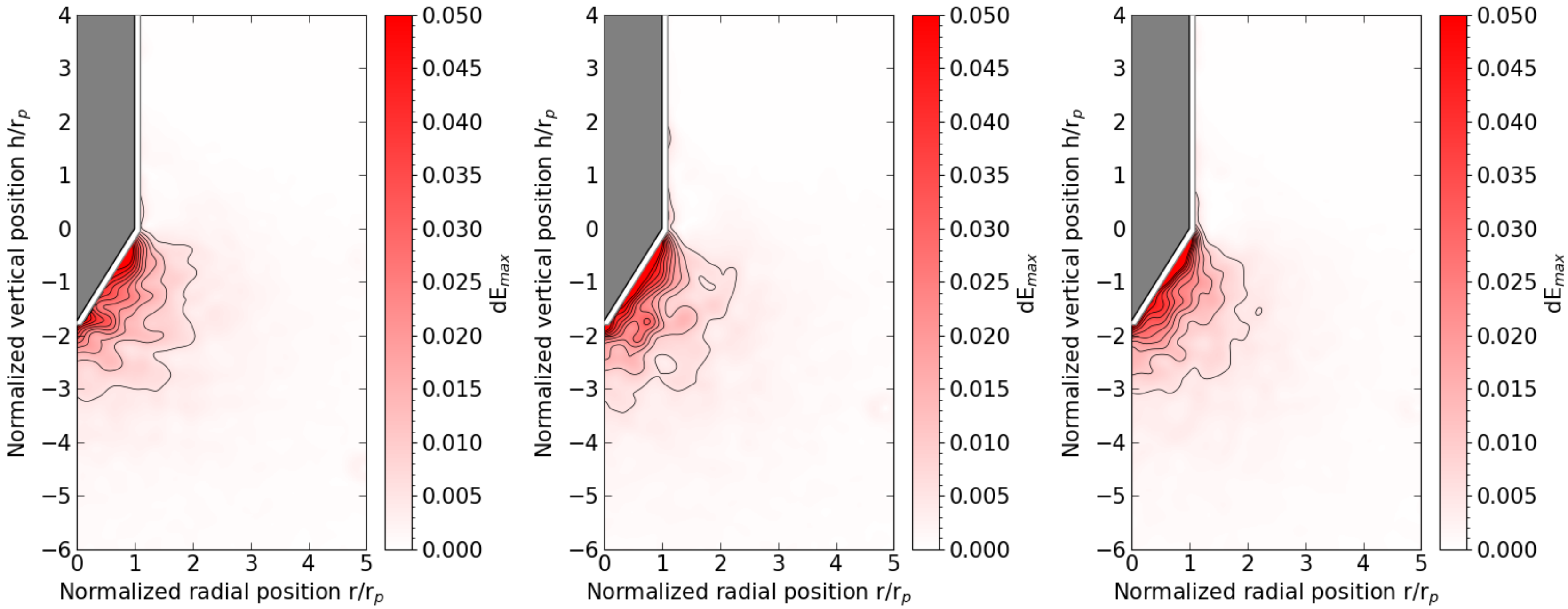

(a) (b) (c)

Figure A 21 Incremental max shear strain field around cone penetrometer for a 2 mm penetration increment in dense OTC sand under a vertical pressure of (a) 17 kPa, (b) 33 kPa, and (c) 57 kPa.

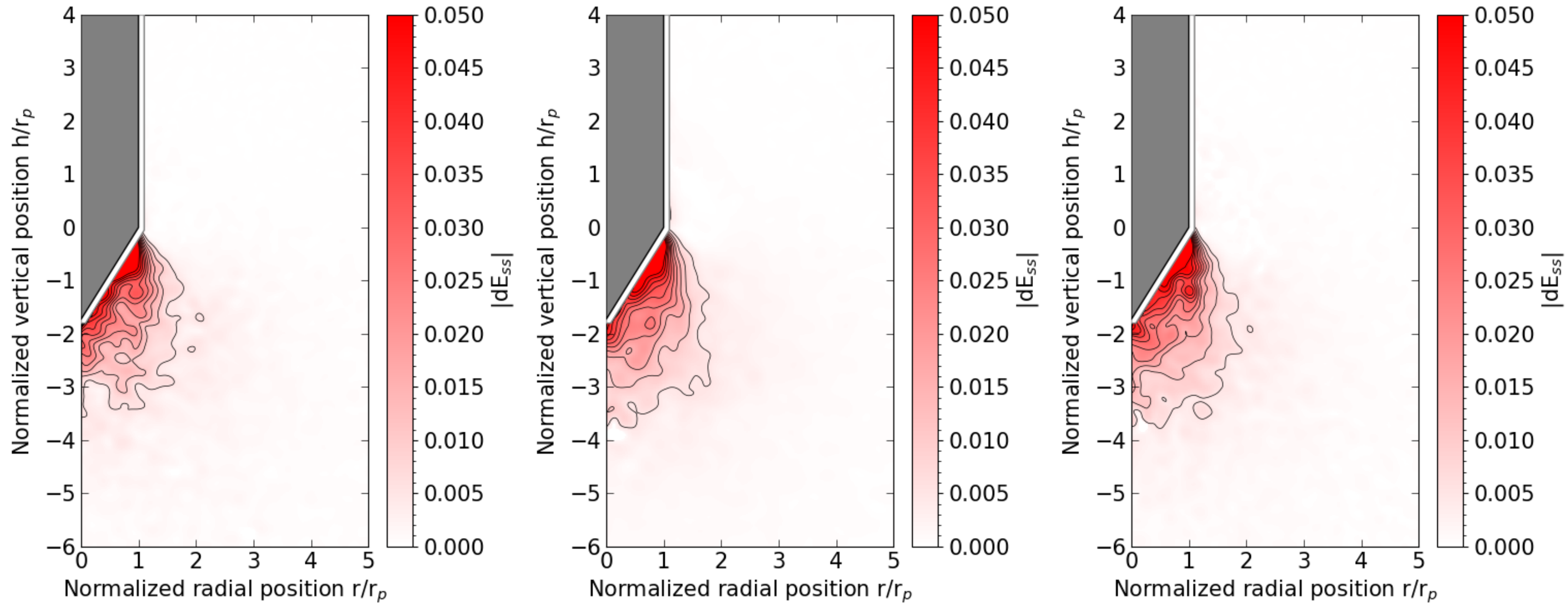

(a) (b) (c)

Figure A 22 Incremental shear strain (along zero extension lines) field around cone penetrometer for a 2 mm penetration increment in dense 2QR sand under a vertical pressure of (a) 17 kPa, (b) 33 kPa, and (c) 57 kPa.

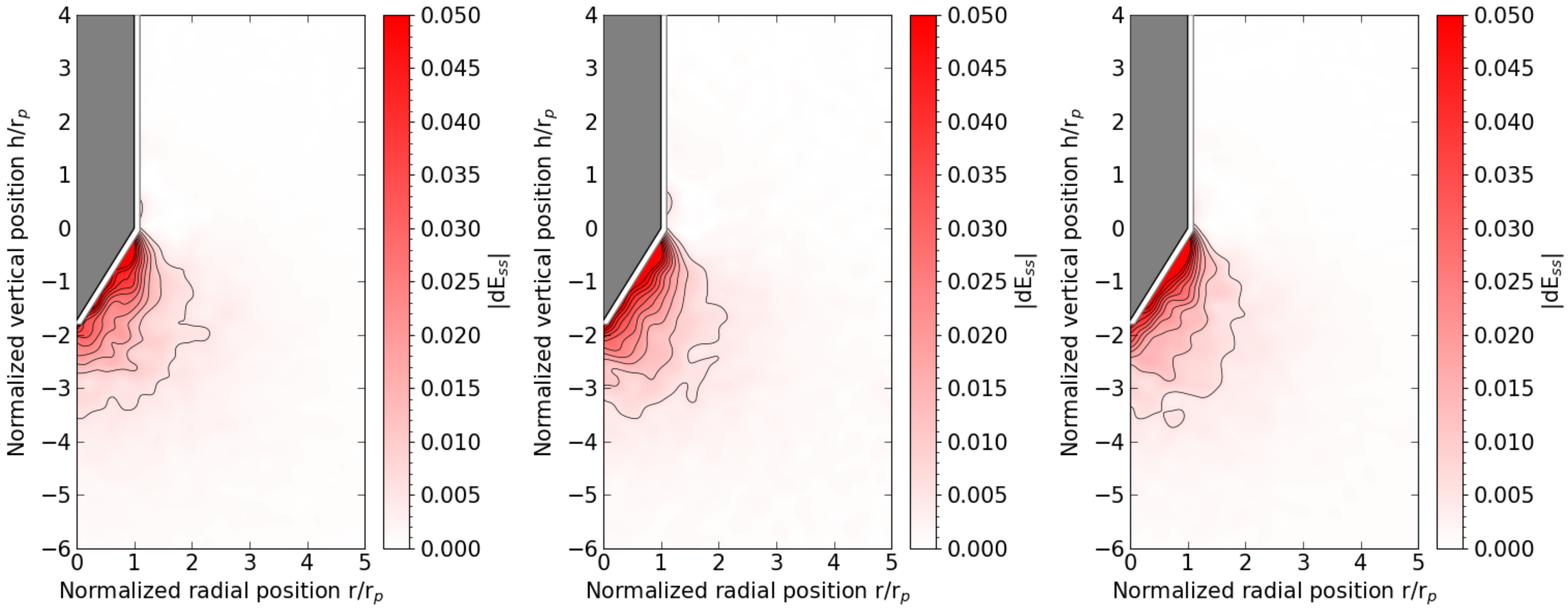

(a) (b) (c)

Figure A 23 Incremental shear strain (along zero extension lines) field around cone penetrometer for a 2 mm penetration increment in dense OGF sand under a vertical pressure of (a) 17 kPa, (b) 33 kPa, and (c) 57 kPa.

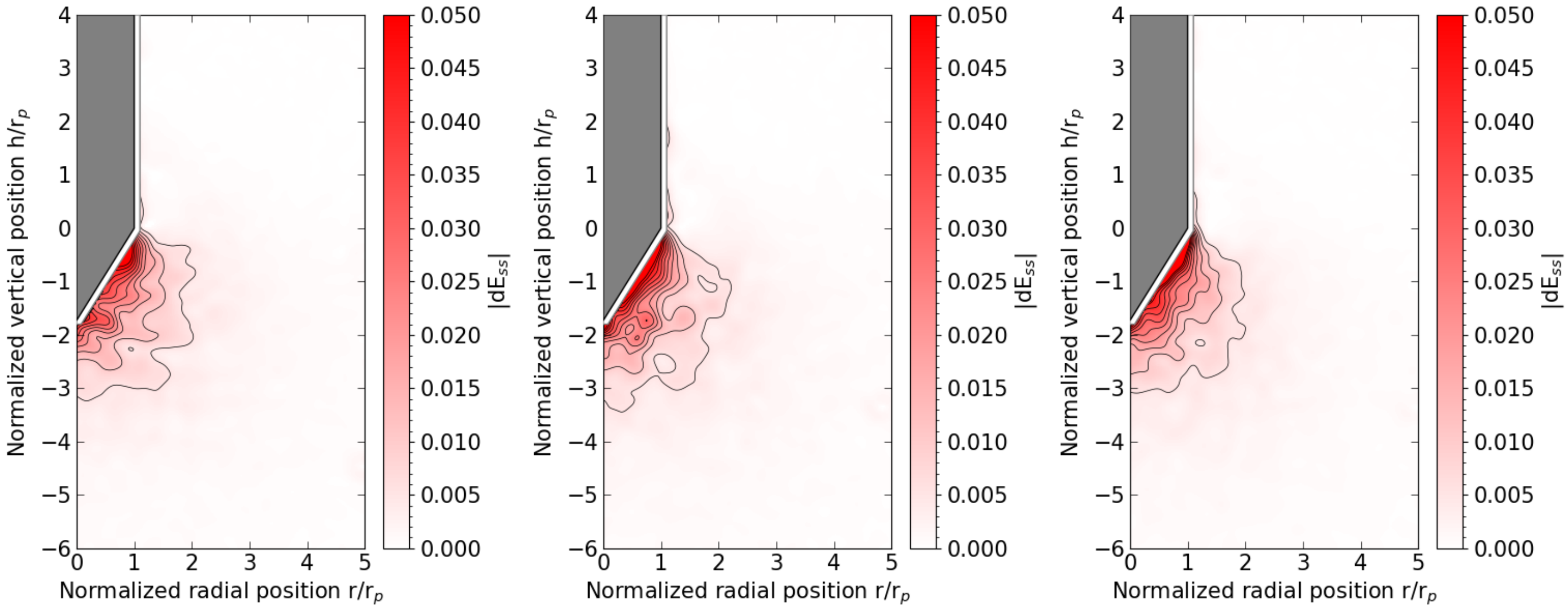

(a) (b) (c)

Figure A 24 Incremental shear strain (along zero extension lines) field around cone penetrometer for a 2 mm penetration increment in dense OTC sand under a vertical pressure of (a) 17 kPa, (b) 33 kPa, and (c) 57 kPa.

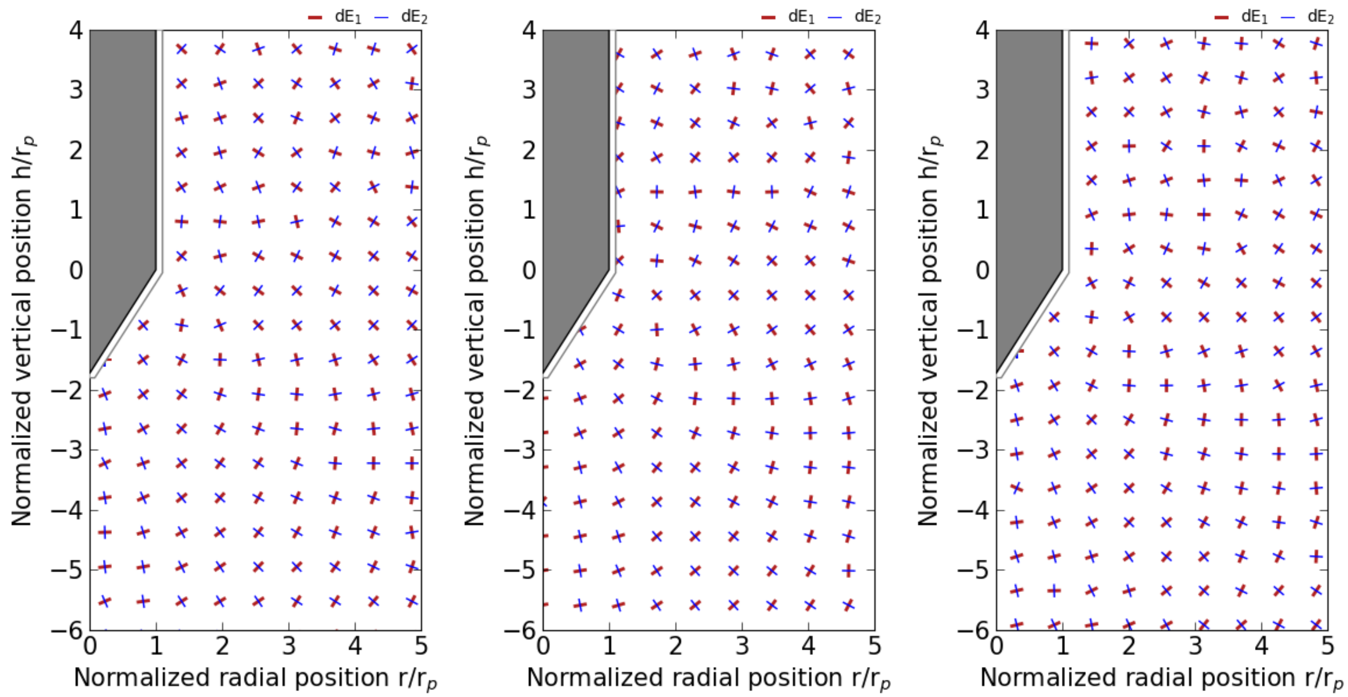

(a) (b) (c)

Figure A 25 Orientations of major (dE_1) and minor (dE_2) principal strains around cone penetrometer for a 2 mm penetration increment in dense 2QR sand under a vertical pressure of (a) 17 kPa, (b) 33 kPa, and (c) 57 kPa.

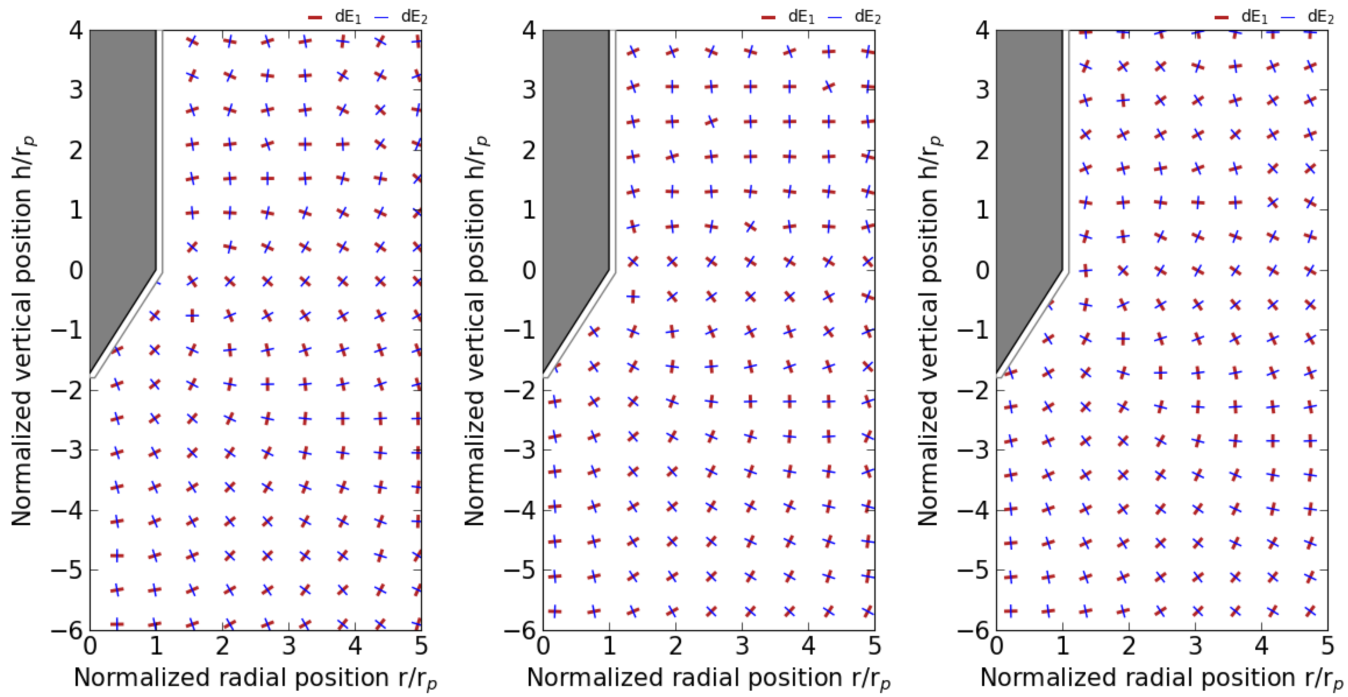

(a) (b) (c)

Figure A 26 Orientations of major (dE_1) and minor (dE_2) incremental principal strains around cone penetrometer for a 2 mm penetration increment in dense OGF sand under a vertical pressure of (a) 17 kPa, (b) 33 kPa, and (c) 57 kPa.

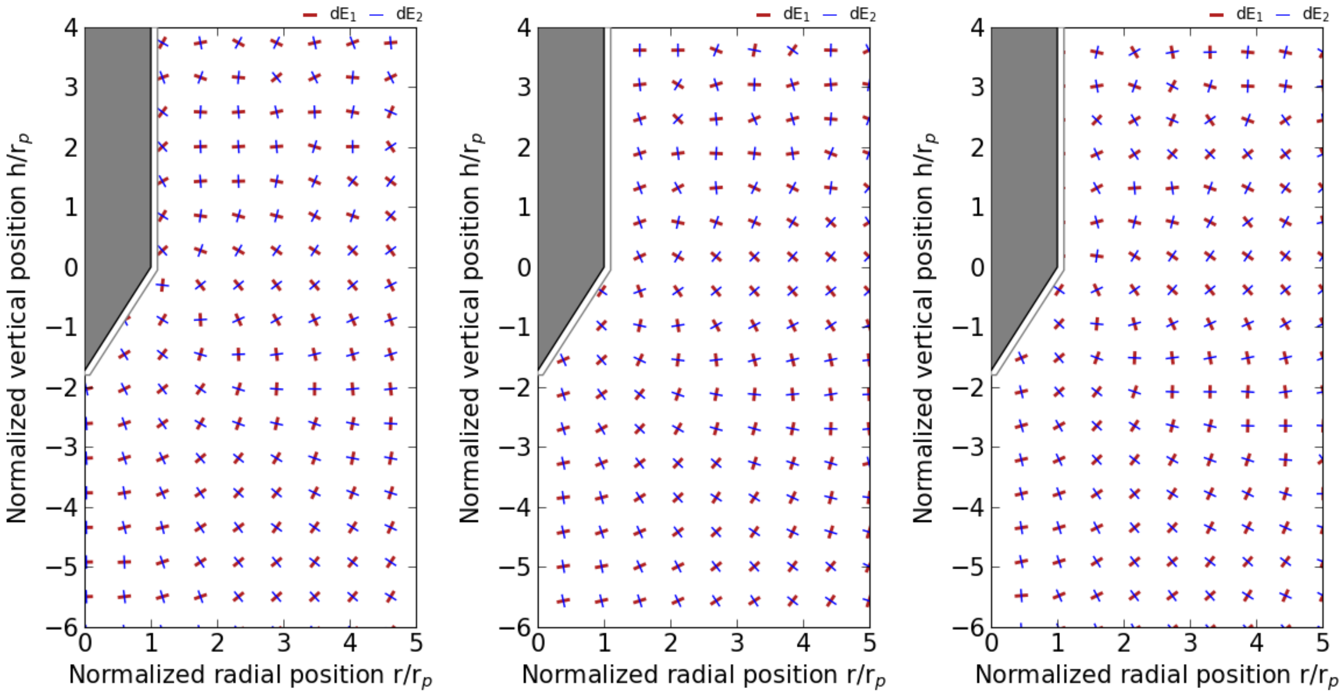

(a) (b) (c)

Figure A 27 Orientations of major (dE_1) and minor (dE_2) incremental principal strains around cone penetrometer for a 2 mm penetration increment in dense OTC sand under a vertical pressure of (a) 17 kPa, (b) 33 kPa, and (c) 57 kPa.

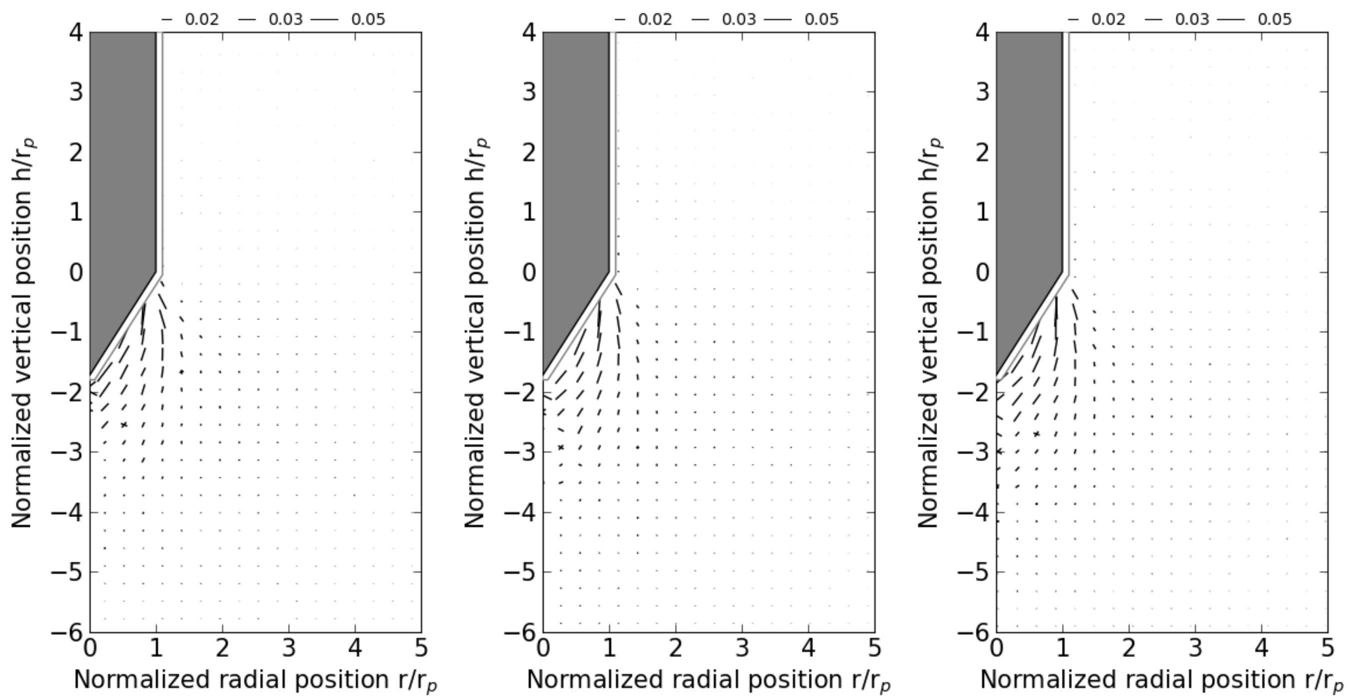

(a) (b) (c)

Figure A 28 Orientations of dominant shear band patterns around cone penetrometer for a 2 mm penetration increment in dense 2QR sand under a vertical pressure of (a) 17 kPa, (b) 33 kPa, and (c) 57 kPa.

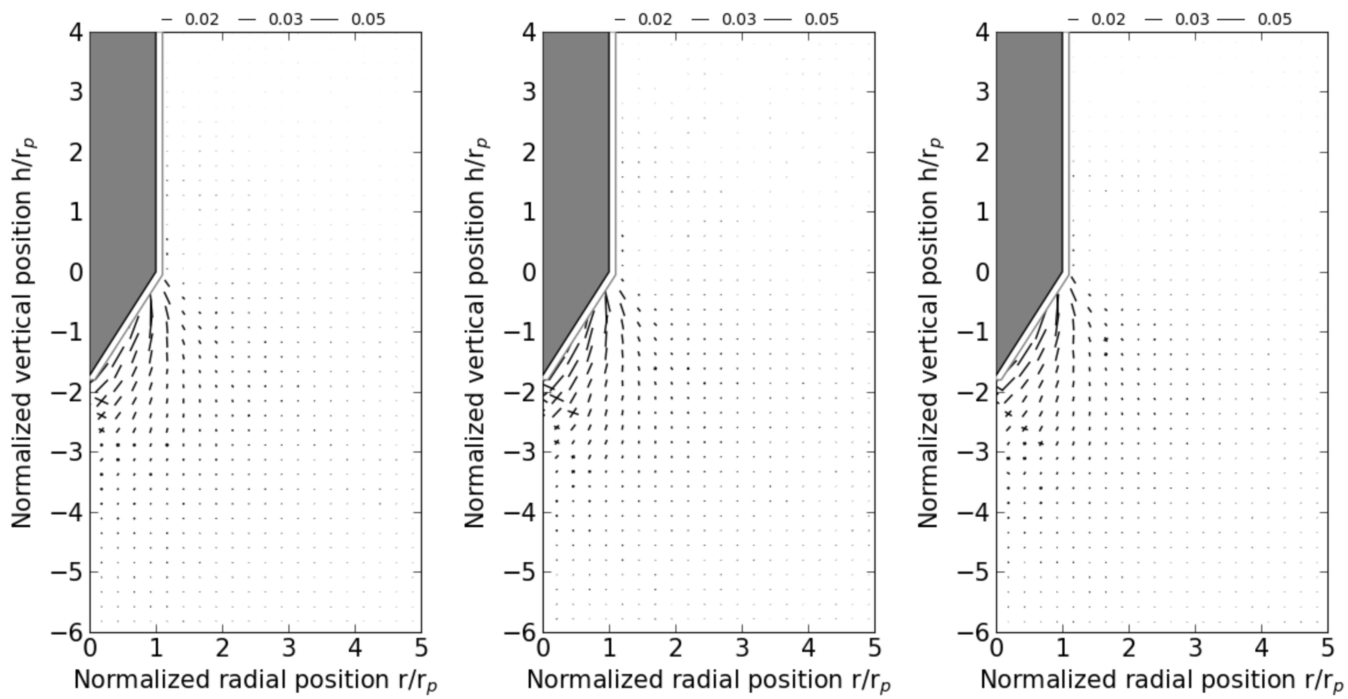

(a) (b) (c)

Figure A 29 Orientations of dominant shear band patterns around cone penetrometer for a 2 mm penetration increment in dense OGF sand under a vertical pressure of (a) 17 kPa, (b) 33 kPa, and (c) 57 kPa.

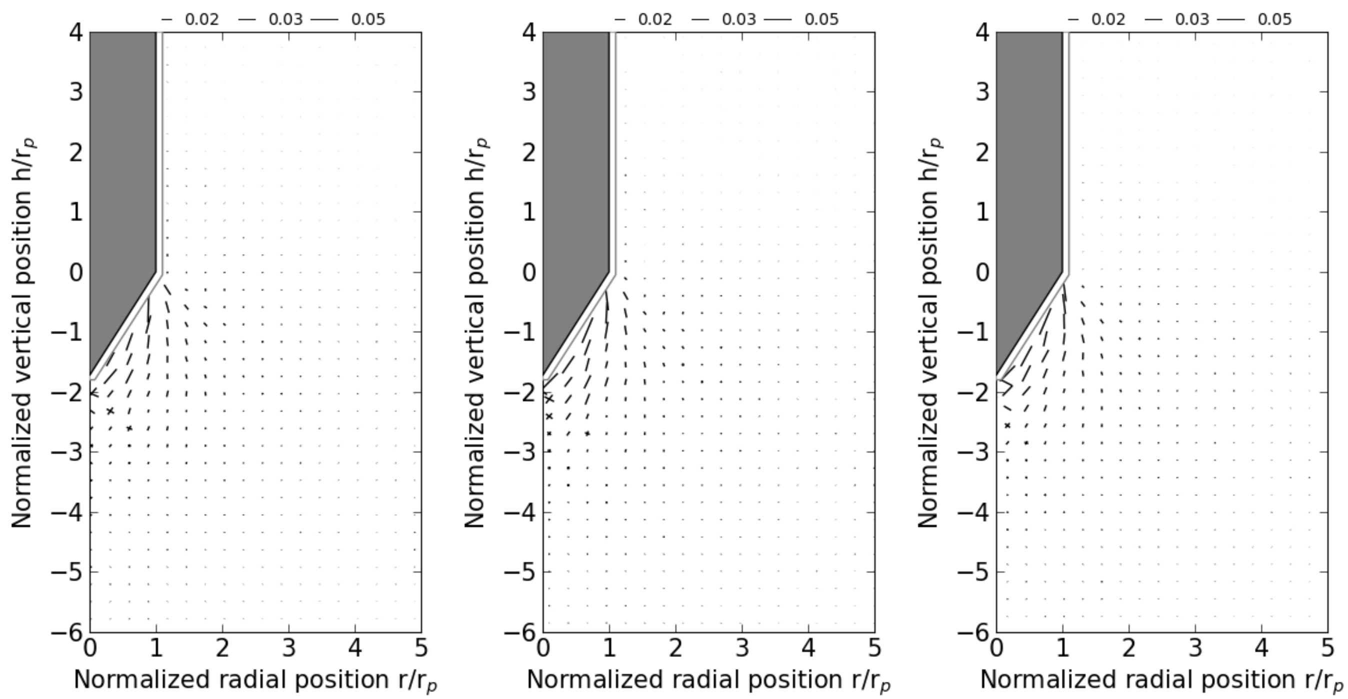

(a) (b) (c)

Figure A 30 Orientations of dominant shear band patterns around cone penetrometer for a 2 mm penetration increment in dense OTC sand under a vertical pressure of (a) 17 kPa, (b) 33 kPa, and (c) 57 kPa.

VITA

Eshan Ganju was born in Manali, India in 1990. He received his Bachelor of Technology (B. Tech) in Civil Engineering from Jaypee University of Engineering Technology (JUIT), India in 2012. After completion of B. Tech, he joined the Master of Science in Civil Engineering (MSCE) program at Purdue University in 2012. In the spring of 2013, he joined the research group headed by Dr. Monica Prezzi and Dr. Rodrigo Salgado [Center for Offshore, Foundation, and Energy Engineering (COFFEE)] as a graduate research assistant. He completed the MSCE in 2014 and continued on to a Ph.D. in Civil Engineering in the same research group.

PUBLICATIONS

Ganju, E., Galvis-Castro, A., Janabi, F., Prezzi, M., and Salgado, R. (2021). “Displacements, strains, and shear bands in deep and shallow penetration processes.” Journal of Geotechnical and Geoenvironmental Engineering. (ACCPETED)

Ganju, E., Han, F., Prezzi, M., and Salgado, R. (2021). “The axial capacity of closed-ended pipe piles driven in gravelly sands.” IFCEE-2021.

Ganju, E., Han, F., Prezzi, M., and Salgado, R. (2020). “Static capacity of closed-ended pipe pile driven in gravelly sand.” Journal of Geotechnical and Geoenvironmental Engineering, 146(4), 04020008.

Ganju, E., Han, F., Castro, A., Prezzi, M., and Salgado, R. (2020). “Experimental Study of Crushing in Cone Penetration Test in Silica Sand.” Geo-Congress 2020, American Society of Civil Engineers, Reston, VA, 132–141.

Ganju, E., Han, F., Prezzi, M., Salgado, R., and Pereira, J. S. (2020). “Quantification of displacement and particle crushing around a penetrometer tip.” Geoscience Frontiers, Elsevier, 11(2), 389–399.

Ganju, E., Salgado, R., and Prezzi, M. (2019). “Site Variability Characterization Using Cone Penetration Test Data.” Geotechnical Special Publication.

Ganju, E., Kim, H., Prezzi, M., Salgado, R., and Siddiki, N. Z. (2018). “Quality assurance and quality control of subgrade compaction using the dynamic cone penetrometer.” International Journal of Pavement Engineering, 19(11), 966–975.

Ganju, E., Prezzi, M., and Salgado, R. (2017). “Algorithm for generation of stratigraphic profiles using cone penetration test data.” Computers and Geotechnics, Elsevier Ltd, 90(10), 73–84.